UCRL 15281

R 7954

DATA REPORT OF A PRETEST ANALYSIS OF SOIL-STRUCTURE INTERACTION AND STRUCTURAL RESPONSE IN LOW-AMPLITUDE EXPLOSIVE TESTING (50 KG) OF THE HEISSDAMPFREAKTOR (HDR)

MASTER

MASTER

D. K. Vaughan
I. Sandler
D. Rubin
J. Isenberg
H. Nikooyeh

Submitted to:

University of California
Lawrence Livermore Laboratory
P. O. Box 808
Livermore, California 94550

Attn: D. Larder DOE/LLL

Submitted by:

Weidlinger Associates
3000 Sand Hill Road
Building 4, Suite 245
Menlo Park, California 94025
Telephone: 415/854-0461

-and-

110 East 59th Street
New York, New York 10022
Telephone: 212/838-2830

29 November 1979

TABLE OF CONTENTS

Section		Page
1	INTRODUCTION	1
2	ANALYTIC MODEL	2
	2.1 Site Model	2
	2.2 Source Model	6
	2.3 Structure Model	6
	2.4 Structural Damping	10
	2.5 Complete TRANAL Model	11
3	FREE FIELD, SOIL-STRUCTURE AND STRUCTURAL RESPONSE	44
	3.1 Free Field	44
	3.2 Soil-Structure Interaction	45
	3.3 Structural Response	47
	3.4 Filtering of Analysis Results	48
4	SUMMARY AND COMMENTS	144
	REFERENCES	146
	APPENDIX A — DETERMINATION OF SITE MODEL AND FREE FIELD MOTIONS	A-1
	A-1 Introduction	A-1
	A-2 Site Profile	A-2
	A-3 Material Models	A-3
	A-4 Source Representation	A-5
	A-5 Summary and Comments	A-10
	References	A-25

LIST OF FIGURES

Figure		Page
2-1	Site profile used in HDR analysis	17
2-2a	Typical yield surface in the cap model for compressive stresses.	18
2-2b	Cap model used to represent properties of soil in HDR analysis. Stress point on cap pushes cap out. When stress point is on failure surface, cap moves in to control dilatancy	19
2-2c	Role of kinematic hardening in producing hysteresis loops for cyclic triaxial stress path	20
2-3	Stress-strain properties (uniaxial strain) of each layer in HDR site profile	21
2-4	Stress path experienced by soils in layers 1 and 4 of HDR site profile when subjected to uniaxial strain.	22
2-5	Model of source used as input for free field and soil-structure interaction analysis.	23
2-6a	Elevation view of HDR containment structure	24
2-6b	Details of HDR foundation	25
2-7	TRANAL model of HDR containment structure	26
2-8a	Variation of mass with height in HDR containment structure and in TRANAL model	27
2-8b	Concrete material properties used in TRANAL structural model of HDR reactor.	28
2-9	Mode shapes and natural frequencies of HDR reactor measured in situ during forced vibration testing (from Ref. 6)	29
2-10	Fixed base mode shape of HDR model (only one plane of elements plotted) a. 1st mode, frequency 2.16 Hz.	30
2-10	(continued) Fixed base mode shape of HDR model b. 2nd mode, frequency 2.71 Hz.	31
2-10	(continued) Fixed base mode shape of HDR model c. 3rd mode, frequency 9.47 Hz.	32
2-10	(continued) Fixed base mode shape of HDR model d. 4th mode, frequency 10.14 Hz	33
2-10	(continued) Fixed base mode shape of HDR model e. 5th mode, frequency 10.85 Hz	34
2-10	(continued) Fixed base mode shape of HDR model f. 6th mode, frequency 16.23 Hz	35

LIST OF FIGURES (Continued)

Figure		Page
2-11	In situ mode shape of HDR model (only one plane of elements plotted) a. 1st mode, frequency 1.87 Hz.	36
2-11	In situ mode shape of HDR model b. 2nd mode, frequency 2.72 Hz.	37
2-11	In situ mode shape of HDR model c. 3rd mode, frequency 7.62 Hz.	38
2-11	In situ mode shape of HDR model d. 4th mode, frequency 11.35 Hz	39
2-12	Viscoelastic model of structural damping.	40
2-13	Fraction of critical damping as function of frequency used in structural elements of HDR model	41
2-14	Elevation view of TRANAL model of HDR site and containment foundation (superstructure not shown)	42
2-15	Isometric view of TRANAL model of HDR site and containment.	43
3-1	Free field horizontal velocity-time history at range 22.5m (74 ft) and three depths (positive is outward from source).	54
3-2	Free field vertical velocity-time history at range 22.5m (74 ft) and three depths (positive is down)	55
3-3	Free field velocity-time histories at a depth of 3m and a range of 22m from source (19m from symmetry plane).	56
3-3	(continued) Free field velocity-time histories at a depth of 3m and a range of 22m from source (19m from symmetry plane)	57
3-4	Free field stress-time histories and stress path for soil element on plane of symmetry at a range of 12m from explosive charge, depth of 5m.	58
3-4	(continued) Free field stress-time histories and stress path for soil element on plane of symmetry at a range of 12m from explosive charge, depth of 5m.	59
3-5	Vertical velocity-time histories at upstream and downstream corners of foundation; differences are primarily a measure of rocking.	60
3-6	Rocking velocity-time history of foundaton (difference between downstream and upstream corner vertical velocities) .	61
3-7	Vertical stress-time histories in soil just beneath upstream and downstream corners of foundation.	62
3-8	Stress in soil acting normal to upstream surface of containment structure.	63

LIST OF FIGURES (Continued)

Figure		Page
3-9	Horizontal acceleration-time history of foundation (elev -11.05m, centerline).	64
3-10	Vertical acceleration-time history of foundation (elev -11.05m, centerline).	65
3-11	Horizontal velocity-time history of foundation (elev -11.05m, centerline).	66
3-12	Vertical velocity-time history of foundaton (elev -11.05m, centerline).	67
3-13a	Response spectra of horizontal motion of foundation (elev -11.05m, centerline).	68
3-13b	Acceleration response spectra of horizontal motion of foundation (elev -11.05m, centerline)	69
3-14a	Response spectra of vertical motion of foundation (elev -11.05m, centerline).	70
3-14b	Acceleration response spectra of vertical motion of foundation (elev -11.05m, centerline)	71
3-15	Horizontal acceleration-time history near upstream corner of foundation (elev -11.05m, 11.35m forward of centerline).	72
3-16	Vertical acceleration-time history near upstream corner of foundation (elev -11.05m, 11.35m forward of centerline).	73
3-17	Horizontal velocity-time history near upstream corner of foundation (elev -11.05m, 11.35m forward of centerline).	74
3-18	Vertical velocity-time history near upstream corner of foundation (elev -11.05m, 11.35m forward of centerline).	75
3-19a	Response spectra of horizontal motion near upstream corner of foundation (elev -11.05m, 11.35m forward of centerline).	76
3-19b	Acceleration response spectra of horizontal motion near upstream corner of foundation (elev -11.05m, 11.35m forward of centerline).	77
3-20	Response spectra of vertical motion near upstream corner of foundation (elev -11.05m, 11.35m forward of centerline).	78
3-21	Horizontal acceleration-time history near downstream corner of foundation (elev -11.05m, 11.35m aft of centerline). . .	79
3-22	Vertical acceleration-time history near downstream corner of foundation (elev -11.05m, 11.35m aft of centerline). . .	80
3-23	Horizontal velocity-time history near downstream corner of foundation (elev -11.05m, 11.35m aft of centerline). . .	81
3-24	Vertical velocity-time history near downstream corner of foundation (elev -11.05m, 11.35m aft of centerline). . .	82

LIST OF FIGURES (Continued)

Figure		Page
3-25a	Response spectra of horizontal motion near downstream corner of foundation (elev -11.05m, 11.35m aft of centerline)	83
3-25b	Acceleration response spectra of horizontal motion near downstream corner of foundation (elev -11.05m, 11.35m aft of centerline)	84
3-26	Response spectra of vertical motion near downstream corner of foundation (elev -11.05m, 11.35m aft of centerline)	85
3-27	Horizontal acceleration-time history at top of inner structure (elev 47.35m, centerline)	86
3-28	Vertical acceleration-time history at top of inner structure (elev 47.35m, centerline)	87
3-29	Horizontal velocity-time history at top of inner structure (elev 47.35m, centerline)	88
3-30	Vertical velocity-time history at top of inner structure (elev 47.35m, centerline)	89
3-31a	Response spectra of horizontal motion at top of inner structure (elev 47.35m, centerline)	90
3-31b	Acceleration response spectra of horizontal motion at top of inner structure (elev 47.35m, centerline)	91
3-32	Response spectra of vertical motion at top of inner structure (elev 47.35m, centerline)	92
3-33	Horizontal acceleration-time history on inner structure (elev 30.85m, 3.2m outside and forward of centerline)	93
3-34	Vertical acceleration-time history on inner structure (elev 30.85m, 3.2m outside and forward of centerline)	94
3-35	Horizontal velocity-time history on inner structure (elev 30.85m, 3.2m outside and forward of centerline)	95
3-36	Vertical velocity-time history on inner structure (elev 30.85m, 3.2m outside and forward of centerline)	96
3-37	Response spectra of horizontal motion on inner structure (elev 30.85m, 3.2m outside and forward of centerline)	97
3-38	Response spectra of vertical motion on inner structure (elev 30.85m, 3.2m outside and forward of centerline)	98
3-39	Horizontal acceleration-time history on inner structure (elev 17.25m, centerline)	99
3-40	Vertical acceleration-time history on inner structure (elev 17.25m, centerline)	100

LIST OF FIGURES (Continued)

Figure		Page
3-41	Horizontal velocity-time history on inner structure (elev 17.25m, centerline).	101
3-42	Vertical velocity-time history on inner structure (elev 17.25m, centerline).	102
3-43	Response spectra of horizontal motion on inner structure (elev 17.25m, centerline).	103
3-44	Response spectra of vertical motion on inner structure (elev 17.25m, centerline).	104
3-45	Horizontal acceleration-time history on inner structure (elev 8.70m, centerline)	105
3-46	Vertical acceleration-time history on inner structure (elev 8.70m, centerline)	106
3-47	Horizontal velocity-time history on inner structure (elev 8.70m, centerline)	107
3-48	Vertical velocity-time history on inner structure (elev 8.70m, centerline)	108
3-49	Response spectra of horizontal motion on inner structure (elev 8.70m, centerline)	109
3-50	Response spectra of vertical motion on inner structure (elev 8.70m, centerline)	110
3-51	Horizontal acceleration-time history at top of outer structure (elev 50.35m, centerline)	111
3-52	Vertical acceleration-time history at top of outer structure (elev 50.35m, centerline)	112
3-53	Horizontal velocity-time history at top of outer structure (elev 50.35m, centerline).	113
3-54	Vertical velocity-time history at top of outer structure (elev 50.35m, centerline).	114
3-55a	Response spectra of horizontal motion at top of outer structure (elev 50.35m, centerline).	115
3-55b	Acceleration response spectra of horizontal motion at top of outer structure (elev 50.35m, centerline)	116
3-56	Response spectra of vertical motion at top of outer structure (elev 50.35m, centerline)	117
3-57	Horizontal acceleration-time history on outer structure (elev 31.73m, 11.35m forward of centerline).	118
3-58	Vertical acceleration-time history on outer structure (elev 31.73m, 11.35m forward of centerline).	119

LIST OF FIGURES (Continued)

Figure		Page
3-59	Horizontal velocity-time history on outer structure (elev 31.73m, 11.35m forward of centerline).	120
3-60	Vertical velocity-time history on outer structure (elev 31.73m, 11.35m forward of centerline).	121
3-61	Response spectra of horizontal motion on outer structure (elev 31.73m, 11.35m forward of centerline).	122
3-62	Response spectra of vertical motion on outer structure (elev 31.73m, 11.35m forward of centerline).	123
3-63	Horizontal acceleration-time history on outer structure (elev 15.87m, 11.35m forward of centerline).	124
3-64	Vertical acceleration-time history on outer structure (elev 15.87m, 11.35m forward of centerline).	125
3-65	Horizontal velocity-time history on outer structure (elev 15.87m, 11.35m forward of centerline).	126
3-66	Vertical velocity-time history on outer structure (elev 15.87m, 11.35m forward of centerline).	127
3-67	Response spectra of horizontal motion on outer structure (elev 15.87m, 11.35m forward of centerline).	128
3-68	Response spectra of vertical motion on outer structure (elev 15.87m, 11.35m forward of centerline).	129
3-69	Horizontal velocity-time history perpendicular to symmetry plane of inner containment structure (elev 30.85m, 6.85m in from symmetry plane).	130
3-70	Horizontal velocity-time history perpendicular to symmetry plane of outer structure (elev -3m, 9.85m in from symmetry plane)	131
3-71a	Filtered and unfiltered horizontal velocity-time histories of inner structure at piping attach point (elev 17.25m, centerline).	132
3-71b	Filtered and unfiltered horizontal velocity-time histories at top of inner structure (elev 47.35m, centerline). . . .	133
3-71c	Filtered and unfiltered horizontal velocity-time histories at top of outer structure (elev 50.35m, centerline). . . .	134
3-71d	Filtered and unfiltered vertical velocity-time histories at top of outer structure (elev 50.35m, centerline). . . .	135
3-71e	Filtered and unfiltered horizontal velocity-time histories on outer structure (elev 15.87m, 11.35m forward of centerline).	136

LIST OF FIGURES (Continued)

Figure		Page
3-71f	Filtered and unfiltered vertical velocity-time histories on outer structure (elev 15.87m, 11.35m forward of centerline).	137
3-72a	Unfiltered acceleration response spectra of horizontal motion of foundation (elev -11.05m, centerline).	138
3-72b	Unfiltered acceleration response spectra of vertical motion of foundation (elev -11.05m, centerline).	139
3-72c	Unfiltered acceleration response spectra of horizontal motion near upstream corner of foundation (elev -11.05m, 11.35m forward of centerline).	140
3-72d	Unfiltered acceleration response spectra of horizontal motion near downstream corner of foundation (elev -11.05m, 11.35m aft of centerline).	141
3-72e	Unfiltered acceleration response spectra of horizontal motion at top of inner structure (elev 47.35m, centerline)	142
3-72f	Unfiltered acceleration response spectra of horizontal motion at top of outer structure (elev 50.35m, centerline)	143
A-1	Site profile used in HDR analysis.	A-12
A-2	Cap model used to represent properties of soil in HDR analysis. Stress point on cap pushes cap out. When stress point is on failure surface, cap moves in to control dilatancy.	A-13
A-3	Stress-strain properties (uniaxial strain) of each layer in HDR site profile.	A-14
A-4	Stress path experienced by soils in layers 1 and 4 of HDR site profile when subjected to uniaxial strain	A-15
A-5	Model of source used as input for free field and soil-structure interaction analysis	A-16
A-6	HDR Free Field (Horizontal).	A-17
A-7	HDR Free Field (Vertical).	A-18
A-8	HDR Free Field (Horizontal).	A-19
A-9	HDR Free Field (Vertical).	A-20
A-10	HDR Free Field (Horizontal).	A-21
A-11	HDR Free Field (Vertical).	A-22
A-12	HDR Free Field (Horizontal).	A-23
A-13	HDR Free Field (Vertical).	A-24

LIST OF TABLES

		Page
2-1	CAP MODEL PARAMETERS FOR HDR SITE MODEL	14
2-2	SOIL WAVESPEEDS FOR HDR SITE MODEL.	15
2-3	NATURAL FREQUENCIES OF GENSAP FIXED-BASE AND IN-SITU FINITE ELEMENT MODELS OF HDR REACTOR.	16
3-1	PEAK ACCELERATIONS AND VELOCITIES OUTPUT AT SELECTED POINTS IN HDR STRUCTURAL MODEL FOR SEVERAL FILTER FREQUENCIES	53
A-1	SITE PROFILE FROM REFERENCE A-1	A-11
A-2	WAVESPEEDS IN VARIOUS LAYERS.	A-11

1. INTRODUCTION

This report describes a three-dimensional nonlinear TRANAL finite element analysis of a nuclear reactor subjected to ground shaking from a buried 50 kg explosive source. The analysis is a pretest simulation of a test event which was scheduled to be conducted in West Germany on 3 November 1979.

The scope of the present analysis includes the following:

1. A site model was developed using a nonlinear cap constitutive model fit to data from field observations of wave-speeds and laboratory measurements of shear strength.

2. A model of the explosive source was developed as a spherical cavity with a prescribed pressure-time history.

3. A three-dimensional TRANAL finite element model of the containment, reactor vessel and basemat was developed having the frequency and damping characteristics measured in previous tests.

4. A three-dimensional, nonlinear TRANAL finite element model which combines source, site and structure models was developed.

5. The soil-structure system was analyzed for four seconds of real time. The output of interest includes velocity-time histories at points of attachment of the piping system; velocities are converted to acceleration-time histories by numerical differentiation.

Section 2 of the present report describes the finite element models. Section 3 contains selected results. Observations and conclusions are discussed in Section 4.

2. ANALYTIC MODEL

This section describes the analytic models of the site, source and structure and shows the combined TRANAL model of soil-structure interaction and structural response.

2.1 Site Model

The site profile, based on geologic investigations reported in Refs. 1, 2 is shown in Fig. 2-1. The properties of each layer are represented by a cap model, Ref. 3, whose properties are illustrated in Figs. 2-2a and b. The model is elastic-plastic with an ideally plastic failure surface and an isotropic hardening cap. As shown in Fig. 2-2a, three different modes of behavior are possible for the cap model: elastic, failure and cap. Elastic behavior occurs when the stress point is within the failure envelope and hardening cap. Stress changes result in recoverable deformations. Although various types of nonlinearily elastic behavior can be modeled, the elastic component here is linear. For an isotropic material, such behavior can be described by a constant bulk modulus, K, and a constant shear modulus, G. In the elastic regime, the volumetric and deviatoric components of stress and strain are uncoupled, such that a purely volumetric change in strain does not affect the deviatoric stress components and a purely deviatoric strain increment produces no change in pressure.

During the failure mode of behavior the stress point lies on the failure envelope. In the basic cap model the failure surface is assumed to be fixed in stress space and to be represented by

$$\sqrt{J_2'} = A - C \exp(-3Bp) \qquad (2\text{-}1)$$

where A, B and C are material constants and p is the mean pressure.

The cap mode of behavior occurs when the stress point lies on the movable cap and pushes it outward. The motion of the cap is related to the plastic strain by means of a hardening rule, an example of which is given below. An elliptical surface of the form

$$(p - p_a)^2 + \frac{1}{9} R^2 J_2' = (p_b - p_a)^2 \tag{2-2}$$

has been found acceptable for a wide range of geologic materials. In Eq. 2-2, p_a and p_b represent the values of p at points a and b in Fig. 2-2a, while R is assumed to be constant in the present analysis. The pressures p_a and p_b, which define the extent of the cap are related. Figure 2-2a shows that, because point E lies on both the failure envelope and the cap,

$$\sqrt{J_2'}_E = A - C \exp(-3Bp_E) \tag{2-3}$$

and

$$(p_E - p_a)^2 + \frac{1}{9} R^2 J_{2E}' = (p_b - p_a)^2 . \tag{2-4}$$

Further, since $p_E = p_a$, Eqs. 2-3 and 2-4 lead to

$$p_b - p_a = \frac{1}{3} R \left[A - C \exp(-3Bp_a)\right] \tag{2-5}$$

as the relation between p_a and p_b. Therefore, specifying either p_a or p_b is sufficient to describe the position of the cap.

The cap position is related to the plastic strain history of the material through a hardening rule which is assumed to be

$$\bar{\varepsilon}_v^p = W \left[1 - \exp(-3Dp_B)\right] \tag{2-6}$$

in which W and D are material constants and $\bar{\varepsilon}_v^p$ is related to the plastic

strain history as follows. During purely cap or purely failure behavior, the value of $\bar{\varepsilon}_v^p$ changes precisely as the plastic portion of the volumetric strain. However, during combined failure and cap behavior, when the stress point lies at the intersection of the cap and failure envelope, the change in the value of $\bar{\varepsilon}_v^p$ is limited so that the stress point does not lie outside the cap.

As Fig. 2-2a shows, the associated flow rule requires that during cap action *the plastic strain rate vector be directed upward and to the right.* This implies that the plastic strain rate consists of an irreversible decrease in volume in conjunction with the irreversible shear strain. *This volume reduction,* or compaction, represents the volumetric hysteresis observed during compression of most geologic materials.

As cap action proceeds, the inelastic compaction resulting from the associated flow rule leads to an increase in cap parameter $\bar{\varepsilon}_v^p$, which through Eq. 2-6 leads in turn to an increase of p_b. Therefore, the cap moves to the right in Fig. 2-2b, increasing the extent of the elastic region. Either p or J_2' or both must increase in such a way as to keep the stress point on the cap in order to maintain this mode of behavior.

The soil cap model described above was developed primarily for use in computations of explosions which are characterized by a single peak compressive stress followed by several smaller peaks. As a rule, hysteresis in cyclic loading subsequent to an initial shock is generally viewed as having secondary importance. However, hysteresis becomes quite important for earthquake-induced loadings where cyclic shear is the predominant effect.

In the current simulation of free field response to a 50 kg explosive source, the cap in each soil element of the HDR finite element model is

pushed out by the initial peak of the shock wave induced by the explosion. There is then unloading followed by low amplitude oscillations related to reflections within and vibration of the several layers; this aspect of site response is illustrated in Section 3, which deals with free field response. During unloading, inelasticity may occur but, at later times, oscillations occur entirely within the elastic region defined by the cap and failure surface. There is no hysteresis or material damping for these oscillations in the present model.

In fact, the cap model used for the HDR analysis is a special case of a more general cap model in which hysteretic material damping for low amplitude oscillations is provided, Ref. 4. The extended model has the feature, shown in Fig. 2-2c, of a kinematic hardening yield surface which lies within the failure surface. In this more realistic model, it is not necessary for shear failure to occur in order for inelasticity, and hence hysteresis and material damping to occur. As Fig. 2-2c shows, inelasticity occurs each time the stress point encounters the yield surface.

Although this option was available at the time of the HDR calculation, the experimental data required to fit the three additional material constants were not available. The required data include cyclic triaxial compression tests at various levels of confining pressure. In the absence of such data, it was decided to omit this feature of the model. So far as the primary free field response in the present example is concerned, the absence of this feature is of secondary importance due to the explosive nature of the free field excitation. To have included low amplitude hysteresis would have helped to control noise but would not have changed the response of the structure significantly.

The cap model parameters for each layer of the HDR site model are given in Table 2-1. The properties of each layer are illustrated in Fig. 2-3 in terms of their uniaxial stress-strain relationships. The stress paths in uniaxial strain are shown in Fig. 2-4. The seismic wavespeeds for each layer are summarized in Table 2-2. The model for each layer is based on extremely limited data. Agreement between predicted and measured free field data would almost certainly be improved if a more complete suite of laboratory and field tests were to be conducted. Additional discussion of the site modeling is contained in Appendix A.

2.2 Source Model

A number of free field computations were made using the site model described above and Weidlinger Associates' Eulerian axisymmetric finite difference code LAYER to determine a suitable model of the source (see Appendix A). The model shown in Fig. 2-5 was ultimately chosen. It consists of a spherical zone 8.5 meters in radius whose center is 11.3 meters below the original ground surface within which there is a prescribed pressure-time history. This source model yields ground motions at the target range which resemble a record observed in a previous test scaled to the same yield.

2.3 Structure Model

The physical structure is illustrated in Fig. 2-6a and b. The model of the structure is generated from standard TRANAL continuum elements; an elevation view of the three-dimensional model looking toward the plane of symmetry is shown in Fig. 2-7. The inner and outer containment structure and the foundation or basemat are the three parts of the structure included in the model. The mass and stiffness distributions of the analytic model are shown in Figs. 2-8a and 2-8b. The present idealization requires that the

true properties of each component, especially of the inner containment structure, be distributed in such a way that the model's mode shapes, natural frequencies and damping characteristics agree closely with those of the physical structure. Measurements of these characteristics reported in Ref. 5 were used as the basis of the analytic model. These data, illustrated in Fig. 2-9, were also used by ANCO Engineers in developing the analytic models described in Ref. 6.

The model of the superstructure is designed primarily to represent the lowest three shear and flexural deformational modes. This presents an opportunity to achieve computational efficiency by modifying the containment model such that it has the same mass distribution, normal mode shapes and natural frequencies as the physical structure, yet is constructed with larger elements than the physical structure would suggest. The effect is to permit larger integration time steps to be used in a model which retains correct dynamic properties. In the present case, the wall thickness of the outer containment structure was increased from 0.62 meters to 3 meters and the radius of the inner structure was decreased from 10 meters to 6.85 meters and was treated as if it were solid, as shown in Fig. 2-7.

The following procedure was used to refine dynamic characteristics of the finite element model of the HDR structure detailed above. For the modified structural geometry just discussed, the mass distribution with height of each component of the structure was kept consistent with that of the physical structure by adjustments of the mass density of the structural material. An initial estimate of stiffness properties was made by attempting to match the effective shearing and bending stiffness characteristics of each horizon-

tal cross section of the structure even though the cross sectional area of the model has been modified.

Once the stiffness and mass properties of the model were defined, the first few mode shapes and frequencies of the model, both fixed base and in situ, were extracted in order to assess their degree of correspondence with the measured modes and frequencies of the actual structure. TRANAL is an explicit finite element code having no global stiffness and mass matrices. Since these are required to extract normal modes for the discretized system, an implicit finite element code, GENSAP, a derivative of SAP IV, was used in this portion of the study. Initial estimates of effective structural stiffness resulted in reasonable in situ structural mode shapes; however, frequencies were on the order of 25 to 30% higher than measured. Two iterations on stiffness characteristics refined the stiffness properties to those presented in Fig. 2-8b. The corresponding fixed base mode shapes are given in Fig. 2-10(a-f) and the in situ mode shapes are shown in Fig. 2-11(a-d). Table 2-3 contains the frequencies of the analytic model and the actual measured values. Measurements exist only for the in situ case. As expected, the first mode, which involves rigid body rocking as well as in-phase shearing and bending deformation of the inner and outer containment structures, is significantly affected by embedment in soil. The second deformational mode, out-of-phase shearing and bending of the two containment structures, is essentially independent of embedment.

The refined structural model agrees well with the mode shapes and frequencies measured for the physical structure. The largest difference between measurement and model is in the frequency value (1.52 Hz compared with 1.87 Hz, respectively) of the first deformational and rigid body rocking mode. Since the frequency of the second mode is in good agreement with the

measurement and since the first mode is significantly influenced by the soil properties around and underneath the foundation for which sparse data exist, it is possible that additional laboratory test data might improve this aspect of the soil-structure interaction model. Also, it is worth noting that extracting modes from a soil island with finite boundaries instead of those consistent with the assumption of a continuum may tend to over-constrain modes with significant soil deformation, while having little effect on localized structural modes. This effect would be less significant in the TRANAL soil-structure interaction simulation due to its use of absorbing boundaries to represent more correctly the actual boundary conditions.

As a final step, the agreement between similar finite element models in GENSAP and TRANAL was checked by determining the free vibration of the TRANAL structural model (fixed base) to a transient "pluck" test. The frequency content of the structural response in the deformational modes of interest were then examined. Only the frequencies of the first two deformational modes could be reasonably well evaluated in this manner. The predominant frequency of response of the structure in its first deformational mode was about 10% lower than the GENSAP model predicted. Excellent agreement with GENSAP (within 2%) was obtained for the predominant frequency of the second deformational mode. The small difference in the observed first mode frequency in TRANAL, when compared with the result from GENSAP, is attributed to the transient nature of the TRANAL "pluck" test in which a large number of structural modes are excited and to the difference in the finite element representation used in the two computer codes (i.e. TRANAL elements use one-point integration while GENSAP uses a two-point integration procedure).

2.4 Structural Damping

Structural damping is included in structural elements through the mechanism of viscoelasticity, Ref. 4. The mechanical analog also referred to as a standard solid, is shown in Fig. 2-12. The parameters which define the model are the instantaneous shear and bulk modulus G_F and K_F, respectively; long term moduli G_S and K_S; and a relaxation rate τ. Since damping occurs in an analogous form in both bulk and shear, only the shear contribution is described below. The fraction of critical damping is the ratio of the area enclosed by the hysteresis loop in Fig. 2-12 to the total change in elastic strain energy during the cycle, Ref. 7. In terms of model parameters defined above

$$\text{damping ratio} = \frac{C}{C_{cr}} = 1/2 \; \frac{\omega\tau\left(1-\dfrac{G_S}{G_F}\right)}{\left[\left(1+\omega^2\tau^2\right)\left(\dfrac{G_S^2}{G_F^2}+\omega^2\tau^2\right)\right]^{\frac{1}{2}}} \qquad (2\text{-}7)$$

where ω is the circular frequency of the cycle.

The damping ratio is frequency-dependent such that the maximum damping ratio can be specified at only one frequency. In the present analysis, this frequency is chosen to be 2.7 Hz, the natural frequency of the second deformational mode (inner and outer containment structures out-of-phase), and the damping ratio at this frequency is 0.025 as measured in the forced vibration tests on the physical structure. The reason for centering the damping model around this frequency is that the second mode is the lowest mode which involves structural deformation exclusively; the fundamental mode also involves soil-structure interaction. The damping ratio at all other frequen-

cies is lower, as is shown in Fig. 2-13; for example, the damping ratio at the first mode frequency of 1.5 Hz is about 0.02. The parameters for this model are as follows:

$$\frac{G_S}{G_F} = \frac{K_S}{K_F} = .905$$

$$\tau = 0.0533 \text{ sec}$$

Using this model to simulate structural damping is an adequate representation for frequencies up to about 10 Hz. It appears likely that the present analytic model is somewhat underdamped at frequencies above this level.

2.5 Complete TRANAL Model

The complete TRANAL model for the source, site and structure is shown in Figs. 2-14 and 2-15. The model uses approximately 8500 finite elements and 30,000 degrees of freedom. Symmetry boundary conditions are used on the x-y and x-z planes (Fig. 2-15) which intersect the source. Absorbing boundary conditions are used on all other subsurface boundaries.

Certain near-field details indicated in Fig. 2-6b were incorporated into the complete soil-structure interaction model. The underground retaining wall surrounding the foundation is included as well as the effect of the stiffer backfill material. The stiffness properties of Soil 3 are similar to those indicated for the backfill region and therefore Soil 3 is used as backfill material in the analysis.

Interface elements are included in the model surrounding the structural foundation. In addition to representing the continuum behavior of the

soil, these elements have the capability to represent slip and cavitation-rebonding at the soil-structure interface. This is accomplished by limiting shear and normal forces transferred across the interface.

While gravity is not explicitly taken into account in the analysis, static overburden stress levels are included in debonding criteria for the interface elements. Also, the effect of soil overburden on soil stiffness characteristics is accounted for within the framework of the cap model.

TRANAL uses a substructuring approach called "subcycling" which allows significant computational economies by optimizing the integration time step for the equations of motion within different regions of the TRANAL grid. The time step is controlled by the Courant stability criterion which requires the integration time step for an element to be less than the wave propagation time across the element. In the HDR analysis, the largest time step in the soil was .00132 sec, while the minimum time step required in the structure was .000165 sec.

The number of element-time steps required for the HDR model is approximately 16×10^6 element-time steps per second of real time. On a CDC 7600, this is equivalent to approximately 3 hours of cpu time per second of real time. The cost of this calculation is high in spite of the efficiencies provided by subcycling. The cost is exaggerated in the present calculations due to the small integration time steps required by the site and structural models. The soil portion of the grid consists mainly of fully saturated soil having a dilatational wavespeed of about 1600 m/sec. Since time step size is inversely proportional to wavespeed, the benefits usually available through subcycling are greatly diminished in this case. The second factor is the structural model which, in order to produce accurate support motions

for piping analysis, requires a fine discretization with accompanying penalties in computational time step. More efficient use of TRANAL is possible, although not within the time allowed for this project.

TABLE 2-1. CAP MODEL PARAMETERS FOR HDR SITE MODEL

	SOIL-1	SOIL-2	SOIL-3	SOIL-4
Depth (m)	0-3	3-6	6-12	12-
X (ksi)	20.	25.	100.	600.
G (ksi)	4.	8.	20.	75.
A (ksi)	15.	30.	0.2	0.2
B (ksi^{-1})	0.02	0.01	10.	10.
C (ksi)	15.	30.	0.2	0.2
D (ksi^{-1})	1.7	1.4	1.4	0.7
R	3.0	3.0	3.0	3.0
W	0.15	0.1	0.05	0.03
ρ (lb/ft^3)	100.	100.	110.	120.

TABLE 2-2. SOIL WAVESPEEDS FOR HDR SITE MODEL

(See Figure 2-1)

	Layer 1	Layer 2	Layer 3	Layer 4
Depth (m)	0-3	3-6	6-12	12-
Wavespeeds (m/sec)				
Model				
c_p	330.	392.	703.	1585.
c_s	131.	185.	280.	519.
Measured				
c_p	297.	(not measured)	595.	1585.
c_s	---------- not measured ----------			

TABLE 2-3. NATURAL FREQUENCIES OF GENSAP FIXED-BASE AND IN-SITU FINITE ELEMENT MODELS OF HDR REACTOR

	Frequency (Hz) of Mode					
	1	2	3	4	5	6
Fixed Base (no soil)						
GENSAP	2.16	2.71	9.47	10.14	10.85	16.23
In-Situ						
GENSAP	1.97	2.72	7.62	11.35		
MEASUREMENT (Ref. 6)	1.52	2.63	-	12.25		

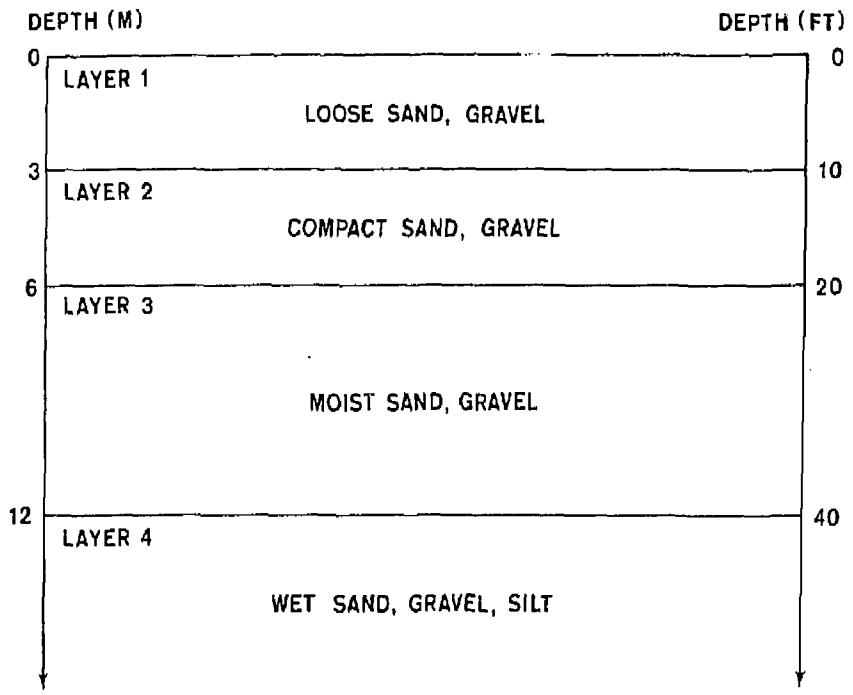

Figure 2-1. Site profile used in HDR analysis.

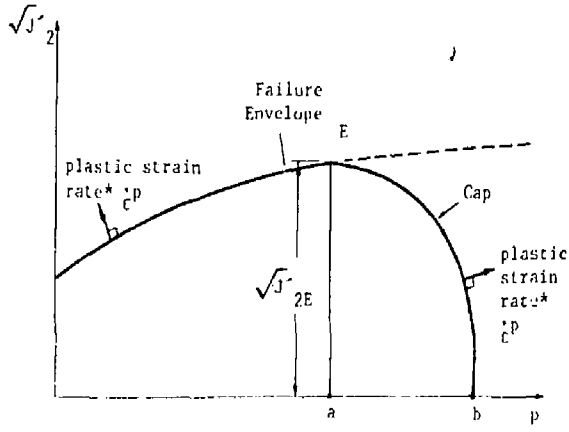

Failure envelope: $\sqrt{J'_2} = A - C \exp(-3Bp)$

cap: $\sqrt{J'_{2E}} = (p_b - p_a)/R = f(\bar{\varepsilon}_v^p)$

*The plastic strain rate $\dot{\varepsilon}^p$ is governed by the associated flow rule whereby the plastic strain rate vector is normal to the yield surface when plotted to the appropriate scale parallel to the p-axis (plastic volumetric strain rate) and the $\sqrt{J'_2}$ axis (plastic deviatoric strain rate)

Figure 2-2a. Typical yield surface in the cap model for compressive stresses.

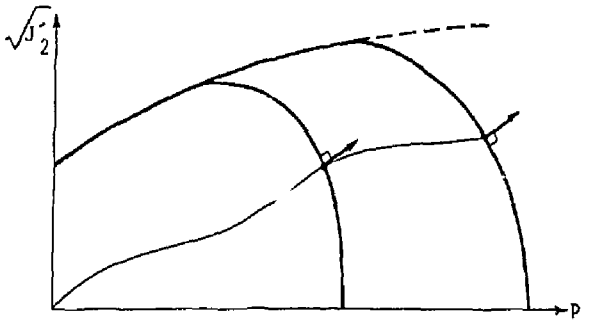

a. Stress point initially pushes cap out

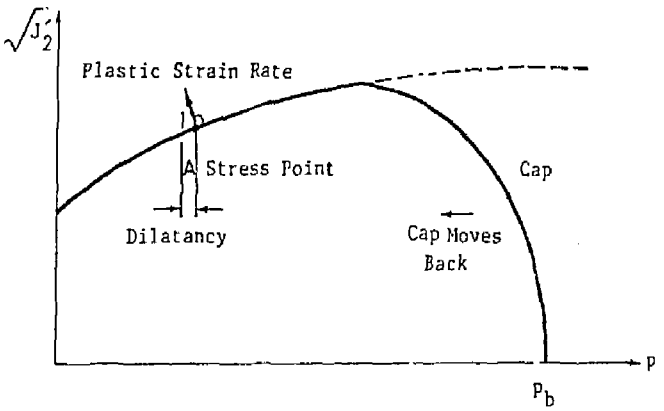

b. In soil model the cap moves back when failure occurs

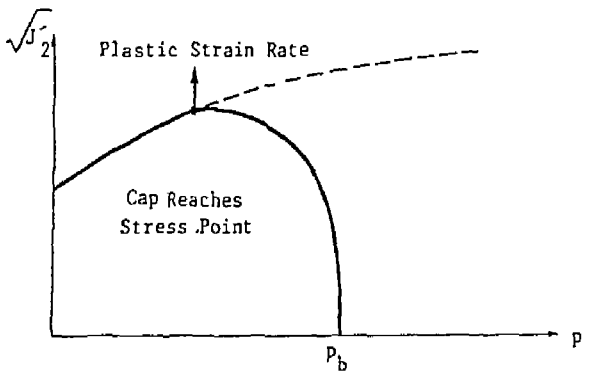

c. The backward cap movement is limited when the cap reaches the stress point

Figure 2-2b. Cap model used to represent properties of soil in HDR analysis. Stress point on cap pushes cap out. When stress point is on failure surface, cap moves in to control dilatancy.

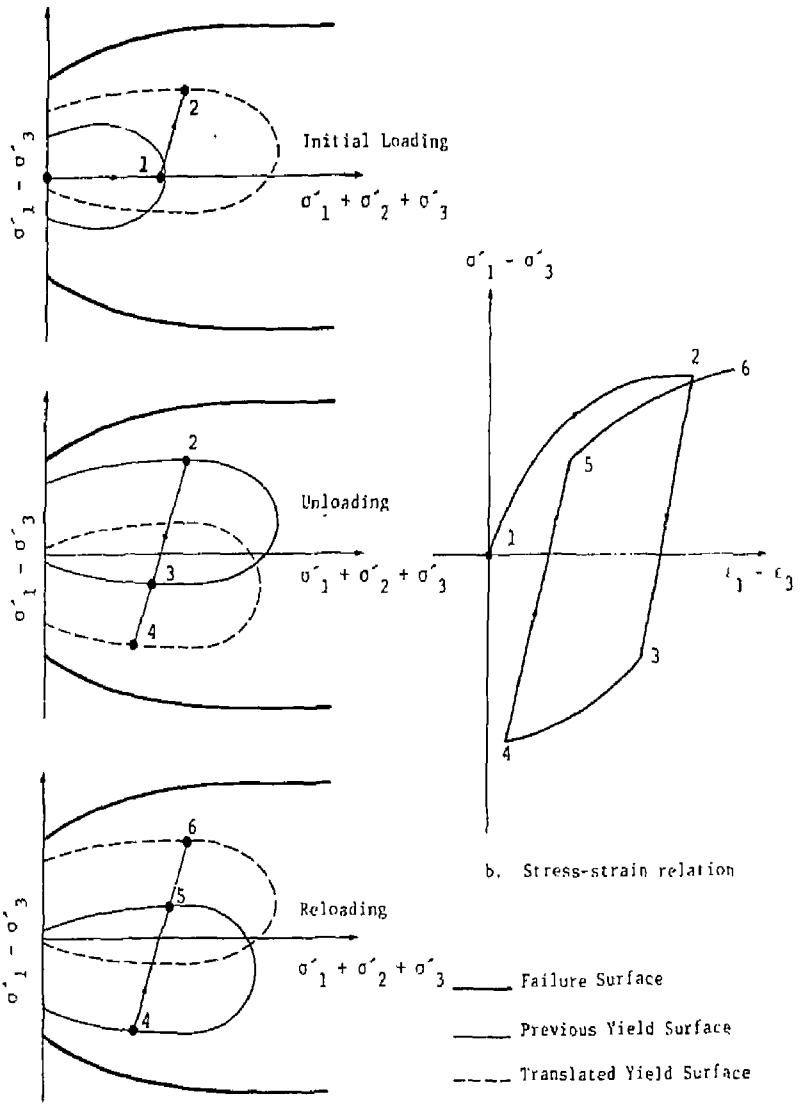

Figure 2-2c. Role of kinematic hardening in producing hysteresis loops for cyclic triaxial stress path.

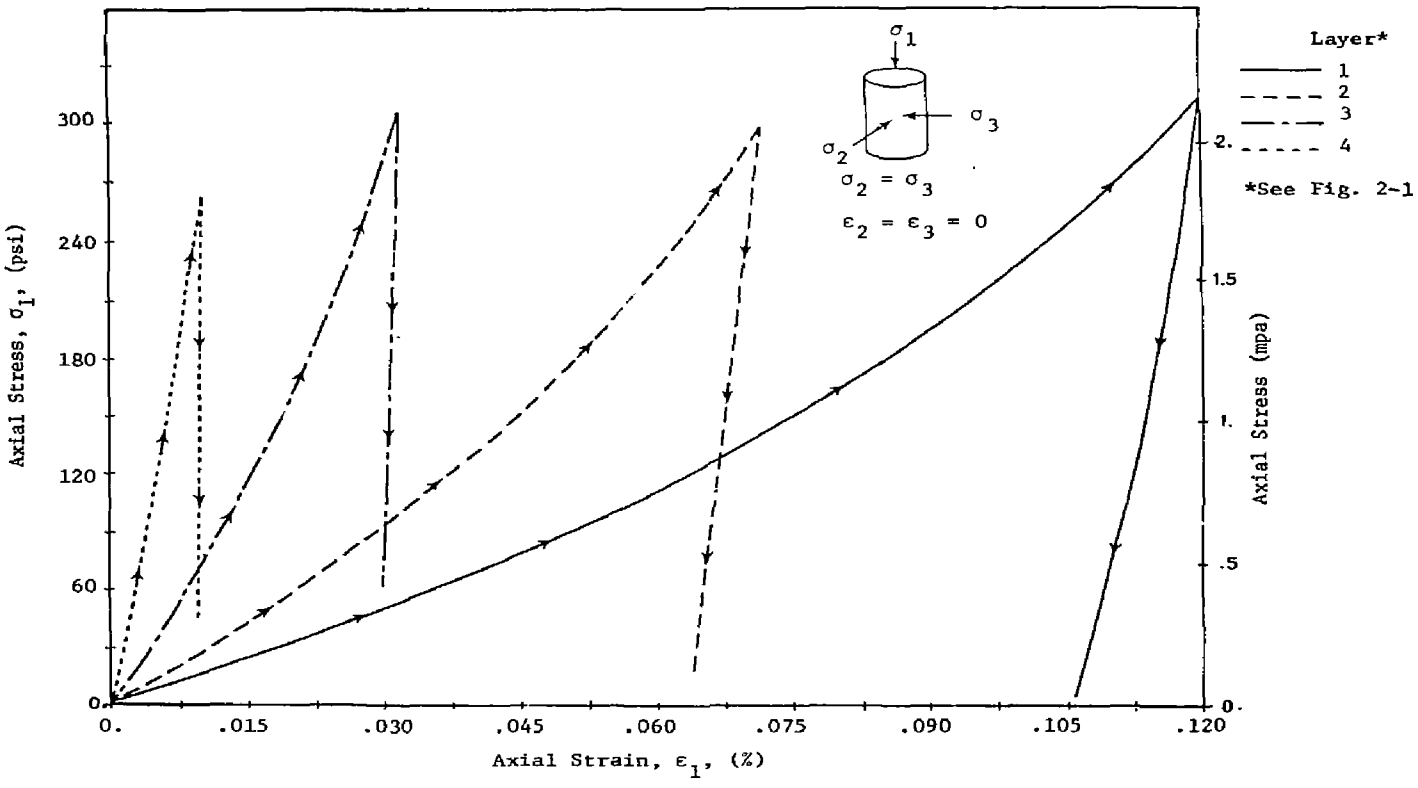

Figure 2-3. Stress-strain properties (uniaxial strain) of each layer in HDR site profile.

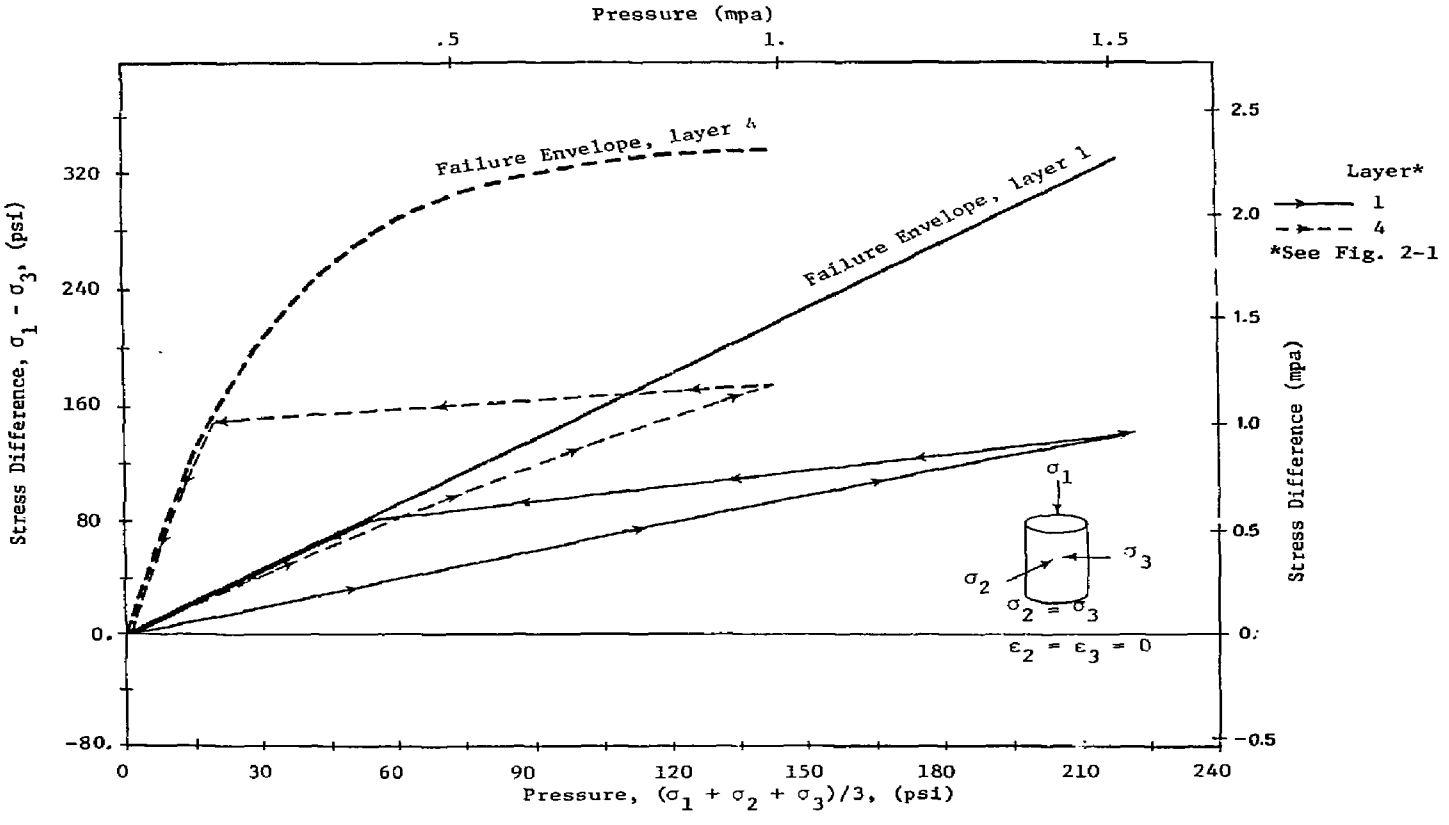

Figure 2-4. Stress path experienced by soils in layers 1 and 4 of HDR site profile when subjected to uniaxial strain.

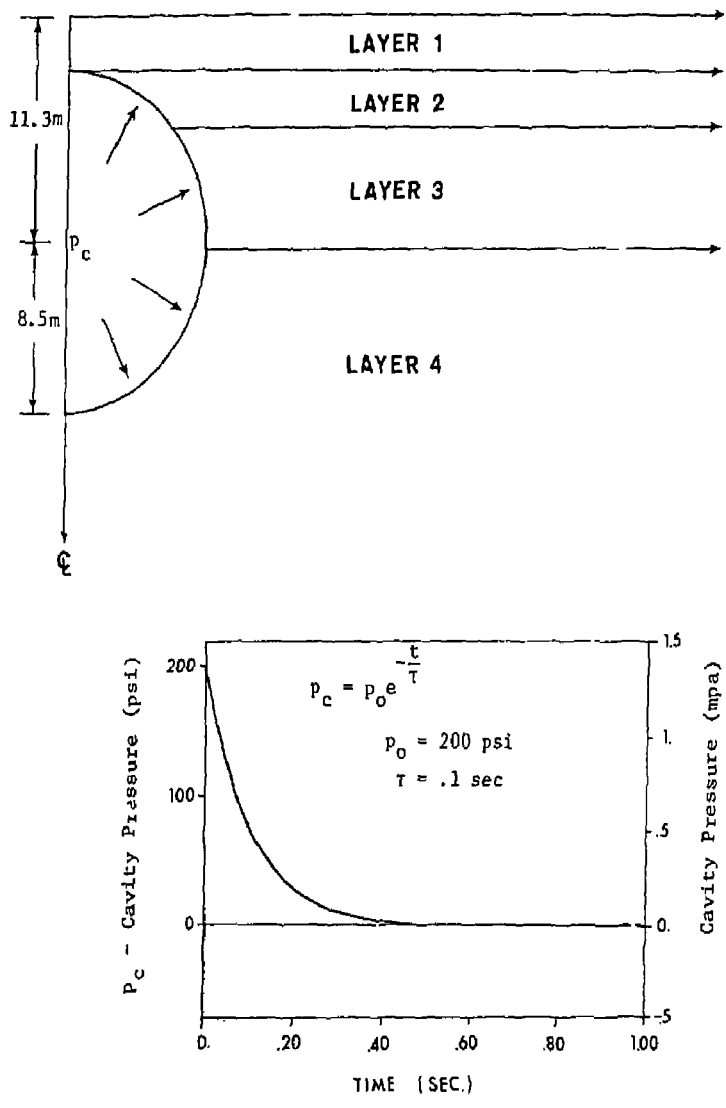

Figure 2-5. Model of source used as input for free field and soil-structure interaction analysis.

Figure 2-6a. Elevation view of HDR containment structure.

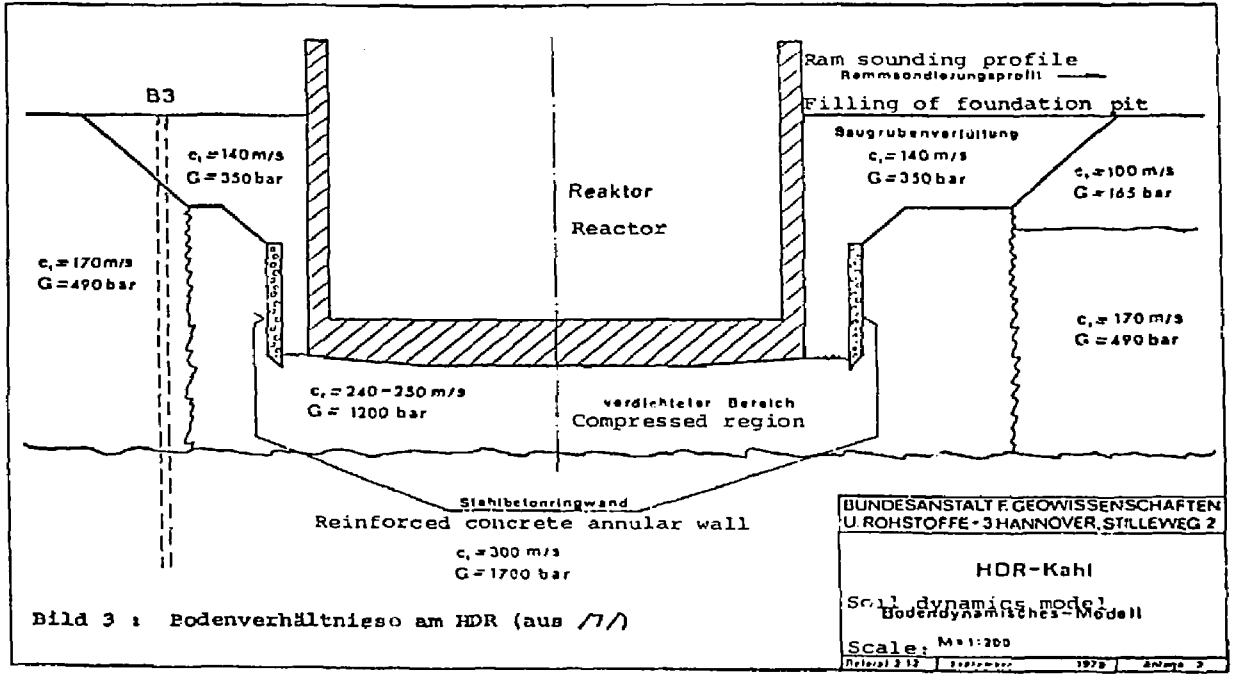

Figure 2-6b. Details of HDR foundation.

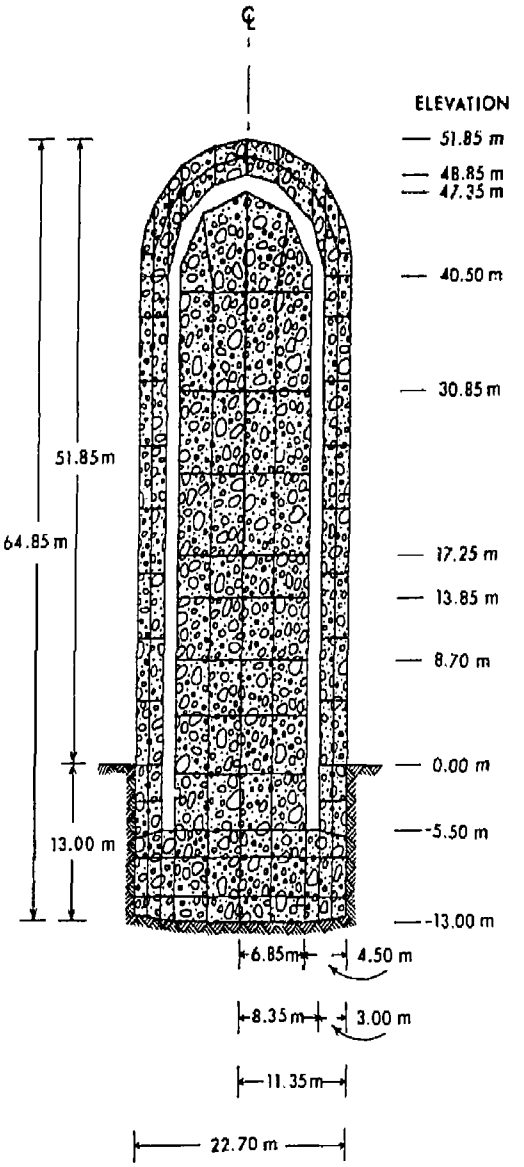

Figure 2-7. TRANAL model of HDR containment structure.

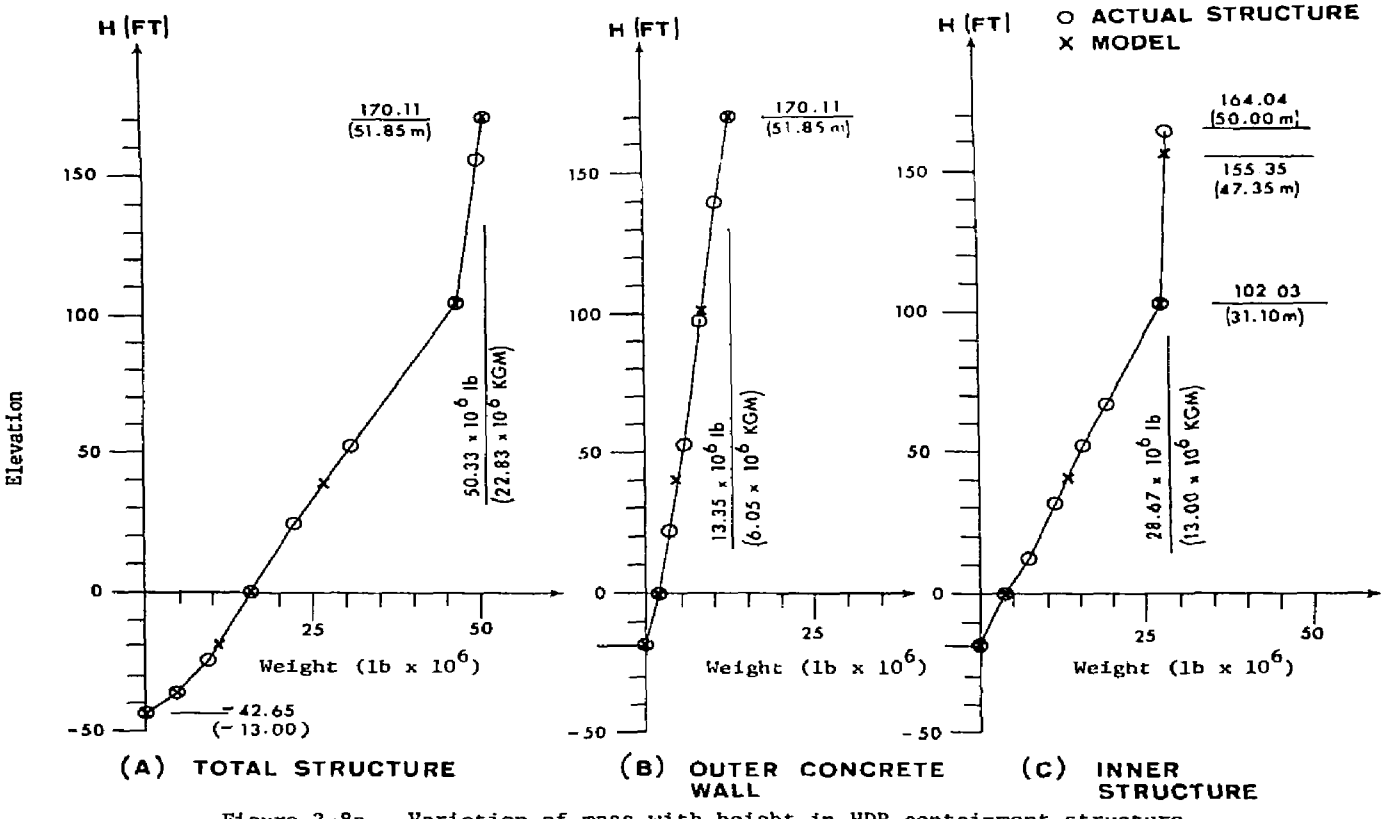

Figure 2-8a. Variation of mass with height in HDR containment structure and in TRANAL model.

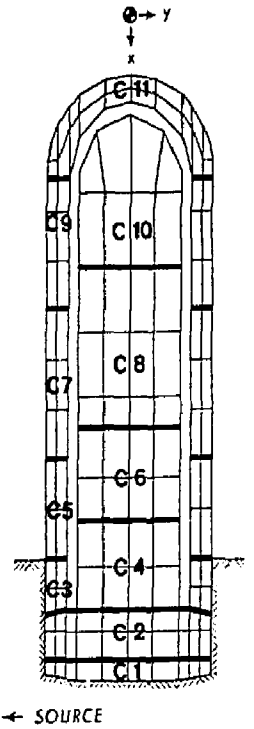

Material	K(ksi)	G(ksi)
C_1	1017.82	929.30
C_2	545.24	497.82
C_3	386.70	353.07
C_4	714.97	646.21
C_5	280.49	256.10
C_6	664.42	606.66
C_7	262.22	239.42
C_8	774.97	707.07
C_9	246.28	224.87
C_{10}	79.95	73.00
C_{11}	263.41	240.50

Figure 2-8b. Concrete material properties used in TRANAL structural model of HDR reactor.

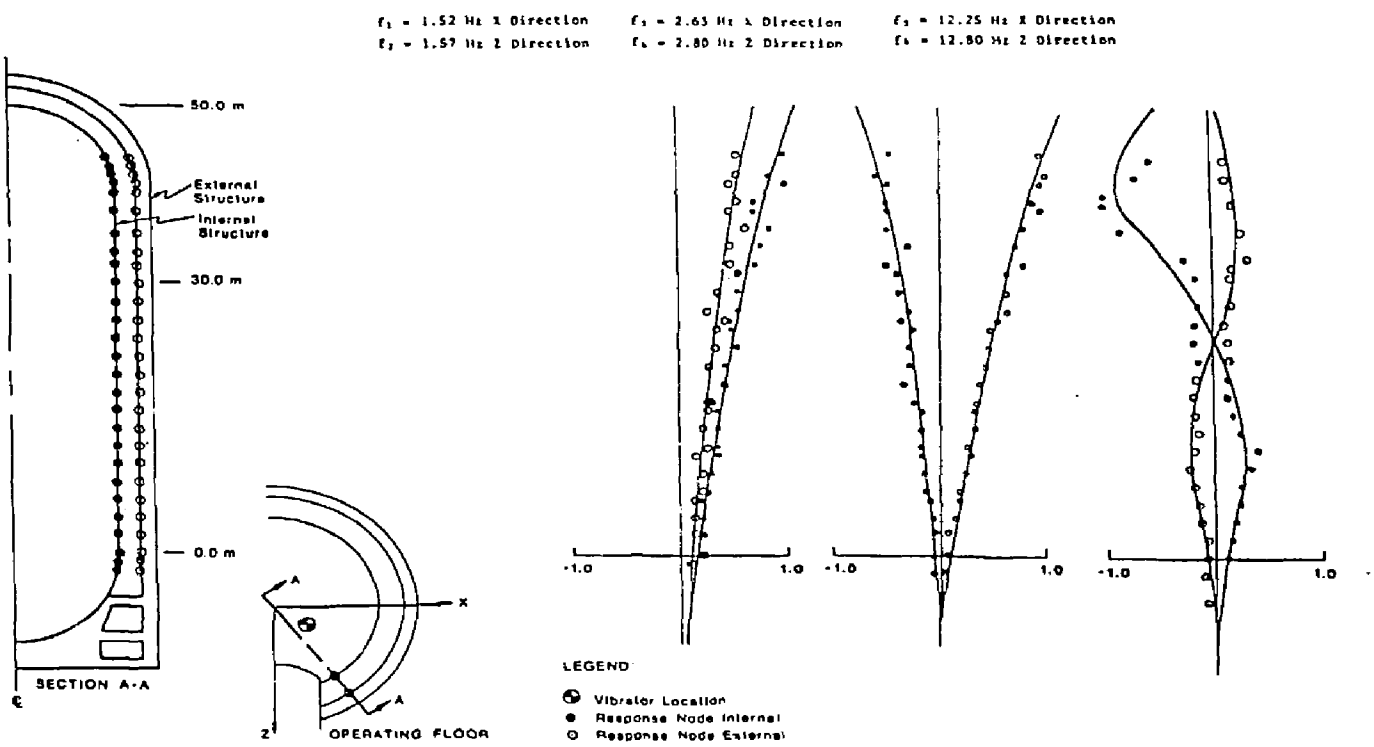

Figure 2-9. Mode shapes and natural frequencies of HDR reactor measured in situ during forced vibration testing (from Ref. 6).

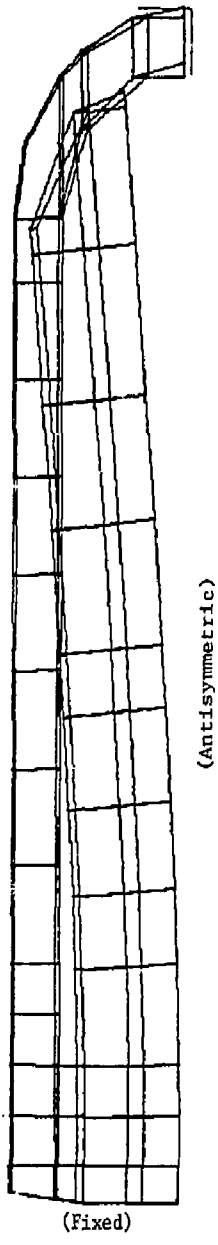

Figure 2-10. Fixed base mode shape of HDR model (only one plane of elements plotted)

a. 1st mode, frequency 2.16 Hz.

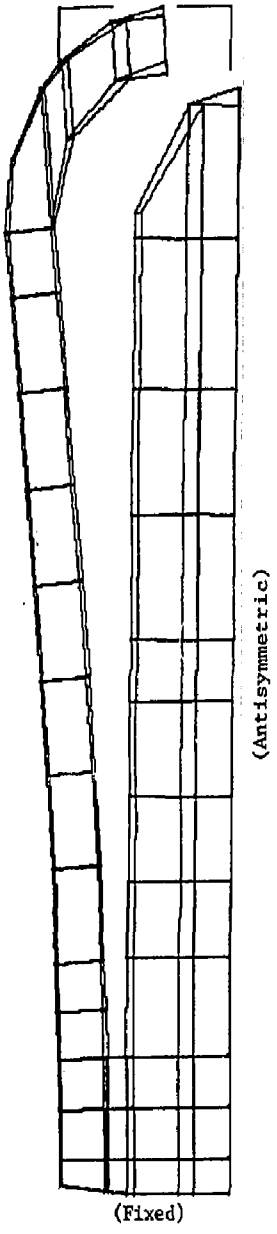

Figure 2-10 (continued). Fixed base mode shape of HDR model
b. 2nd mode, frequency 2.71 Hz.

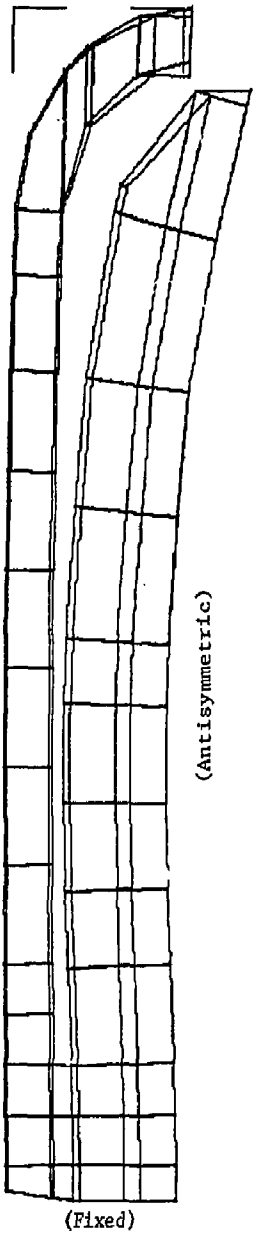

Figure 2-10 (continued). Fixed base mode shape of HDR model
c. 3rd mode, frequency 9.47 Hz.

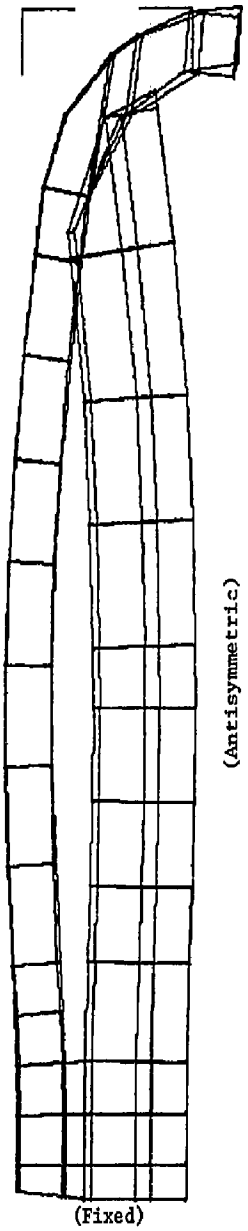

Figure 2-10 (continued). Fixed base mode shape of HDR model d. 4th mode, frequency 10.14 Hz.

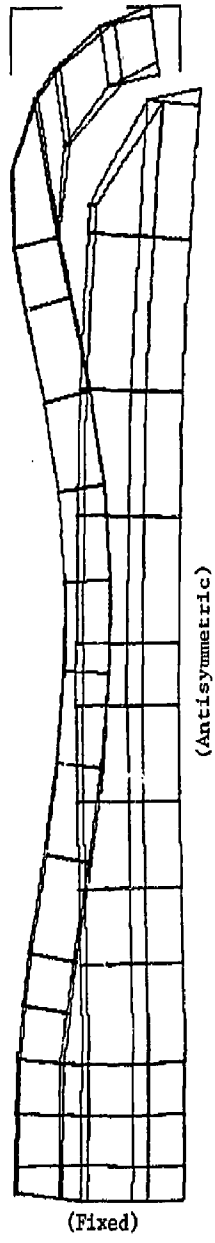

Figure 2-10 (continued). Fixed base mode shape of HDR model e. 5th mode, frequency 10.85 Hz.

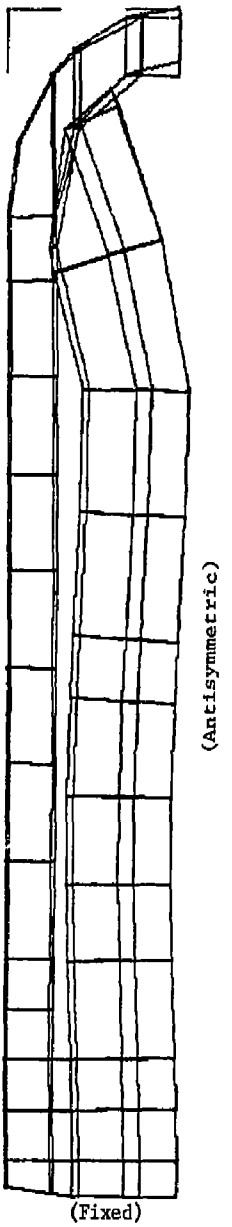

Figure 2-10 (continued). Fixed base mode shape of HDR model f. 6th mode, frequency 16.23 Hz.

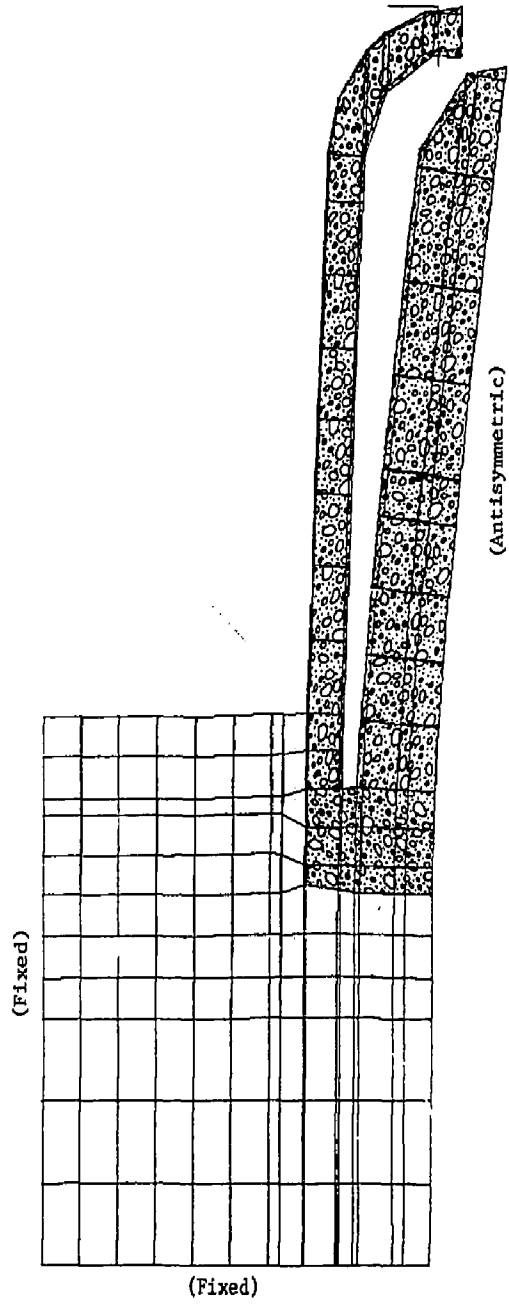

Figure 2-11. In situ mode shape of HDR model (only one plane of elements plotted)

a. 1st mode, frequency 1.87 Hz.

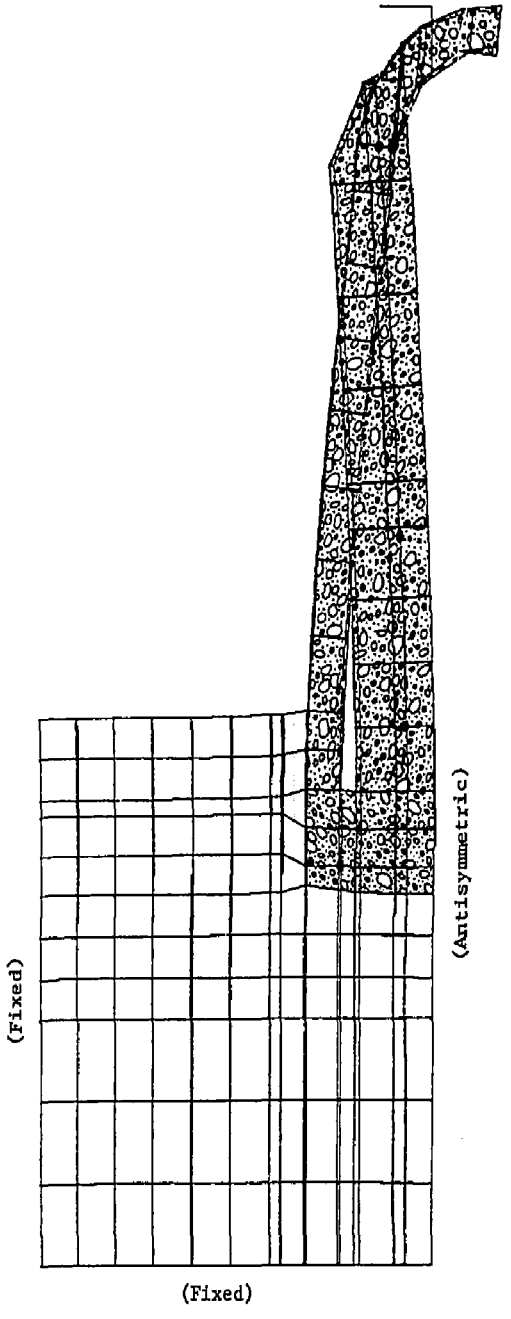

Figure 2-11. In situ mode shape of HDR model (continued) b. 2nd mode, frequency 2.72 Hz.

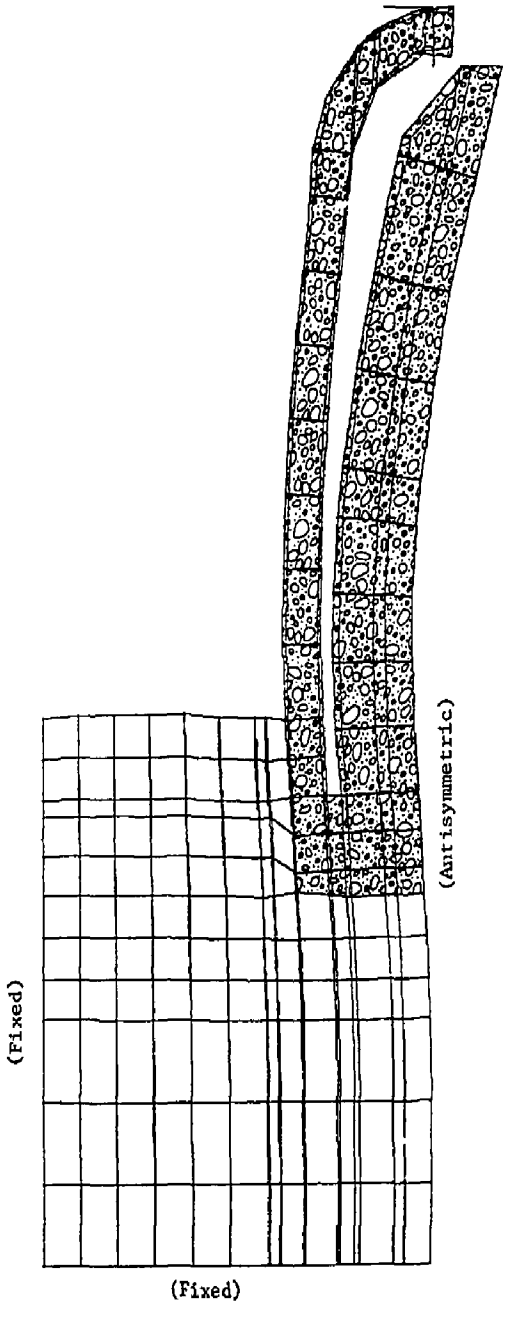

Figure 2-11 (continued). In-situ mode shape of HDR model c. 3rd mode, frequency 7.62 Hz.

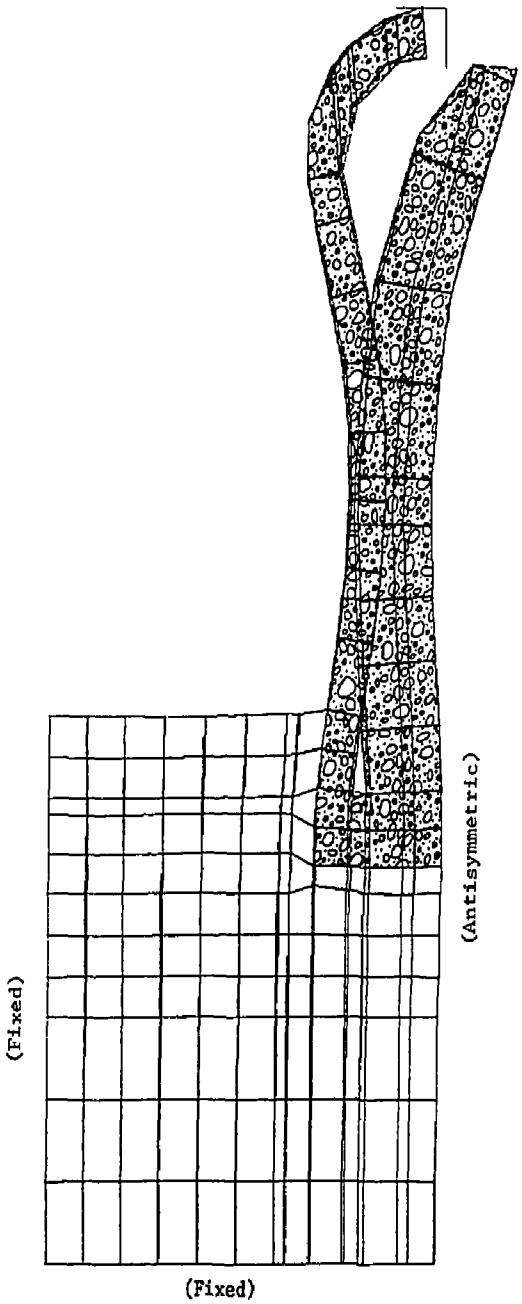

Figure 2-11 (continued). In situ mode shape of HDR model d. 4th mode, frequency 11.35 Hz.

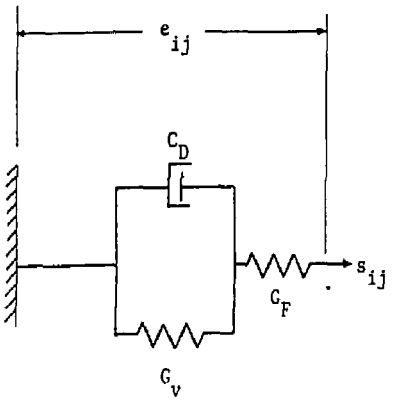

a. Analog (Standard Solid)

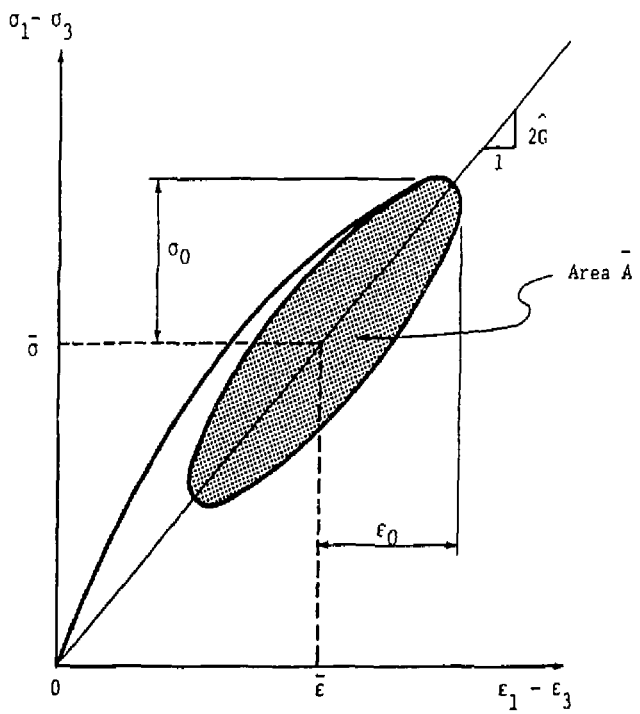

b. Cyclic Triaxial Test

Figure 2-12. Viscoelastic model of structural damping.

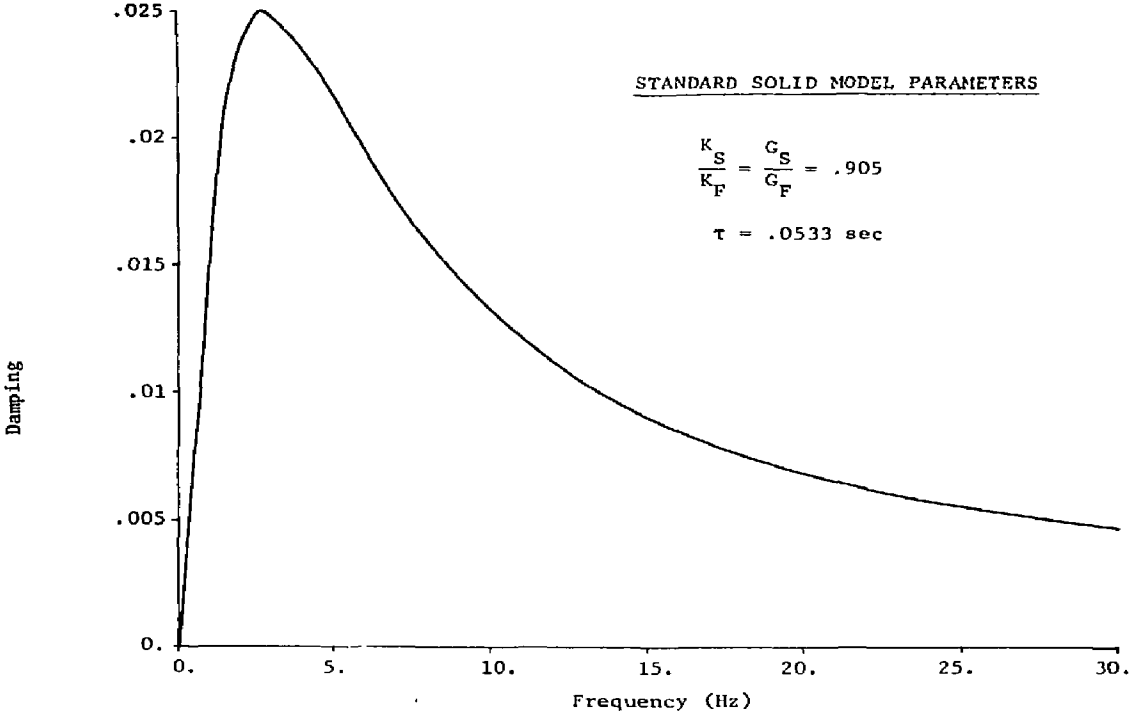

Figure 2-13. Fraction of critical damping as function of frequency used in structural elements of HDR model.

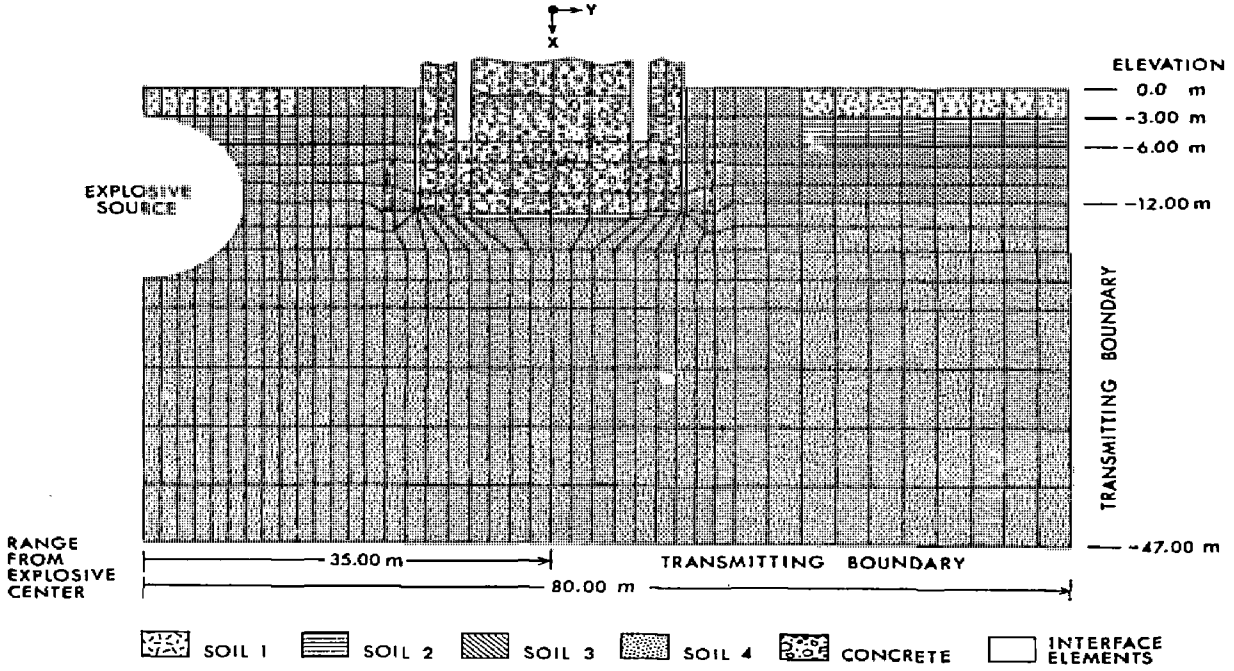

Figure 2-14. Elevation view of TRANAL model of HDR site and containment foundation (superstructure not shown).

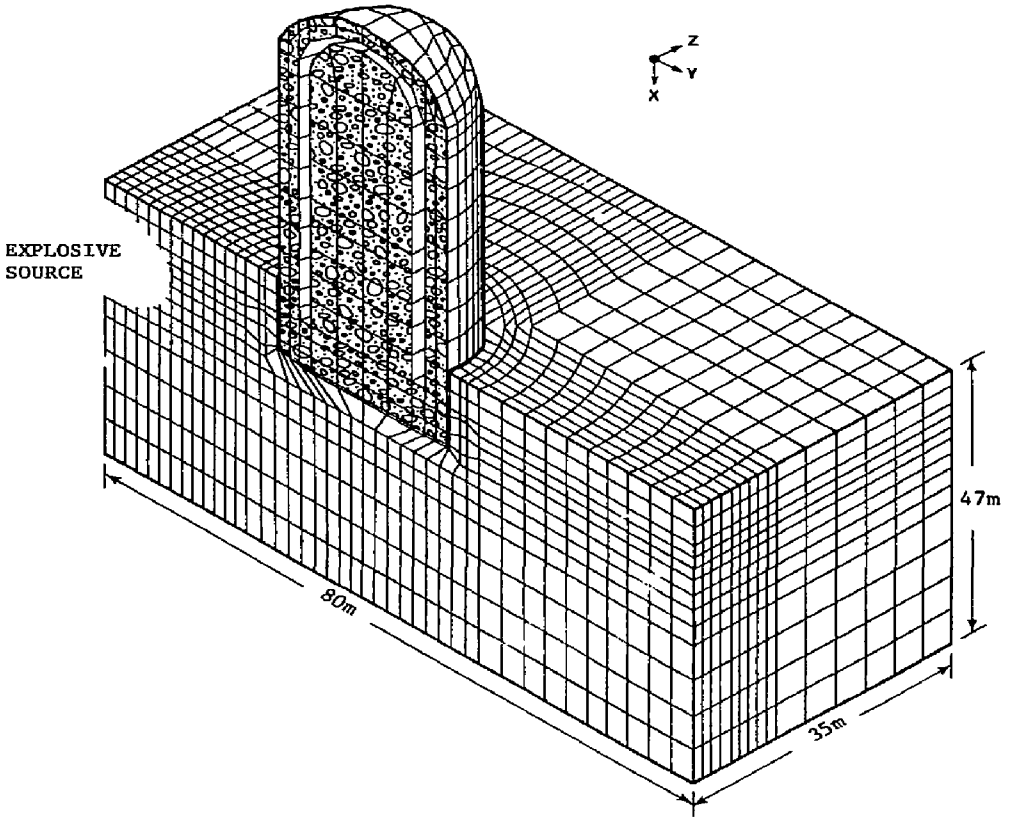

Figure 2-15. Isometric view of TRANAL model of HDR site and containment.

3. FREE FIELD, SOIL-STRUCTURE AND STRUCTURAL RESPONSE

This section describes the results of the LAYER free field and TRANAL soil-structure and structural response analyses. Except for the results presented in Section 3.1, all time histories have been filtered to eliminate numerical oscillations above 25 Hz.

3.1 Free Field

As discussed in Section 2, the site and source models were refined in free field analyses using the axisymmetric finite difference code LAYER. A complete description of this study is contained in Appendix A. Figures 3-1 and 3-2 contain representative results from this work. These figures show the radial- and vertical-velocity time histories at a range of 22.5m (74 ft) from the source and at depths of approximately .3m (1 ft), 6m (19 ft) and 12m (39 ft) below the surface. These points correspond to the upstream face of the containment structure near the surface, mid-depth and bottom of the foundation. These figures indicate that the predominant motions are outward and downward, and that the strong motion phase is over by about t = .3 sec after detonation.

The source and site models developed using LAYER were used in the TRANAL soil structure interaction analysis. Figure 3-3 (a-c) presents horizontal and vertical velocity-time histories for a point in the soil obtained in the TRANAL analysis. The grid point is located at a depth of 3m and at ranges of 22m from the explosion and 20m from the structure. The grid point is located off the centerline of the model, hence the global horizontal components (y and z) of motion are not alligned with the radial direction from the source. Upon transforming the global horizontal velocities into the radial direction, the peak radial velocity is .28 m/sec. The peak vertical

velocity is .11 m/sec. These values agree reasonably well with results from the axisymmetric LAYER calculation, Figs. 3-1 and 3-2.

The predominant free field motion is produced by the stress wave propagating outward from the 50 kg explosive charge. Figures 3-4 (a-d) show the σ_x, σ_y and σ_z stress-time histories and the stress path (plotted in stress invariant space) for a soil element located on the centerline of the model halfway between the explosive charge and the structure. The peak stress at this range is about .37 mpa. The stress path plot, Fig. 3-3d, indicates the type of cap model behavior described in Section 2.1. With the arrival of the compression wave in the soil, the cap is pushed out. The shear failure surface is encountered during unloading. After the wave front has passed, approximately .3 sec after detonation, stresses oscillate elastically.

3.2 Soil-Structure Interaction

The soil-structure response includes translation and rocking of the foundation. The rocking is illustrated in Fig. 3-5, where the vertical velocity-time histories at upstream and downstream corners are superposed. The out-of-phase motion, most clearly visible at early times, is due to rocking; subtraction of the two records produces the rocking velocity-time history shown in Fig. 3-6. Rocking is initially backward toward the source. Another indication of rocking is the vertical stress-time histories in the soil just beneath the upstream and downstream corners of the foundation, Fig. 3-7. The predominant oscillations of the two histories are out-of-phase with a frequency of about 2 Hz.

One effect of rocking is to beat back the soil at the soil-structure interface on the upstream side causing permanent separation there.

This is illustrated in Fig. 3-8, where the normal component of stress is shown to reach a constant value equal to the static earth pressure. An inspection of stress components normal to the interface at other points around the structure indicates that separation occurs nowhere else.

The picture of foundation motions is completed in Figs. 3-9 through 3-26, where the horizontal and vertical acceleration- and velocity-time histories and corresponding spectra near test measurement locations in the foundation are shown. The predominant motion is primarily outward and downward, following the free field motion, and lasts for about .3 sec. Although the primary action of the foundation is to average out the adjacent free field motions, there are some noteworthy exceptions to this trend. Figures 3-9 through 3-14 show the response at the center of the foundation. The peak vertical and horizontal velocities are about .05 m/sec there. The foundation response upstream, Figs. 3-15 through 3-20, varies somewhat from that observed downstream (Figs. 3-21 through 3-26). Figures 3-15 and 3-21 show the horizontal acceleration-time histories for the upstream and downstream faces and they indicate higher amplitudes of high frequency oscillation on the upstream than on the downstream face. This is due to closer proximity of the upstream face to the explosion. Also, because the surrounding soil has an impedance between 1/2 and 1/3 that of the concrete foundation, the foundation is not rigid relative to the soil, as is usually the case. This results in some deformation of the foundation and leads to variation in response between upstream and downstream locations. Significant differences in the vertical velocity-time histories for the upstream and downstream faces, Figs. 3-18 and 3-24, are caused by rigid body rocking motion which is superposed onto the rigid body vertical translation. This accounts for

the modified response spectra observed at low frequency, Figs. 3-20 and 3-26.

3.3 Structural Response

The response of the inner containment structure is characterized by horizontal and vertical acceleration- and velocity-time histories and their corresponding spectra at selected elevations, Figs. 3-27 through 3-50. A typical result is shown in Fig. 3-39, which indicates that the horizontal motion has a predominant frequency of about 1.75 Hz; the corresponding response spectra, Fig. 3-43, show this and a higher resonant peak at about 7 Hz. There is a large gradient in amplitude of horizontal response with larger accelerations at the top of the inner structure (of order .6g), Fig. 3-27, in response to rocking of the foundation plus deformation of the structure. The horizontal accelerations at lower levels, where the recirculation water piping system is attached, are of order .1g (see Figs. 3-39 and 3-45). The gradient of vertical accelerations is much smaller because the structure is much stiffer vertically and because rocking does not appreciably affect vertical response.

The response of the outer containment structure is also characterized by horizontal and vertical acceleration- and velocity-time histories and their spectra at selected elevations, Figs. 3-51 through 3-68. A typical result is shown in Fig. 3-57, which indicates that the horizontal motion has a predominant frequency of about 2.7 Hz; the corresponding response spectra, Fig. 3-61, shows this and a higher resonant peak at about 12 Hz.

The response locations so far presented lie on the symmetry plane of the structure and therefore the z-velocity component (in and out of plane component) is constrained to be zero. Figures 3-69 and 3-70 show the z-

component of velocity at two points on the centerline of the structure but away from the symmetry plane. Figure 3-69 is located on the inner containment structure at a height of 30.8m above grade level. The peak velocity is about .005 m/sec. Figure 3-70 is for a point located on the outer containment structure near the foundation. Somewhat higher velocity values are seen here due to the greater flexibility of the outer wall, modeled as a shell, relative to the inner structure modeled as a solid cylinder.

To summarize the overall horizontal response of the containment structure, the outer structure responds predominantly in the second deformational mode (approximately 2.7 Hz). The inner structure responds predominantly in the first deformational mode (approximately 1.7 Hz). The inner and outer structures respond almost independently of each other at elevations above grade level. As depth below grade increases, the translational response of the containment structure tends toward that of the free field.

3.4 Filtering of Analysis Results

As in all numerical methods in which the governing equations of motion are discretized, the present TRANAL analysis oscillates about the true solution. This oscillation is often referred to as noise and arises from approximations made in discretizing the equations of motion. The effect is most significant at higher frequencies where the assumed discretizations of space and time result in coarser approximations of the physical response than at lower frequencies.

Explicit finite element codes such as TRANAL may exhibit a greater level of numerical noise than is typical of implicit codes. One reason is that implicit integration rules usually contain inherent damping. This

ensures stability in the analysis at the price of modifying the calculated response. The explicit integration rule in TRANAL is undamped. Second, implicit schemes use integration time steps which are deliberately chosen to represent accurately frequencies up to the highest frequency of interest in the analysis. Frequencies above this level are effectively filtered out of the analysis. In contrast, explicit schemes are required by the Courant stability criteria to use time steps which include and manifest all frequencies capable of being represented by the spatial discretization, not just the frequencies of interest.

Whereas discretization of the equations of motion allows high frequency noise to be sustained and propagated, especially in the stiff elements of the grid, the origin of the high frequency motion is in the boundary conditions and nonlinear behavior of the soil. In the present analysis, the instantaneous rise in applied pressure in the cavity which produces a shock in the soil is the major source of the oscillations.

Several methods are available for minimizing numerical oscillations. Artificial viscosity is one device which has been used in reducing noise within numerical computations. Material hysteresis and structural damping, both of which act as dissipative mechanisms, can also be effective in eliminating noise. Eliminating or modifying the shock by introducing a rise time on the pressure-time history prevents some of the noise from developing. Each of these devices improves the appearance of the solution but in some cases the improvement comes at the expense of accuracy.

Although the HDR analysis does contain some structural and material damping, the effect of this on high frequency response is minimal. As is discussed in Section 2.4, the structural damping in the analysis is quite

small for frequencies above 15 Hz, which corresponds to the frequency range of noise in the present calculation. It is also pointed out in Section 2.1 that there is little or no material hysteresis in the soil after the initial shock passes. Hence, neither of these two possible mechanisms is effective in the present analysis for controlling noise. If more experimental data had been available on which to base a soil model for low amplitude hysteresis in shear, we would have included this effect which probably would reduce the noise.

Putting a rise time on the pressure pulse was briefly considered. This appears to be a reasonable step and probably should be adopted in future calculations. However, the rise time must be short compared with the natural periods of the spherical cavity and some experimentation is needed to determine what rise time can be used without distorting major features of the free field simulation; in the present analysis there was insufficient time for such experimentation.

Our experience with the use of linear and/or quadratic artificial viscosity in TRANAL for controlling noise prompts us to be cautious in using them. In a recent example, the stresses in a cylindrical concrete structure were significantly distorted when a linear artificial viscosity term was added to the equations of motion for the structure. Using quadratic artificial viscosity to spread out the wave front of a shock has on occasion proven to be an acceptable way of reducing noise behind a shock front. However, it is done at the expense of smoothing the wave front and consequently removing some of the high frequency character of the shock.

Selecting values for artificial viscosity coefficients requires numerical experimentation to maximize noise reduction without significantly

modifying important details of the response. In the present project there was insufficient time to perform the necessary experimentation.

The foregoing considerations, especially concern for fidelity of structural response at frequencies of interest, persuaded us not to attempt to minimize noise in analysis. Instead, the analysis was performed and then frequencies above a certain (cutoff) frequency were filtered from the structural response records. This was done by using a Fast Fourier Transform routine supplied to Weidlinger Associates by ANCO Engineers. Since velocity records are output from TRAN*L, this routine transforms these velocity-time histories into their Fourier components; from these are computed the corresponding accerleration- and velocity-time histories containing only frequencies below a frequency chosen by us.

Examples of the numerical noise in the computation and the effects of filtering at frequency cutoffs of 25 and 30 Hz are shown in Figs. 3-71(a-f) for selected points on the structure. It can be seen that there is a tendency for the noise in the stiffer, higher frequency portions of the grid (i.e. the structural elements) to grow with time as these elements absorb high frequency energy from the rest of the grid. Table 3-1 presents the peak values of selected acceleration- and velocity-time histories, both filtered and unfiltered, at frequencies of 30, 25 and 20 Hz. In addition, acceleration response spectra for several selected points are presented in Figs. 3-72(a-f) for the unfiltered case. These spectra indicate significant response at frequencies far above the limit of validity for the finite element discretization chosen (i.e. the choice of soil discretization in the model is only adequate up to about 30 Hz).

While there is no strict rule for choosing a cutoff frequency for filtering, several factors were considered. Limitations on site discretization suggest a cutoff frequency of about 30 Hz. The structural model has been developed to match measured frequencies and mode shapes up to about 12 Hz. Beyond this frequency, the adequacy of the model to represent the physical response of the HDR structure is extrapolated. Examination of Figs. 3-71(a-f) shows significant reduction in the level of numerical oscillation in filtering from 30 Hz to 25 Hz. In general, by filtering above 25 Hz, the frequency range of the osicillations that tend to grow with time is removed. Finally, some insight into acceptable frequency limits can be gained by examining the effect of filtering on the peak acceleration and velocity values shown in Table 3-1. Acceleration values are not well calculated by numerical codes due to their sensitivity to noise. It is clear from the table that increased filtering continues to result in significant modification of peak acceleration values. Velocities on the other hand are much more accurate in part because they are less susceptible to noise. Partly for this reason the standard output from TRANAL is velocity, not acceleration. The change in peak velocity values when time histories are filtered from 30 to 25 Hz is less than 4% for the records shown. However, when the records are filtered from 25 to 20 Hz up to 20% change in peak velocity is observed. This suggests that filtering out all components above 20 Hz may be too restrictive.

Based on the above observations, a filter level of 25 Hz was chosen as an acceptable frequency cutoff for this analysis. Results presented in Sections 3.2 and 3.3 are filtered above this frequency.

TABLE 3-1. PEAK ACCELERATIONS AND VELOCITIES OUTPUT AT SELECTED POINTS IN HDR STRUCTURAL MODEL FOR SEVERAL FILTER FREQUENCIES

Location	Component	Time History Figures	PEAK ACCELERATIONS (G)				PEAK VELOCITY (M/SEC)			
			Unfiltered	Filtered			Unfiltered	Filtered		
				30 Hz	25 Hz	20 Hz		30 Hz	25 Hz	20 Hz
Top Outer Structure	Vertical	3-52 & 3-54	.925	.180	.135	.118	.0485	.0404	.0410	.0409
	Horizontal	3-51 & 3-53	.897	.310	.277	.224	.0792	.0788	.0788	.0734
Side Outer Structure	Vertical	3-64 & 3-66	2.306	.425	.343	.142	.0876	.0802	.0807	.0706
	Horizontal	3-63 & 3-65	2.478	.253	.256	.205	.0516	.0341	.0346	.0287
Near Foundation Outer Structure	Vertical	3-16 & 3-18	5.934	.203	.146	.096	.0718	.0624	.0608	.0584
	Horizontal	3-15 & 3-17	2.052	.202	.179	.174	.0821	.0598	.0596	.0546
Top Inner Structure	Vertical	3-28 & 3-30	.696	.147	.148	.132	.0584	.0542	.0551	.0516
	Horizontal	3-27 & 3-29	1.151	.713	.605	.456	.1302	.1239	.1283	.127
Piping Support Inner Structure	Vertical	3-40 & 3-42	.320	.094	.093	.098	.0495	.0489	.0486	.048
	Horizontal	3-39 & 3-41	.254	.103	.086	.058	.0228	.0213	.0216	.0208
Near Foundation Inner Structure	Vertical	3-10 & 3-12	.733	.127	.101	.079	.0548	.0494	.0502	.0483
	Horizontal	3-9 & 3-11	.678	.119	.083	.078	.0534	.0525	.0519	.0523

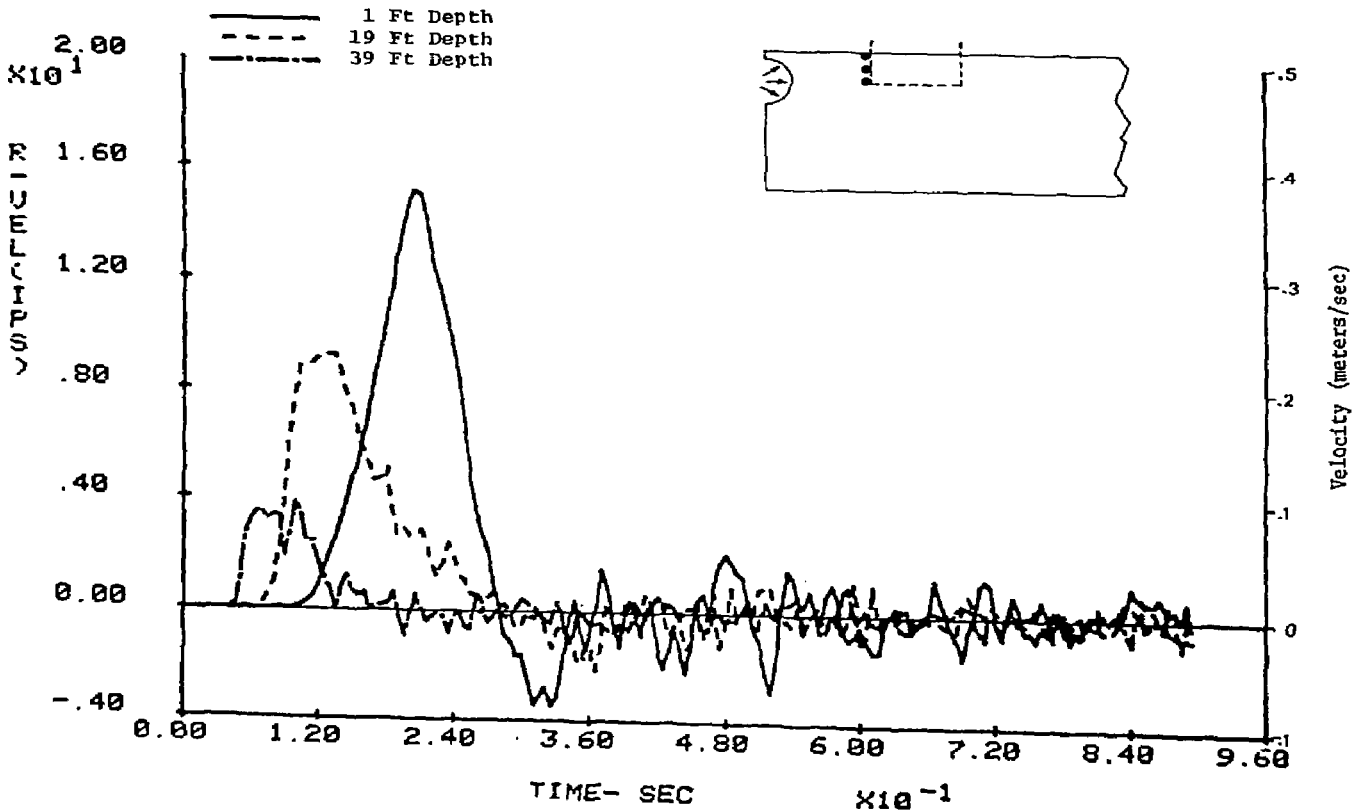

Figure 3-1. *Free field horizontal velocity-time history at range 22.5m (74 ft) and three depths (positive is outward from source).*

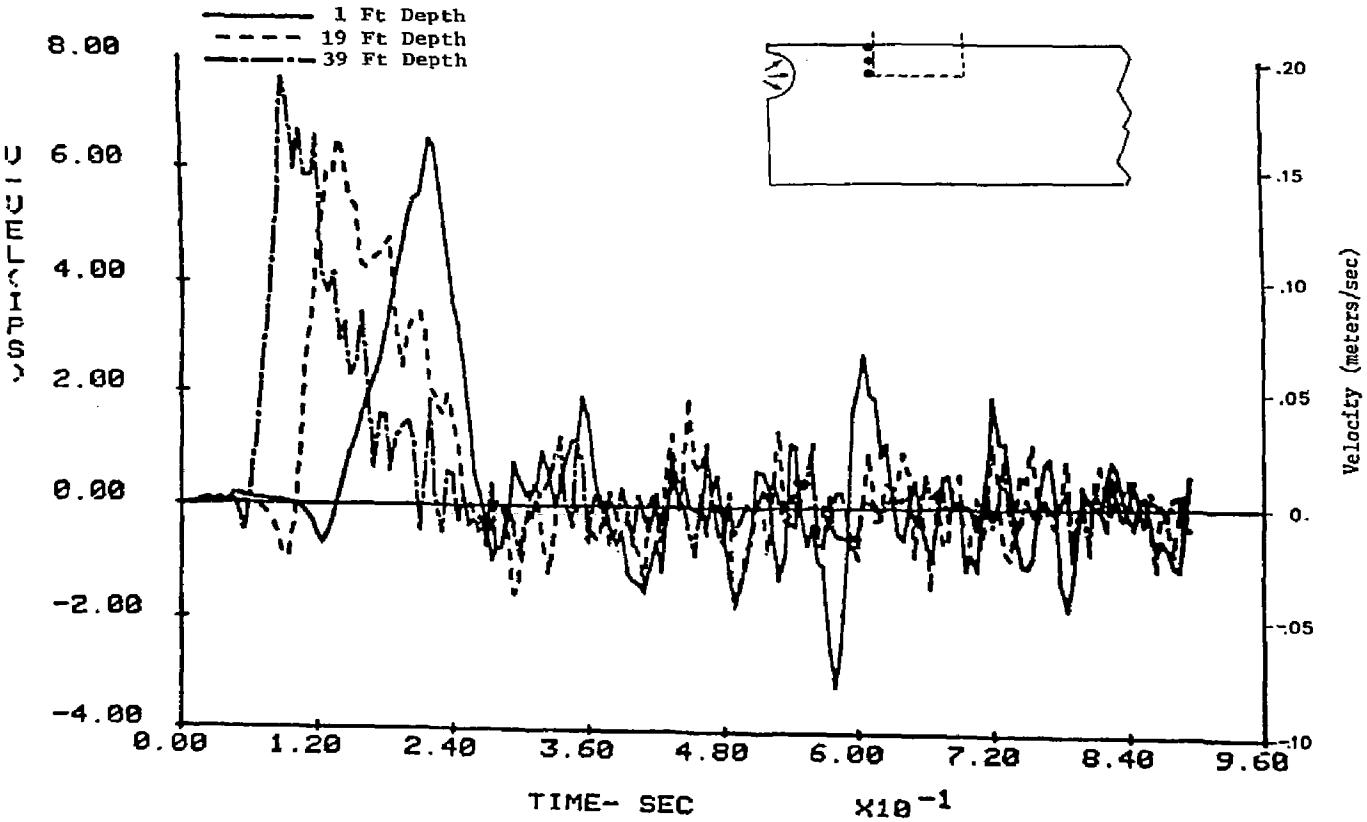

Figure 3-2. Free field vertical velocity-time history at range 22.5m (74 ft) and three depths (positive is down).

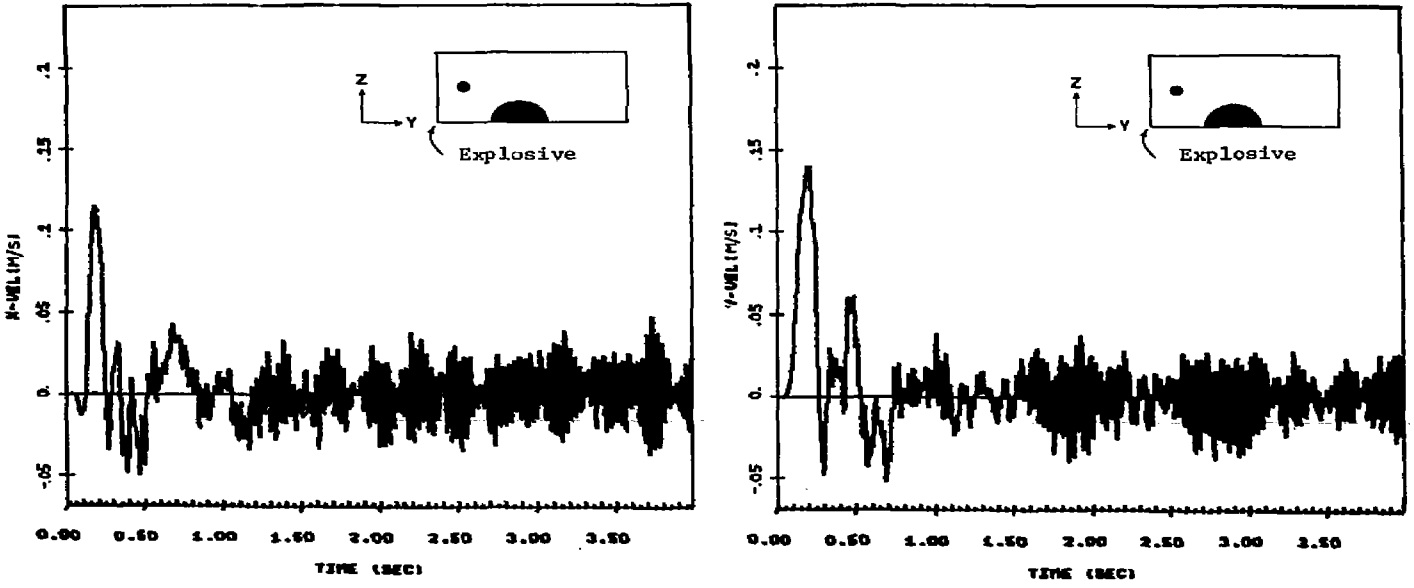

a. Vertical Velocity

b. Y-Component of Horizontal Velocity

Figure 3-3. Free field velocity-time histories at a depth of 3m and a range of 22m from source (19m from symmetry plane).

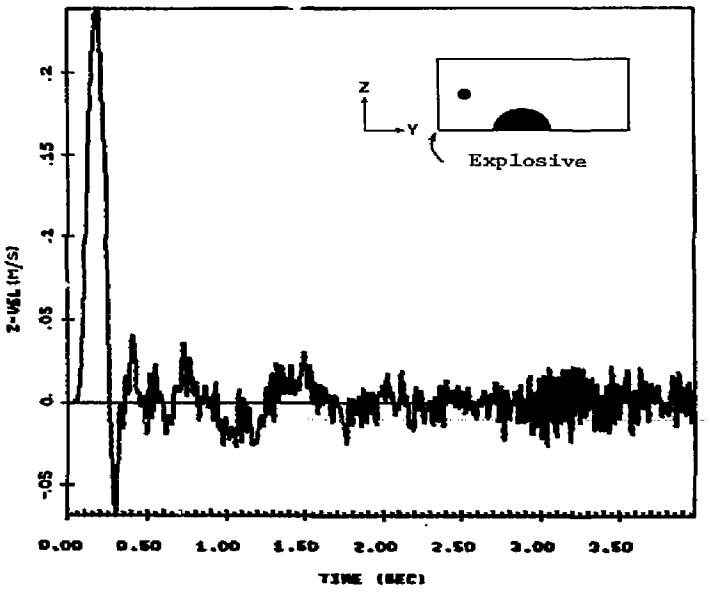

c. Z-Component of Horizontal Velocity

Figure 3-3 (continued). Free field velocity-time histories at a depth of 3m and a range of 22m from source (19m from symmetry plane).

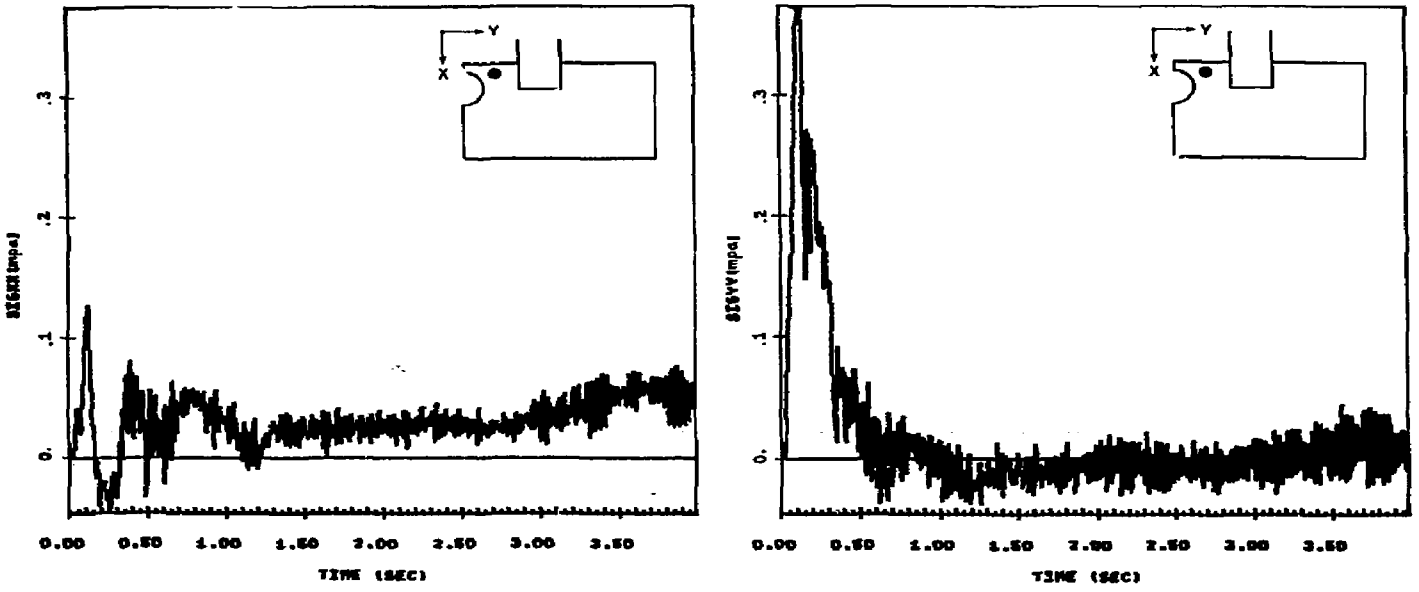

a. Vertical Stress

b. Y-Component of Horizontal Stress

Figure 3-4. Free field stress-time histories and stress path for soil element on plane of symmetry at a range of 12m from explosive charge, depth of 5m.

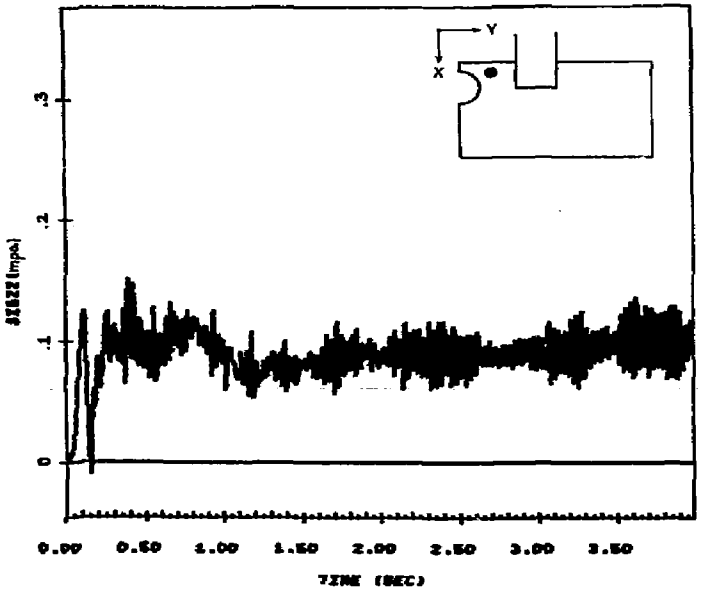

c. Z-Component of Horizontal Stress

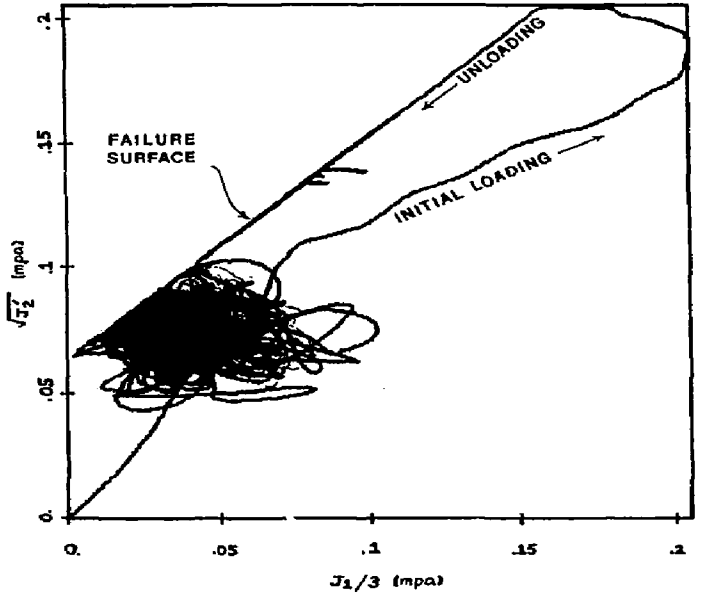

d. Stress Path in Terms of Stress Invariants

Figure 3-4 (continued). Free field stress-time histories and stress path for soil element on plane of symmetry at a range of 12m from explosive charge, depth of 5m.

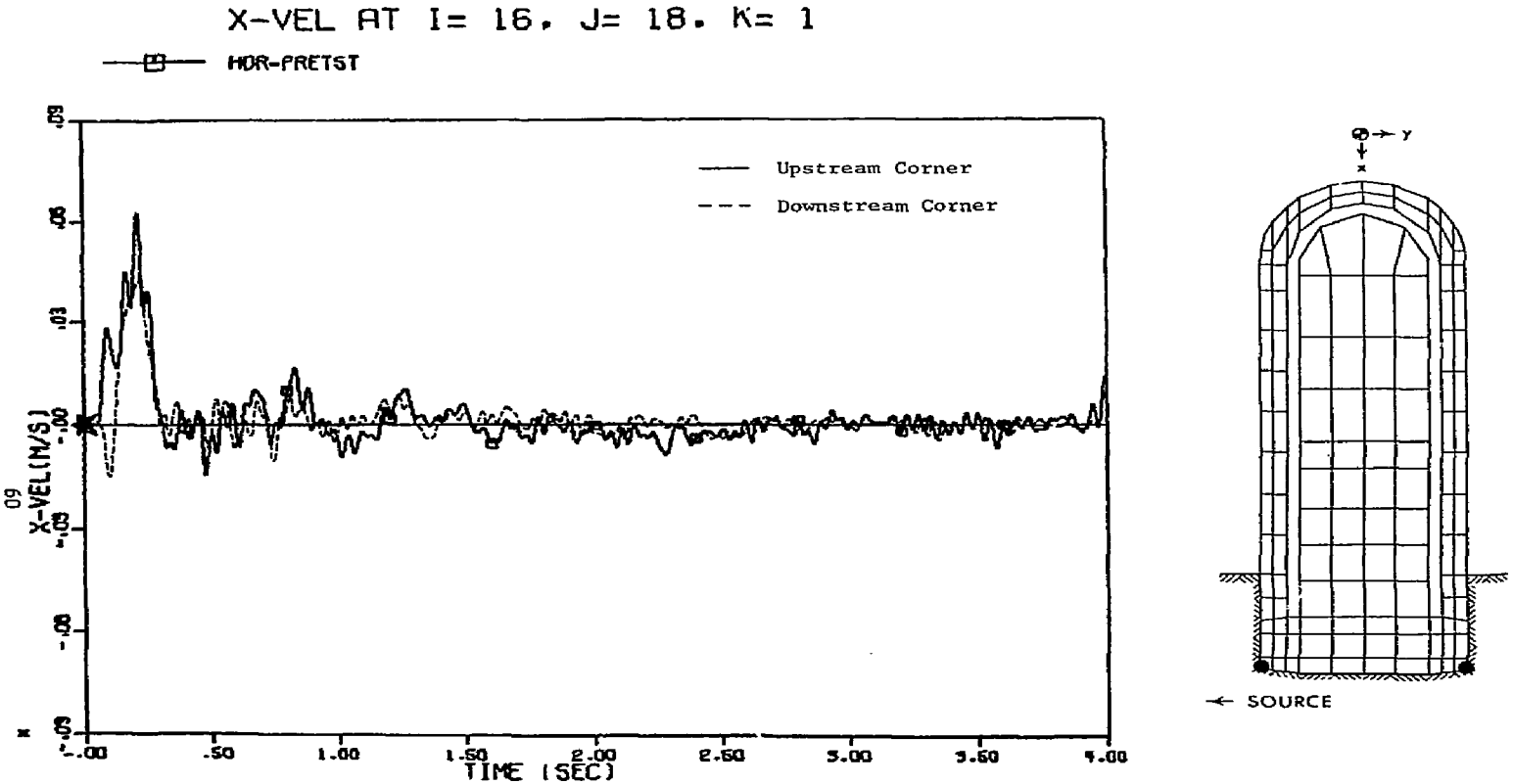

Figure 3-5. Vertical velocity-time histories at upstream and downstream corners of foundation; differences are primarily a measure of rocking.

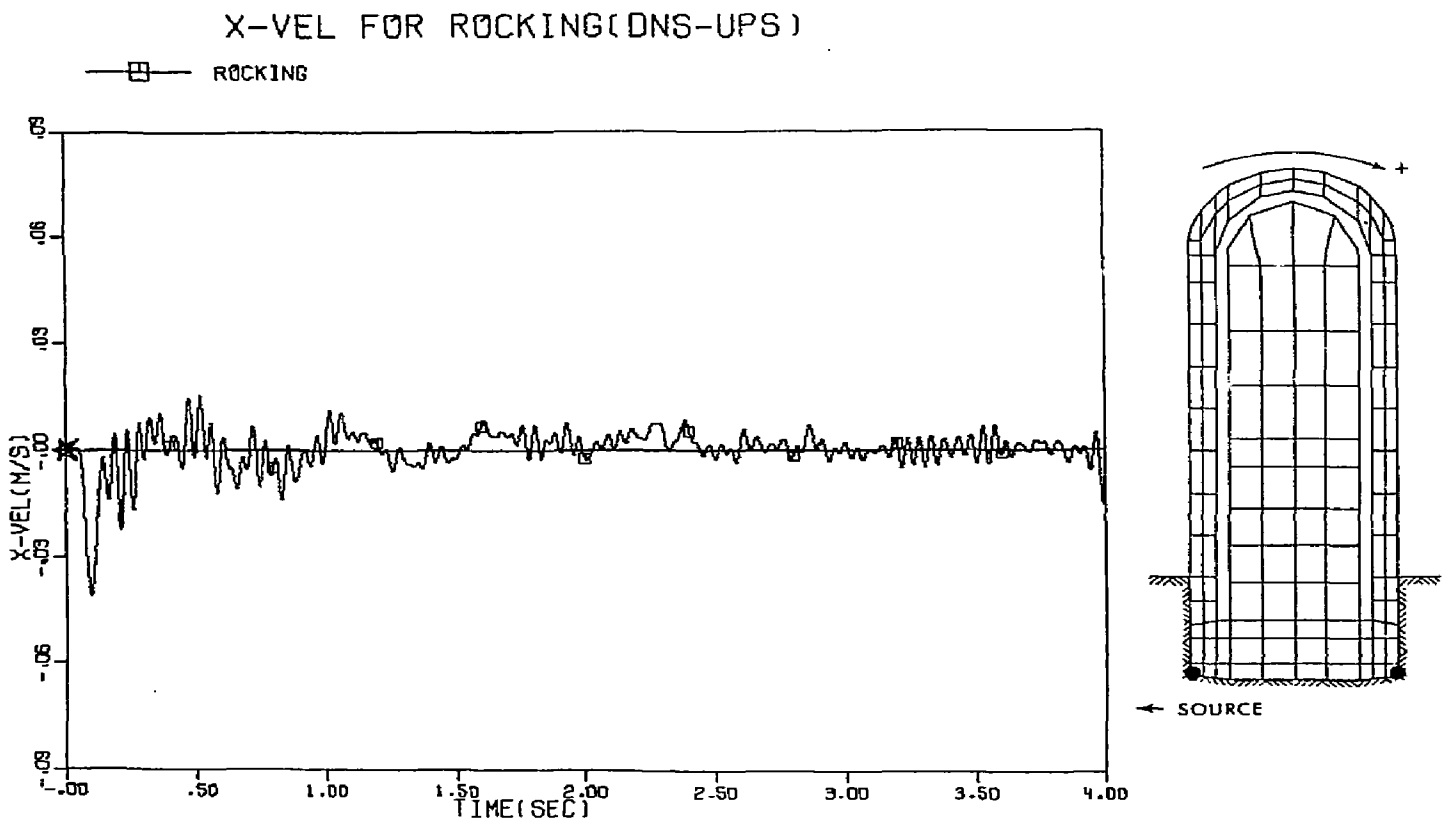

Figure 3-6. Rocking velocity-time history of foundation (difference between downstream and upstream corner vertical velocities).

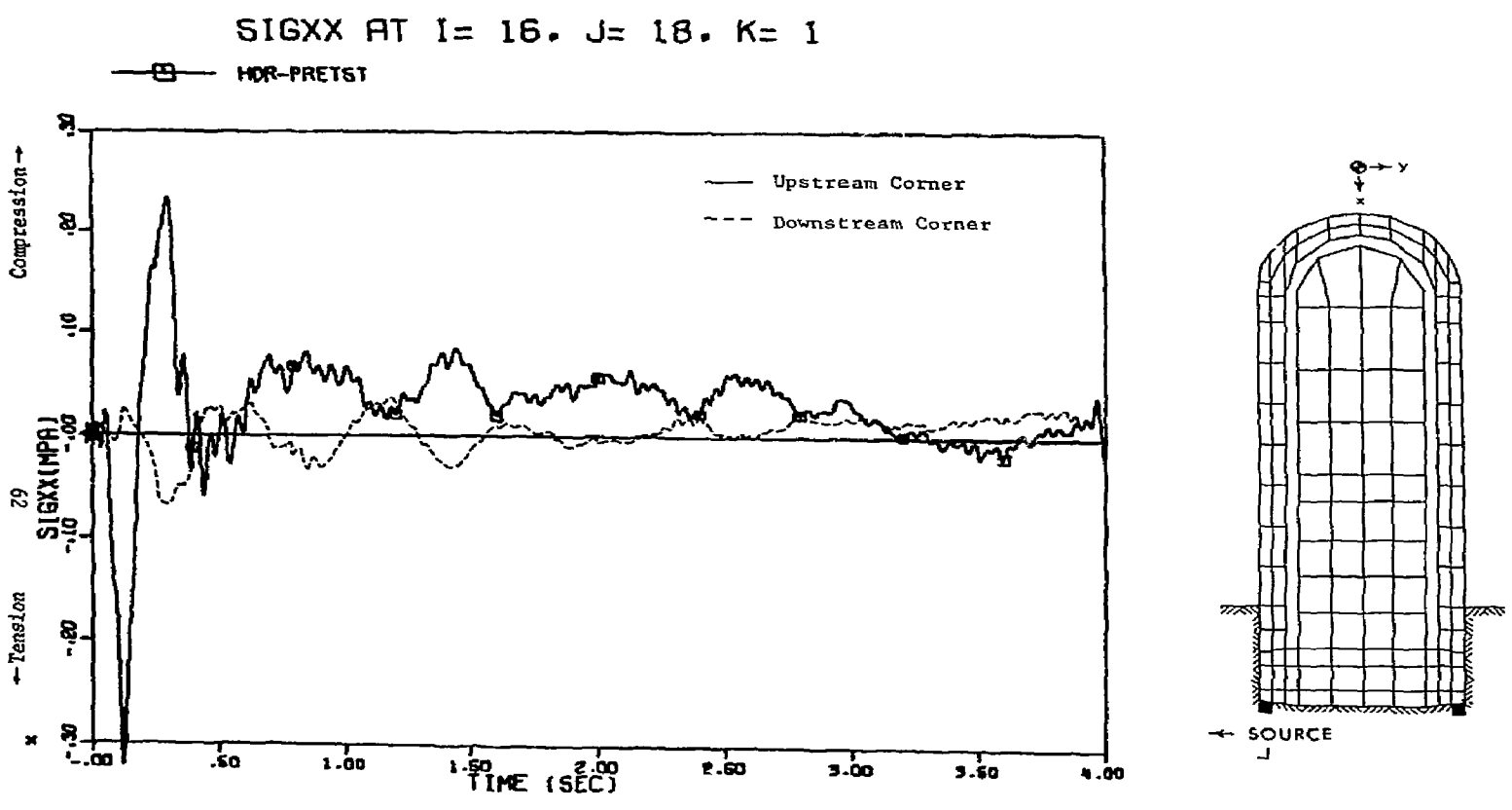

Figure 3-7. Vertical stress-time histories in soil just beneath upstream and downstream corners of foundation.

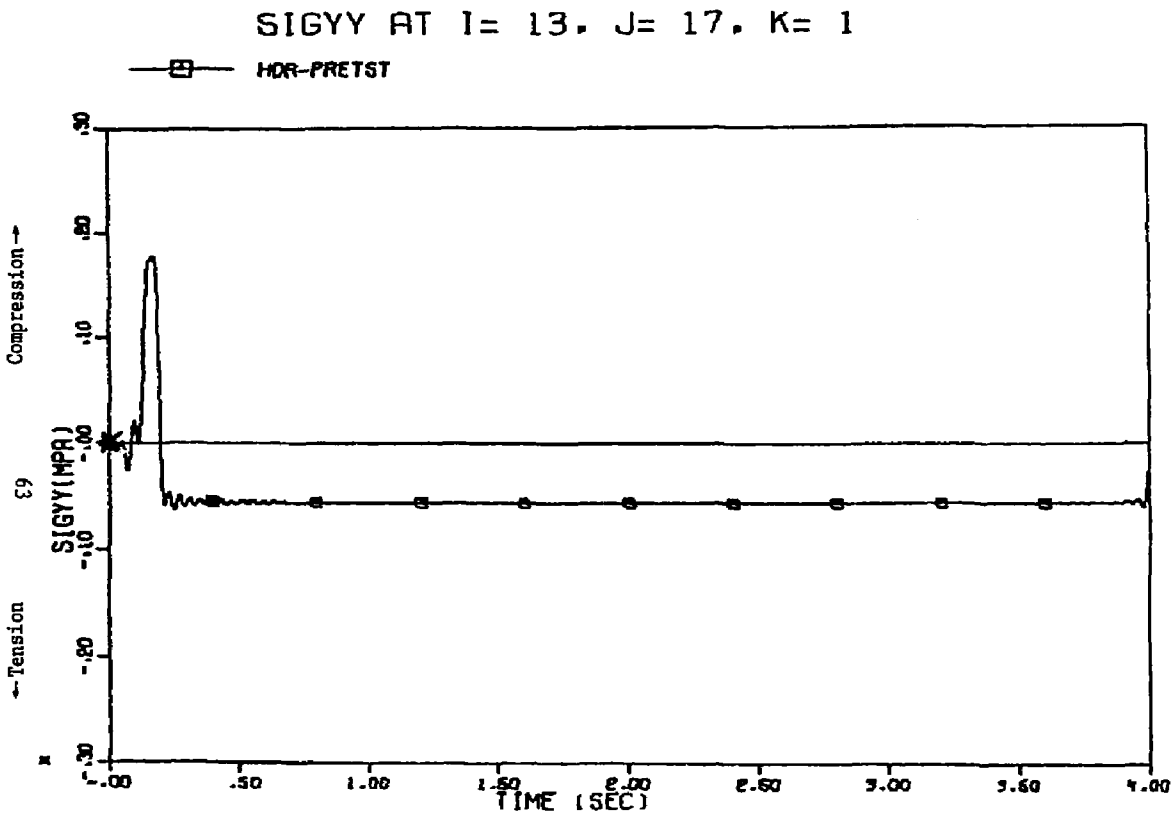

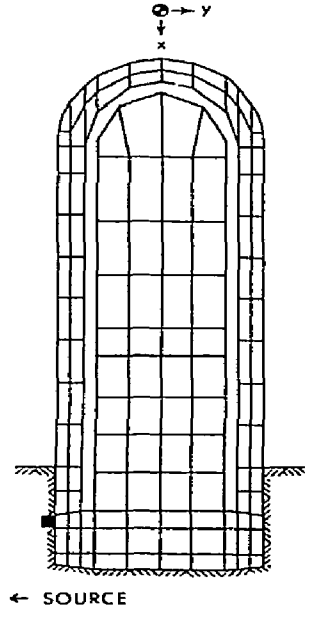

Figure 3-8. Stress in soil acting normal to upstream surface of containment structure.

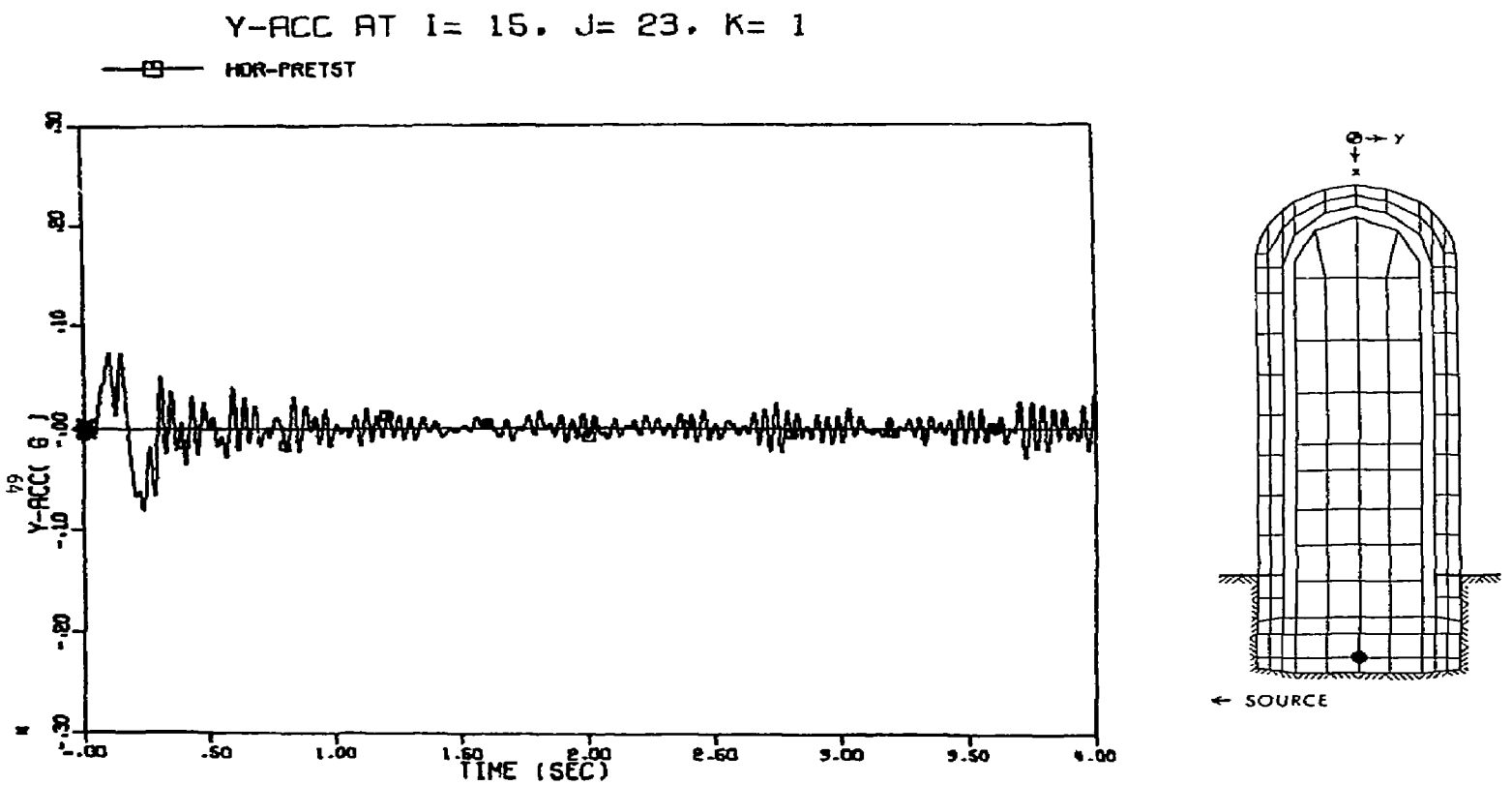

Figure 3-9. Horizontal acceleration-time history of foundation (elev -11.05, centerline).

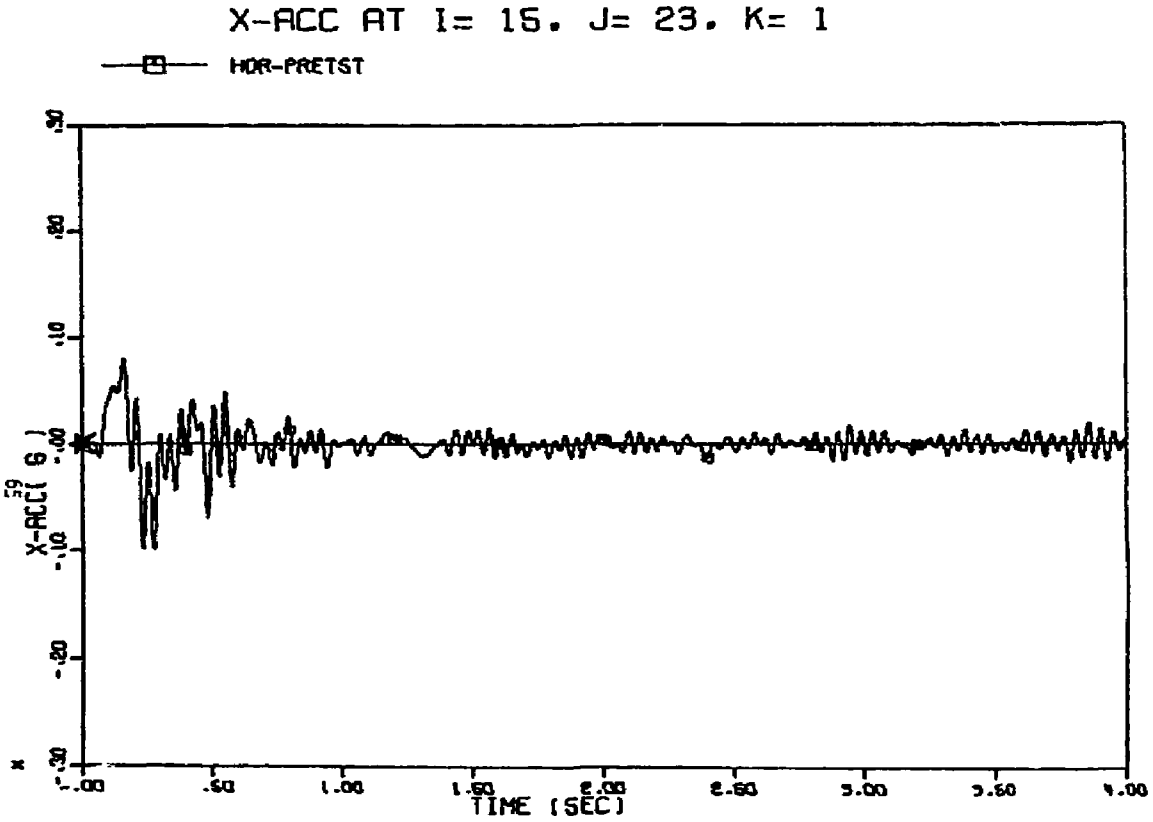

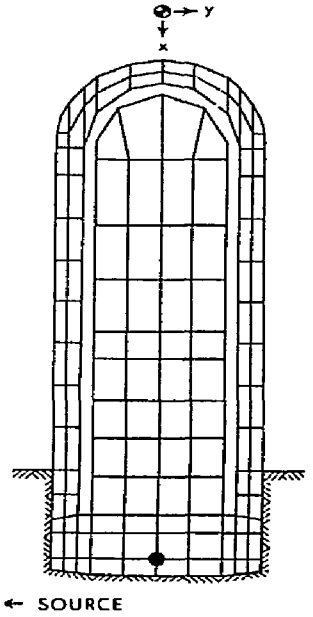

Figure 3-10. Vertical acceleration-time history of foundation (elev -11.05m, centerline).

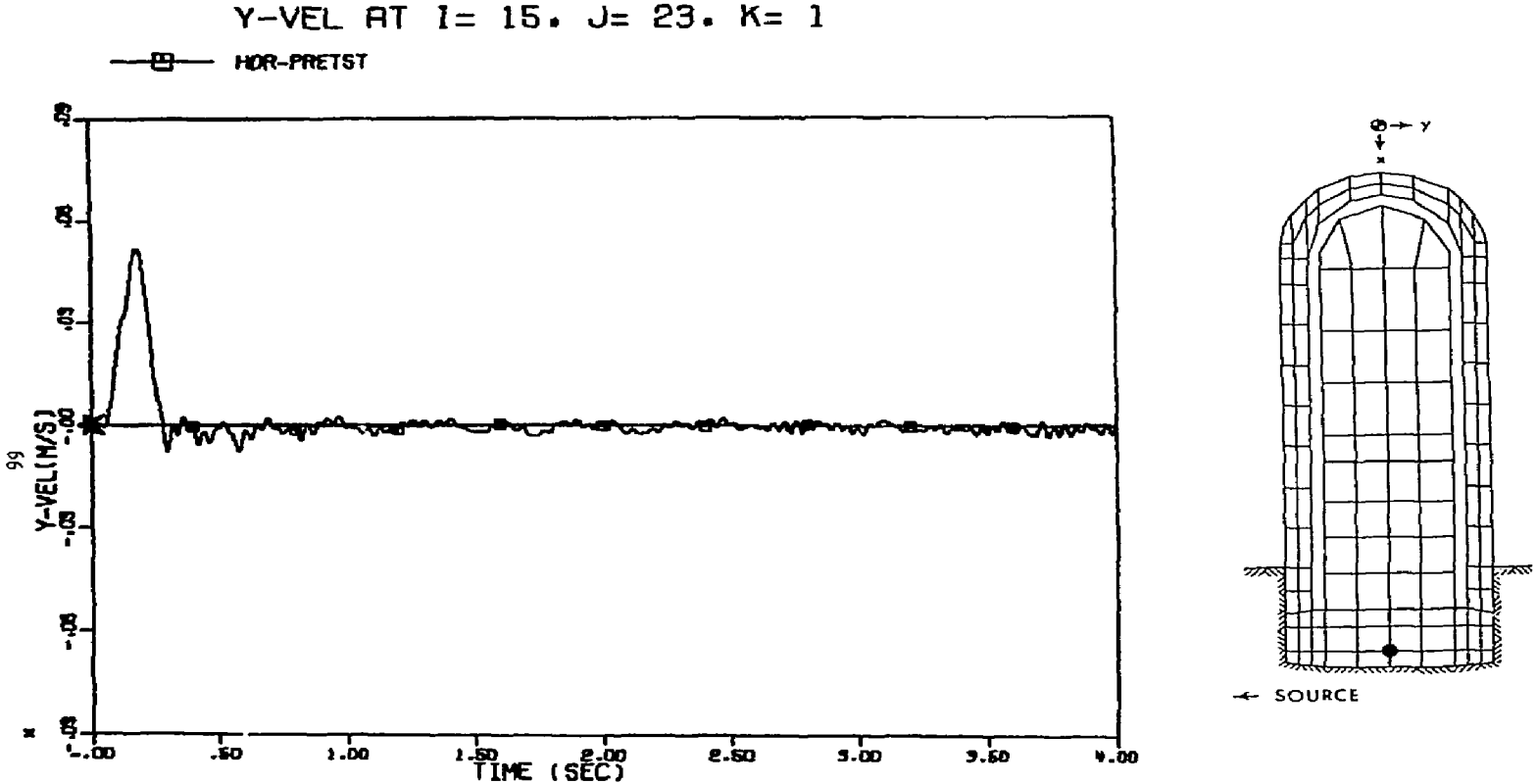

Figure 3-11. Horizontal velocity-time history of foundation (elev -11.05m, centerline).

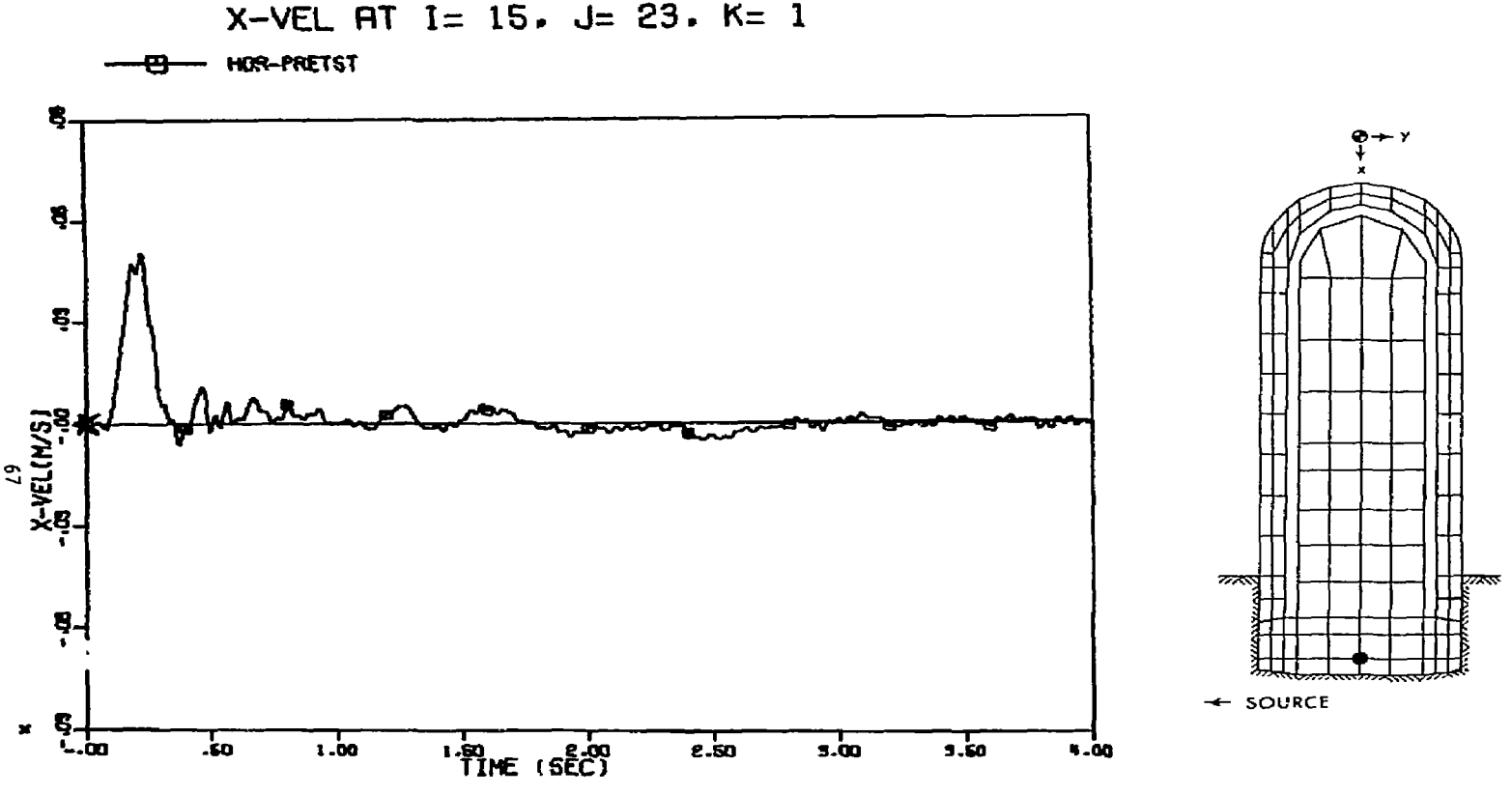

Figure 3-12. Vertical velocity-time history of foundation (elev -11.05m, centerline).

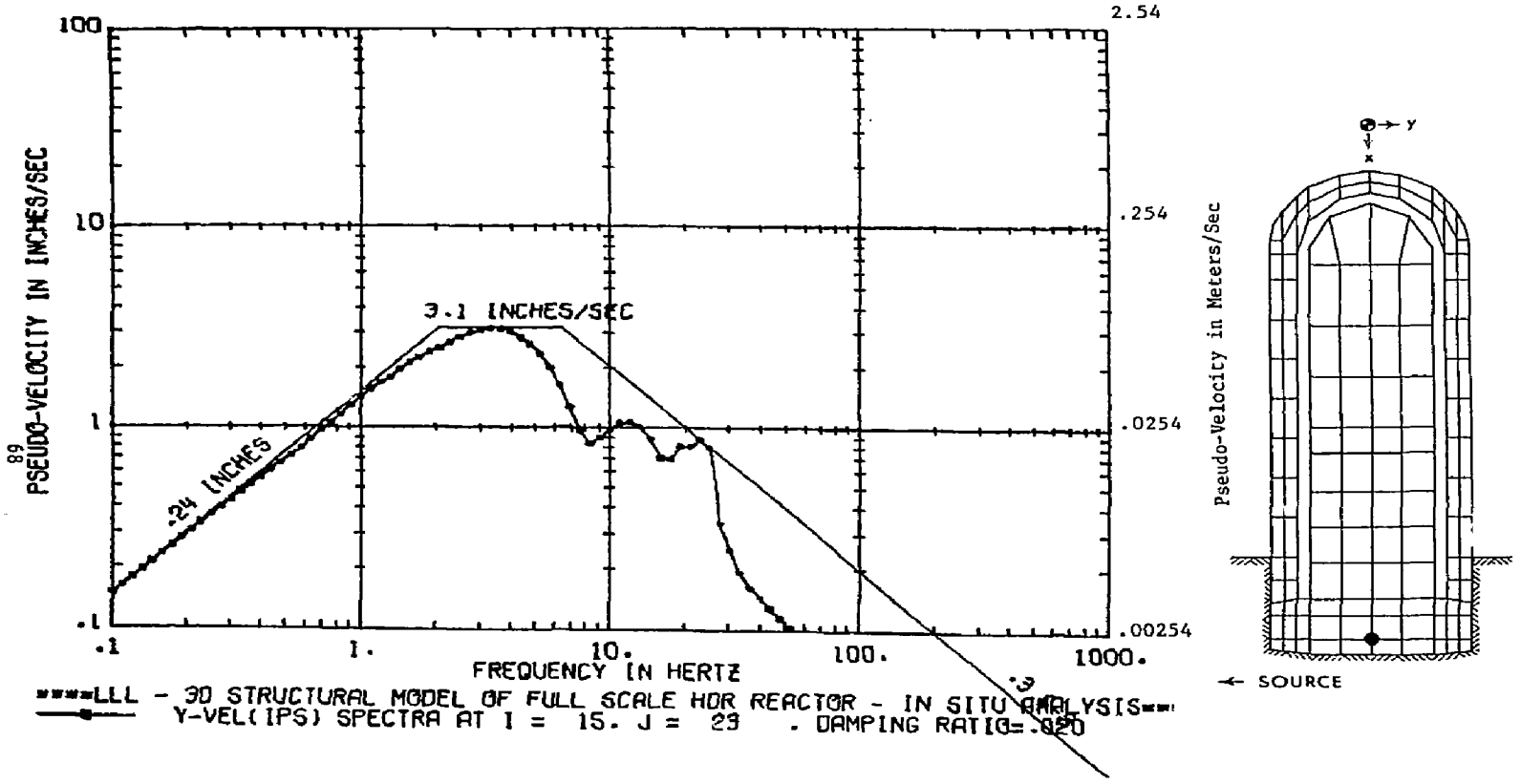

Figure 3-13a. Response spectra of horizontal motion of foundation (elev -11.05m, centerline).

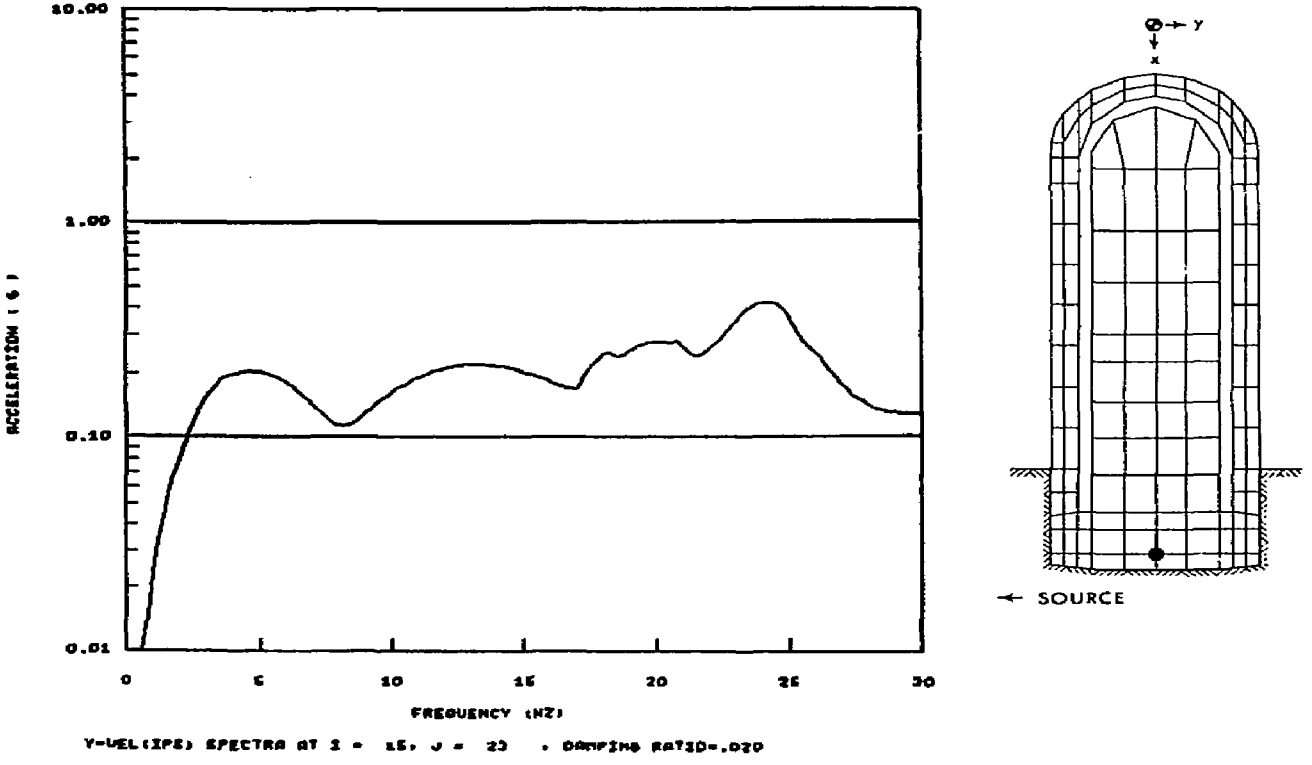

Figure 3-13b. Acceleration response spectra of horizontal motion of foundation (elevation -11.05m, centerline).

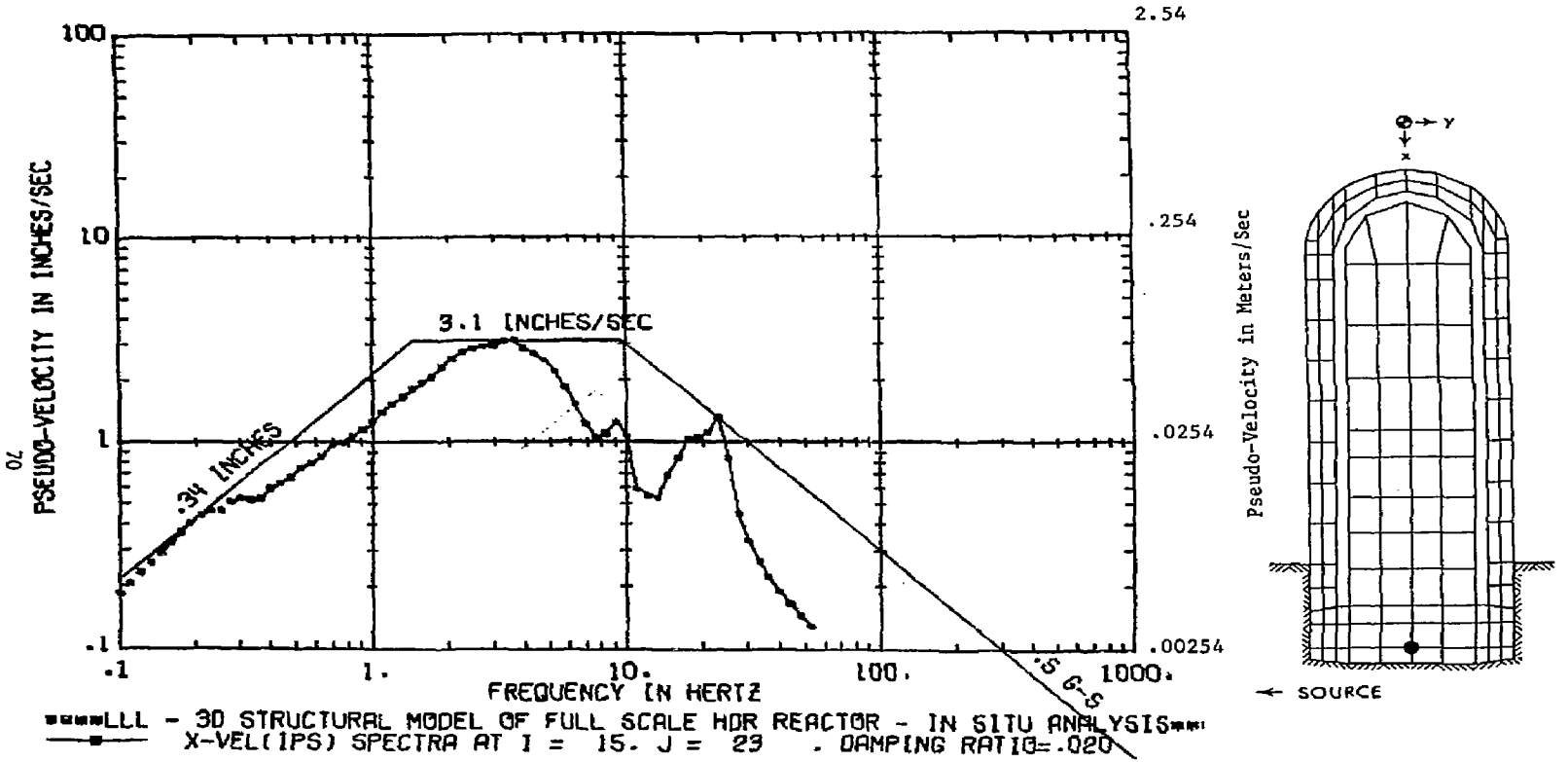

Figure 3-14a. Response spectra of vertical motion of foundation (elev -11.05m, centerline).

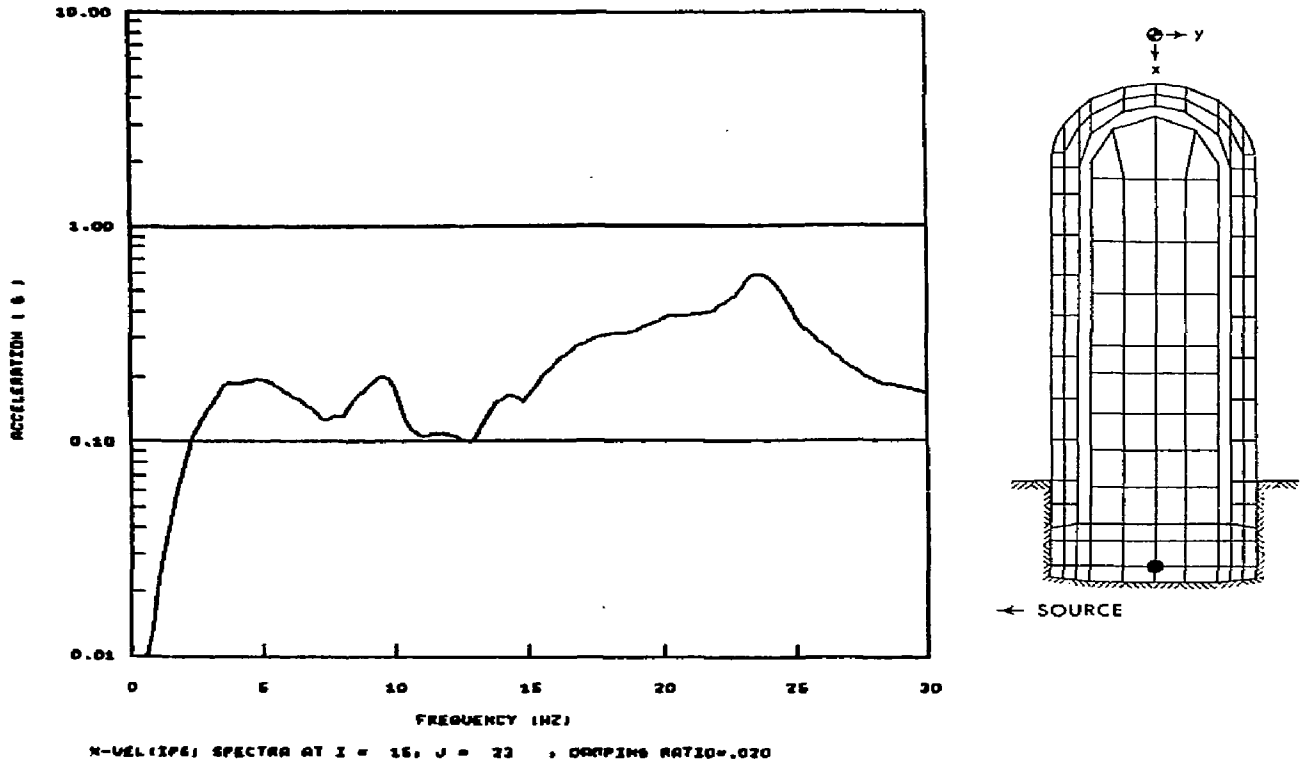

Figure 3-14b. Acceleration response spectra of vertical motion of foundation (elevation -11.05m, centerline).

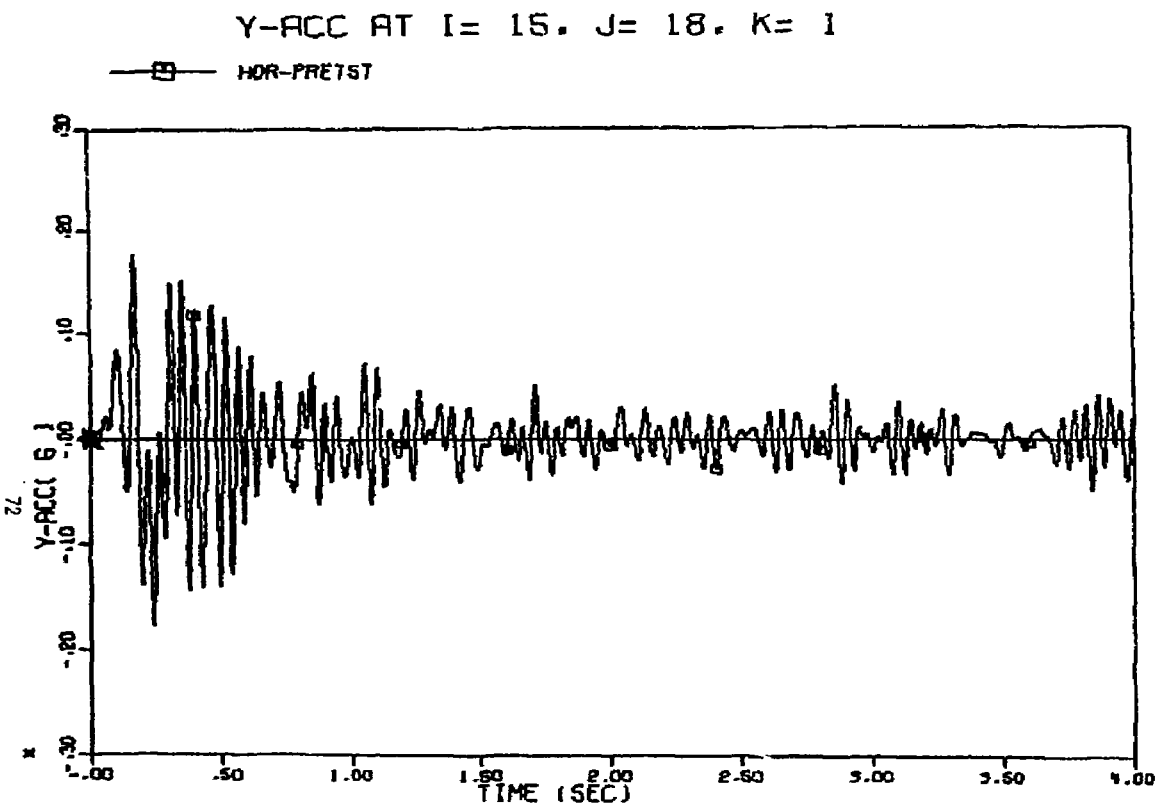

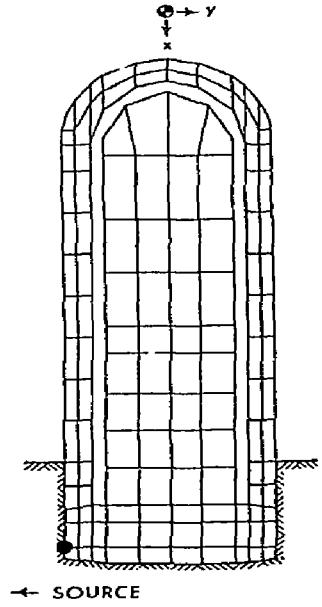

Figure 3-15. Horizontal acceleration-time history near upstream corner of foundation (elev -11.05m, 11.35m forward of centerline).

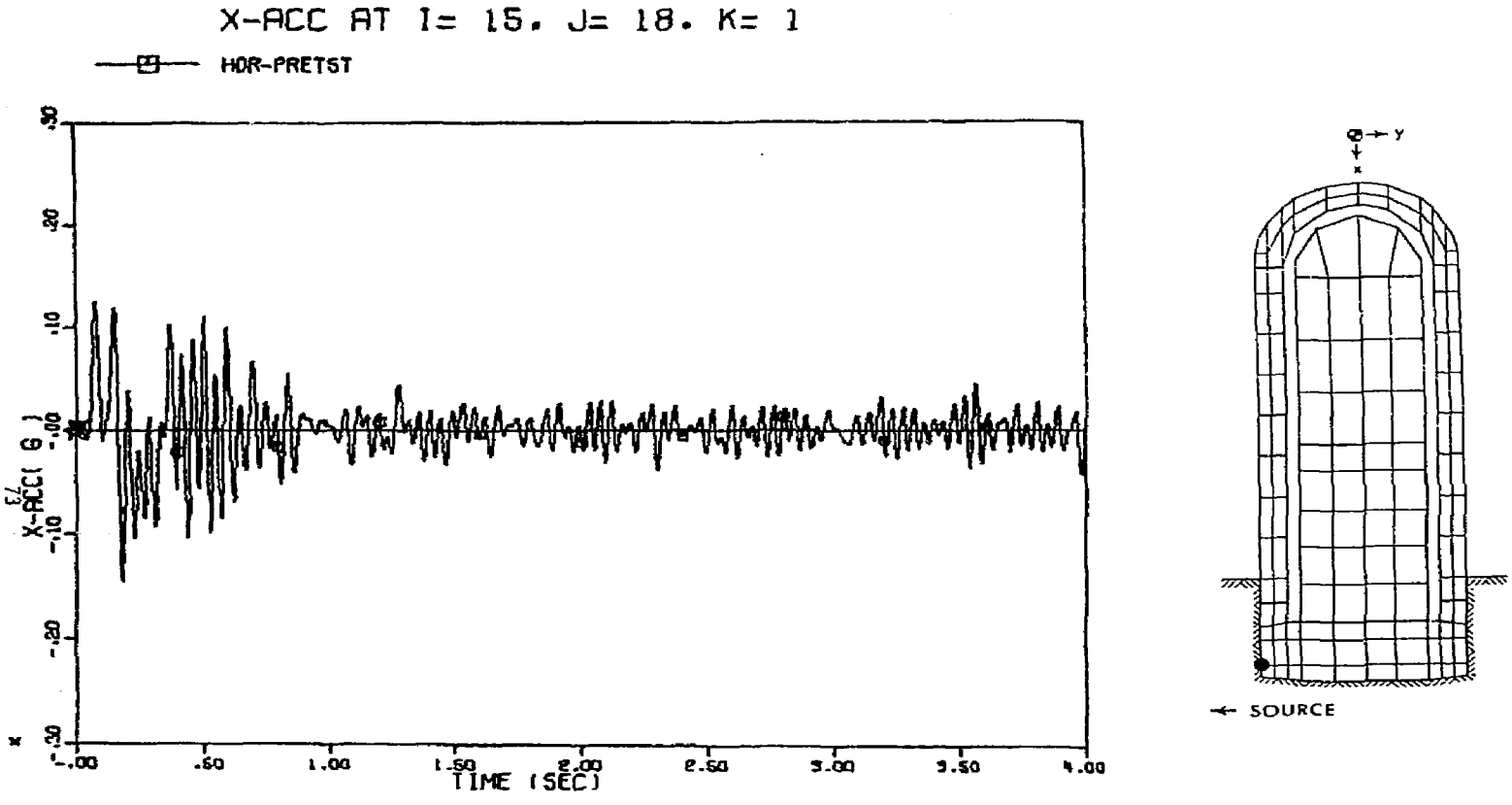

Figure 3-16. Vertical acceleration-time history near upstream corner of foundation (elev -11.05m, 11.35m forward of centerline).

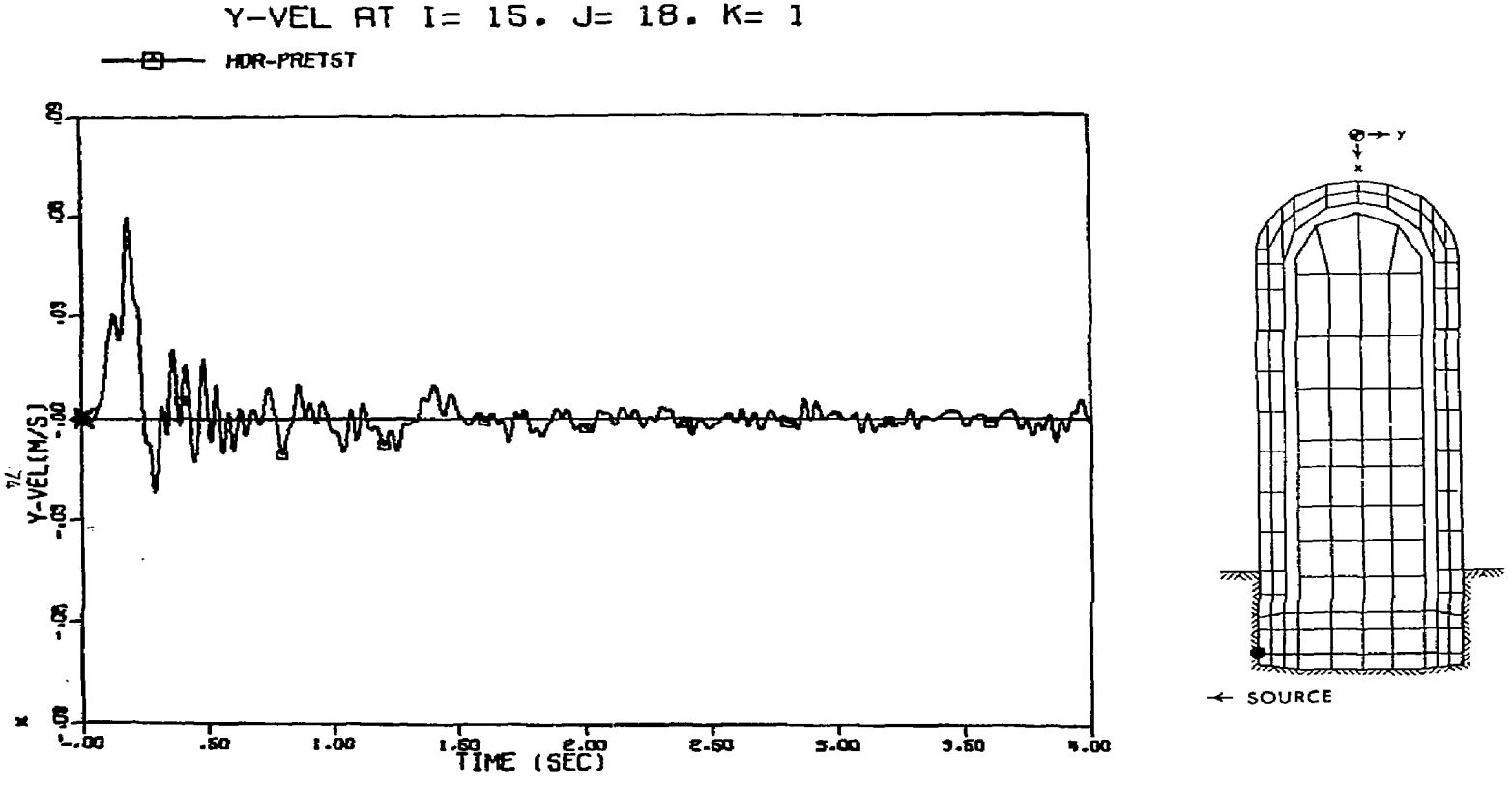

Figure 3-17. Horizontal velocity-time history near upstream corner of foundation (elev -11.05m, 11.35m forward of centerline).

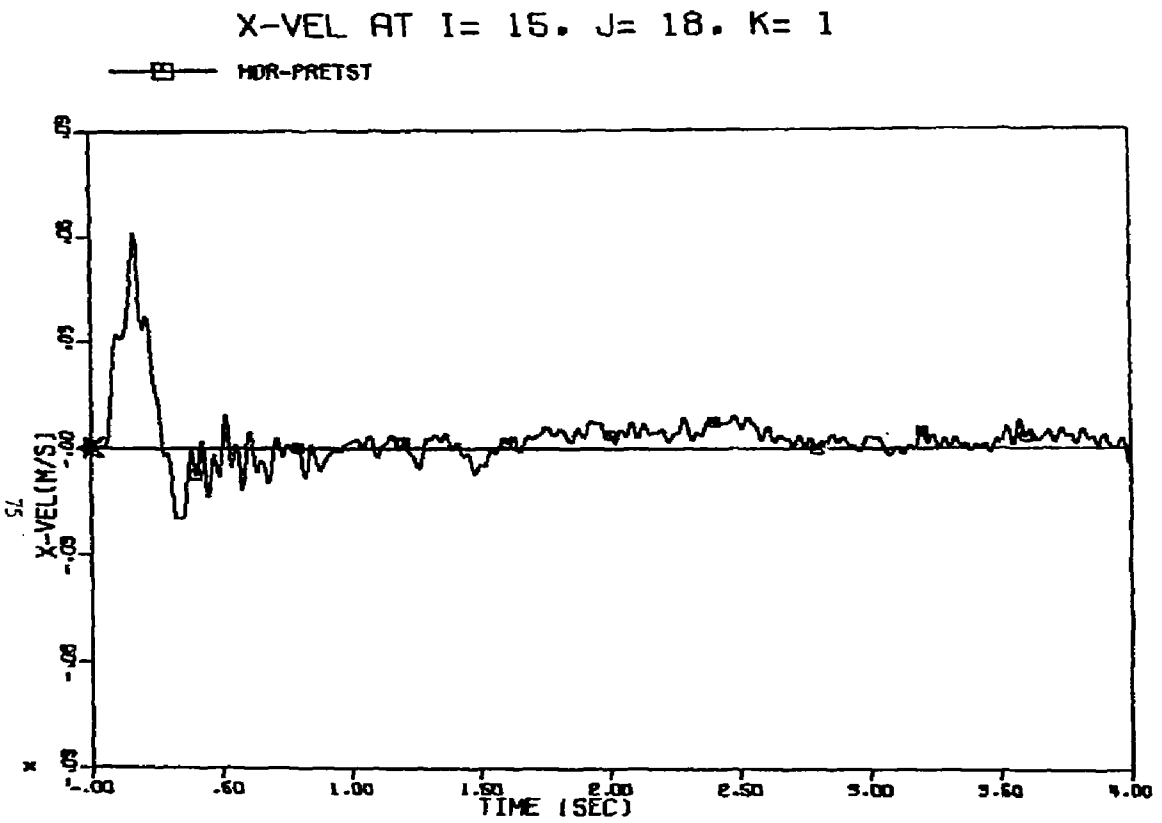

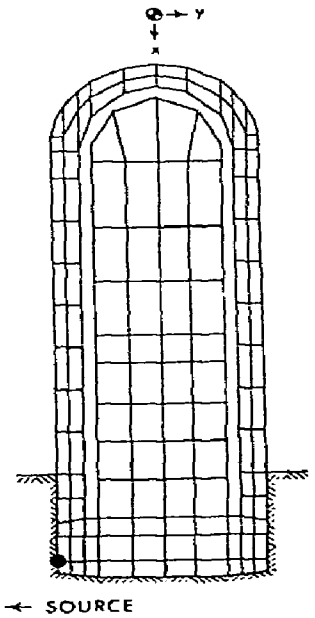

Figure 3-18. Vertical velocity-time history near upstream corner of foundation (elev -11.05m, 11.35m forward of centerline).

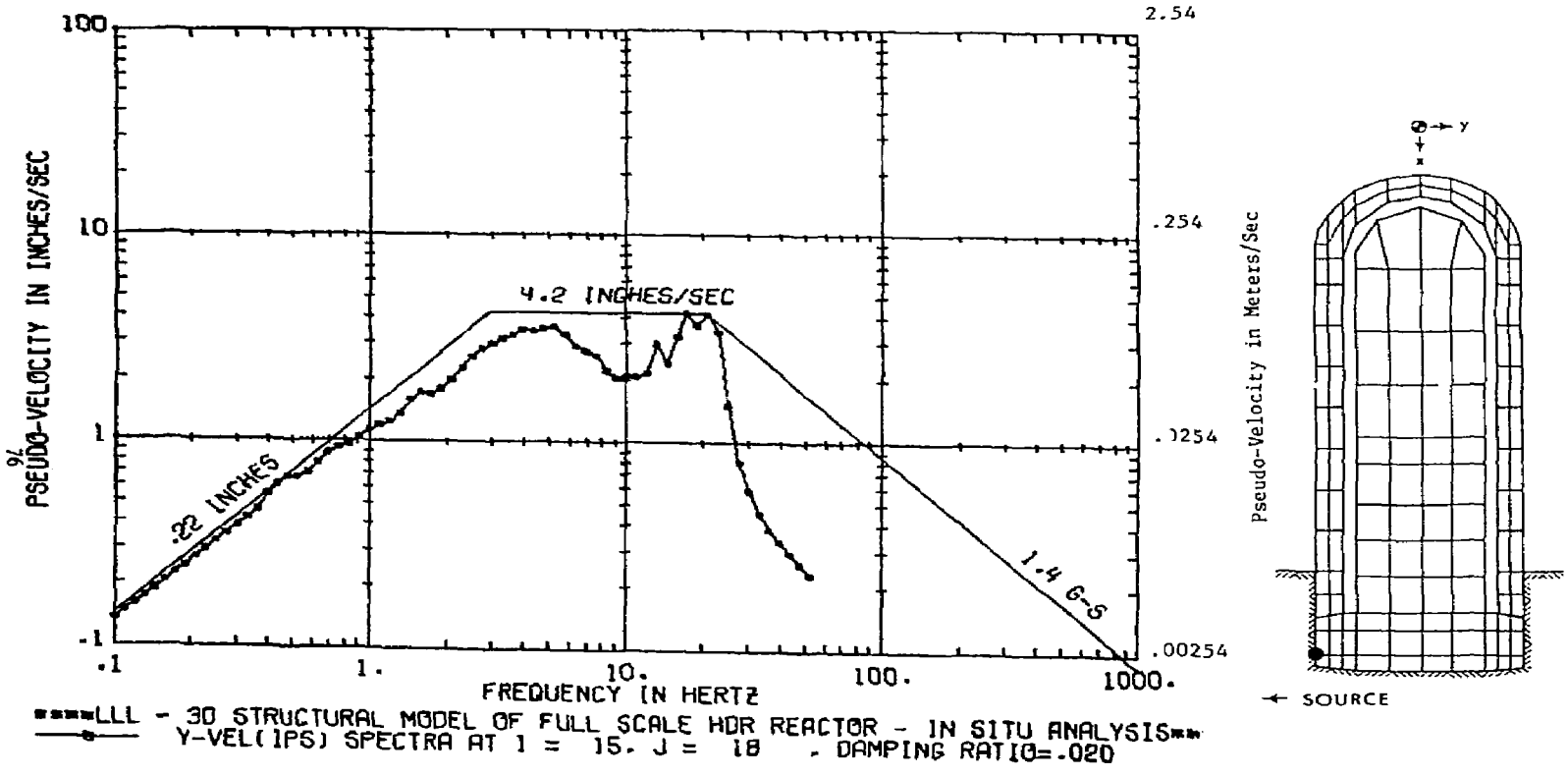

Figure 3-19a. Response spectra of horizontal motion near upstream corner of foundation (elev -11.05m, 11.35m forward of centerline).

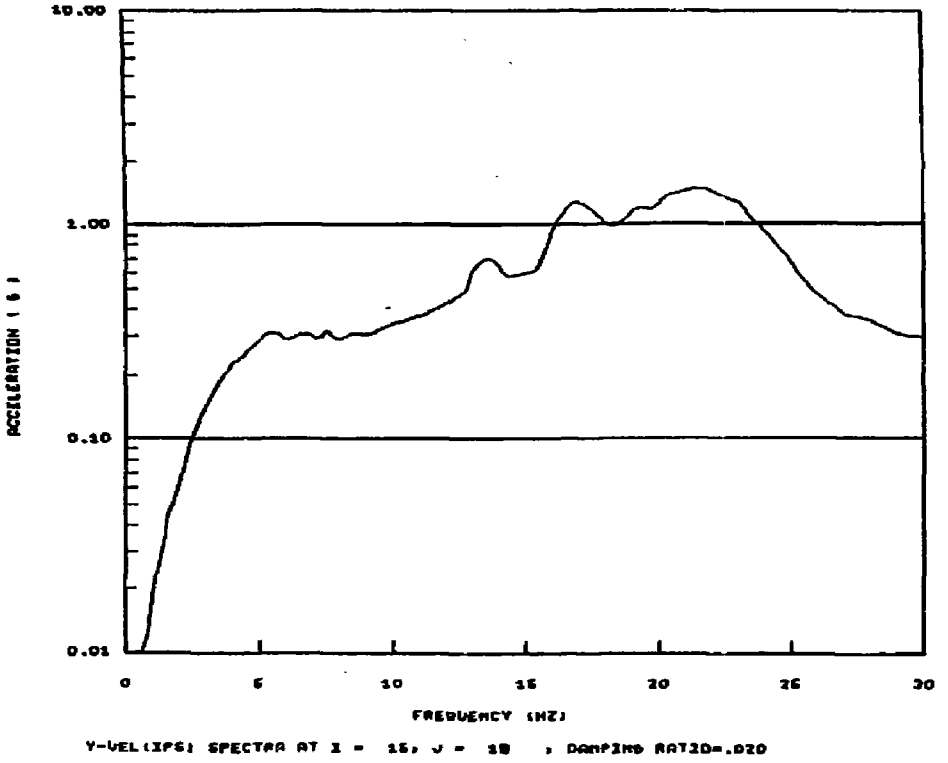

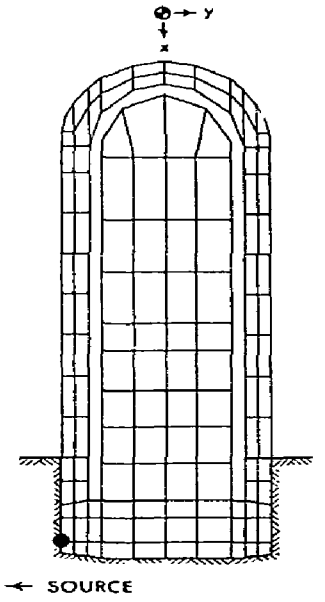

Figure 3-16. Acceleration response spectra of horizontal motion near upstream corner of foundation (elevation -11.05m, 11.35m forward of centerline).

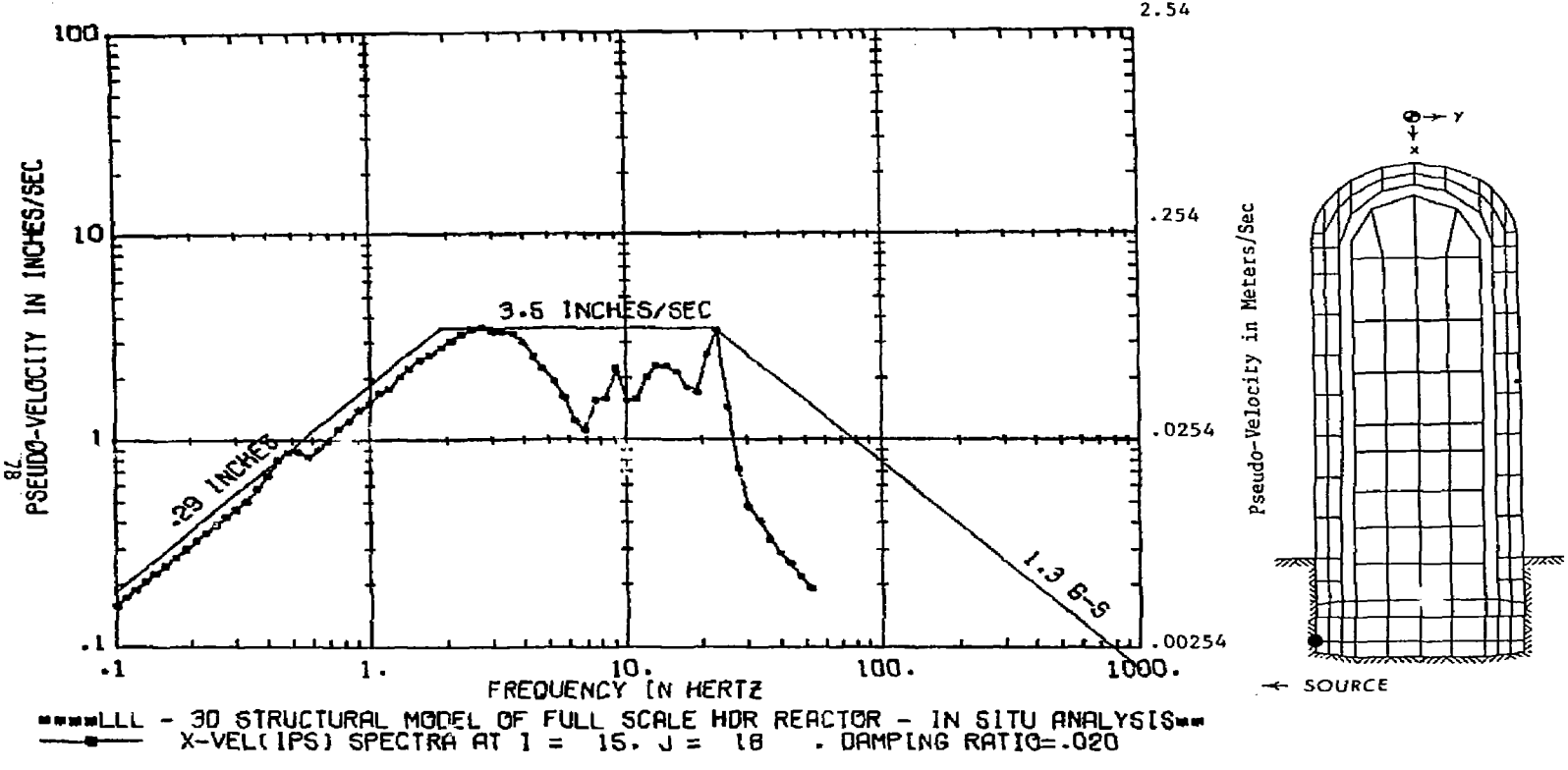

Figure 3-20. Response spectra of vertical motion near upstream corner of foundation (elev -11.05m, 11.35m forward of centerline).

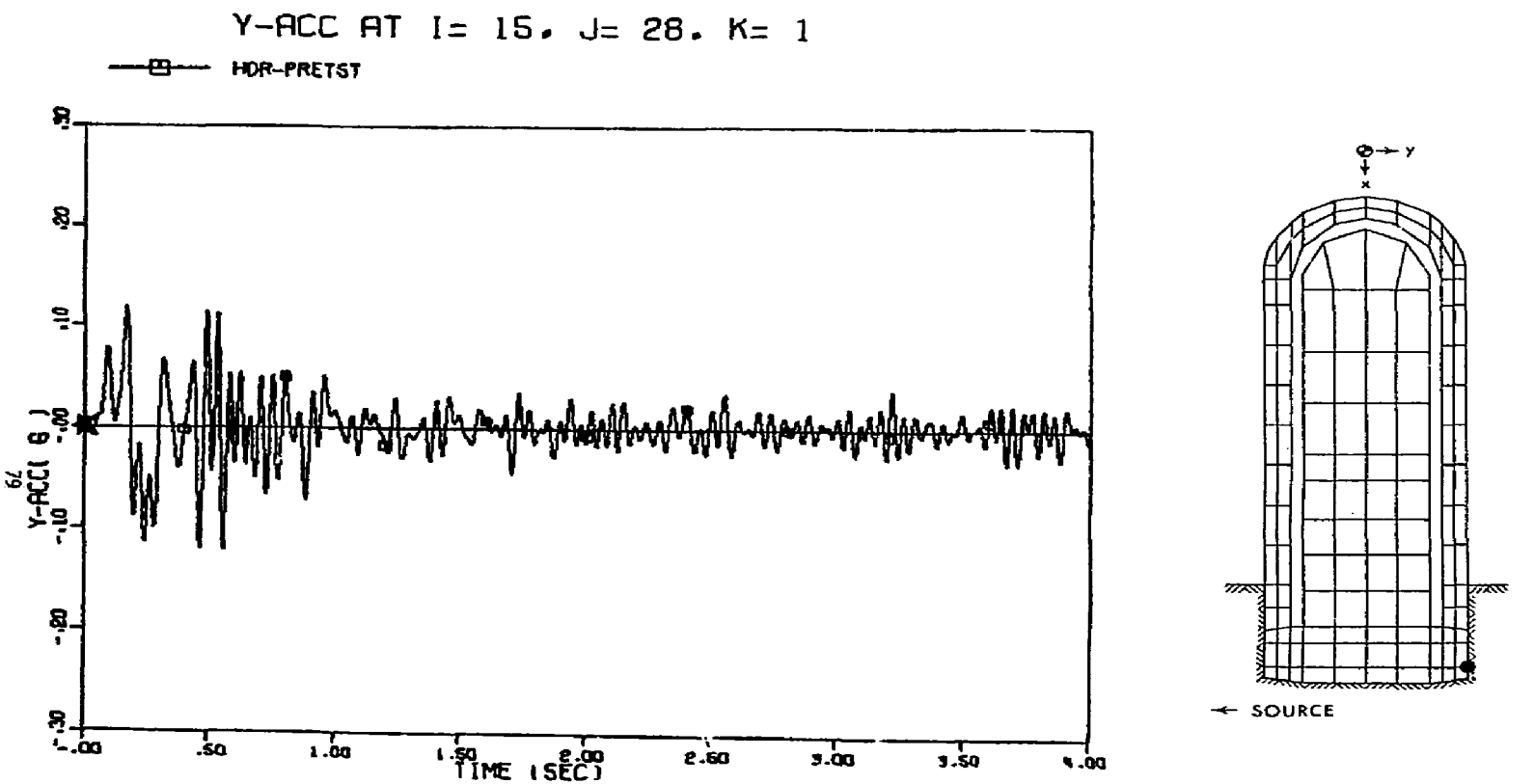

Figure 3-21. Horizontal acceleration-time history near downstream corner of foundation (elev -11.05m, 11.35m aft of centerline).

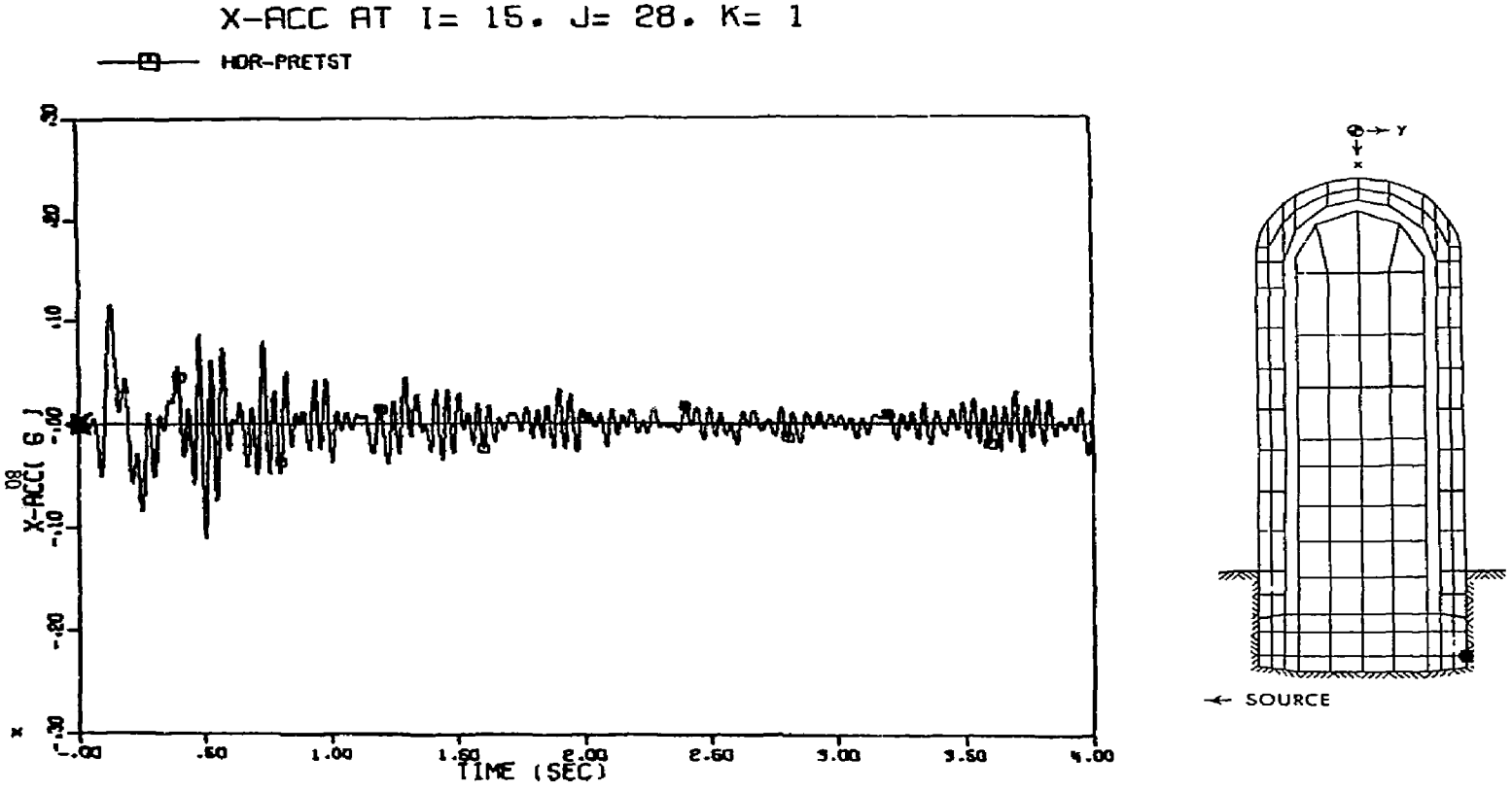

Figure 3-22. Vertical acceleration-time history near downstream corner of foundation (elev -11.05m, 11.35m aft of centerline).

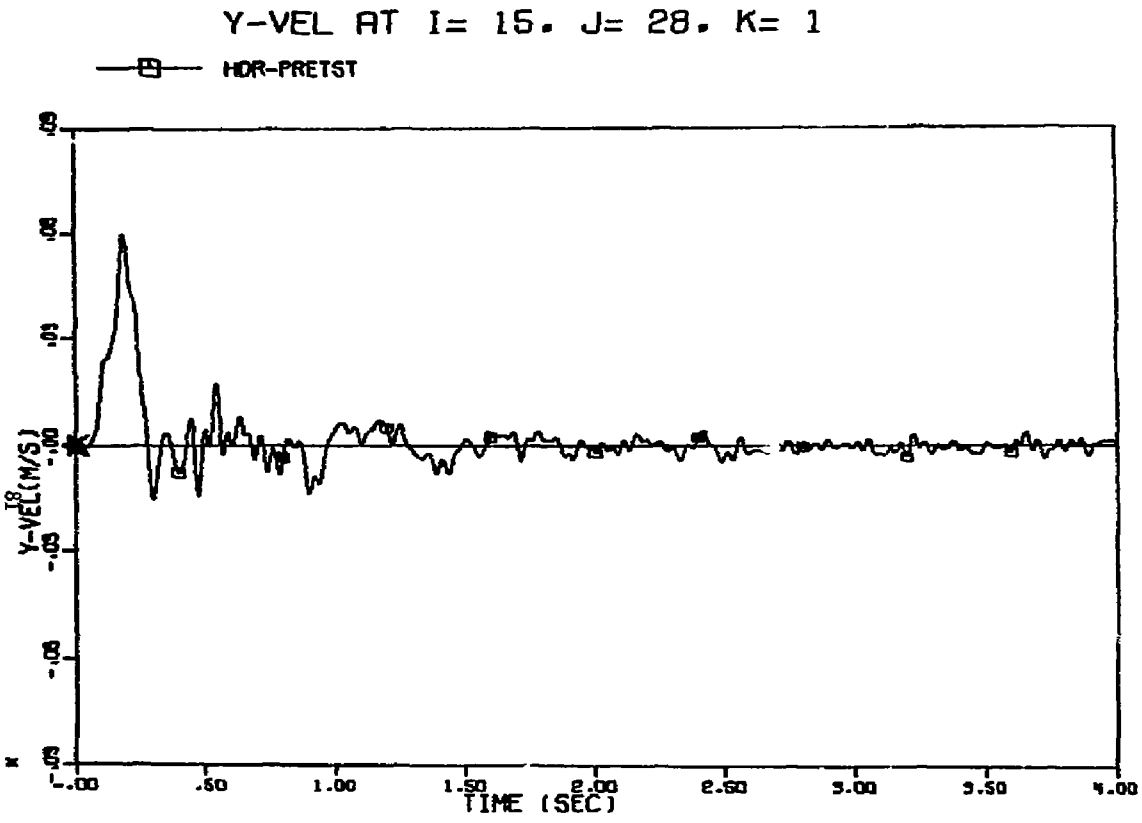

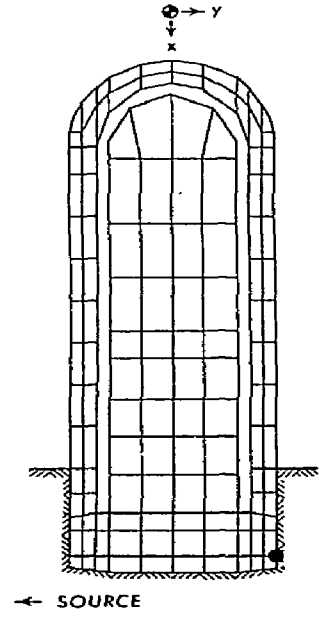

Figure 3-23. Horizontal velocity-time history near downstream corner of foundation (elev -11.05m, 11.35m aft of centerline).

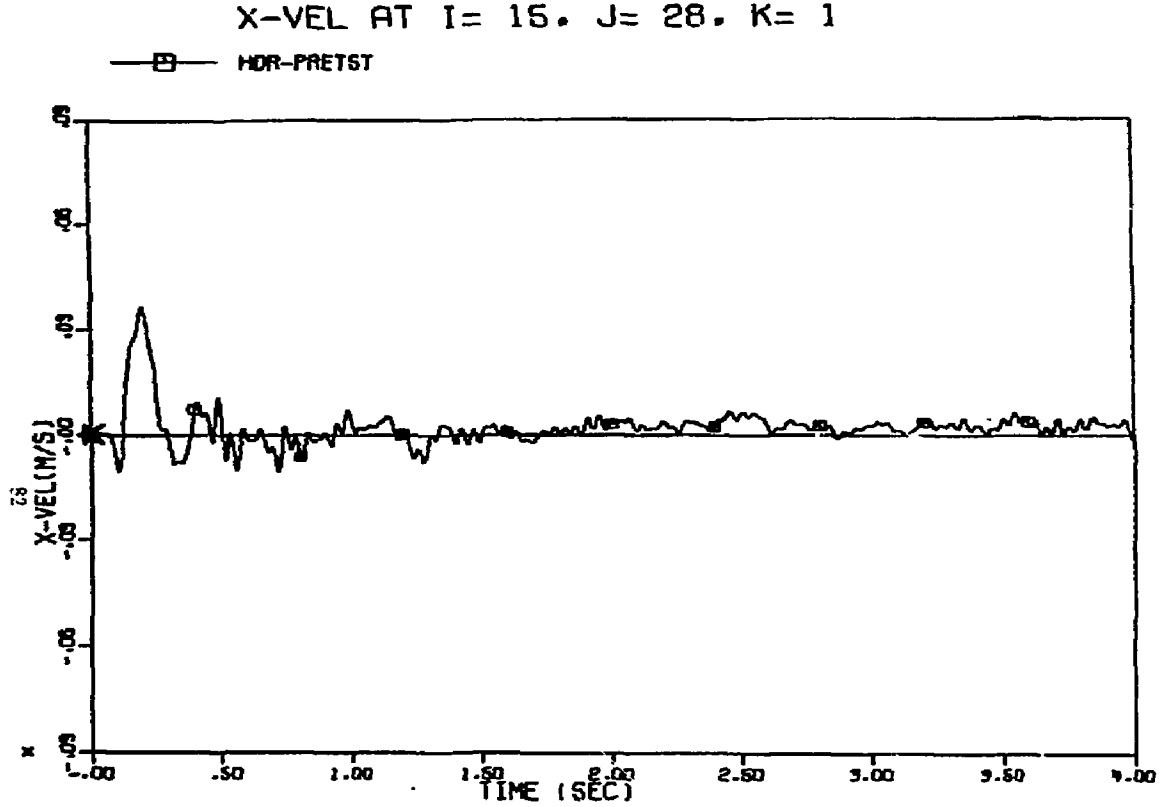

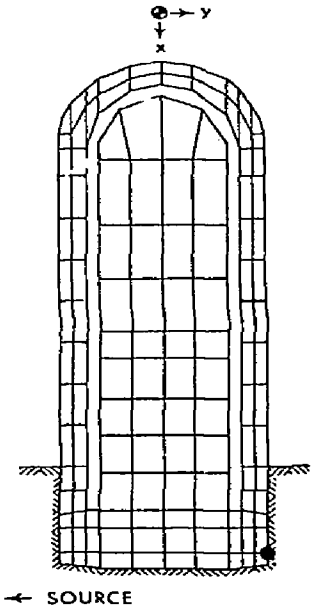

Figure 3-24. Vertical velocity-time history near downstream corner of foundation (elev -11.05m, 11.35m aft of centerline).

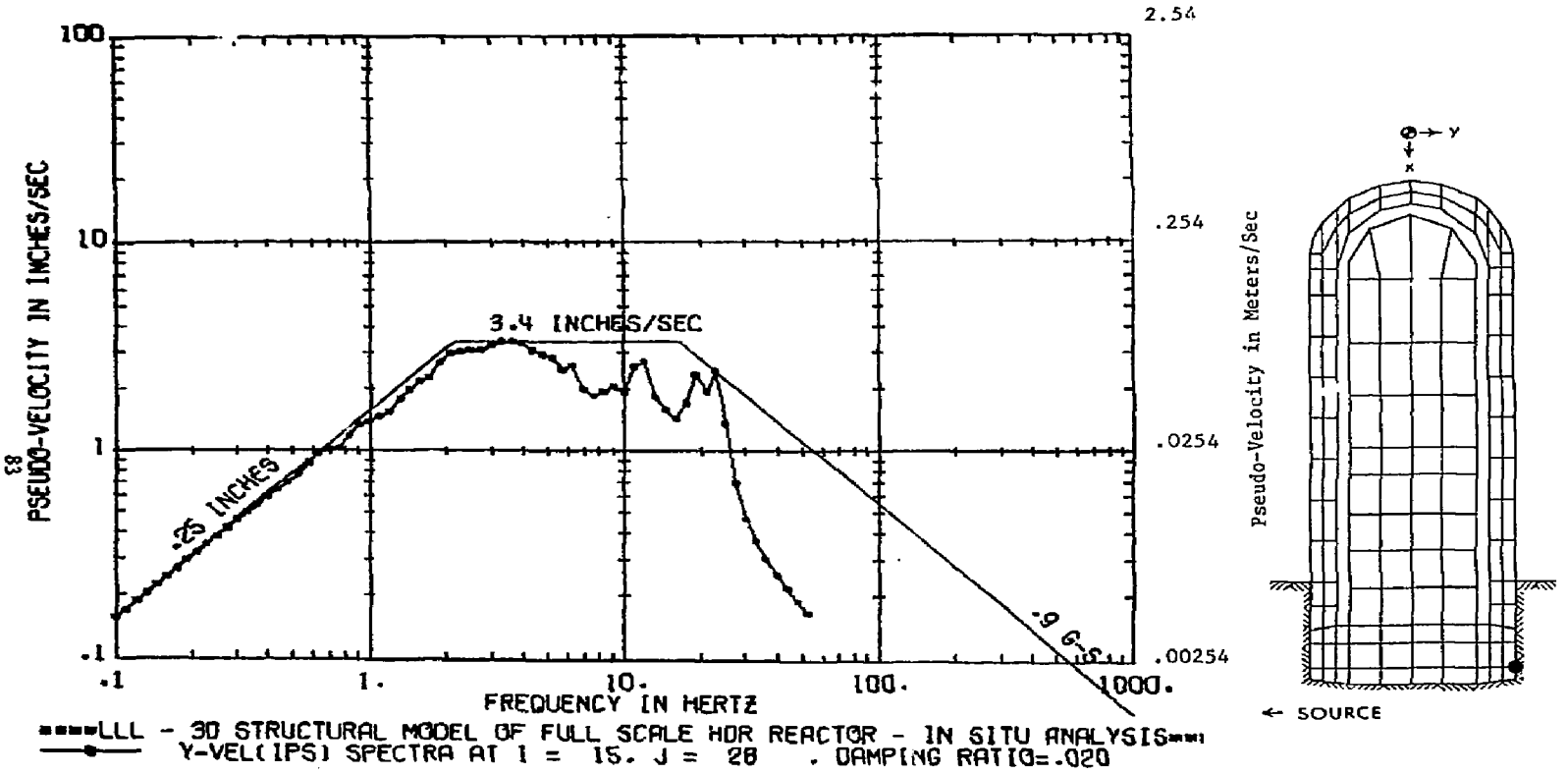

Figure 3-25a. Response spectra of horizontal motion near downstream corner of foundation (elev -11.05m, 11.35m aft of centerline).

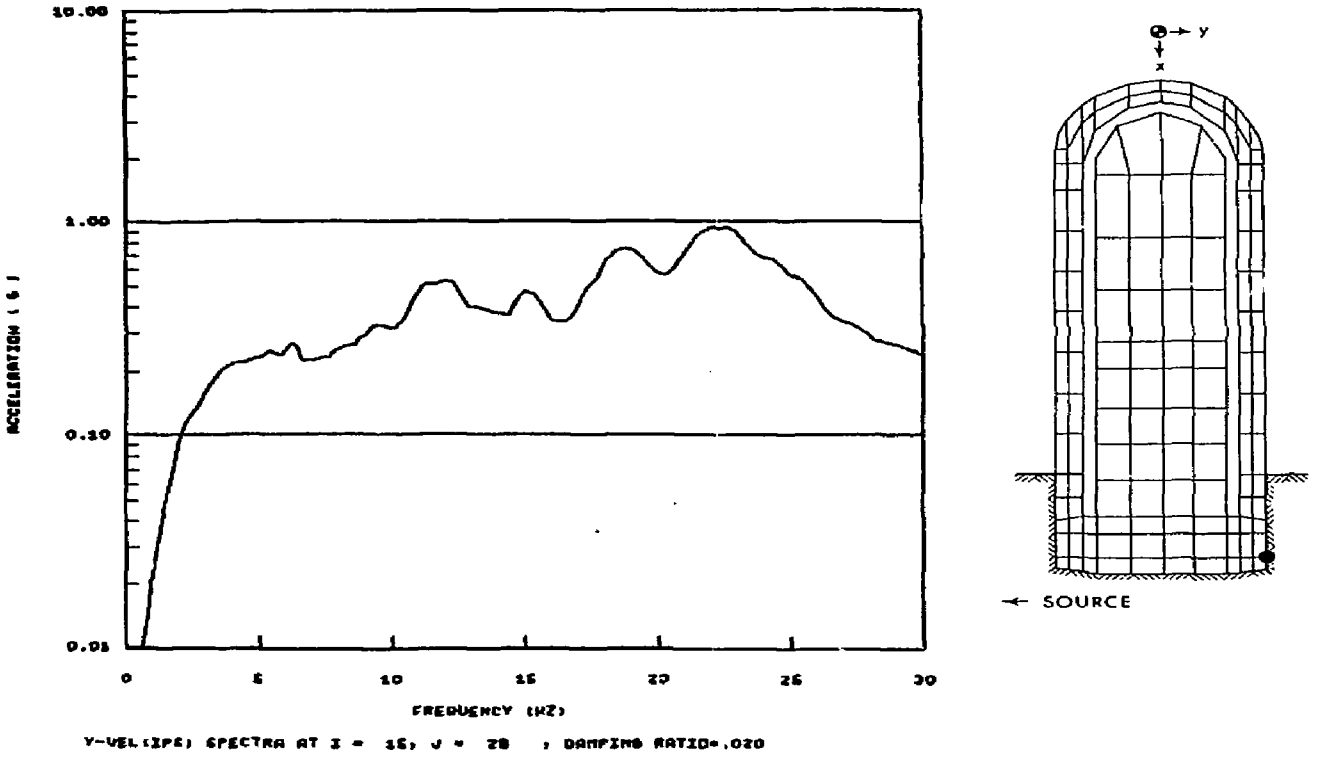

Figure 3-25b. Acceleration response spectra of horizontal motion near downstream corner of foundation (elevation -11.05m, 11.35m aft of centerline).

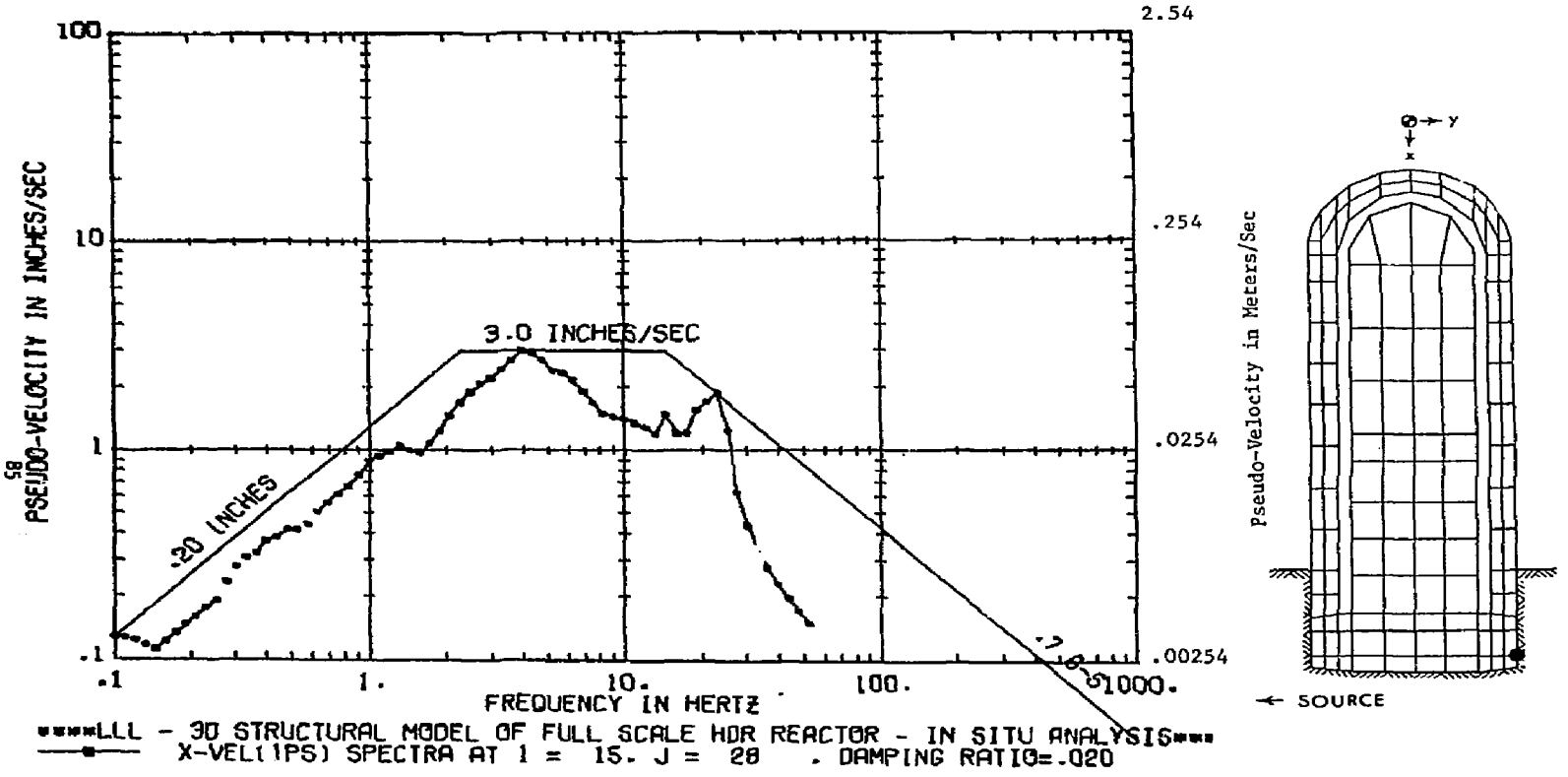

Figure 3-26. Response spectra of vertical motion near downstream corner of foundation (elev -11.05m, 11.35m aft of centerline).

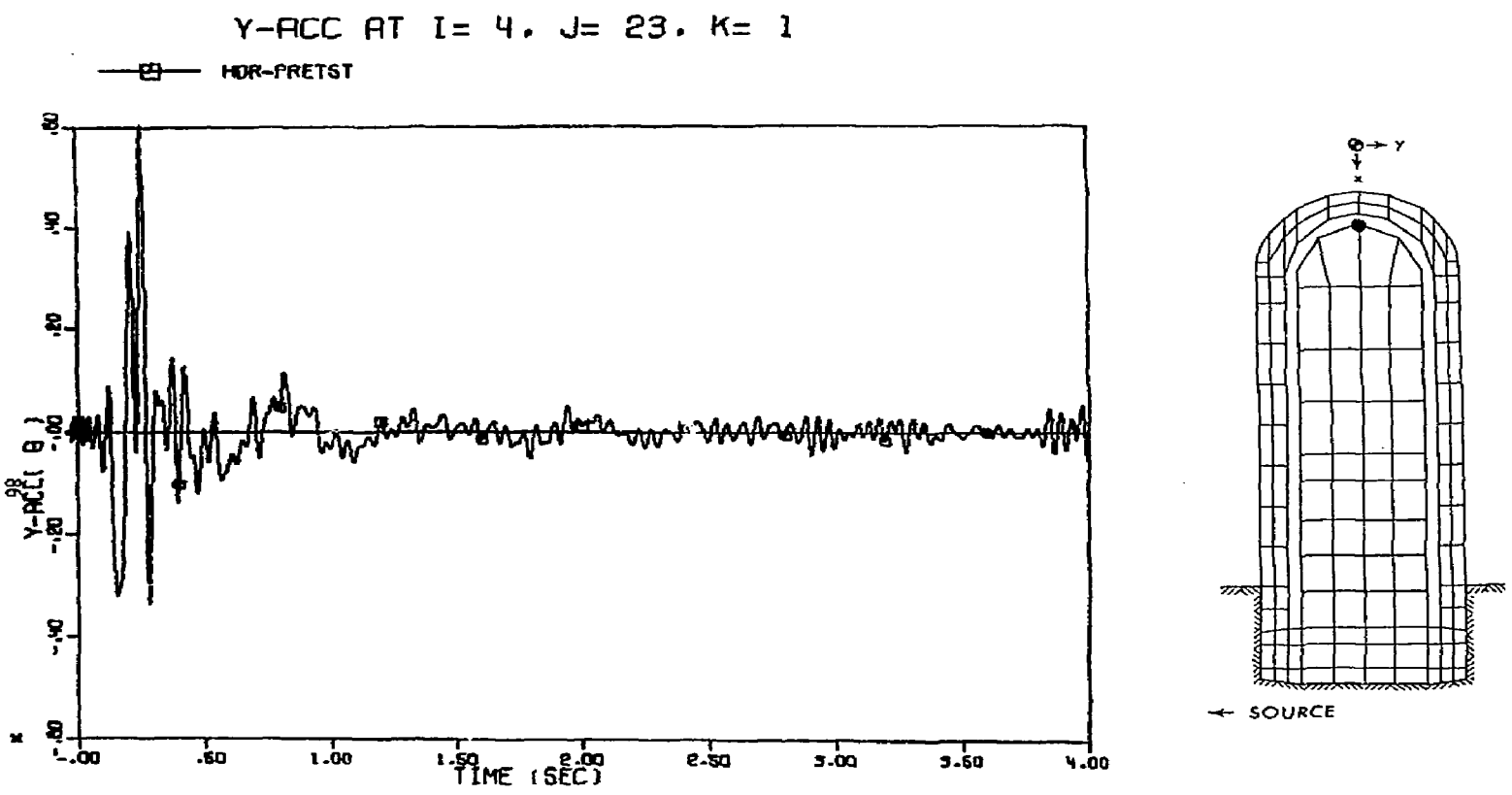

Figure 3-27. Horizontal acceleration-time history at top of inner structure (elev 47.35m, centerline).

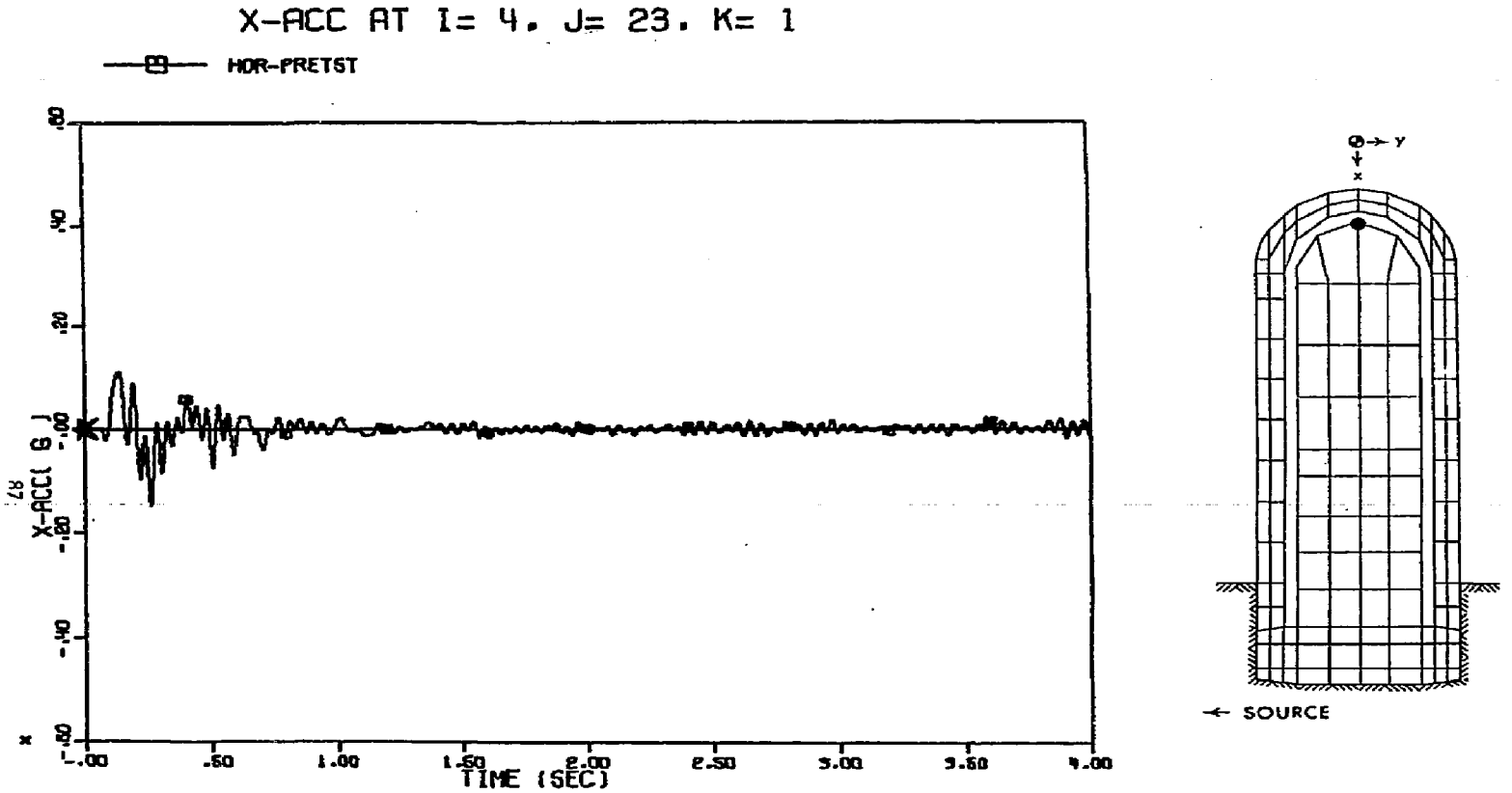

Figure 3-28. Vertical acceleration-time history at top of inner structure (elev 47.35m, centerline).

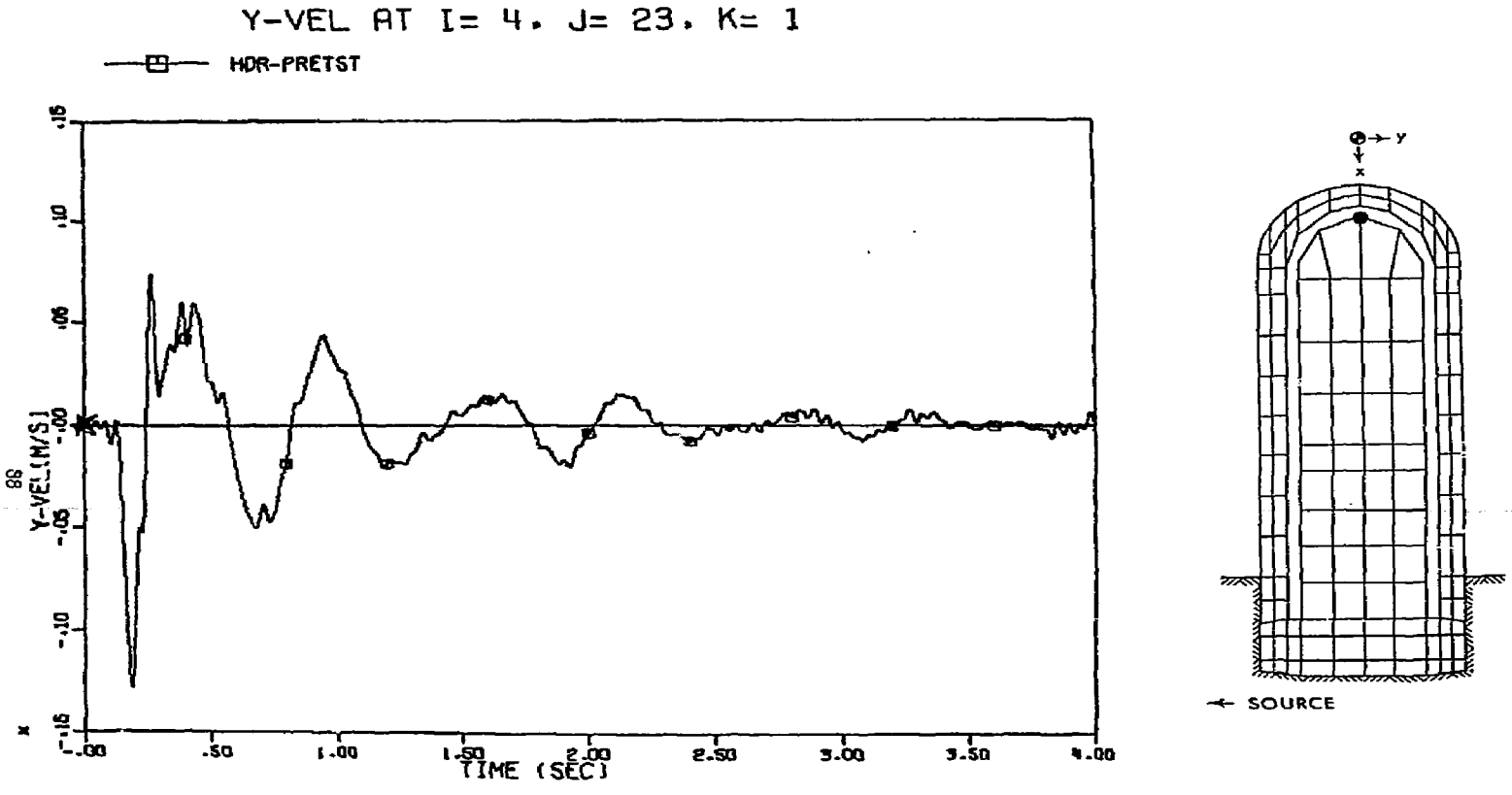

Figure 3-29. Horizontal velocity-time history at top of inner structure (elev 47.35m, centerline).

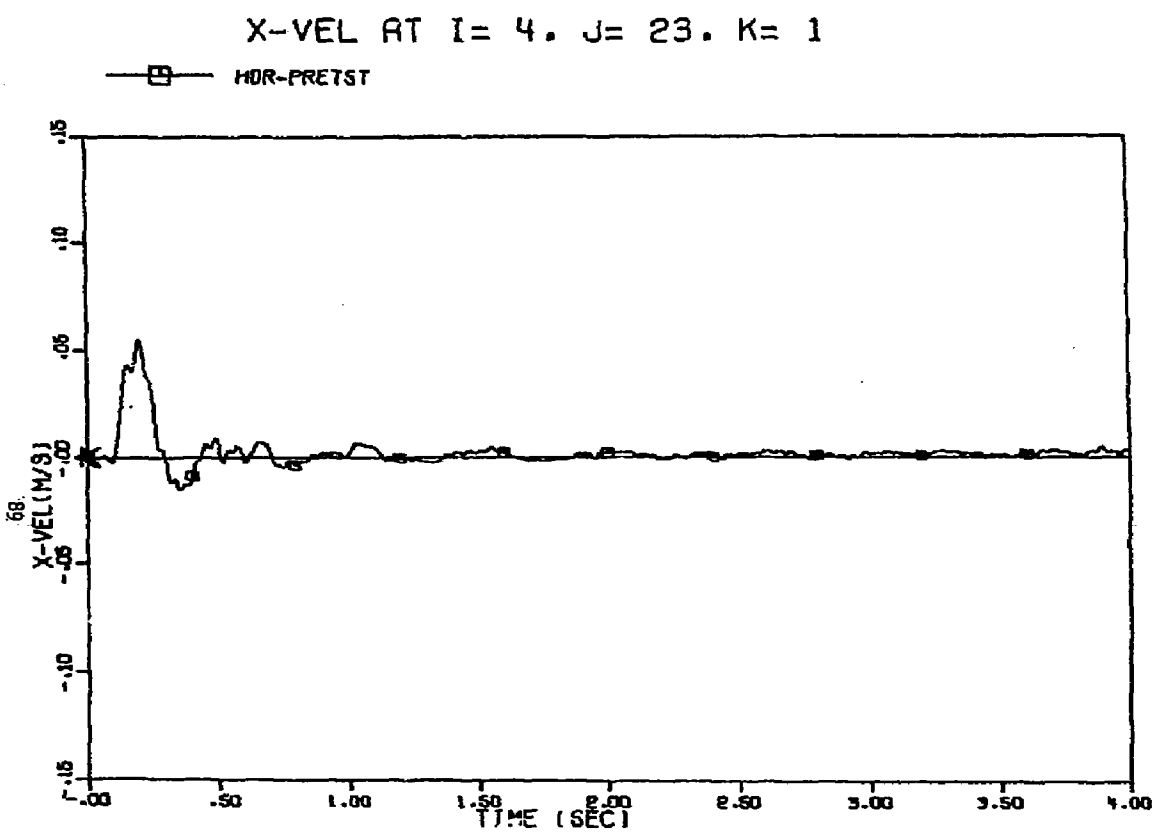

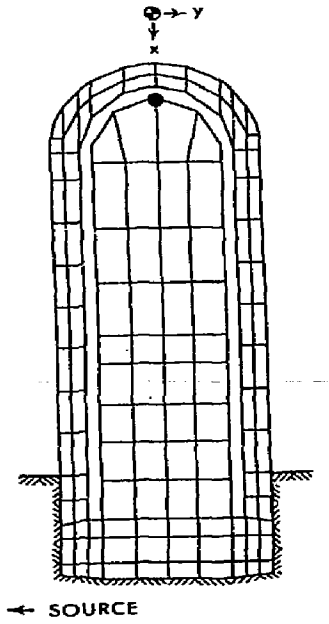

Figure 3-30. Vertical velocity-time history at top of inner structure (elev 47.35m, centerline).

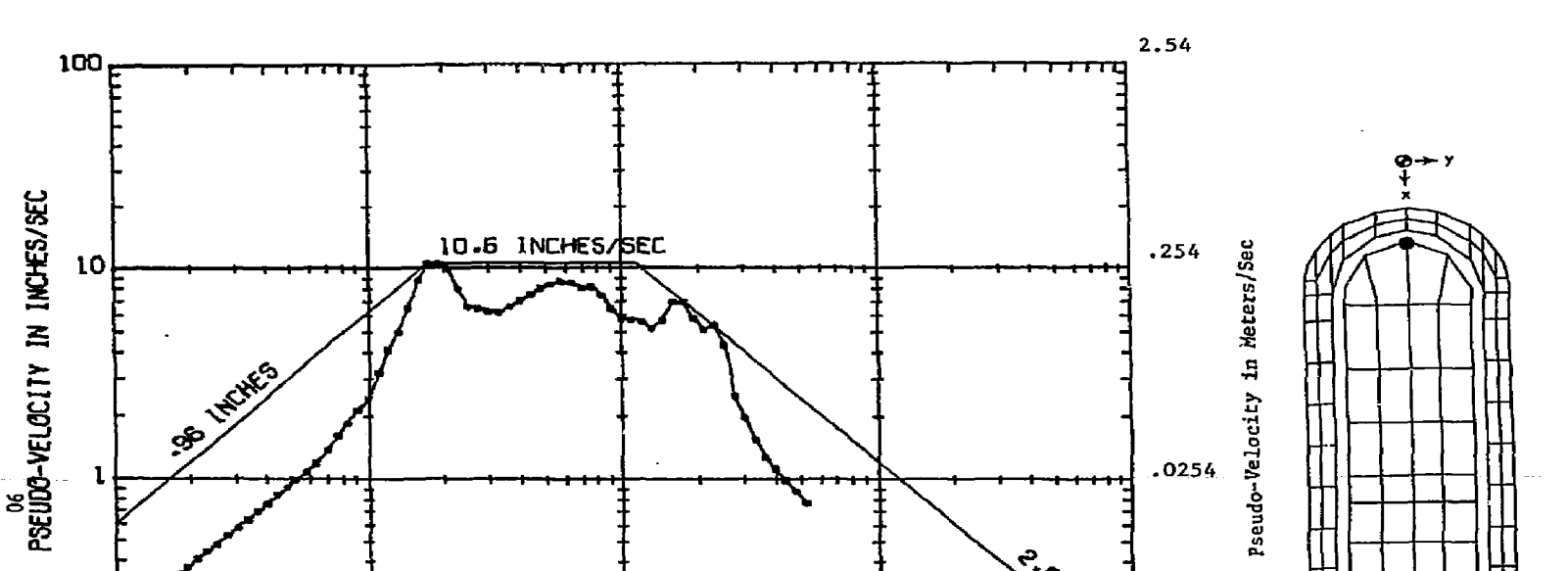

Figure 3-31a. Response spectra of horizontal motion at top of inner structure (elev 47.35m, centerline).

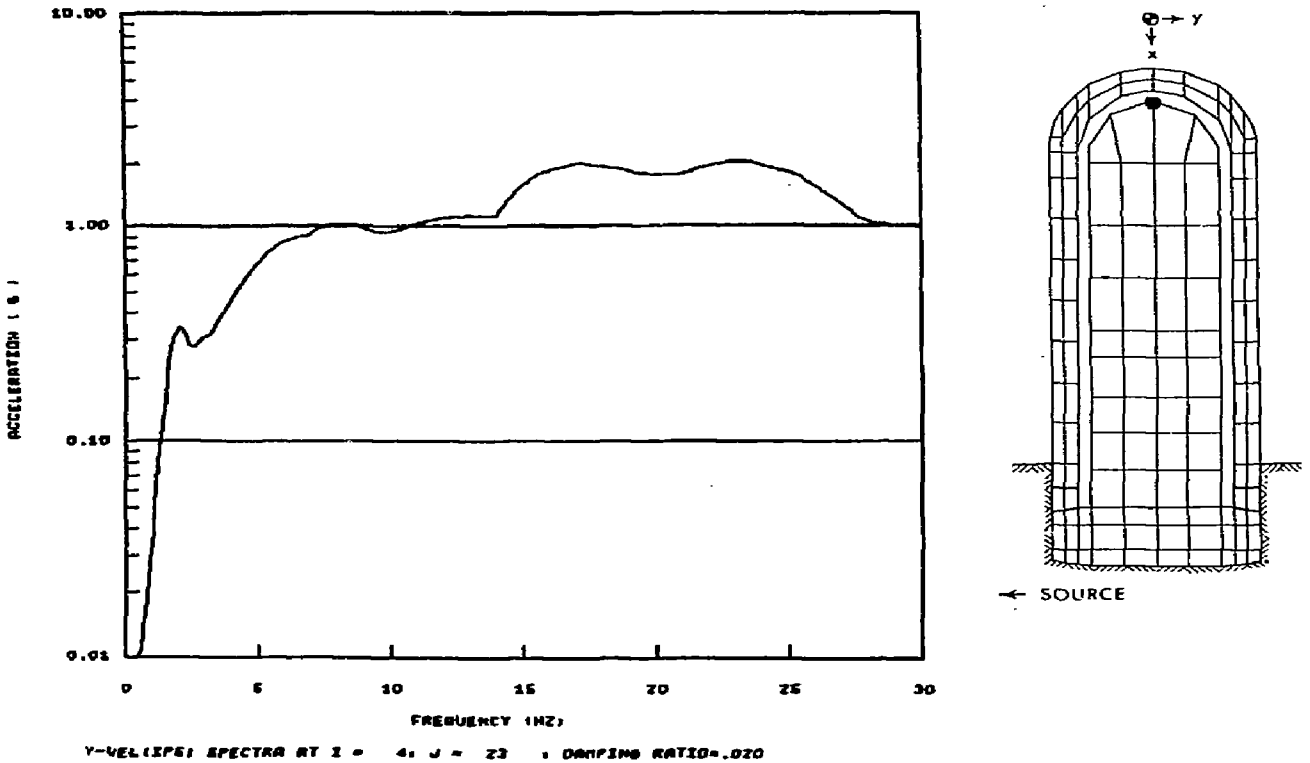

Figure 3-31b. Acceleration response spectra of horizontal motion at top of inner structure (elevation 47.35m, centerline).

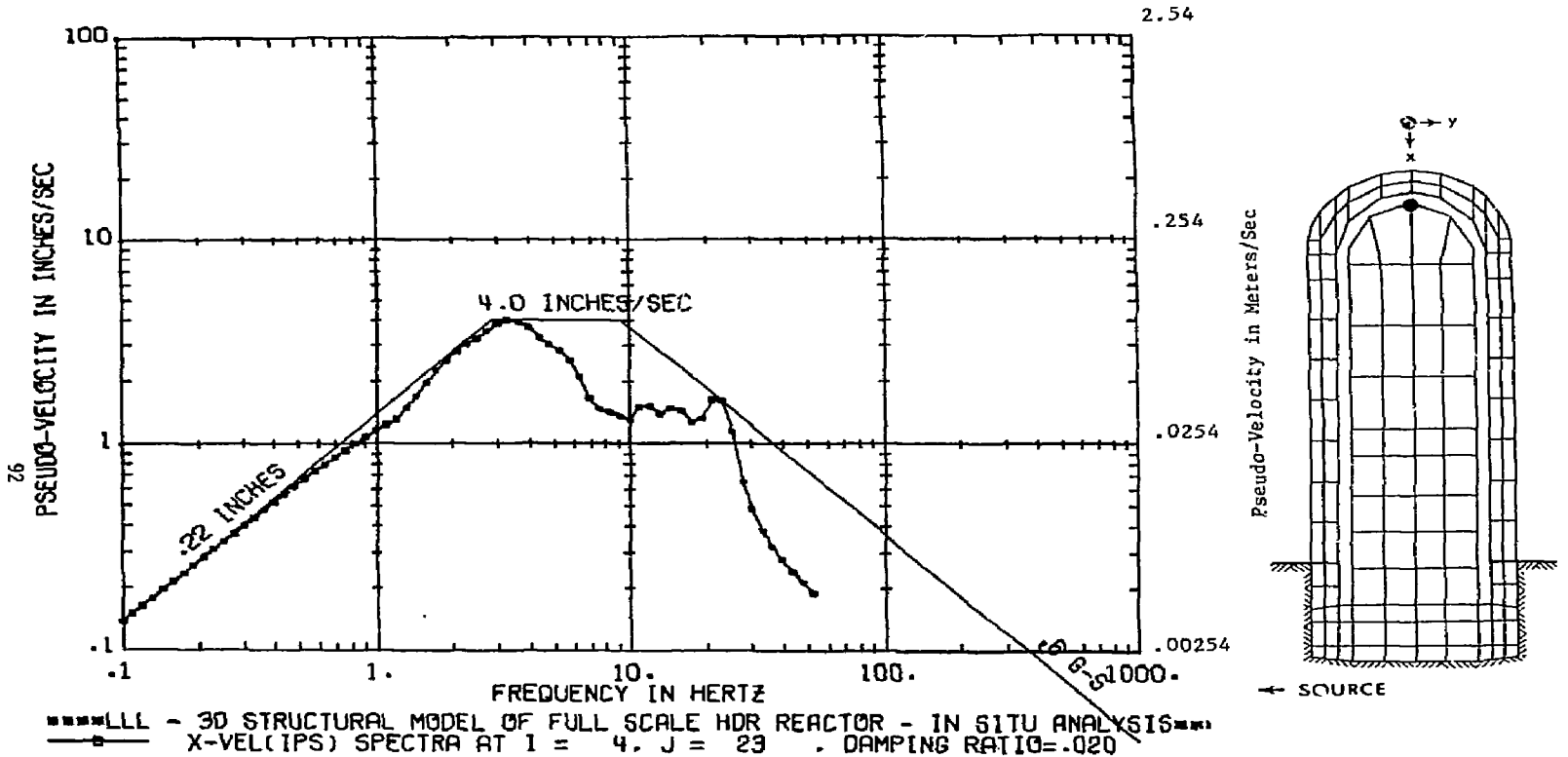

Figure 3-32. Response spectra of vertical motion at top of inner structure (elev 47.35m, centerline).

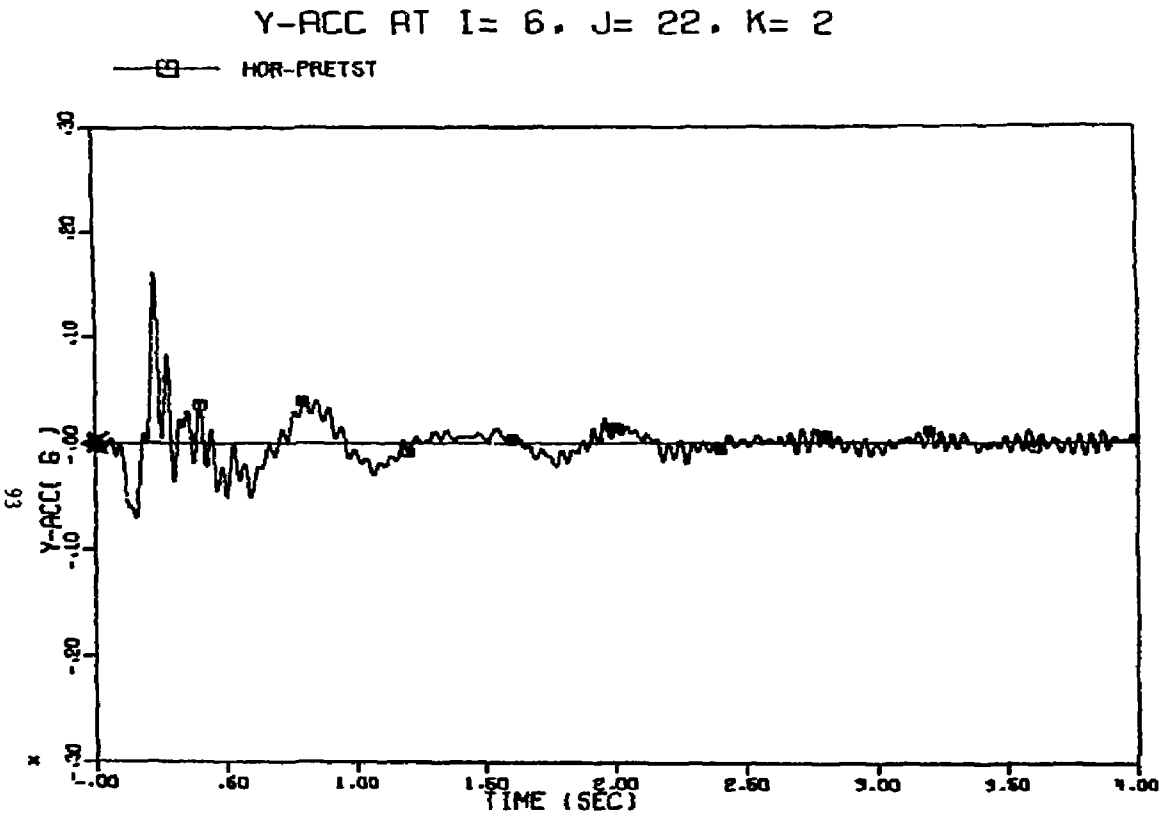

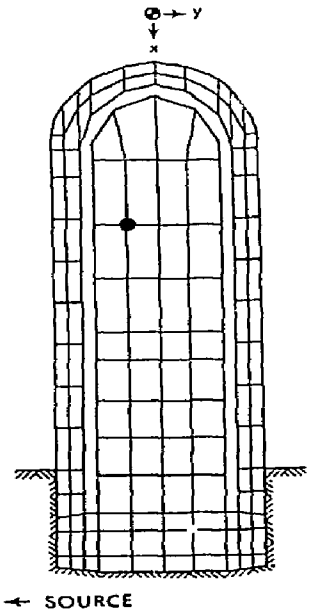

Figure 3-33. Horizontal acceleration-time history on inner structure (elev 30.85m, 3.2m outside and forward of centerline).

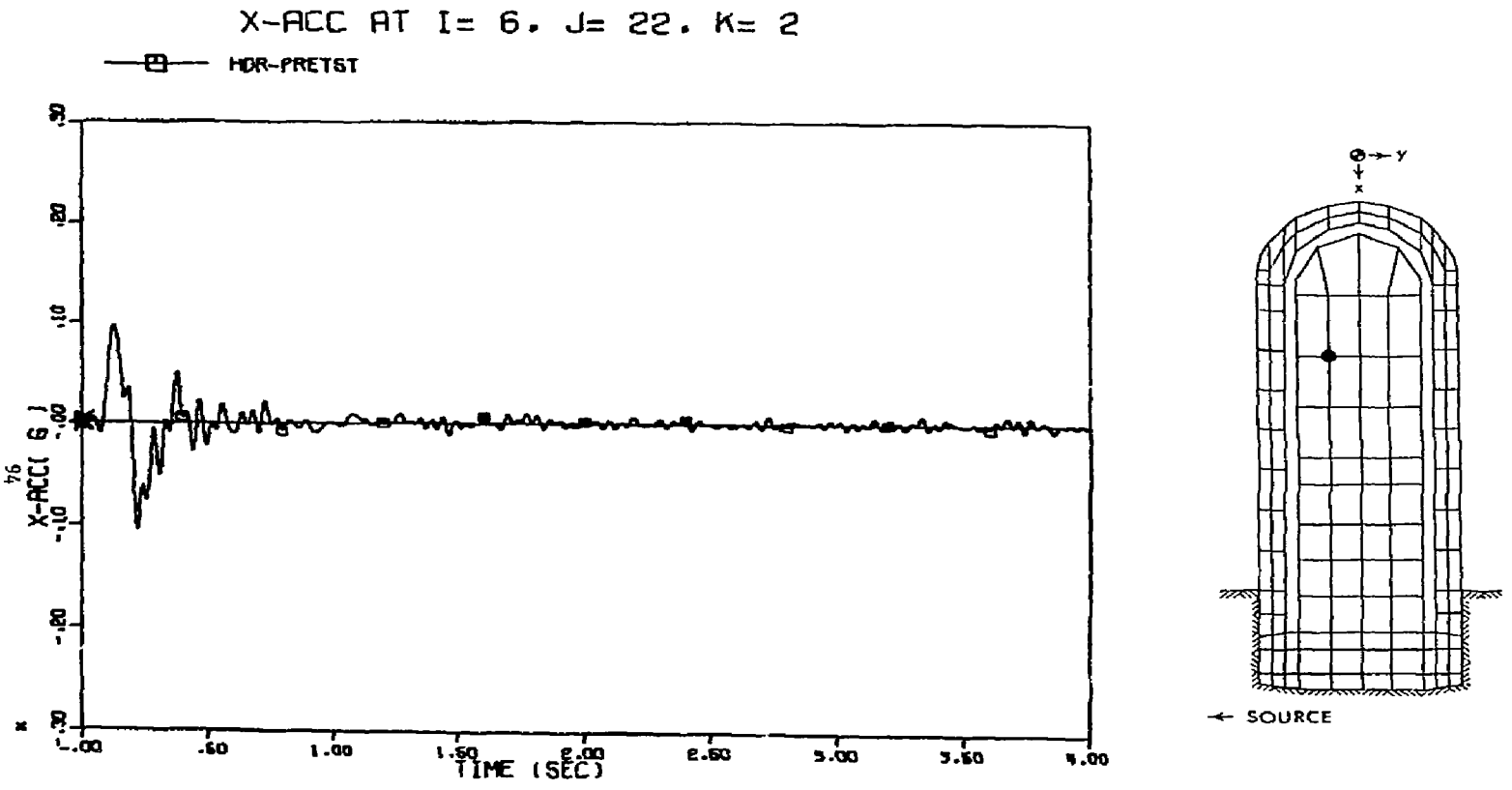

Figure 3-34. Vertical acceleration-time history on inner structure (elev 30.85m, 3.2m outside and forward of centerline).

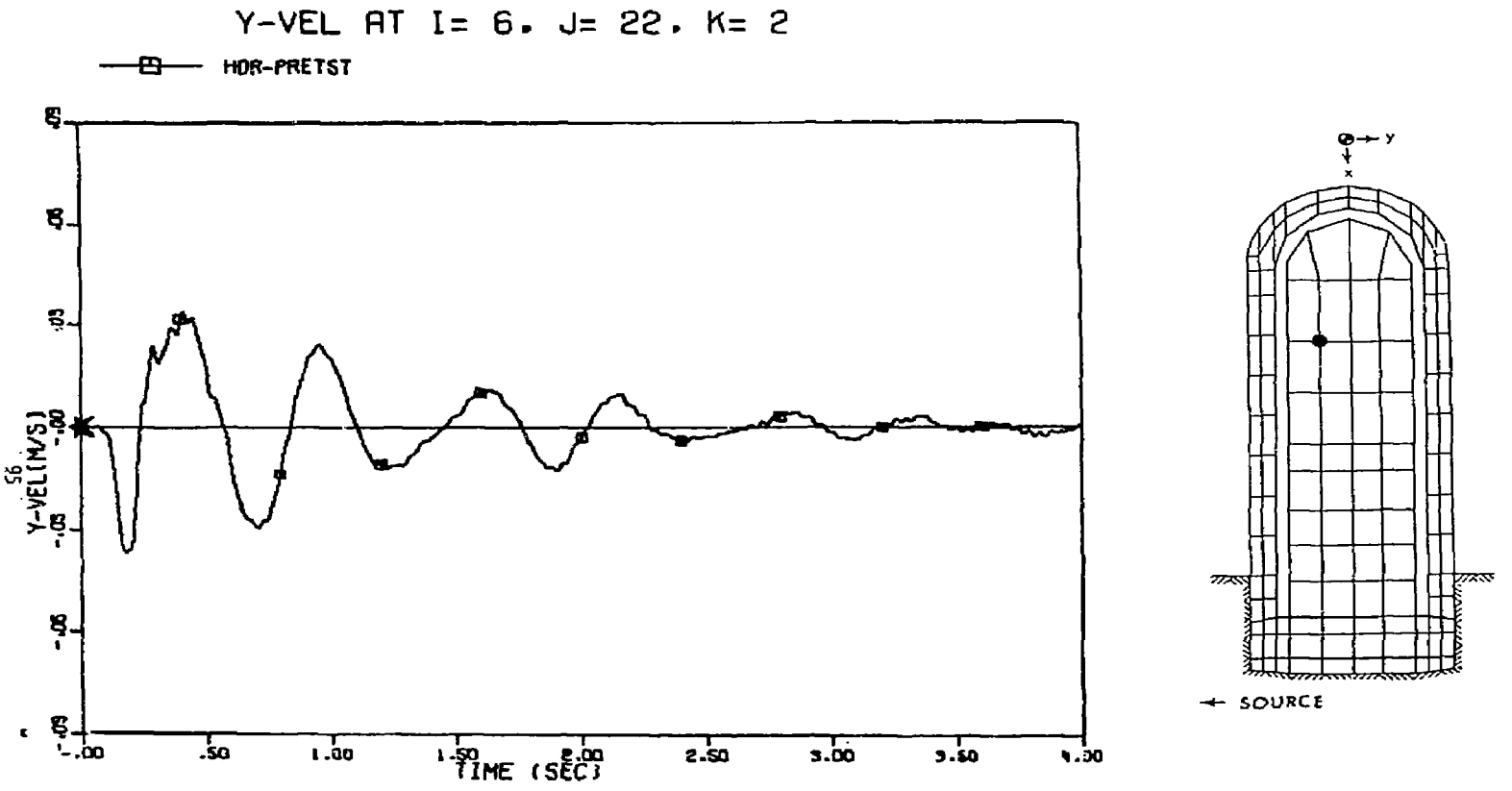

Figure 3-35. Horizontal velocity-time history on inner structure (elev 30.85m, 3.2m outside and forward of centerline).

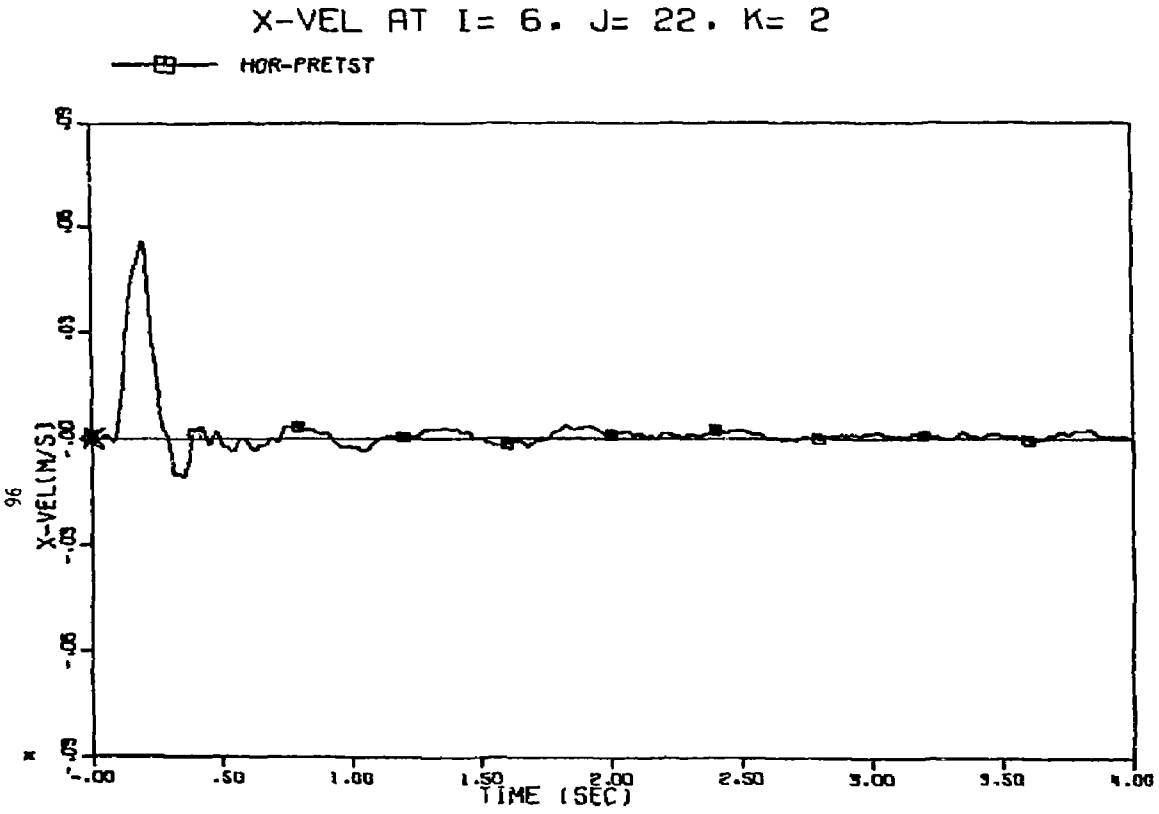

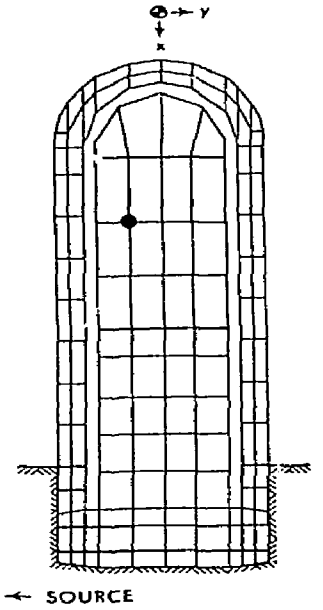

Figure 3-36. Vertical velocity-time history on inner structure (elev 30.85m, 3.2m outside and forward of centerline).

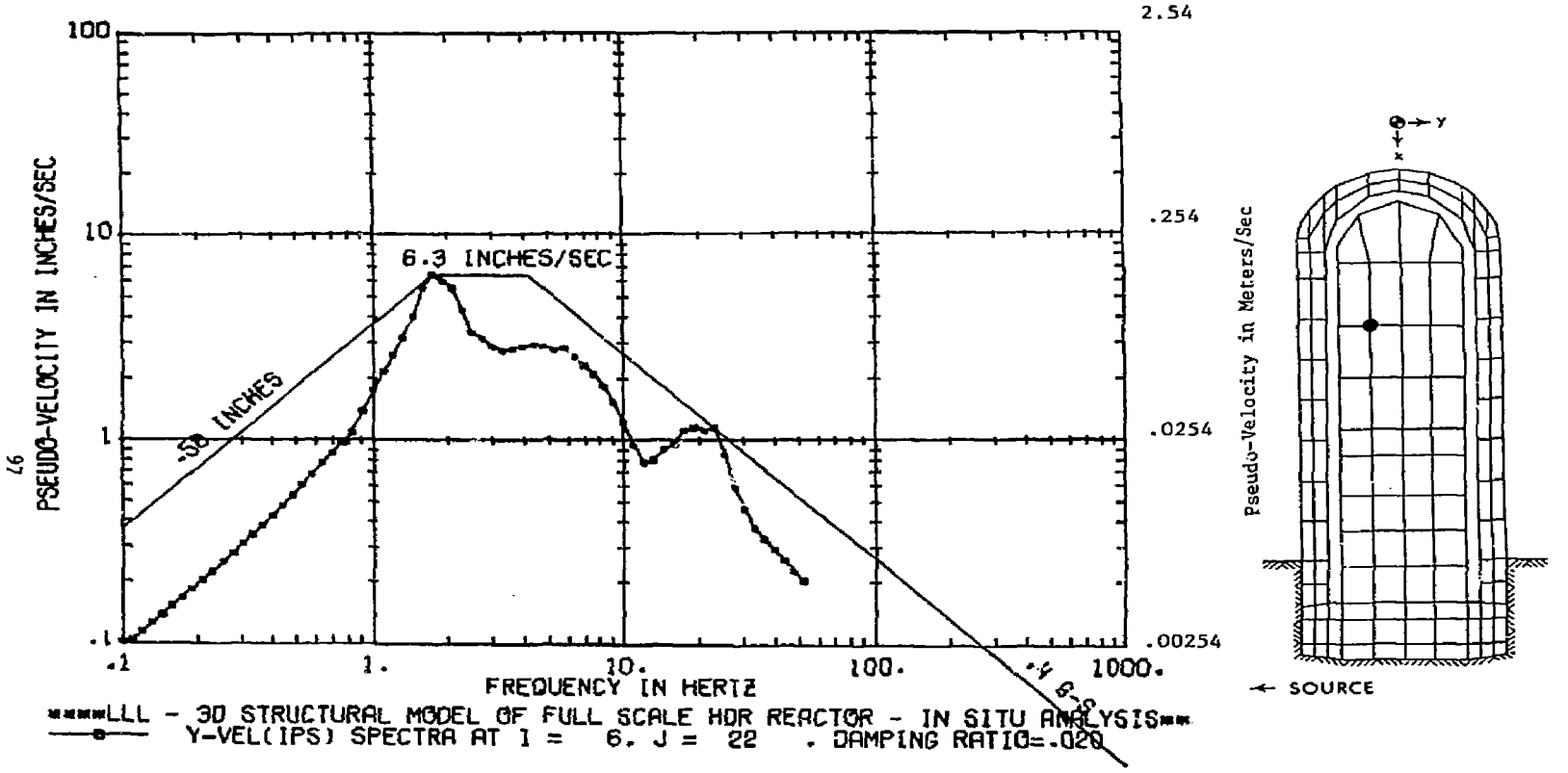

Figure 3-37. Response spectra of horizontal motion on inner structure (elev 30.85m, 3.2m outside and forward of centerline).

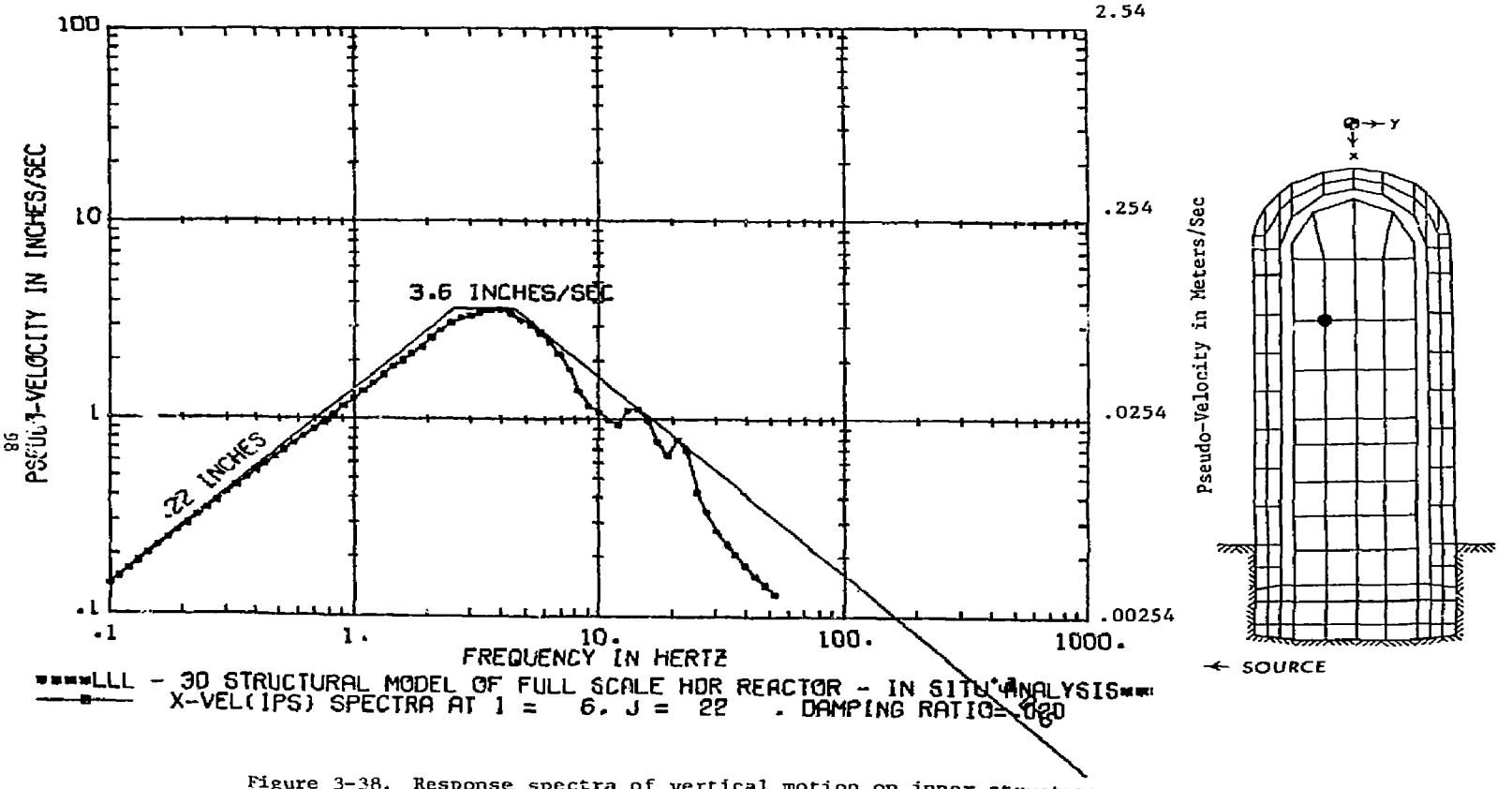

Figure 3-38. Response spectra of vertical motion on inner structure (elev 30.85m, 3.2m outside and forward of centerline).

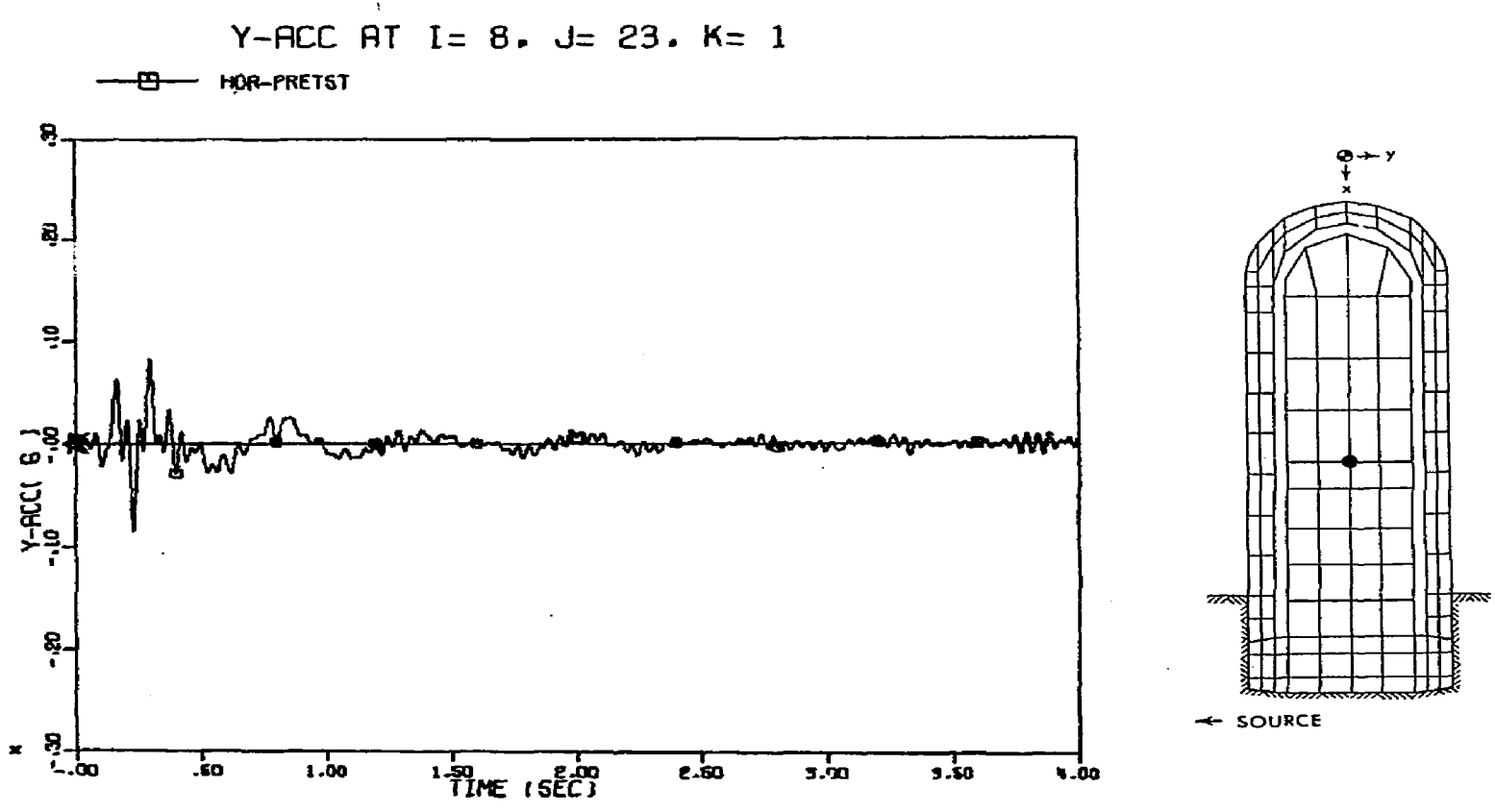

Figure 3-39. Horizontal acceleration-time history on inner structure (elev 17.25m, centerline).

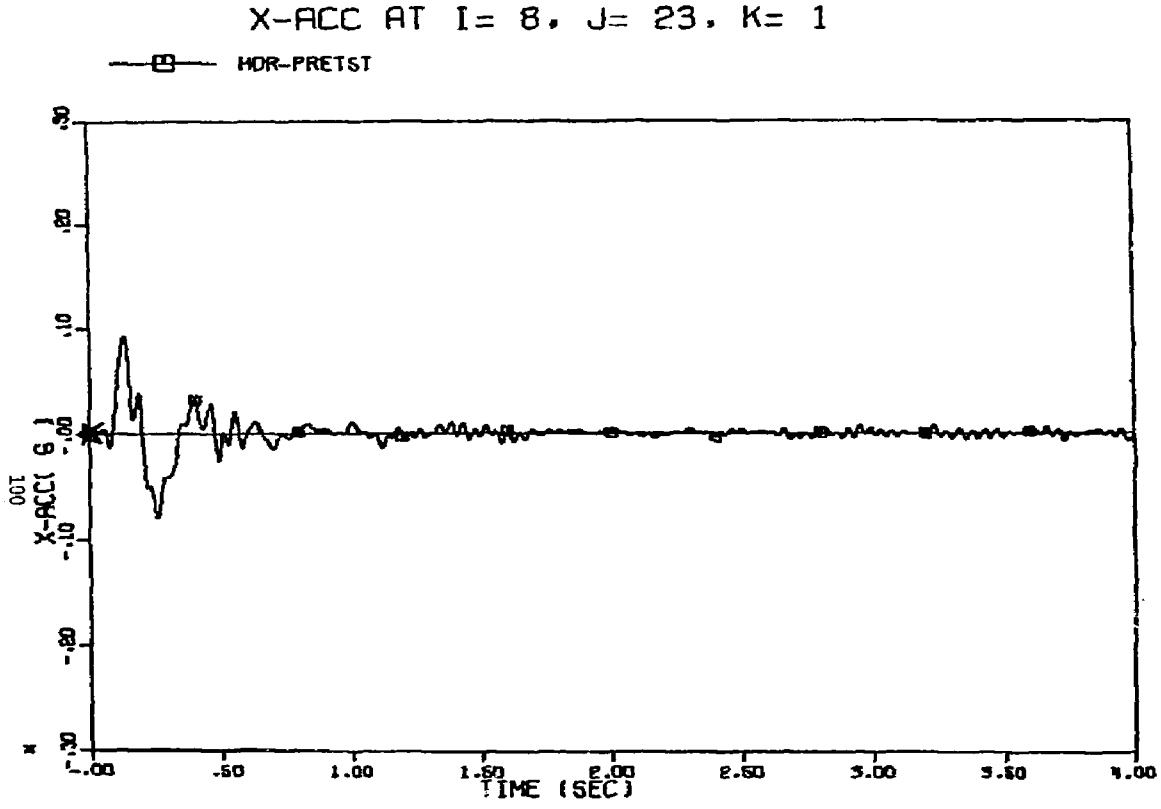

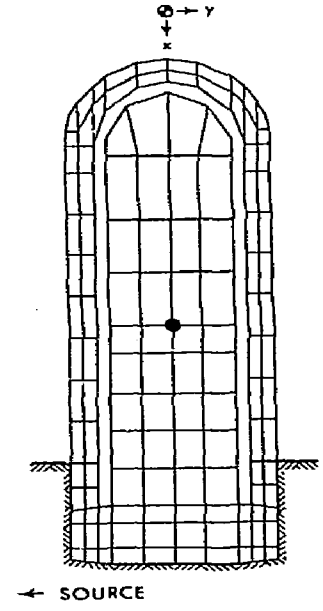

Figure 3-40. Vertical acceleration-time history on inner structure (elev 17.25m, centerline).

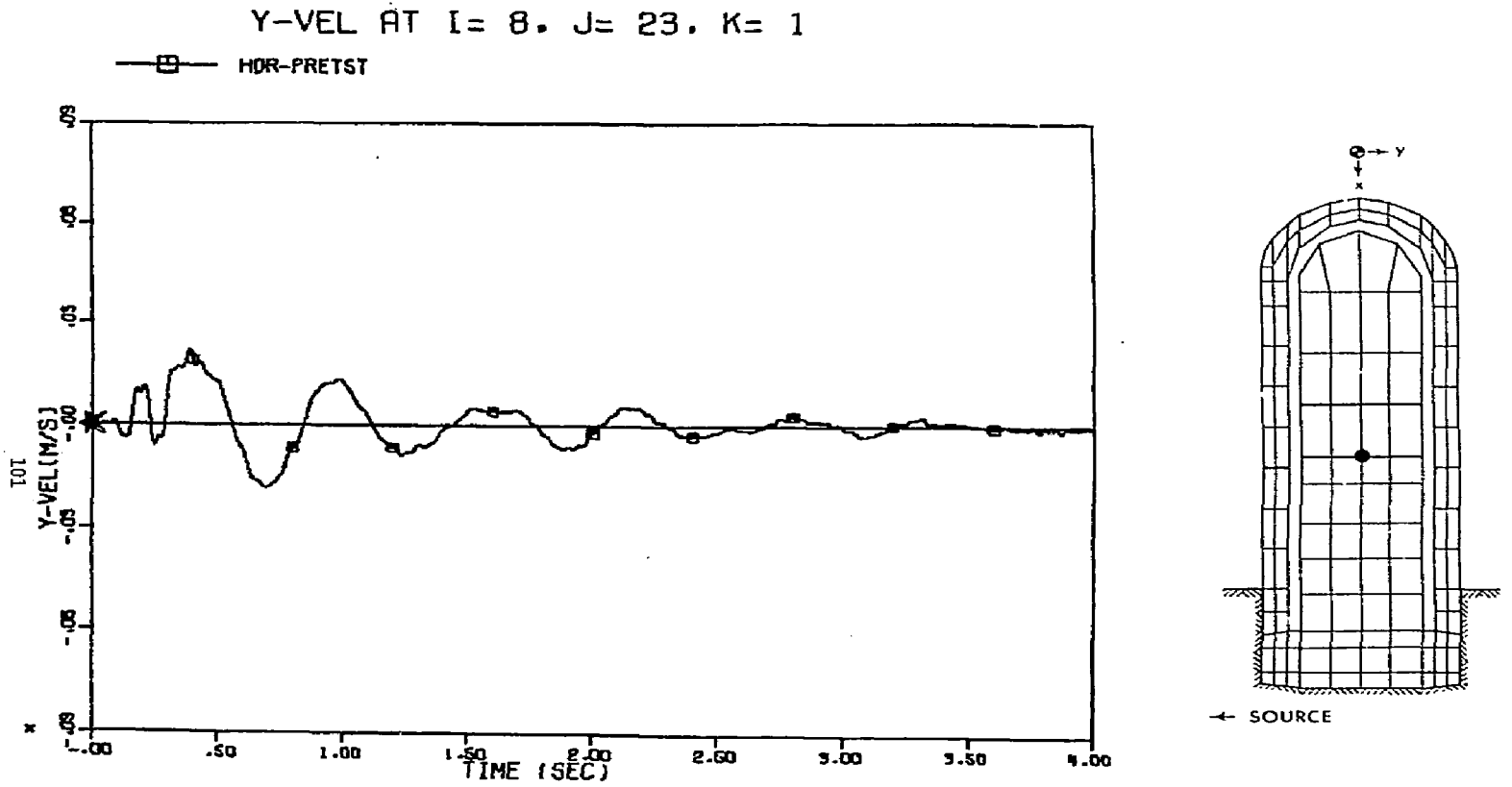

Figure 3-41. Horizontal velocity-time history on inner structure (elev 17.25m, centerline).

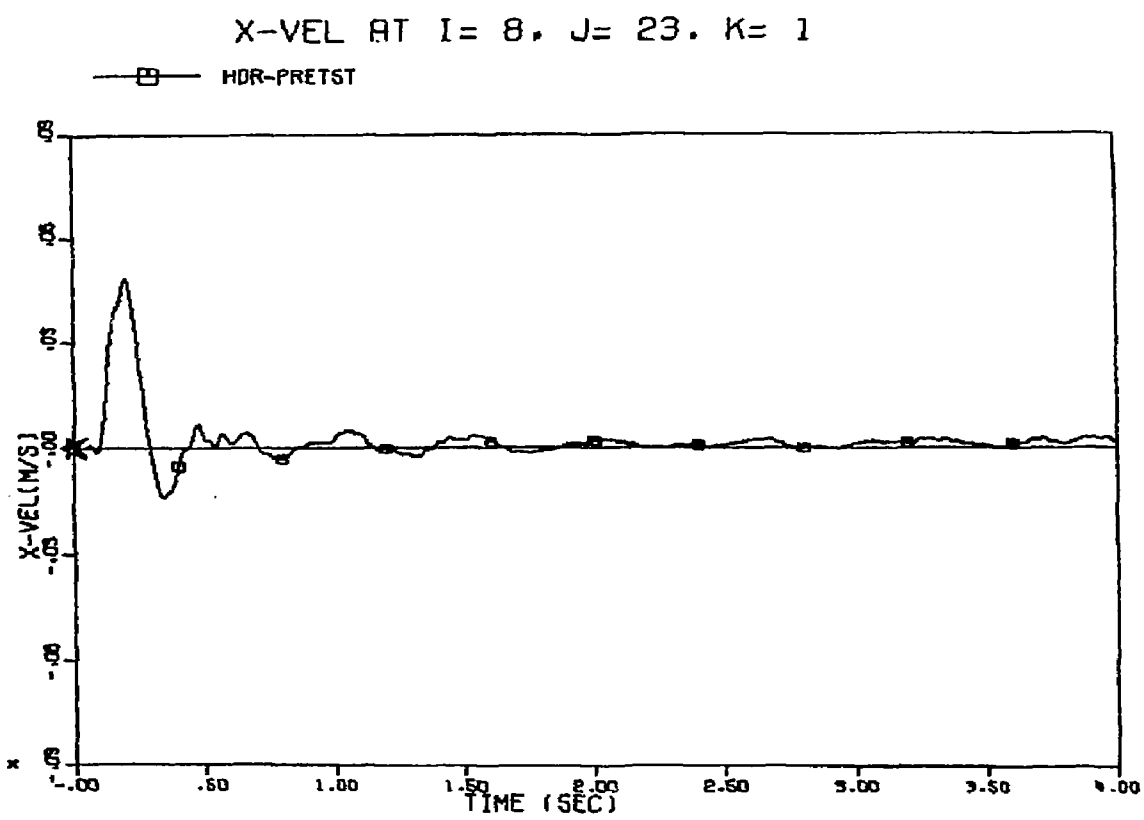

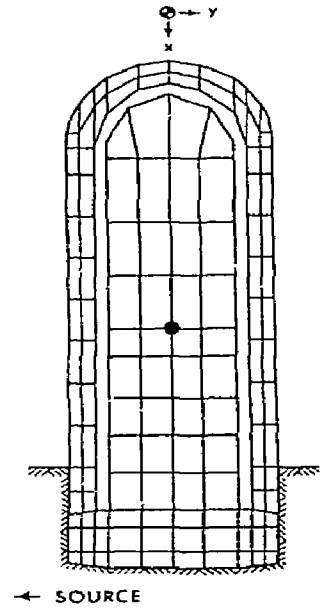

Figure 3-42. Vertical velocity-time history on inner structure (elev 17.25m, centerline).

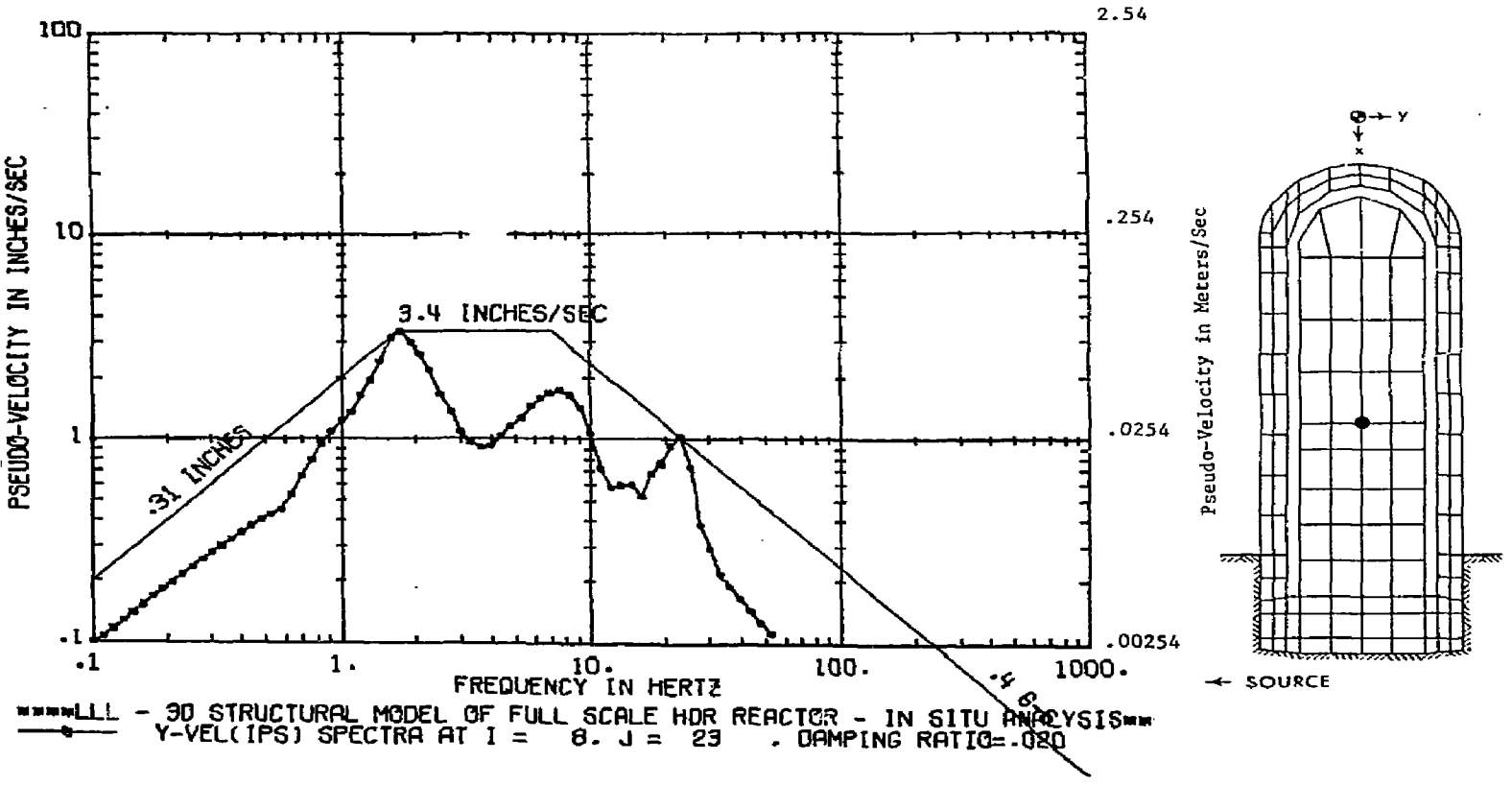

Figure 3-43. Response spectra of horizontal motion on inner structure (elev 17.25m, centerline).

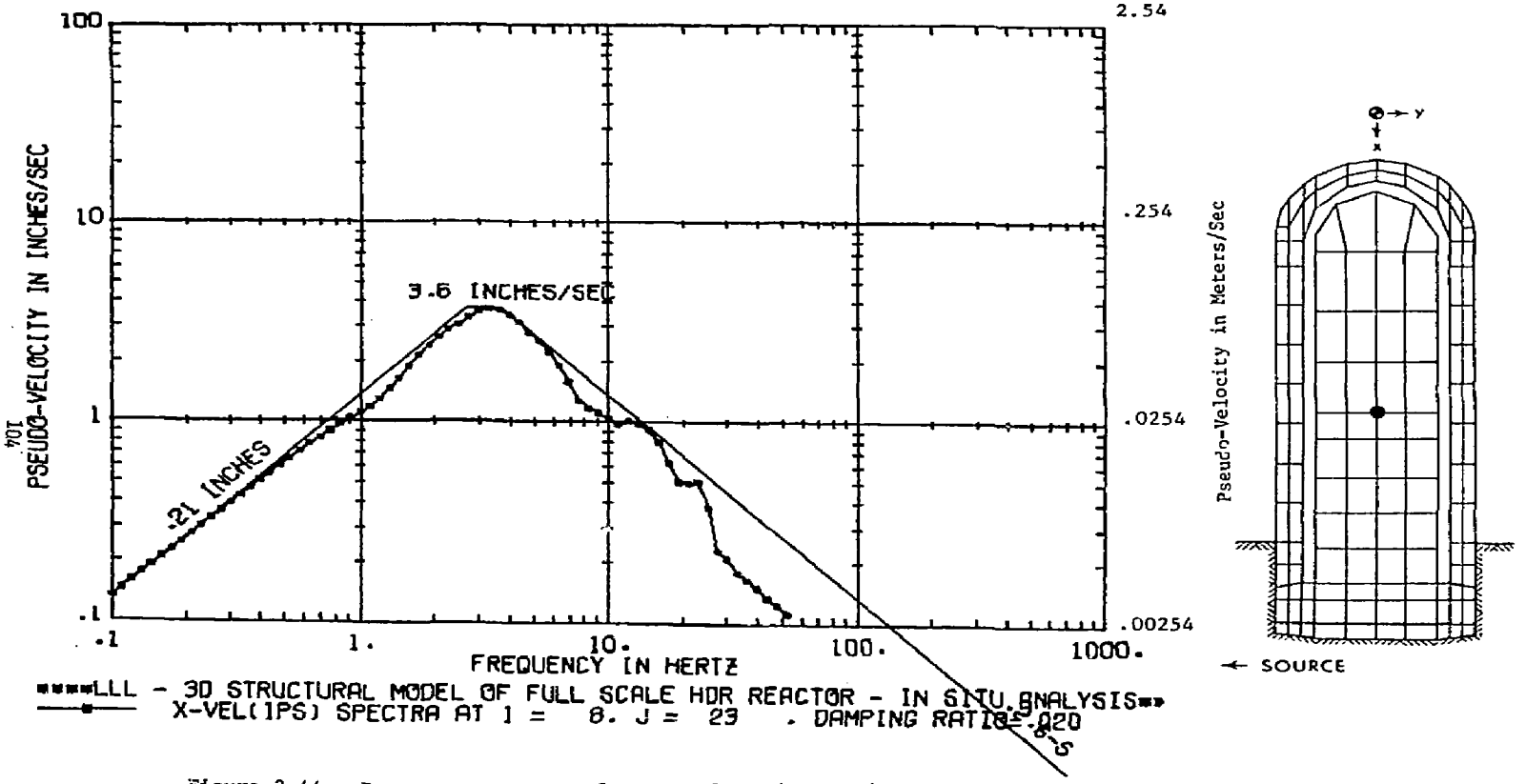

Figure 3-44. Response spectra of vertical motion on inner structure (elev 17.25m, centerline).

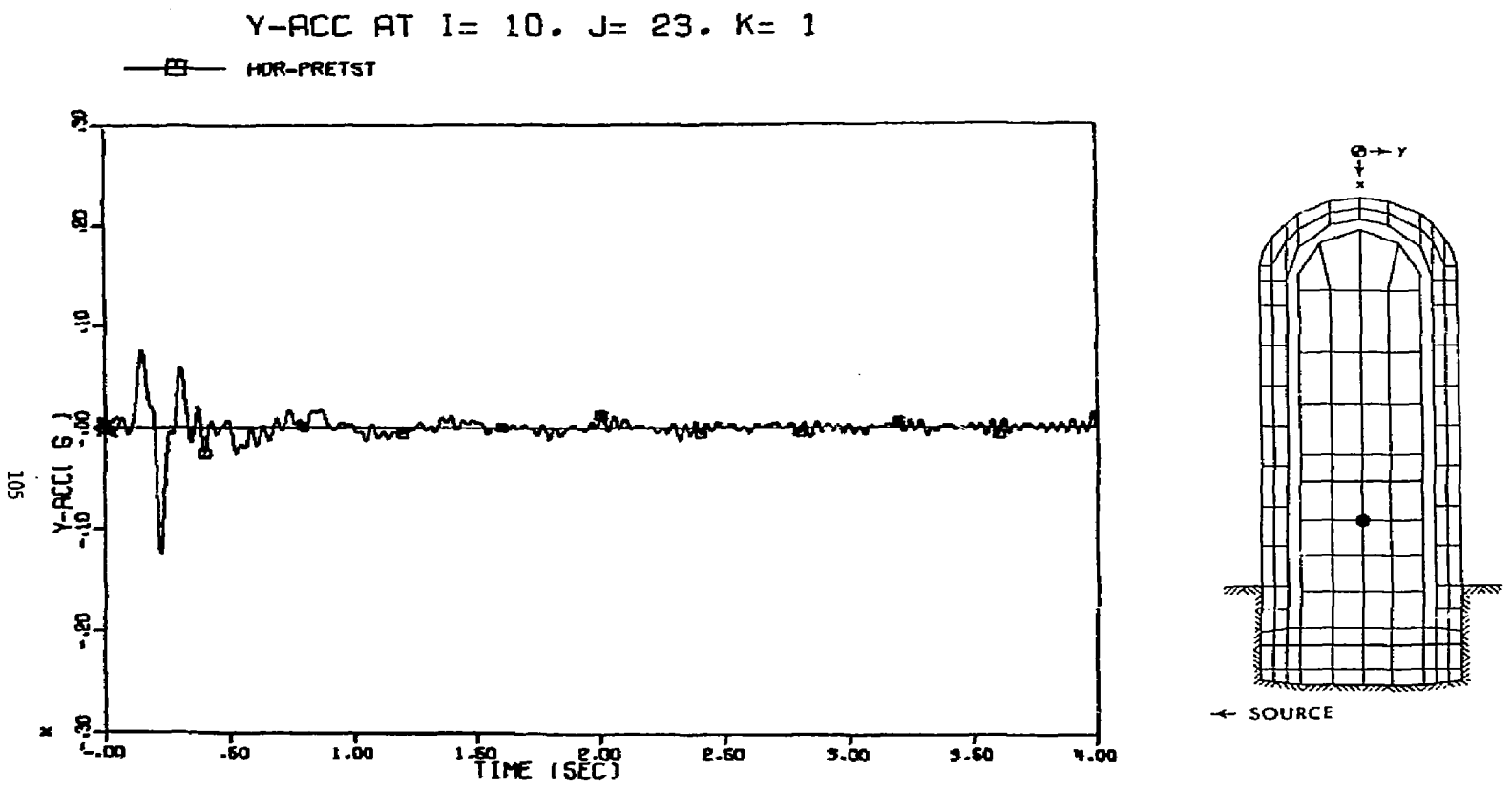

Figure 3-45. Horizontal acceleration-time history on inner structure (elev 8.70m, centerline).

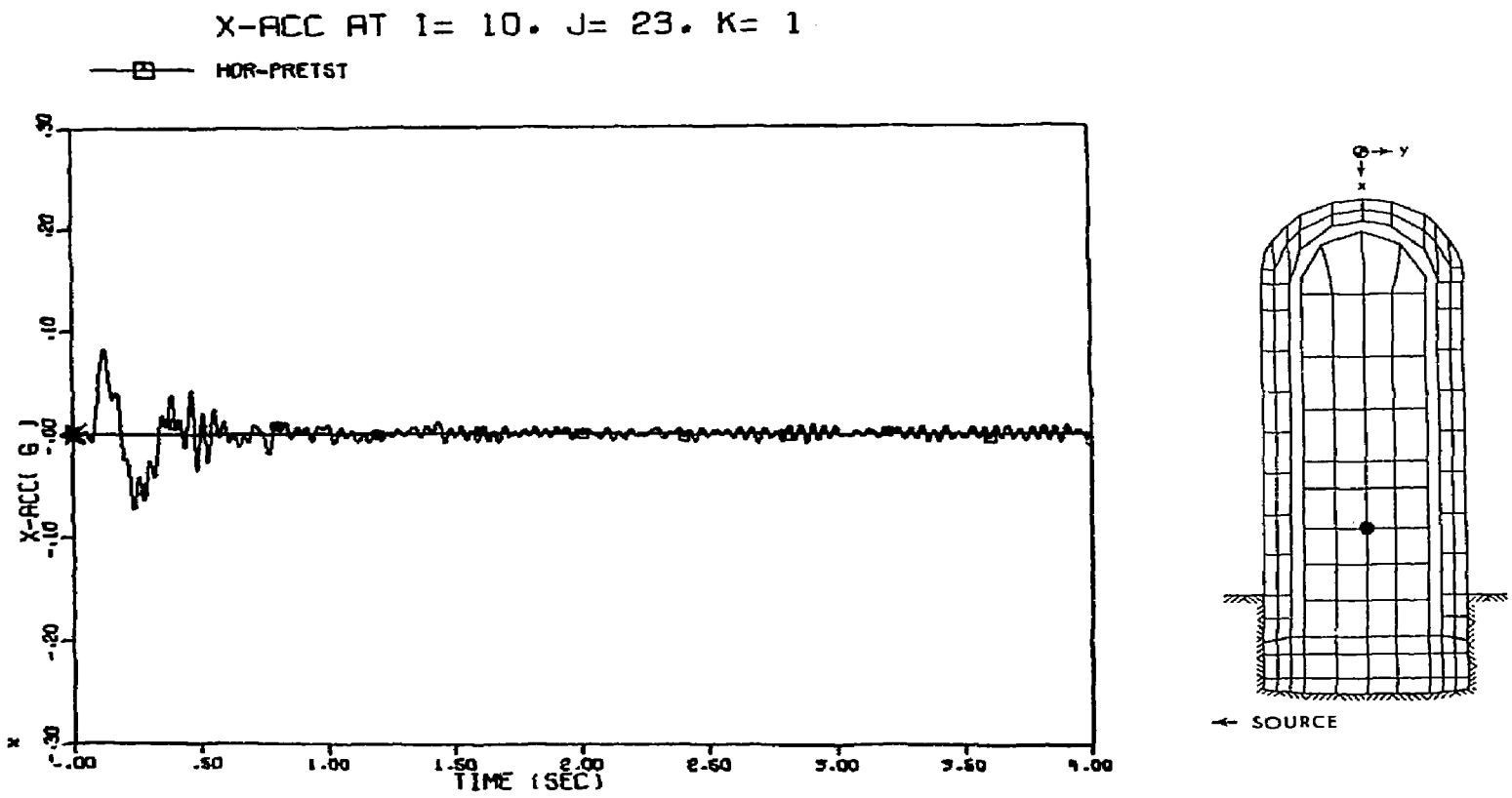

Figure 3-46. Vertical acceleration-time history on inner structure (elev 8.70m, centerline).

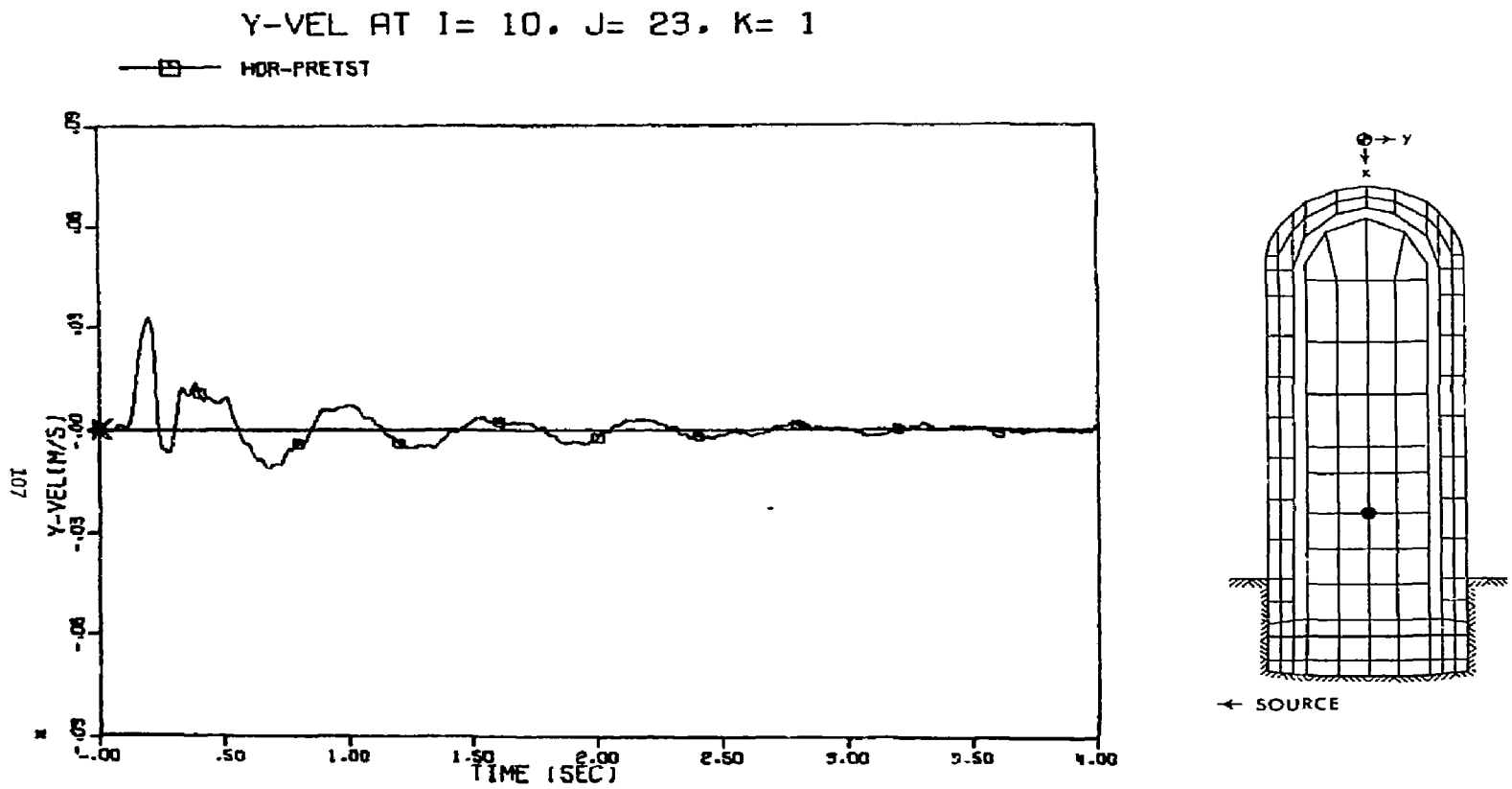

Figure 3-47. Horizontal velocity-time history on inner structure (elev 8.70m, centerline).

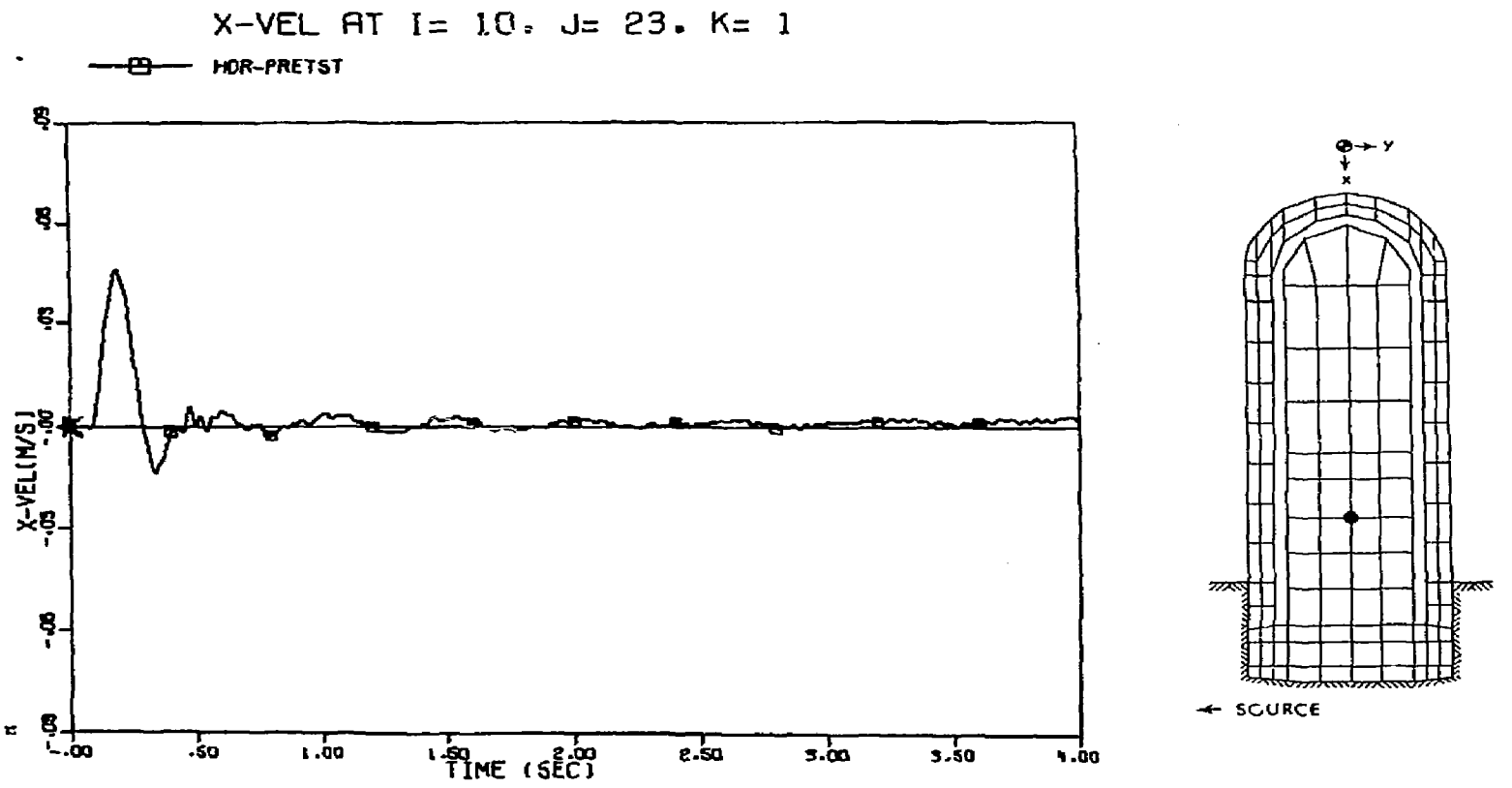

Figure 3-48. Vertical velocity-time history on inner structure (elev 8.70m, centerline).

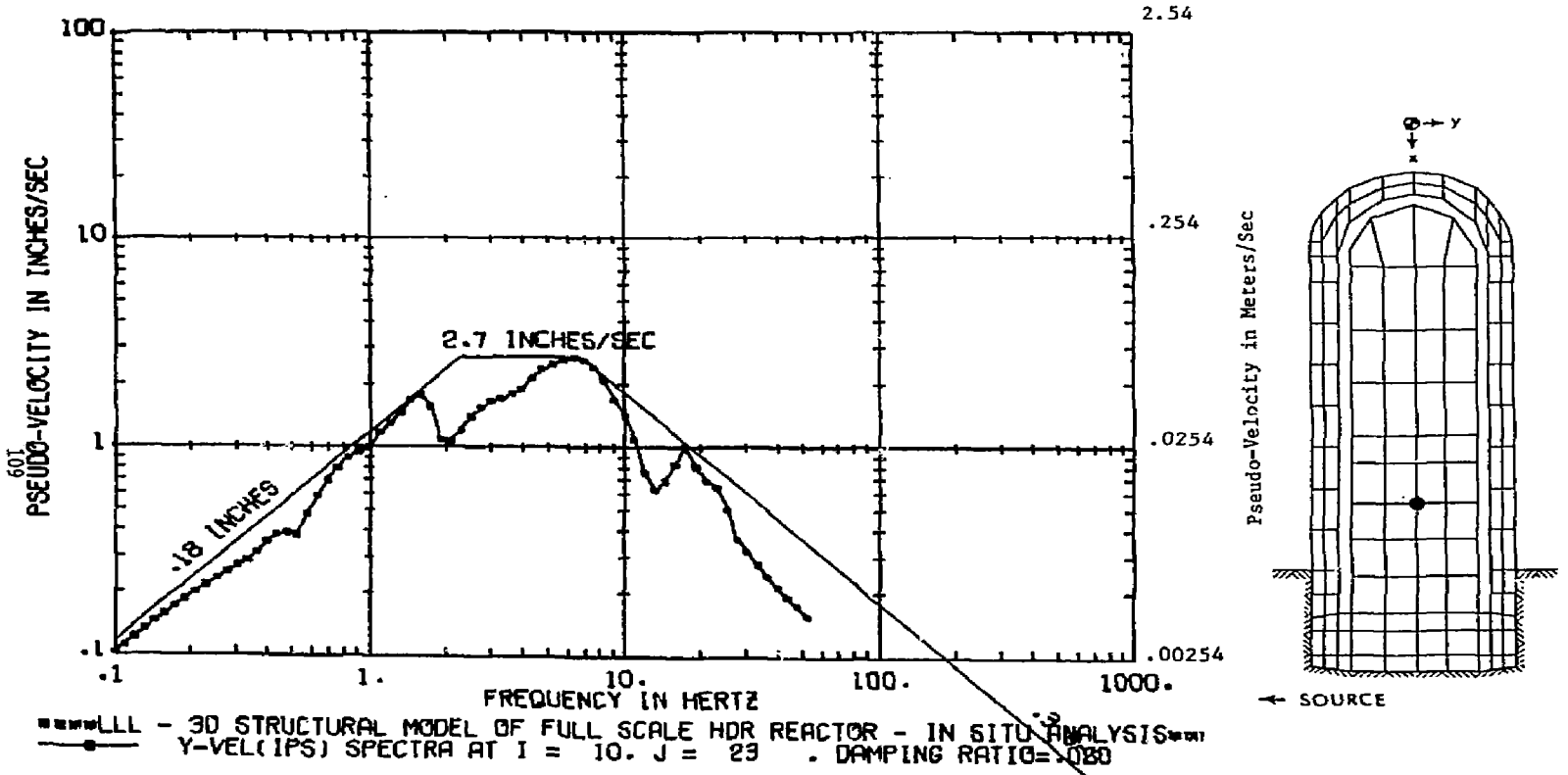

Figure 3-49. Response spectra of horizontal motion on inner structure (elev 8.70m, centerline).

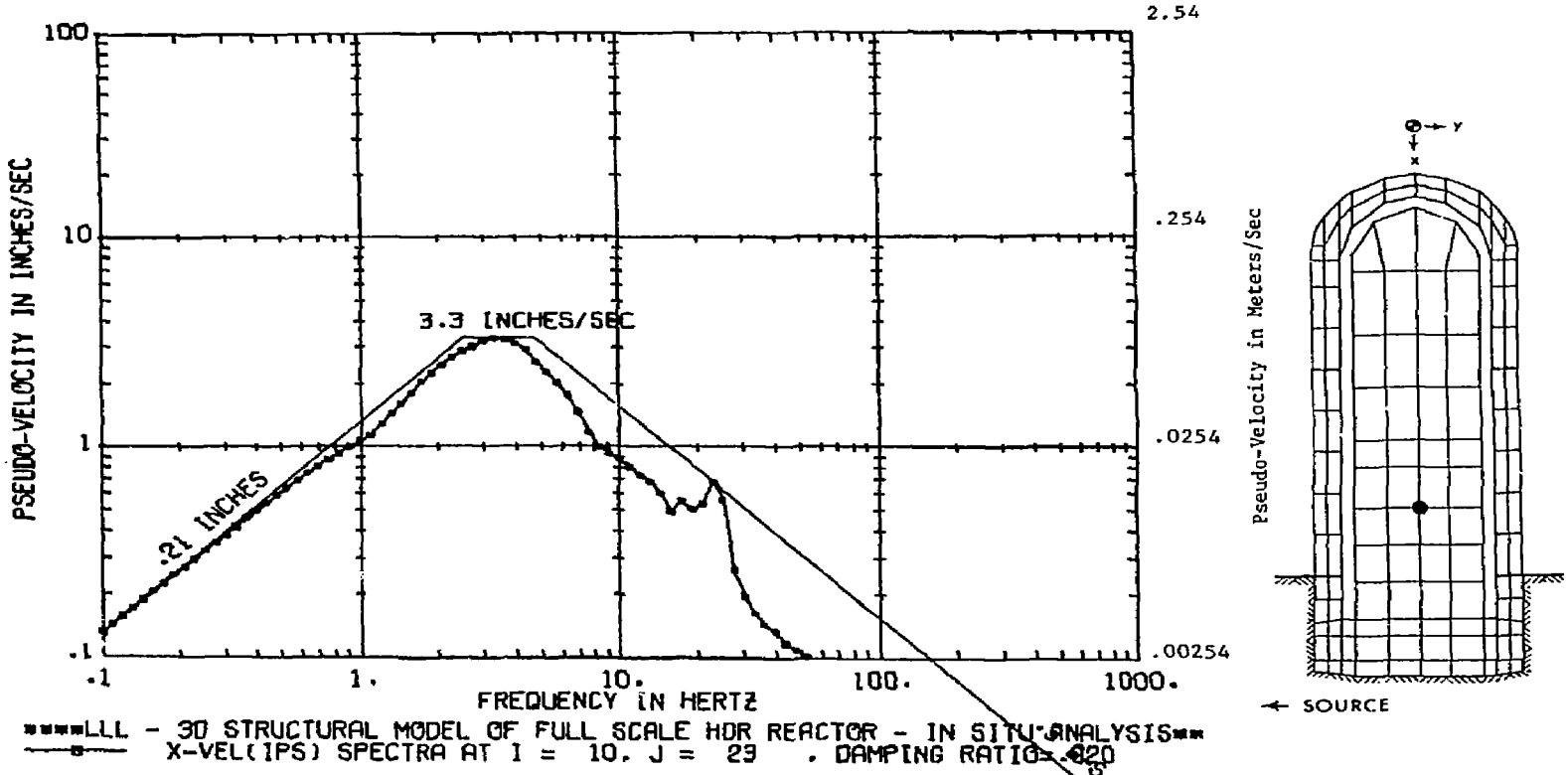

Figure 3-50. Response spectra of vertical motion on inner structure (elev 8.70m, centerline).

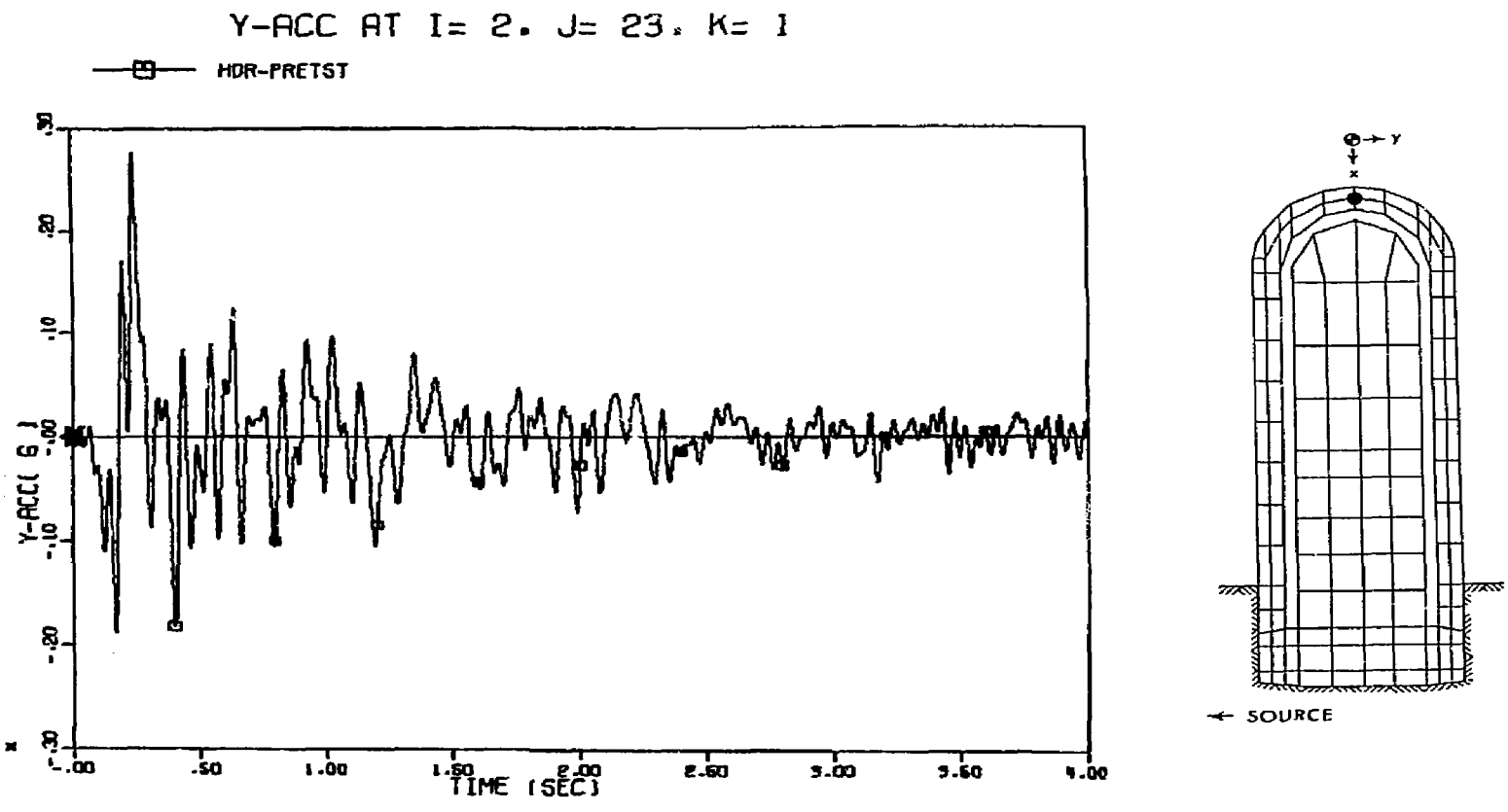

Figure 3-51. Horizontal acceleration-time history at top of outer structure (elev 50.35m, centerline).

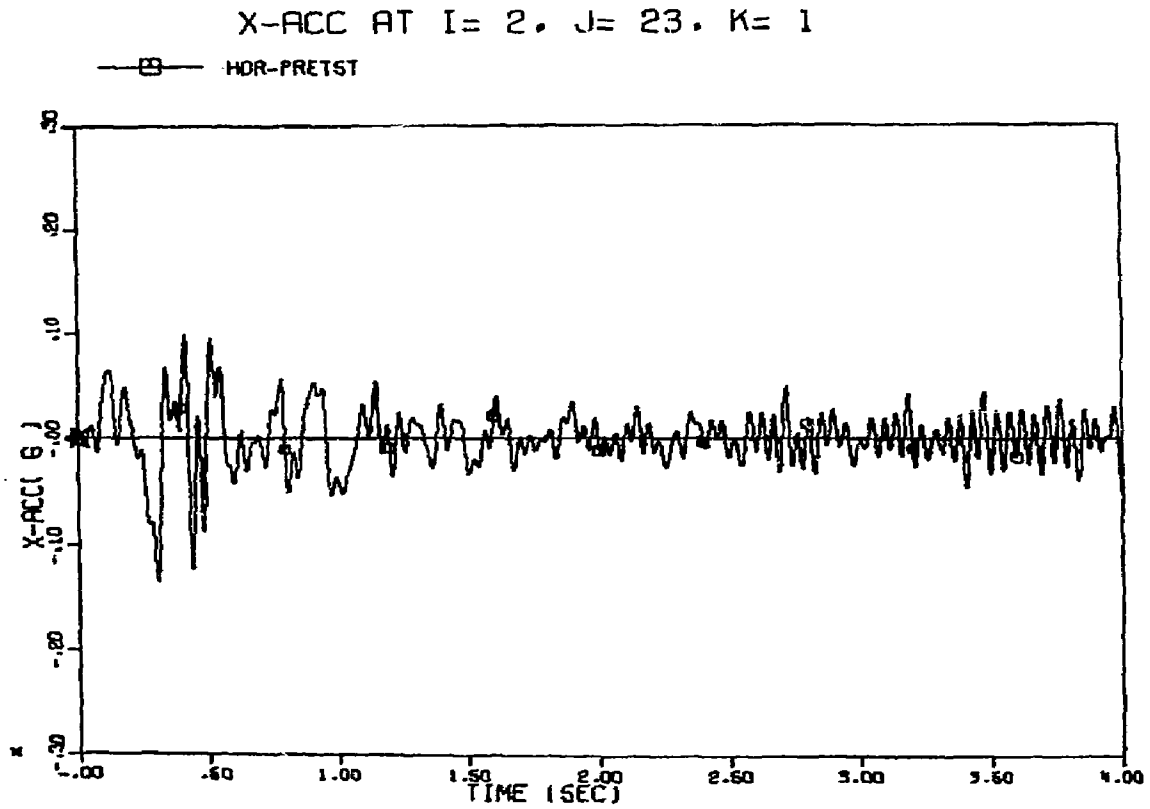

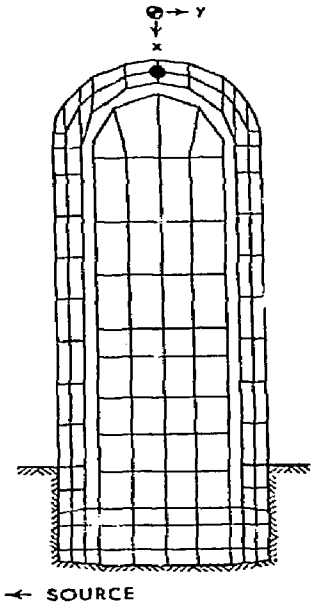

Figure 3-52. Vertical acceleration-time history at top of outer structure (elev 50.35m, centerline).

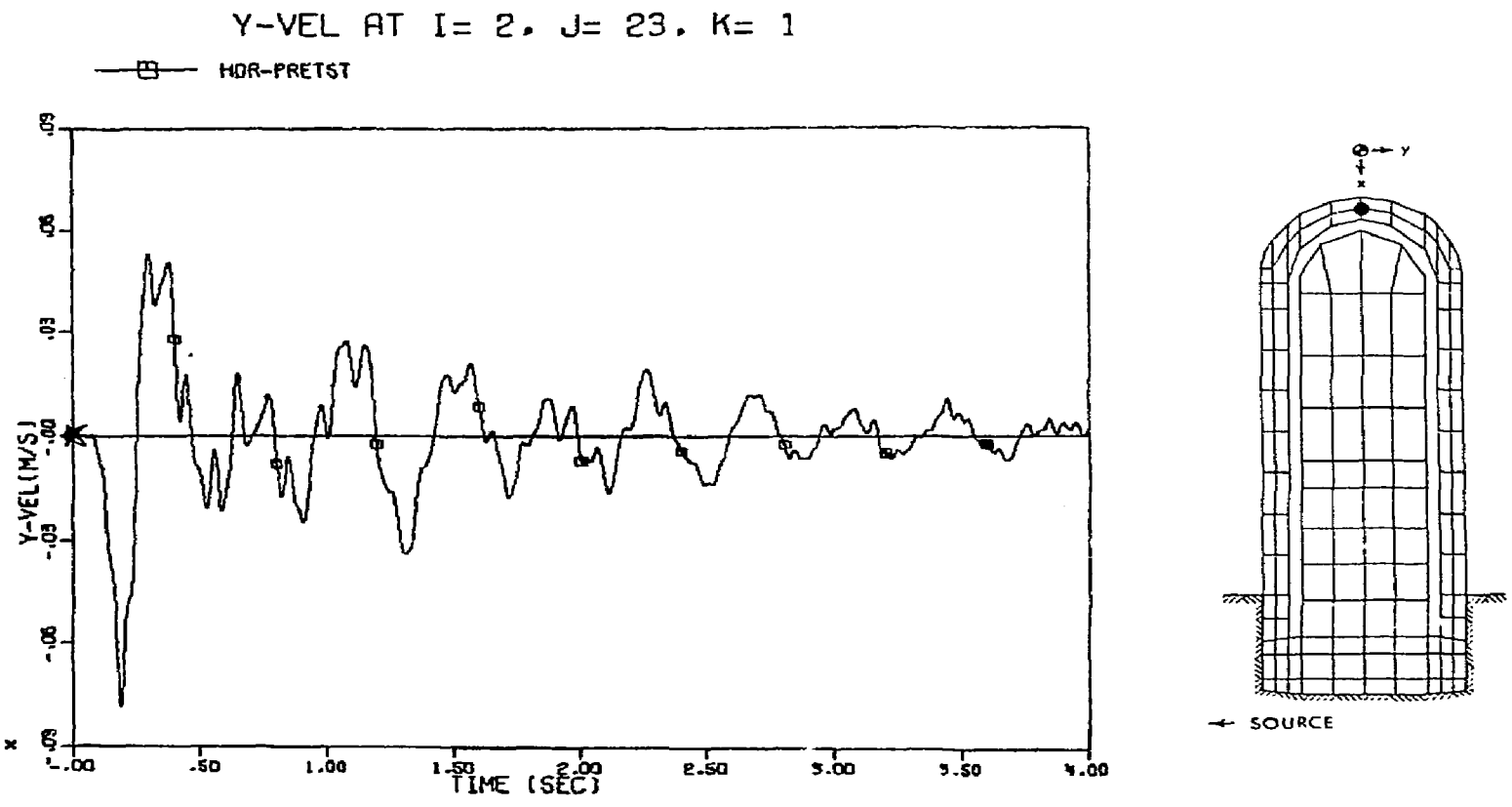

Figure 3-53. Horizontal velocity-time history at top of outer structure (elev 50.35m, centerline).

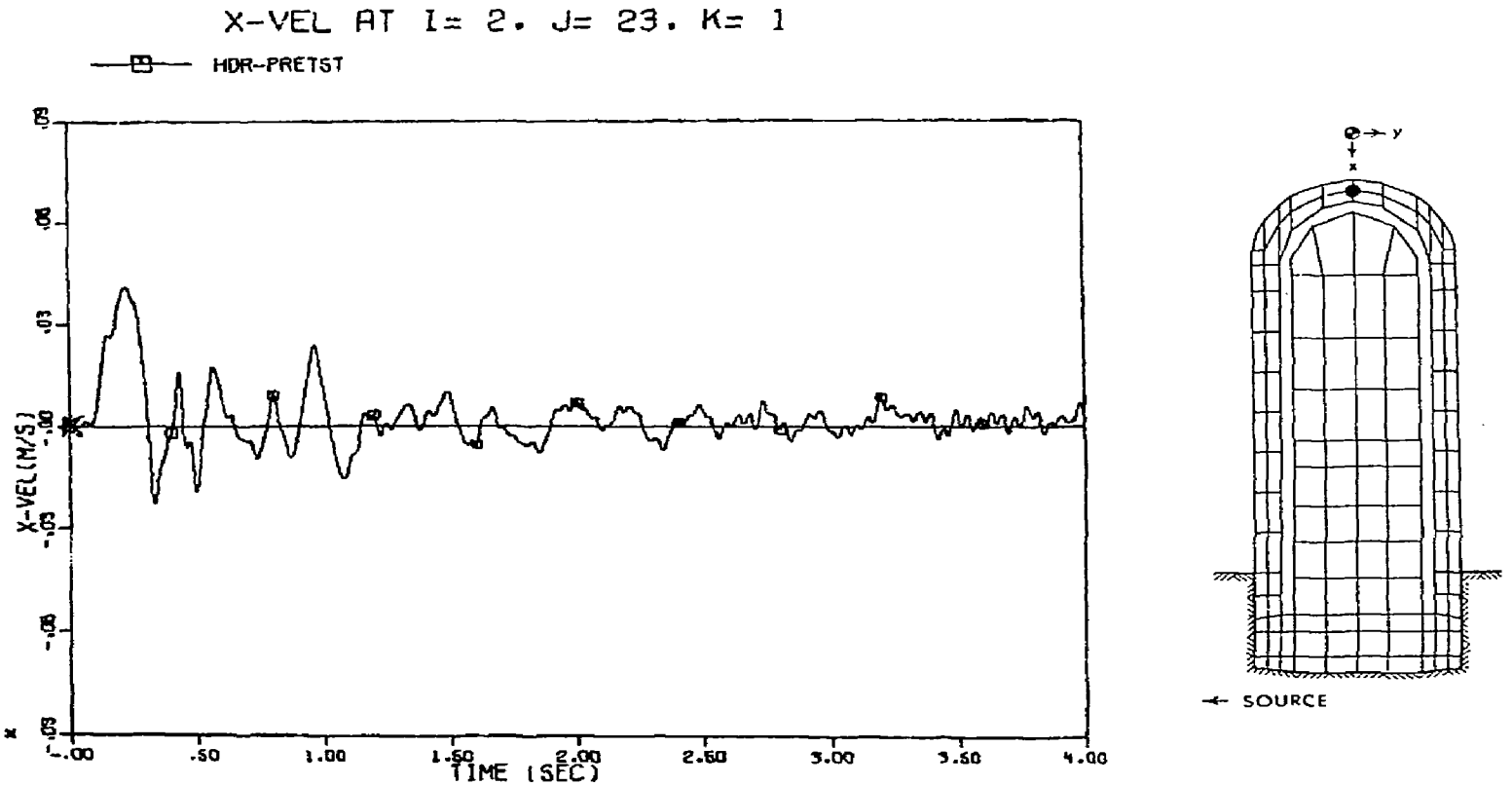

Figure 3-54. Vertical velocity-time history at top of outer structure (elev 50.35m, centerline).

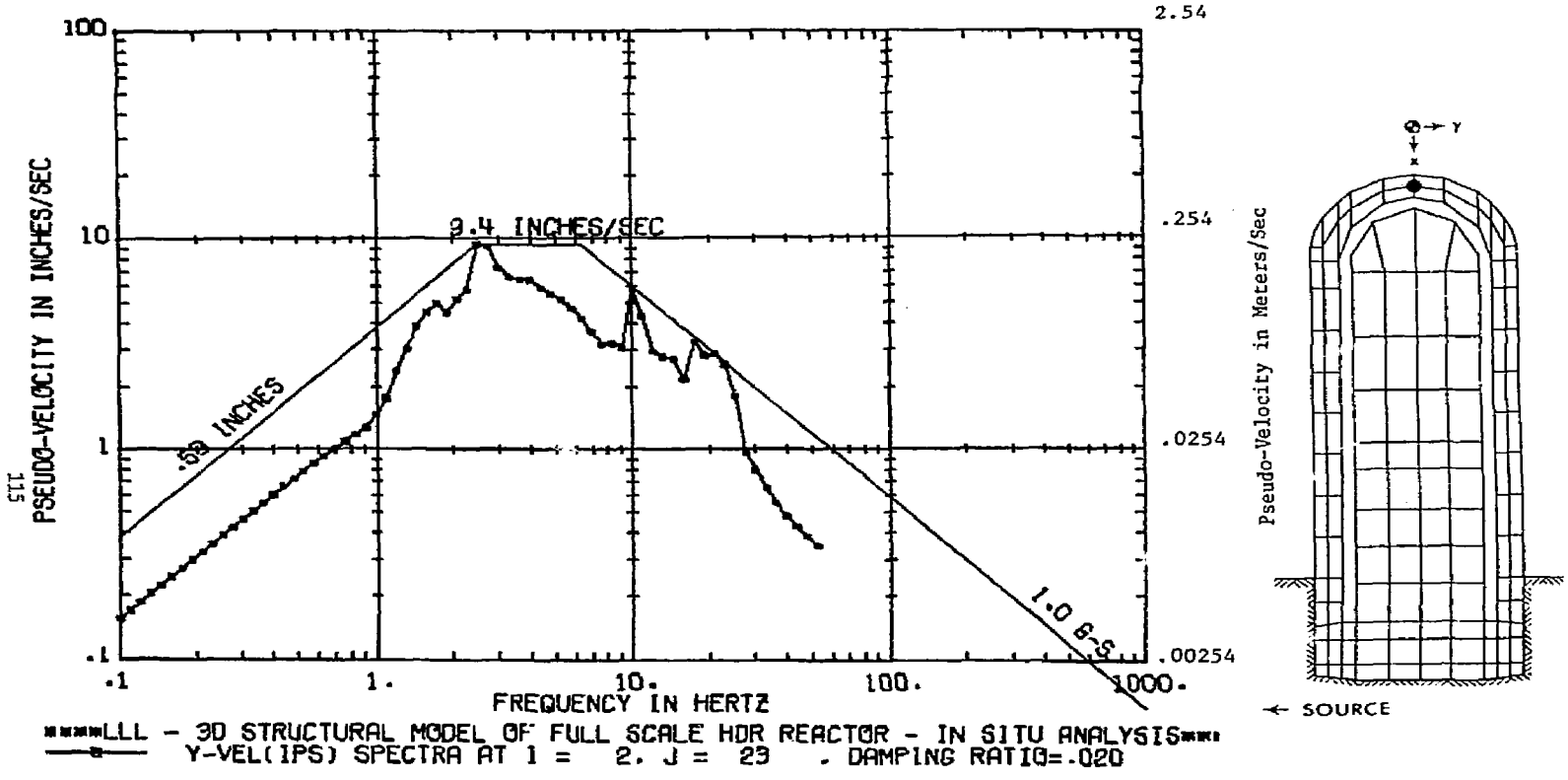

Figure 3-55a. Response spectra of horizontal motion at top of outer structure (elev 50.35m, centerline).

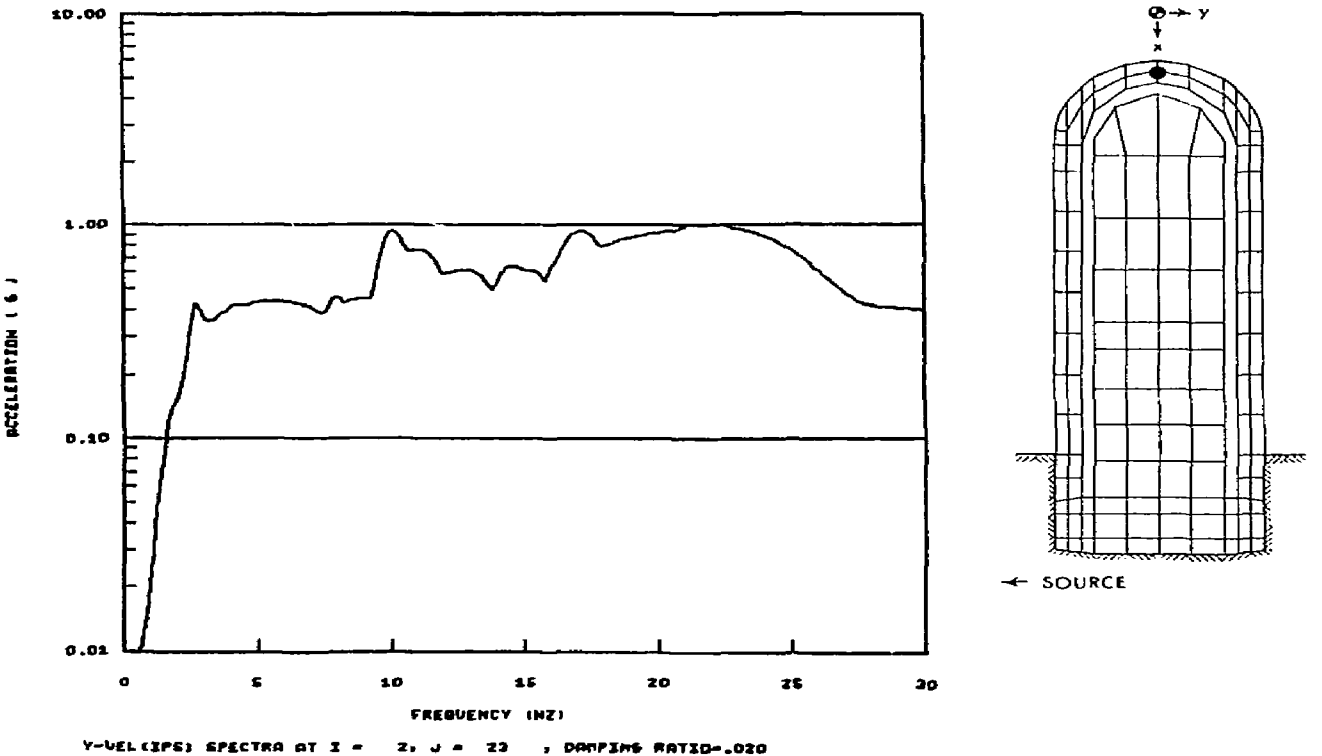

Figure 3-55b. Acceleration response spectra of horizontal motion at top of outer structure (elevation 50.35m, centerline).

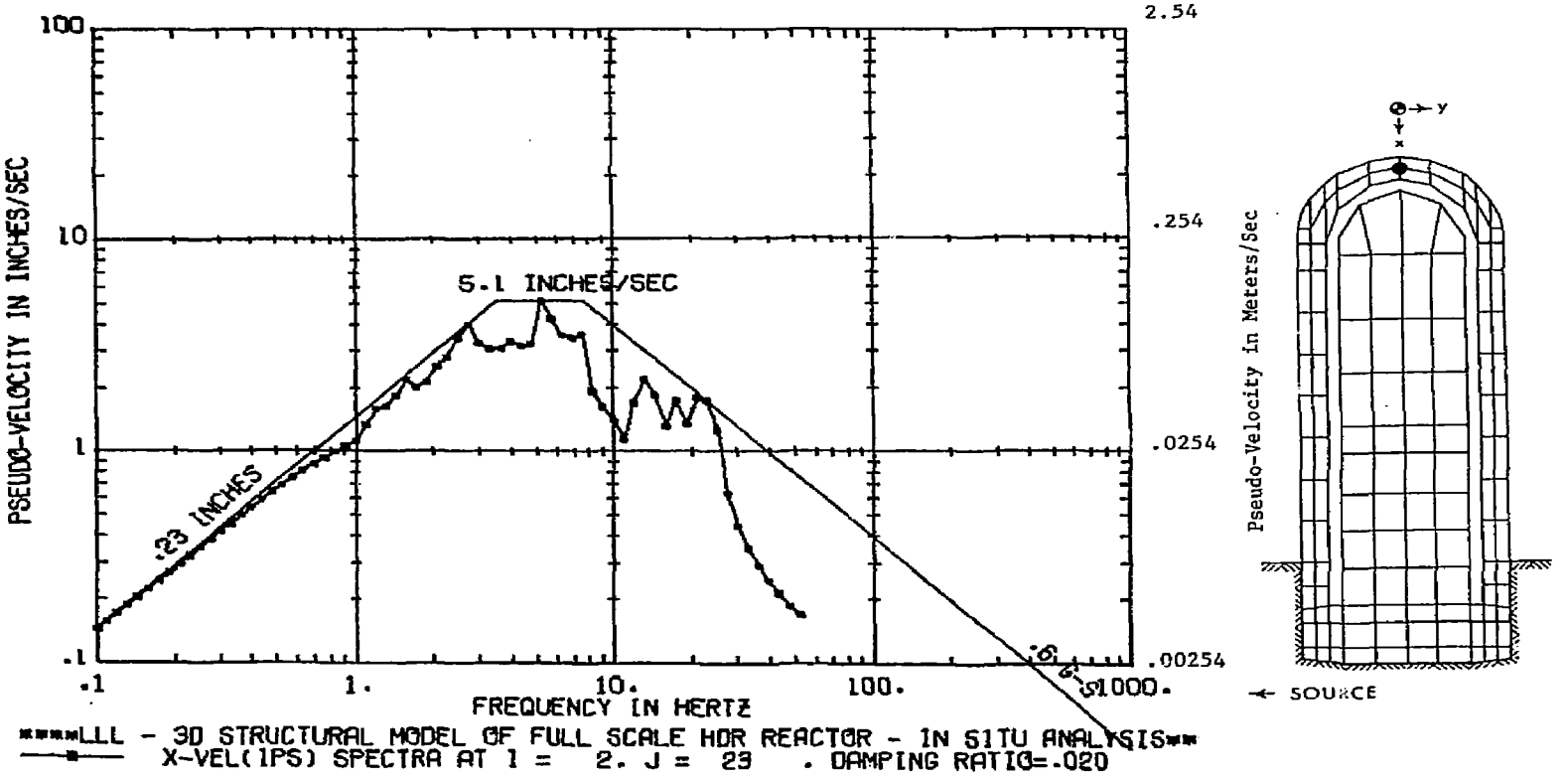

Figure 3-56. Response spectra of vertical motion at top of outer structure (elev 50.35m, centerline).

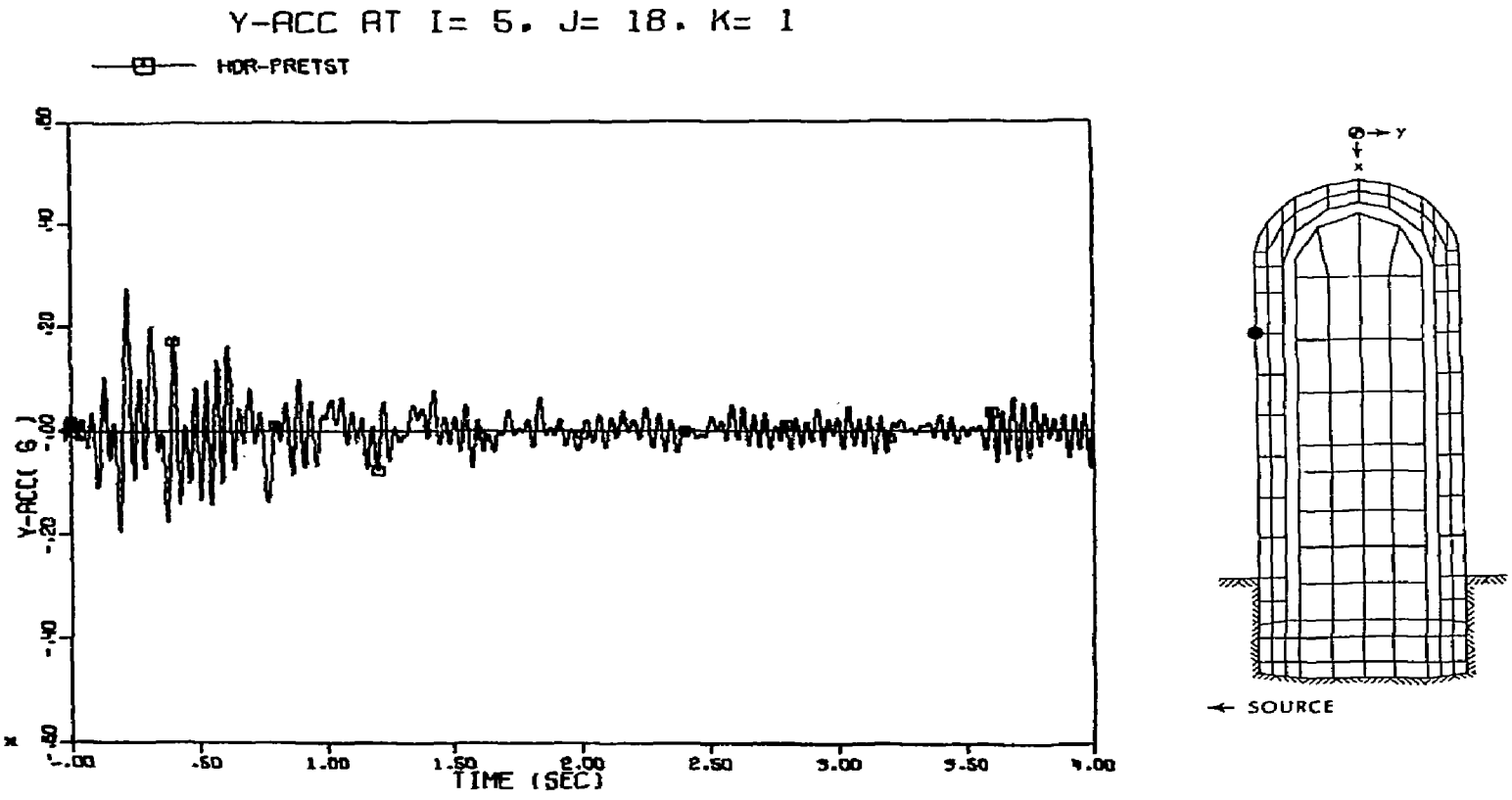

Figure 3-57. Horizontal acceleration-time history on outer structure (elev 31.73m, 11.35m forward of centerline).

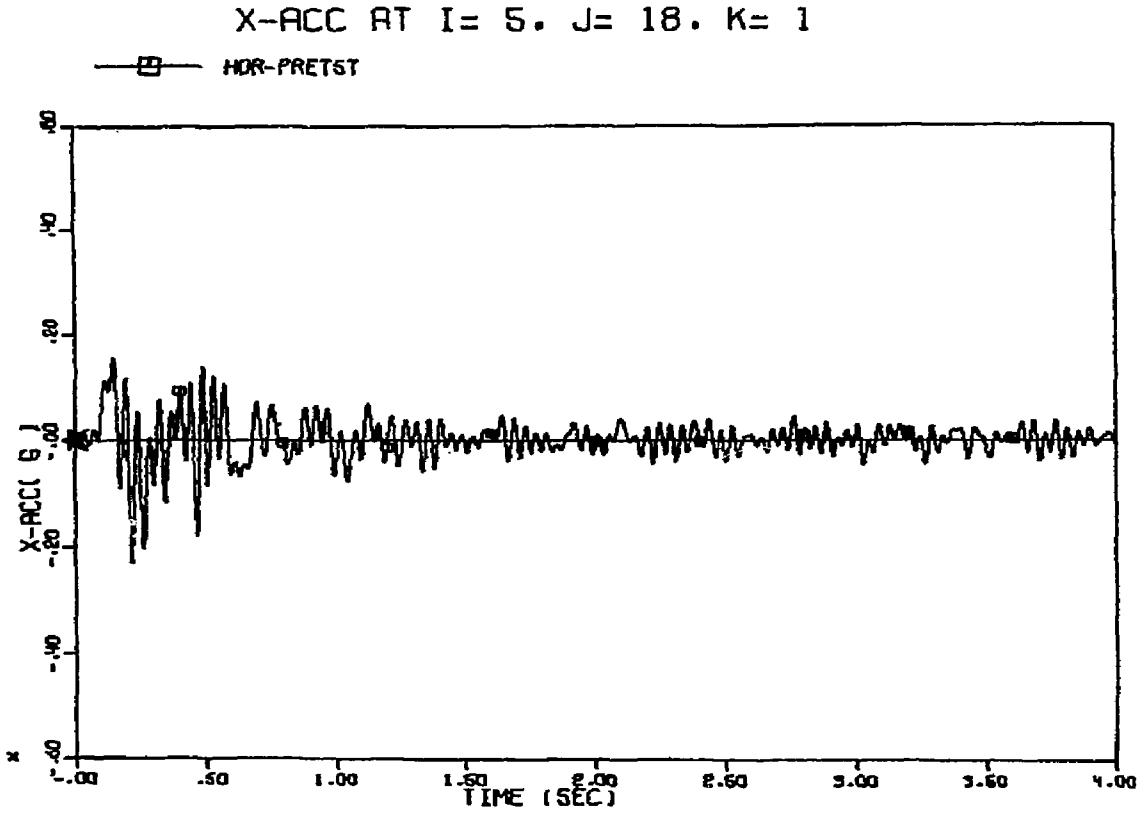

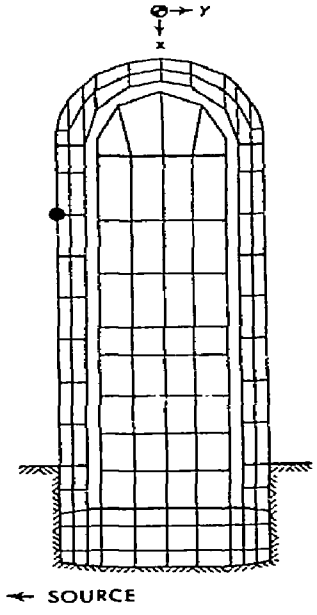

Figure 3-58. Vertical acceleration-time history on outer structure (elev 31.73m, 11.35m forward of centerline).

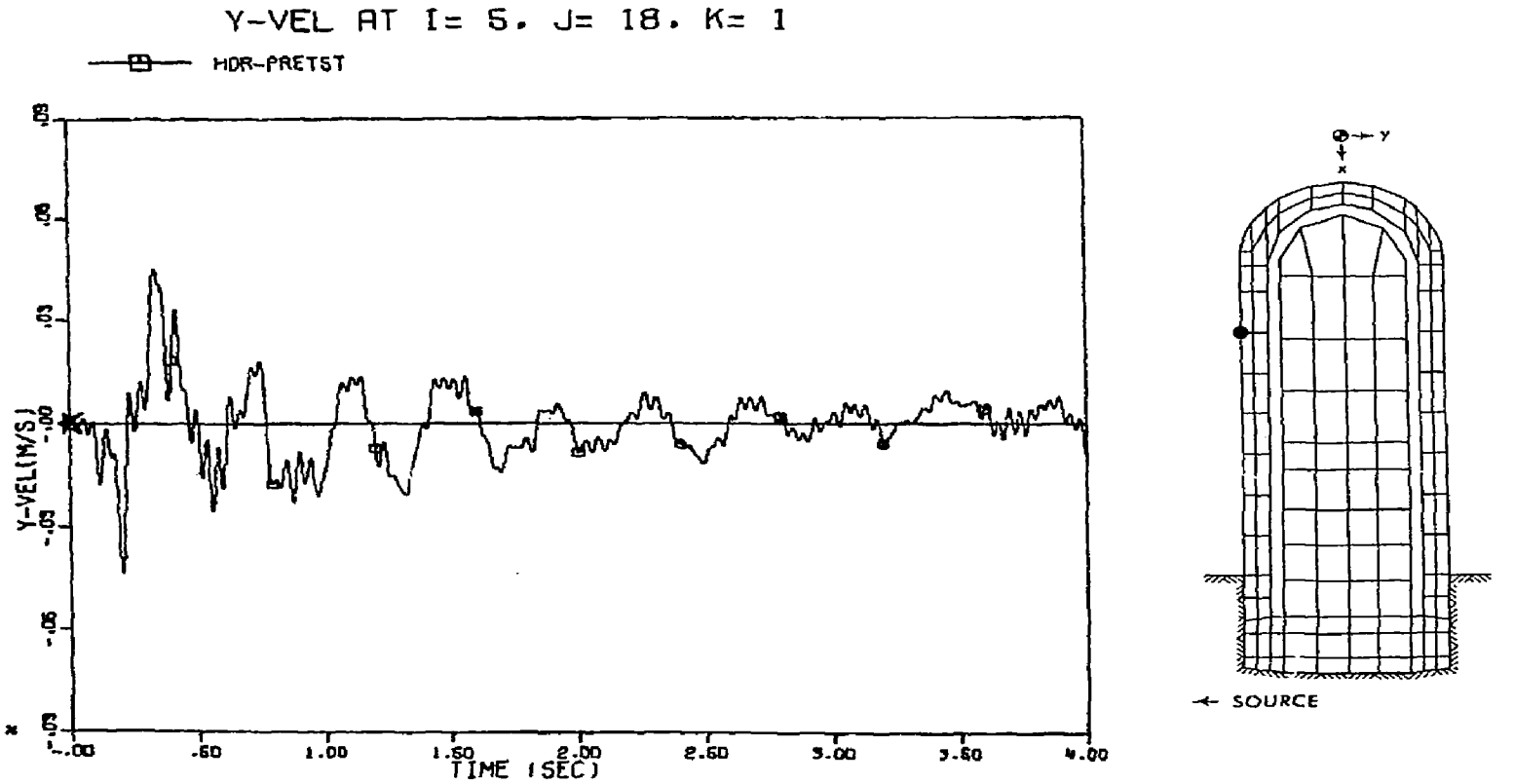

Figure 3-59. Horizontal velocity-time history on outer structure (elev 31.73m, 11.35m forward of centerline).

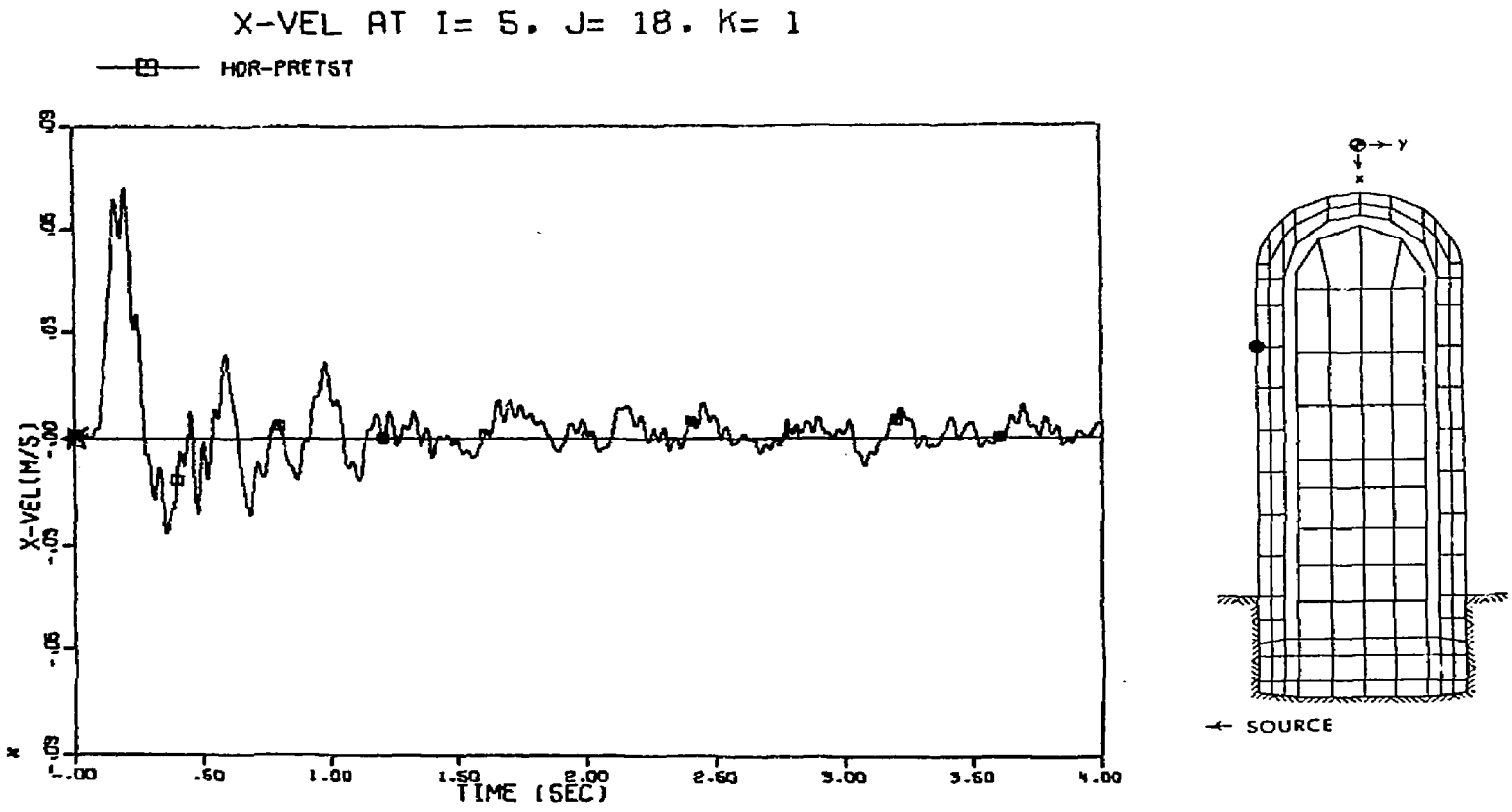

Figure 3-60. Vertical velocity-time history on outer structure (elev 31.73m, 11.35m forward of centerline).

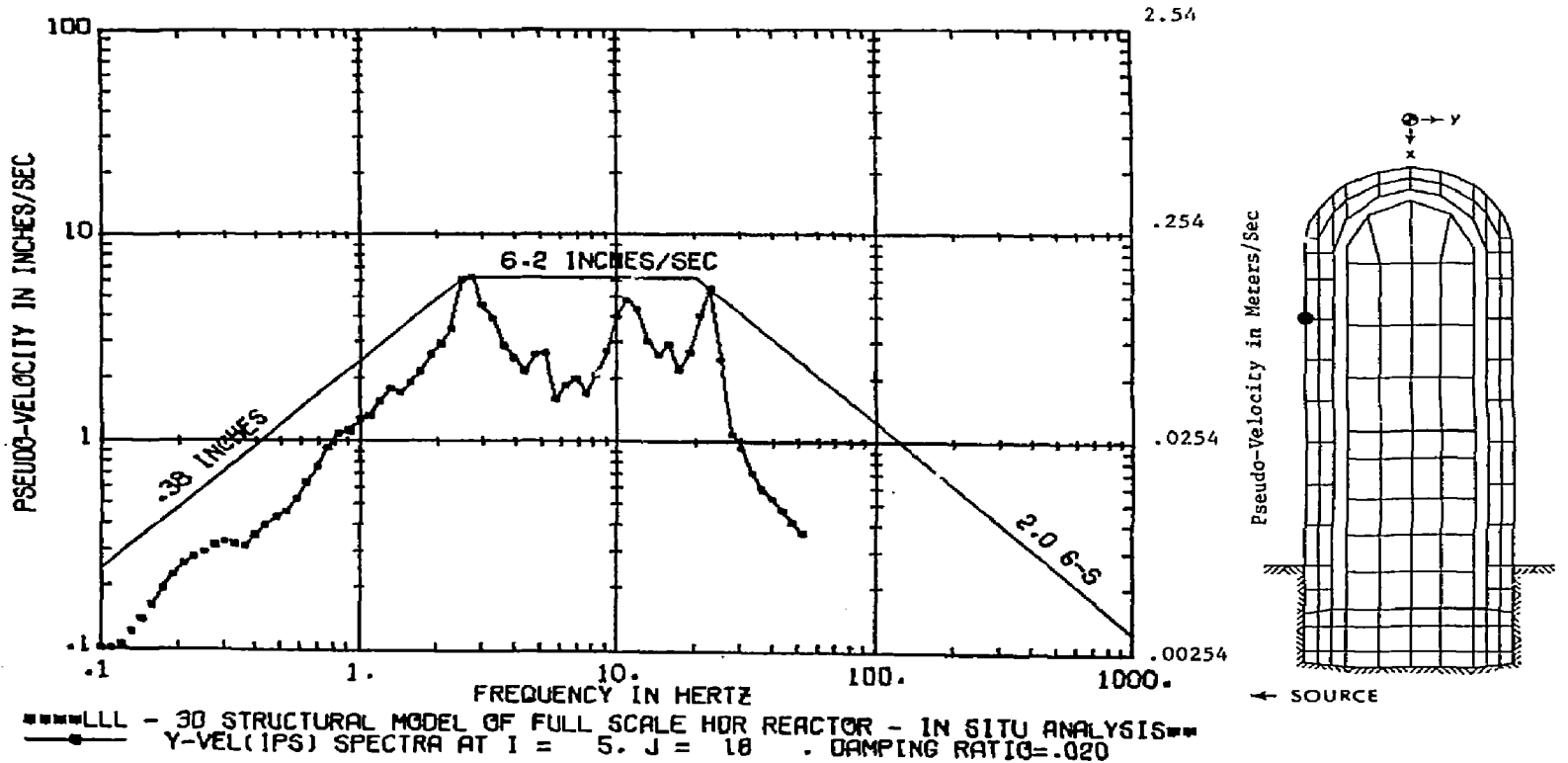

Figure 3-61. Response spectra of horizontal motion on outer structure (elev 31.73m, 11.35m forward of centerline).

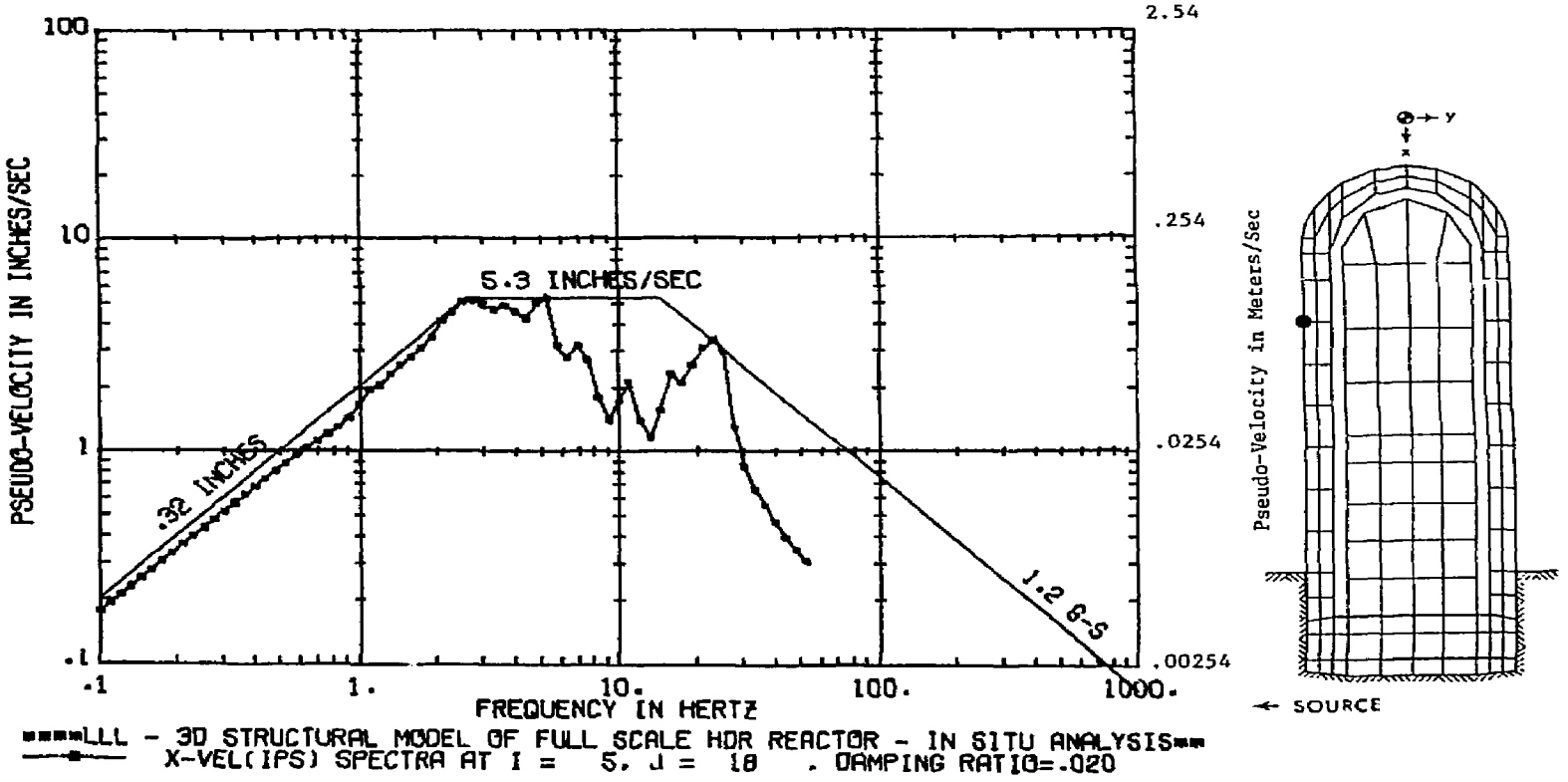

Figure 3-62. Response spectra of vertical motion on outer structure (elev 31.73m, 11.35m forward of centerline).

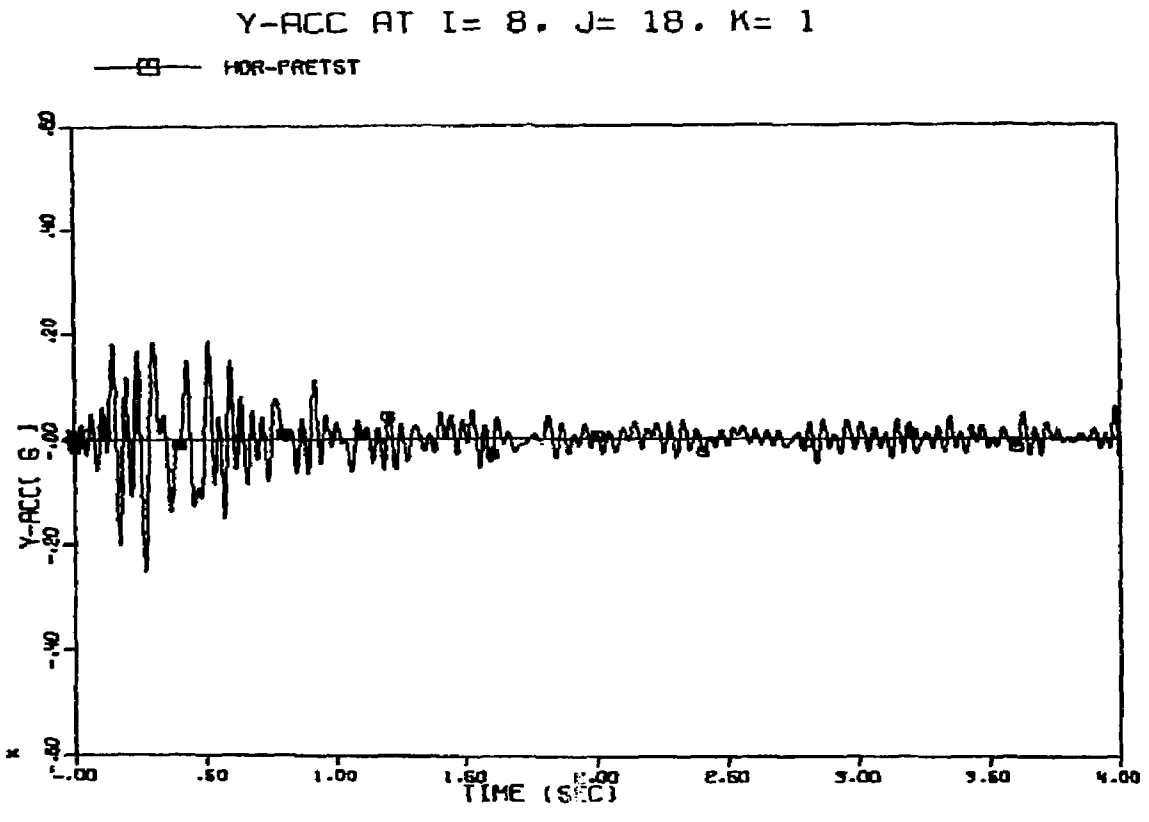

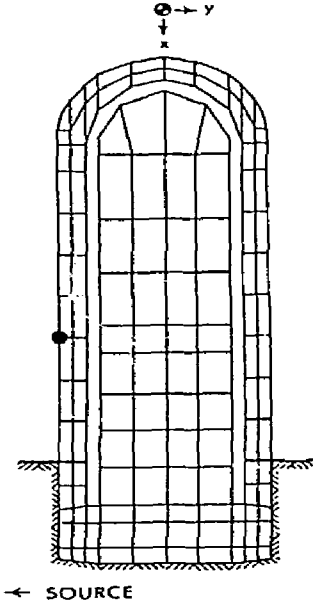

Figure 3-63. Horizontal acceleration-time history on outer structure (elev 15.87m, 11.35m forward of centerline).

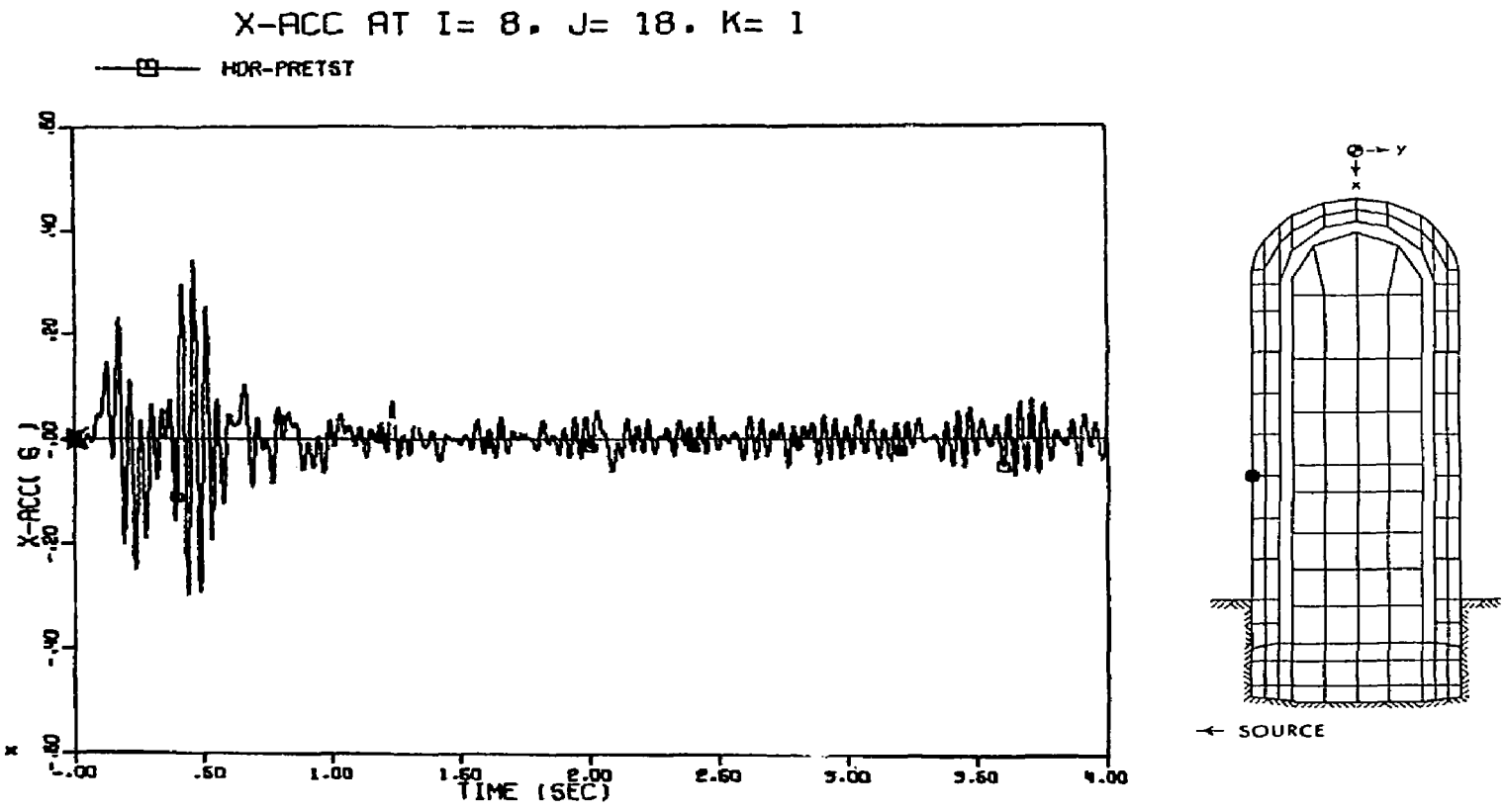

Figure 3-64. Vertical acceleration-time history on outer structure (elev 15.87m, 11.35m forward of centerline).

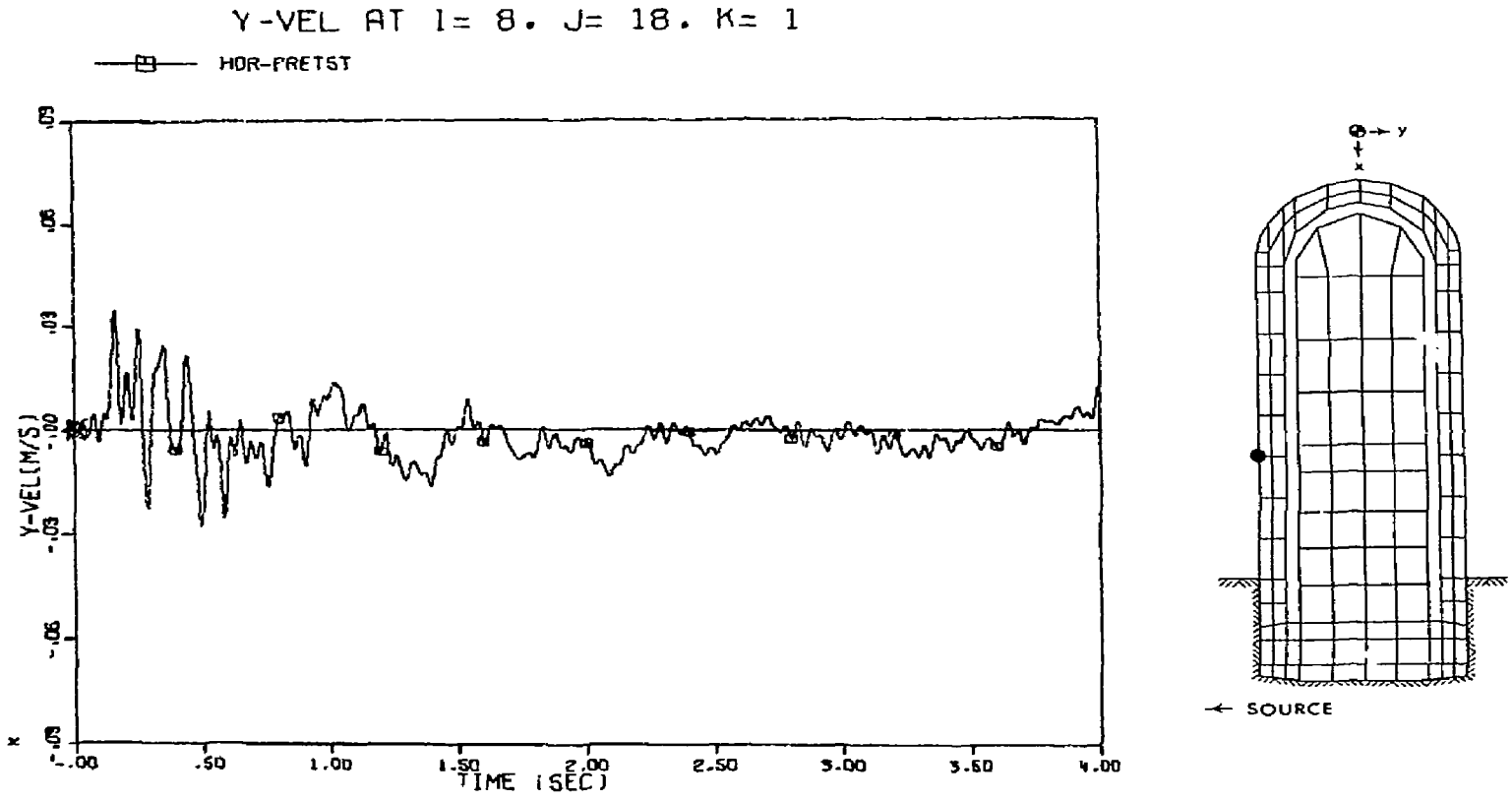

Figure 3-65. Horizontal velocity-time history on outer structure (elev 15.87m, 11.35m forward of centerline).

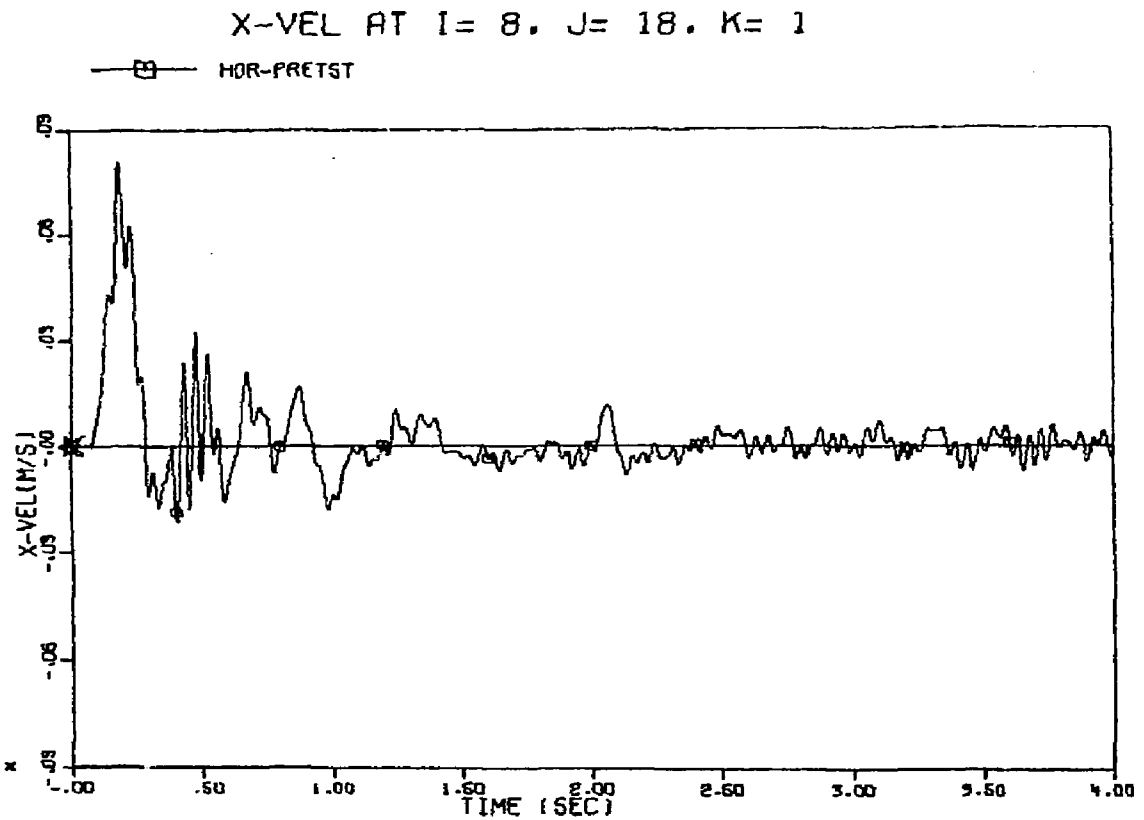

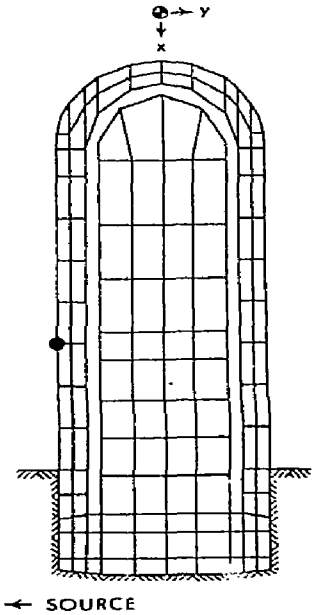

Figure 3-66. Vertical velocity-time history on outer structure (elev 15.87m, 11.35m forward of centerline).

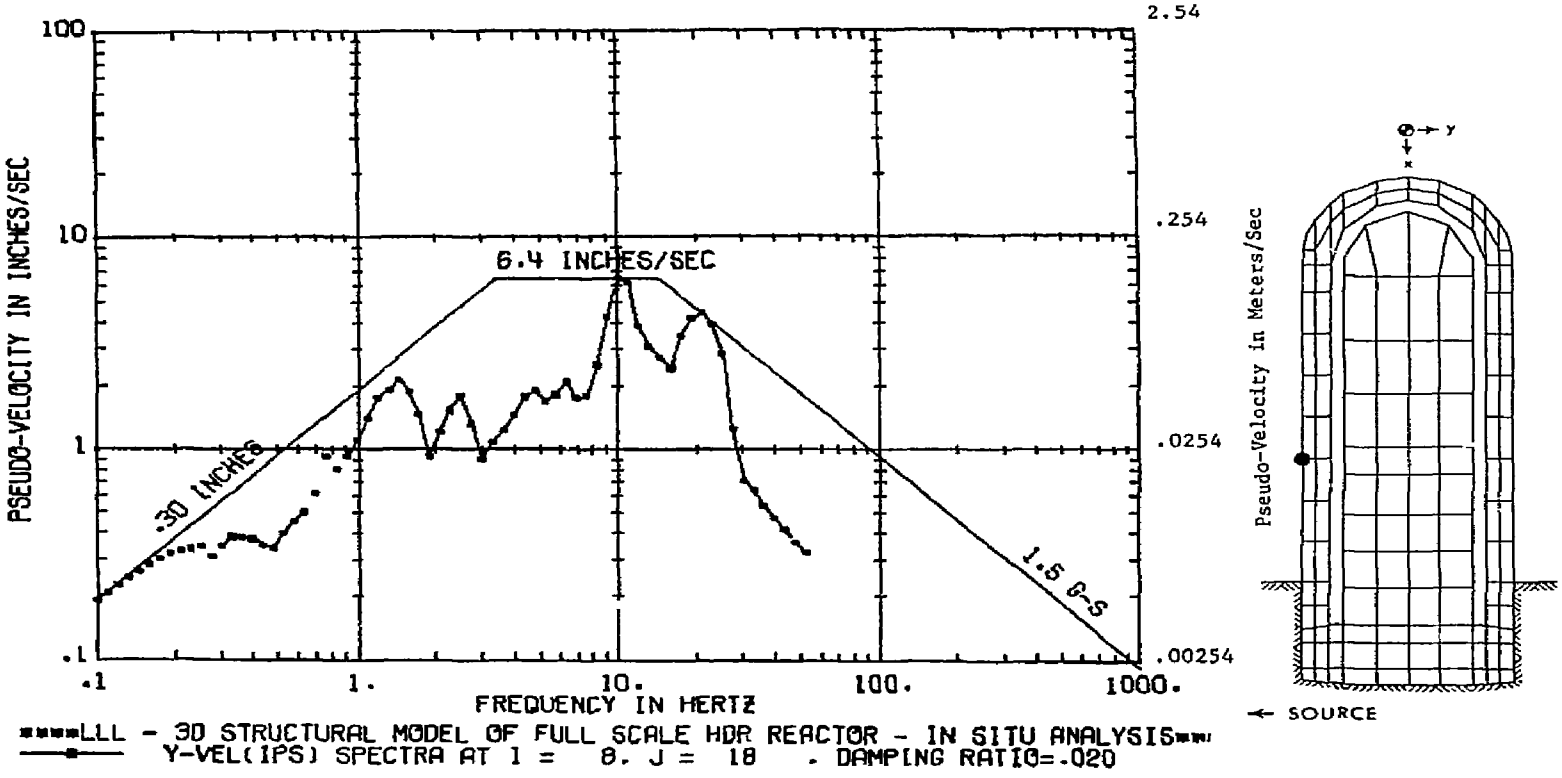

Figure 3-67. Response spectra of horizontal motion on outer structure (elev 15.87m, 11.35m forward of centerline).

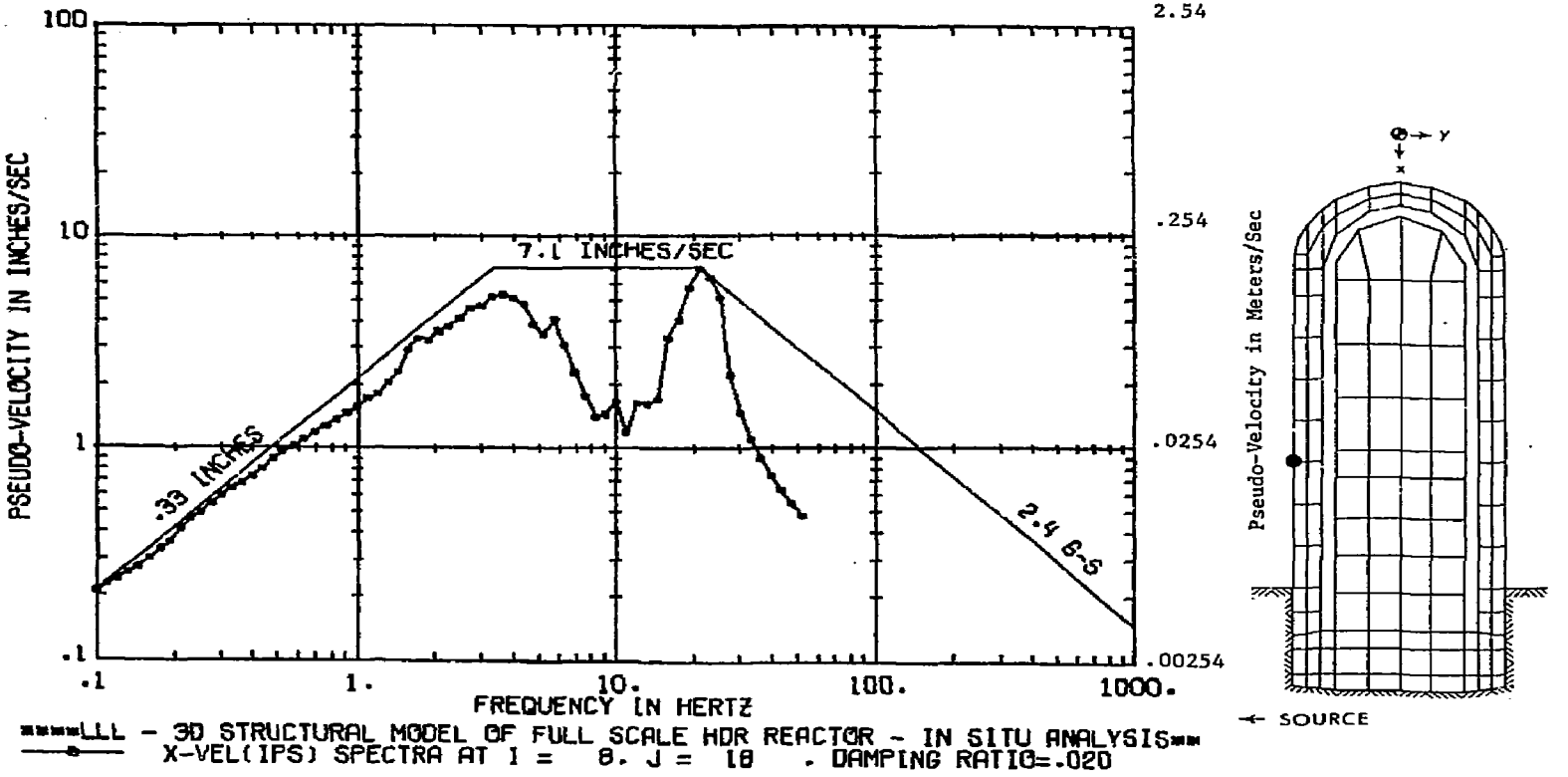

Figure 3-68. Response spectra of vertical motion on outer structure (elev 15.87m, 11.35m forward of centerline).

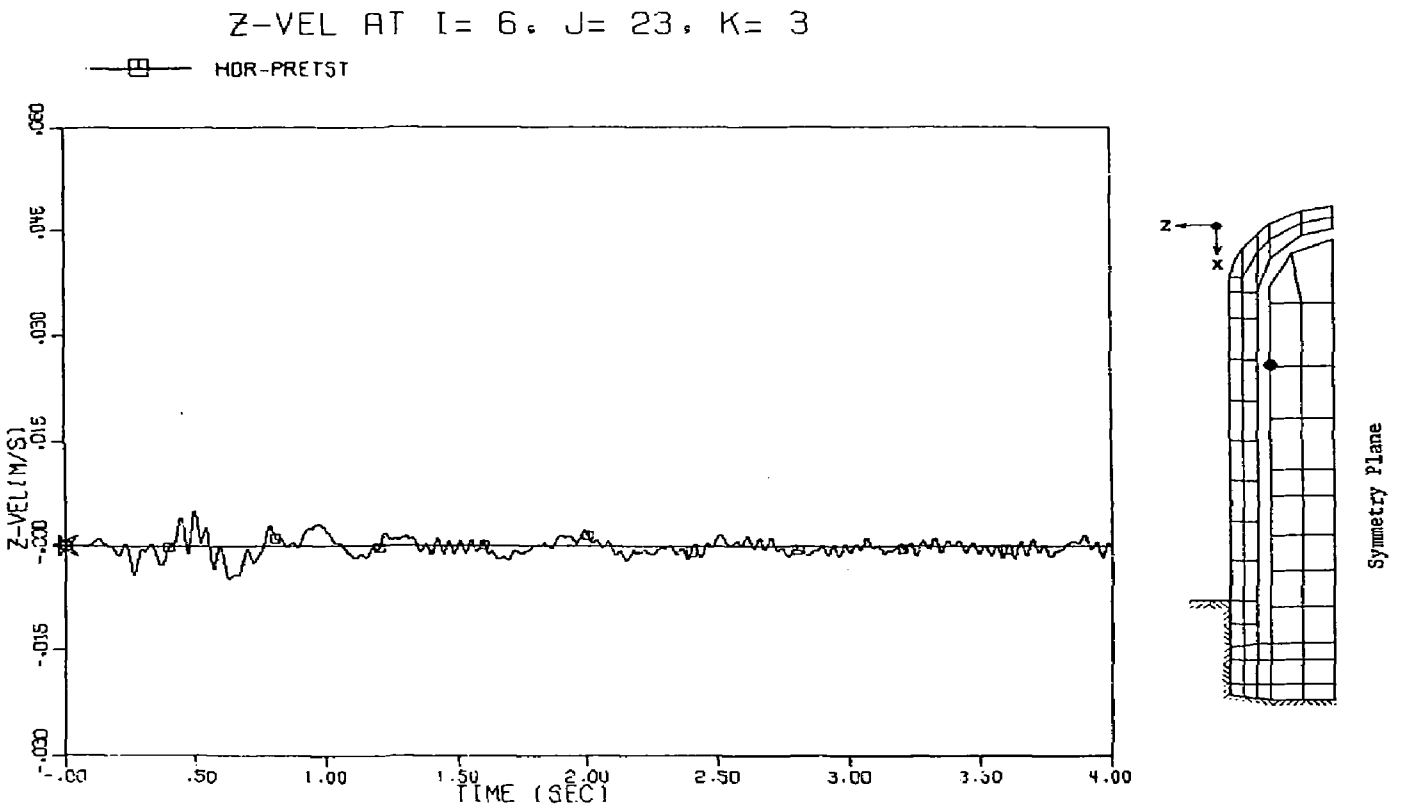

Figure 3-69. Horizontal velocity-time history perpendicular to symmetry plane of inner containment structure (elev 30.85m, 6.85m in from symmetry plane).

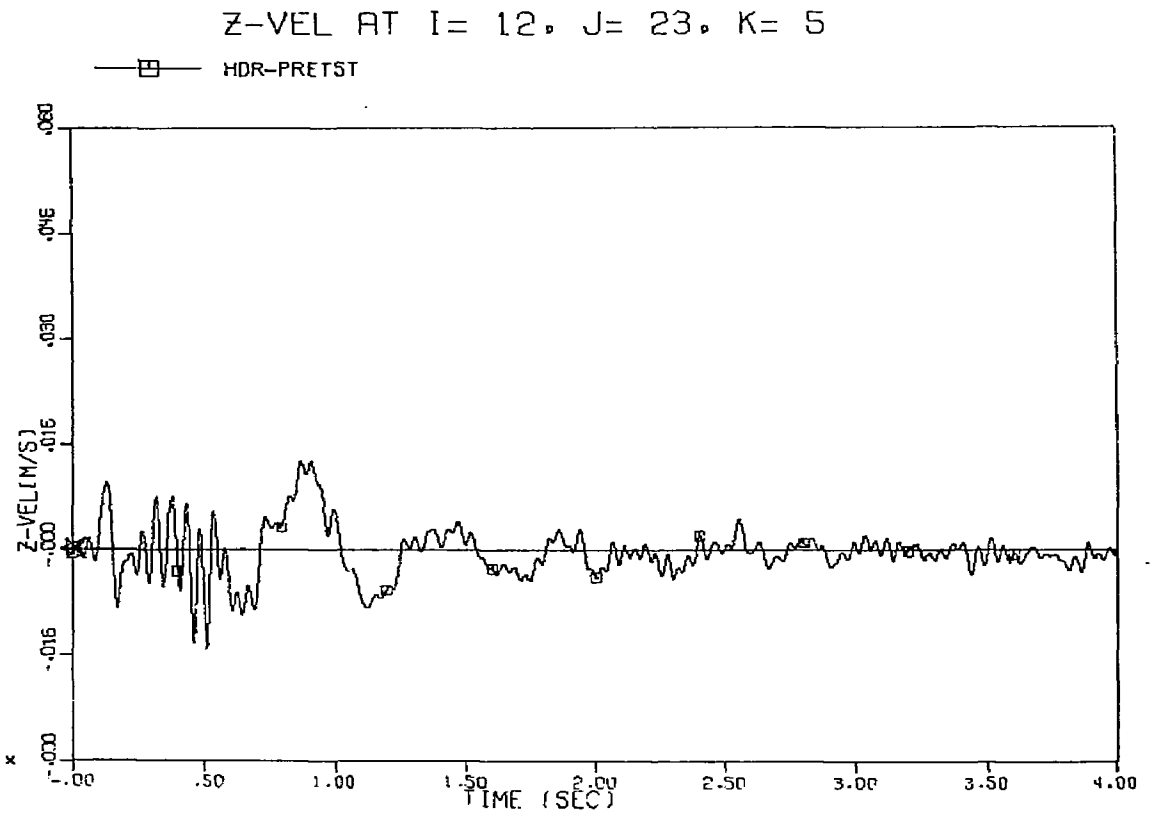

Figure 3-70. Horizontal velocity-time history perpendicular to symmetry plane of outer structure (elev -3m, 9.85m in from symmetry plane).

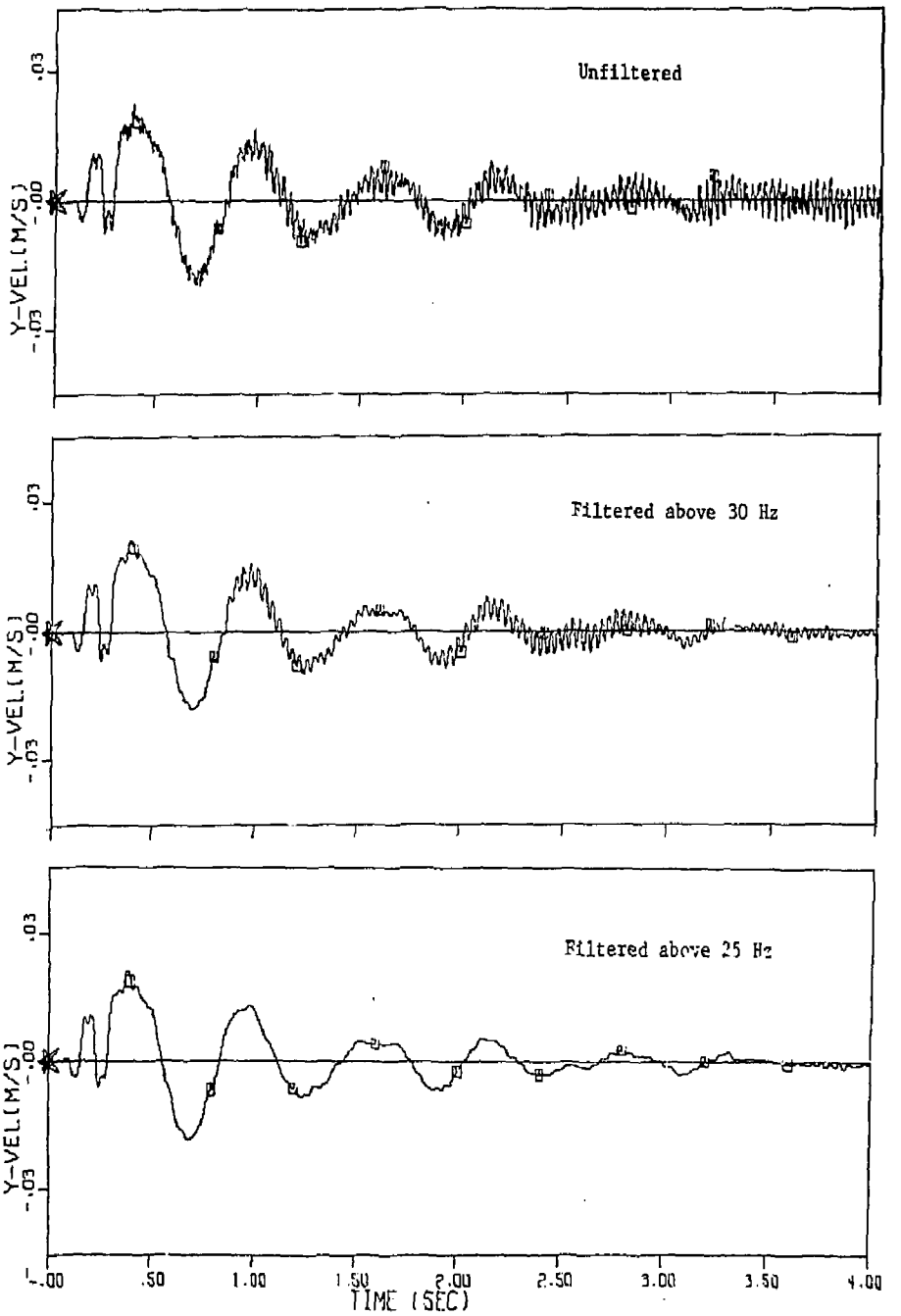

Figure 3-71a. Filtered and unfiltered horizontal velocity-time histories of inner structure at piping attach point (elev 17.25m, centerline).

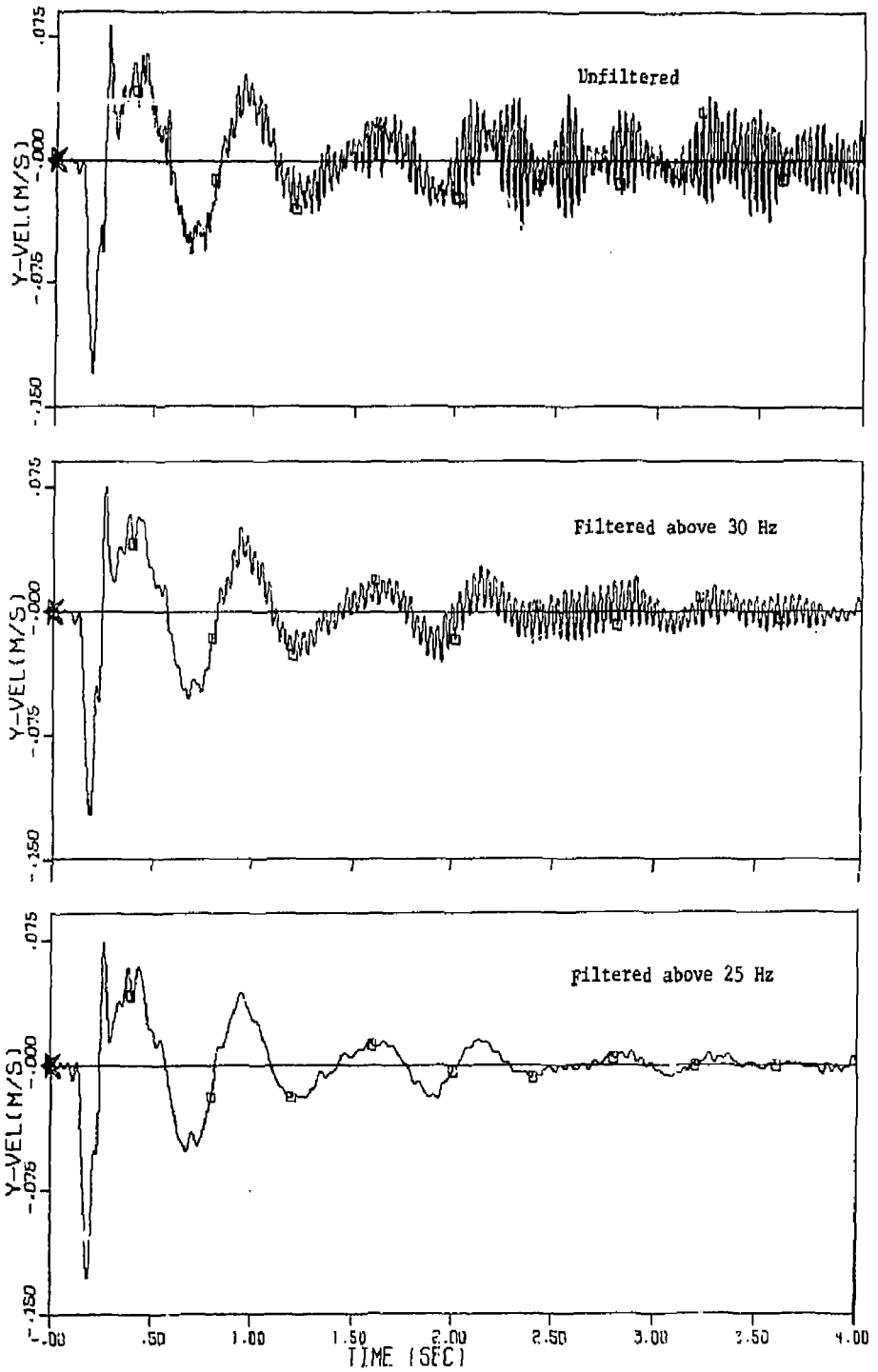

Figure 3-71b. Filtered and unfiltered horizontal velocity-time histories at top of inner structure (elev 47.35m, centerline).

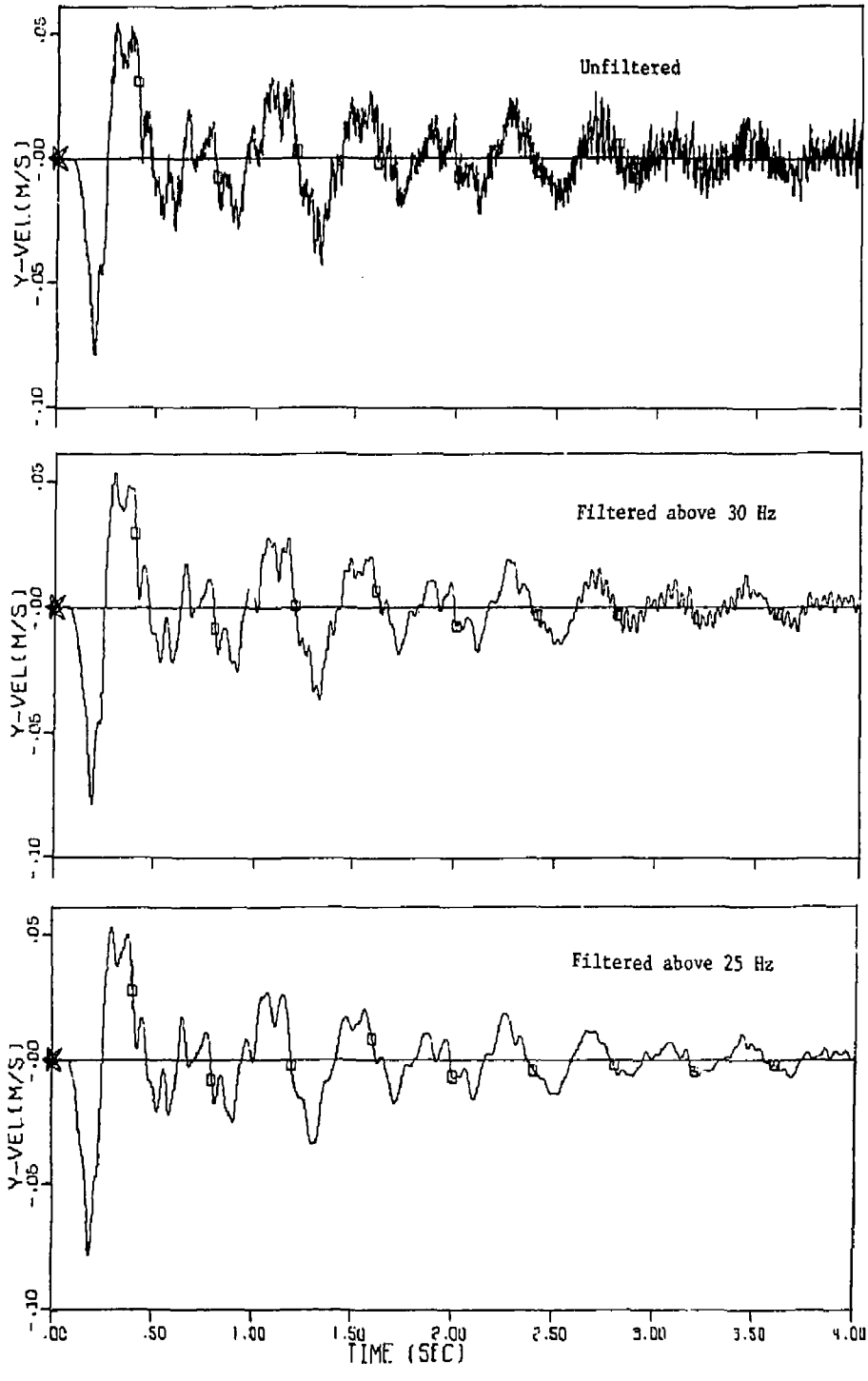

Figure 3-71c. Filtered and unfiltered horizontal velocity-time histories at top of outer structure (elev 50.35m, centerline).

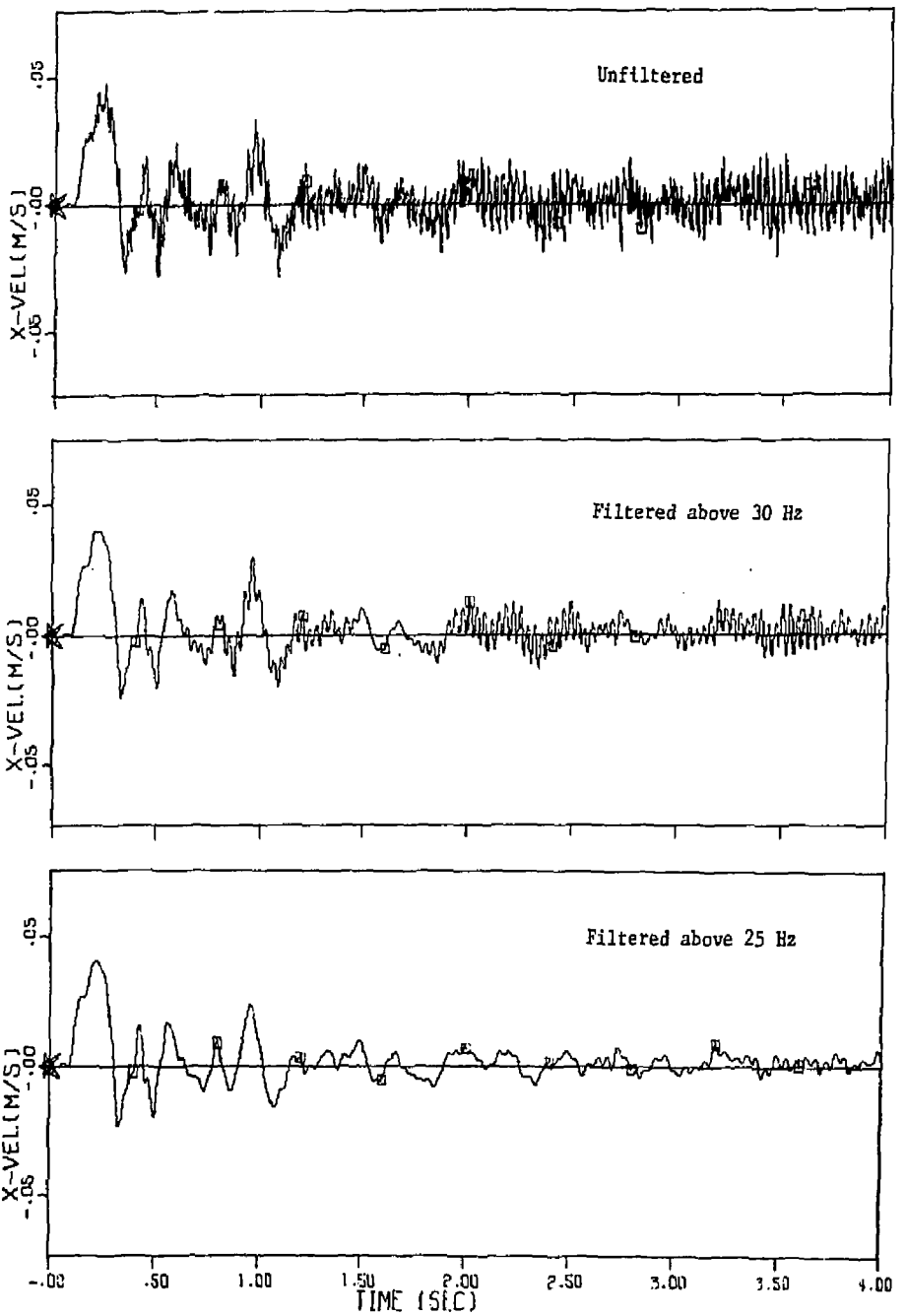

Figure 3-71d. Filtered and unfiltered vertical velocity-time histories at top of outer structure (elev 50.35m, centerline).

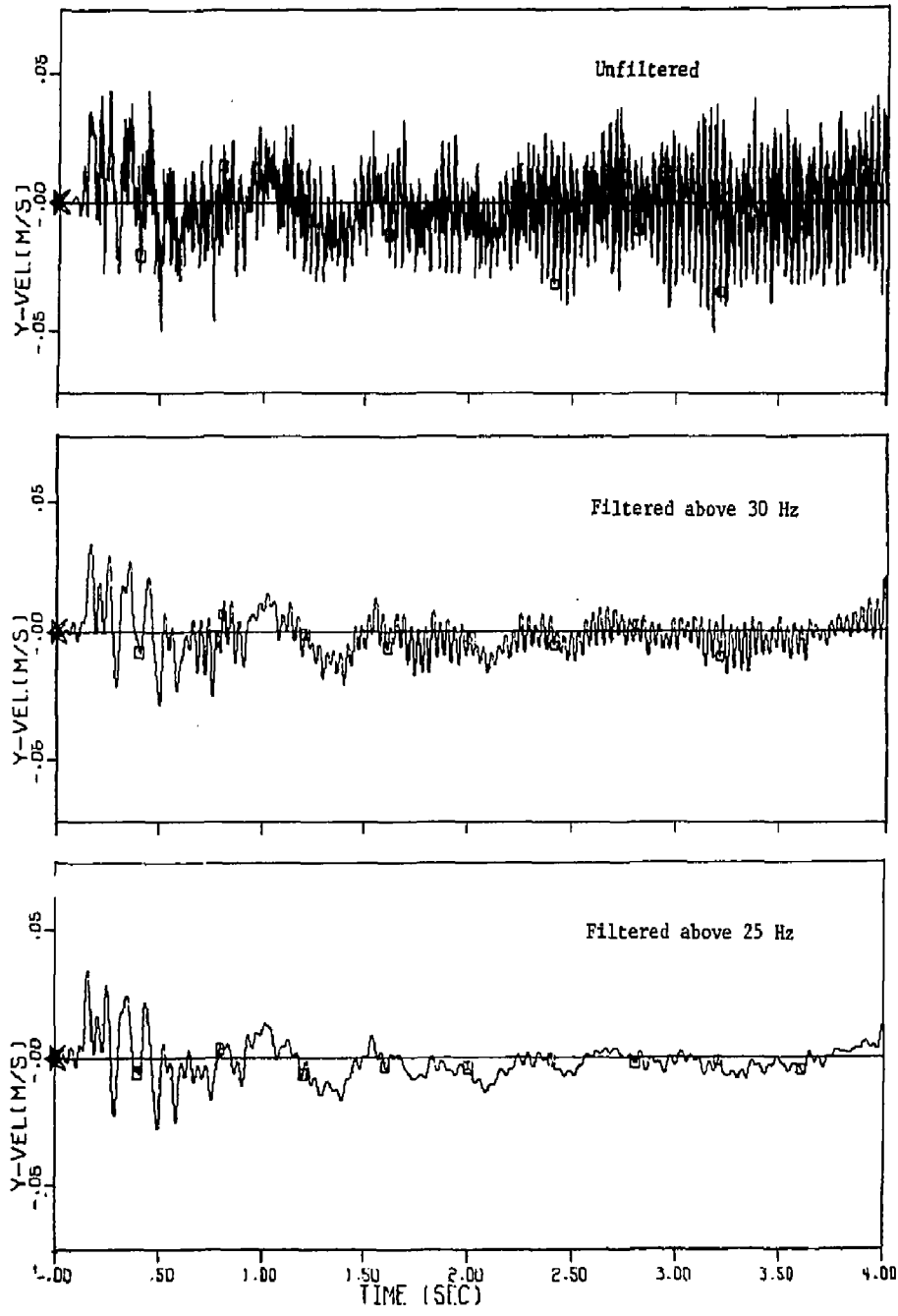

Figure 3-71e. Filtered and unfiltered horizontal velocity-time histories on outer structure (elev 15.87m, 11.35m forward of centerline).

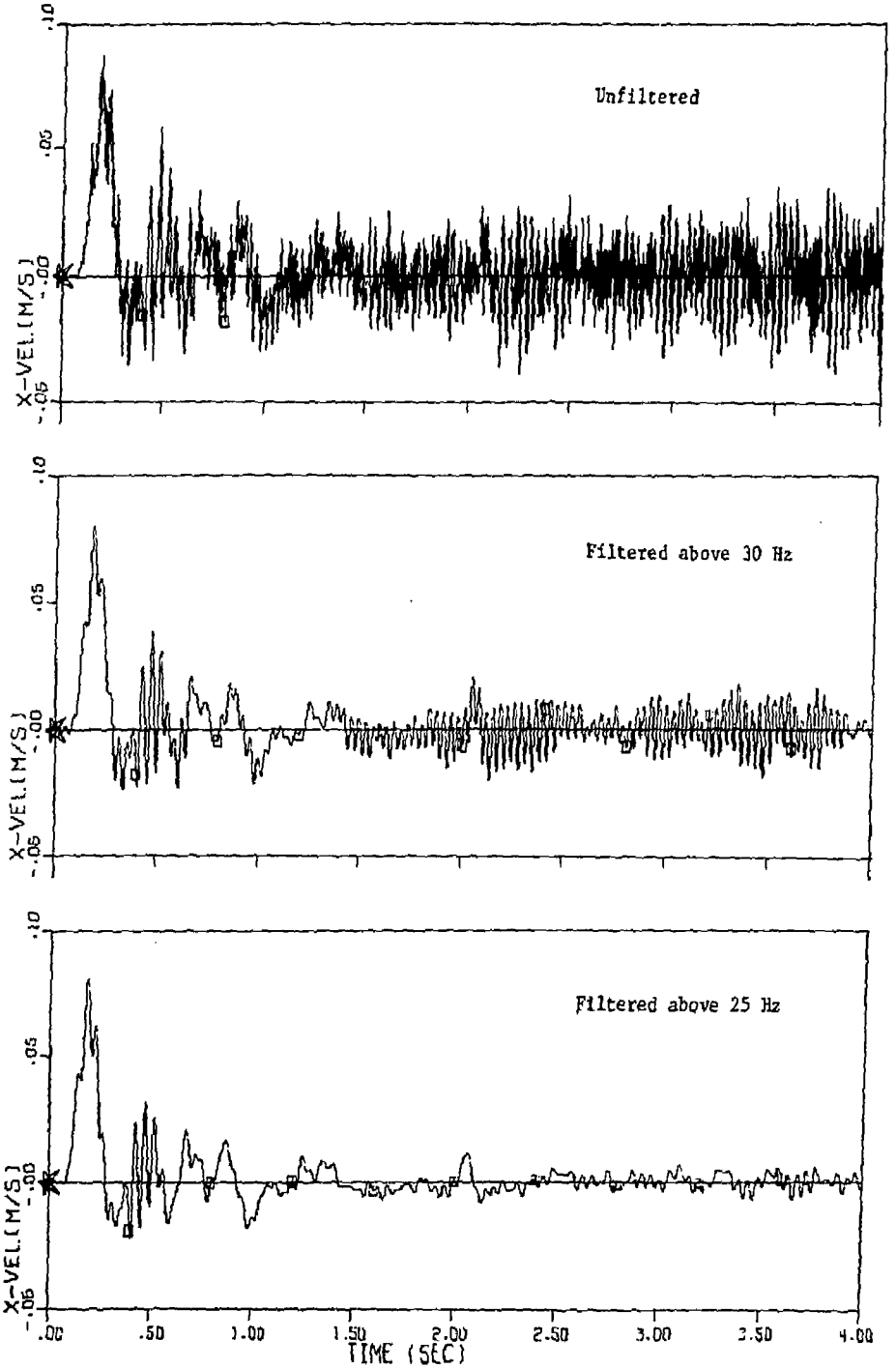

Figure 3-71f. Filtered and unfiltered vertical velocity-time histories on outer structure (elev 15.87m, 11.35m forward of centerline).

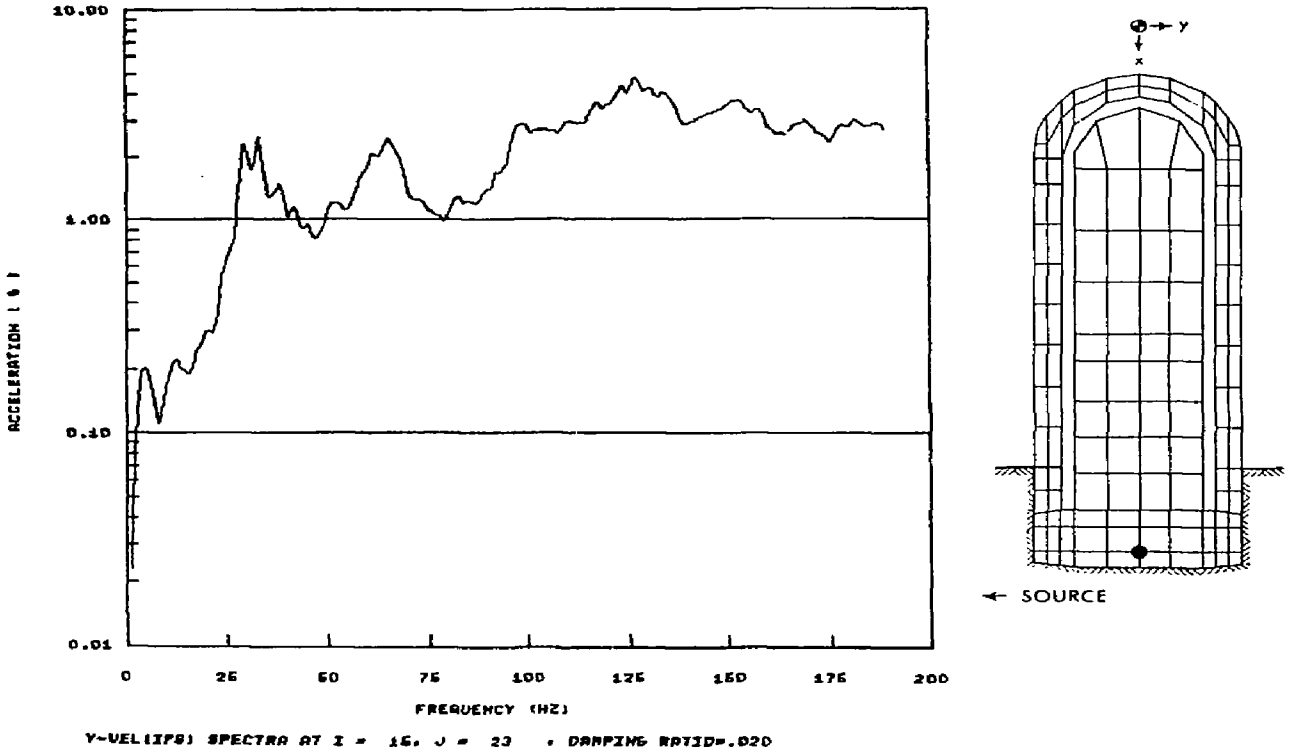

Figure 3-72a. Unfiltered acceleration response spectra of horizontal motion of foundation (elev -11.05m, centerline). (See Fig. 3-13b for filtered response spectra.)

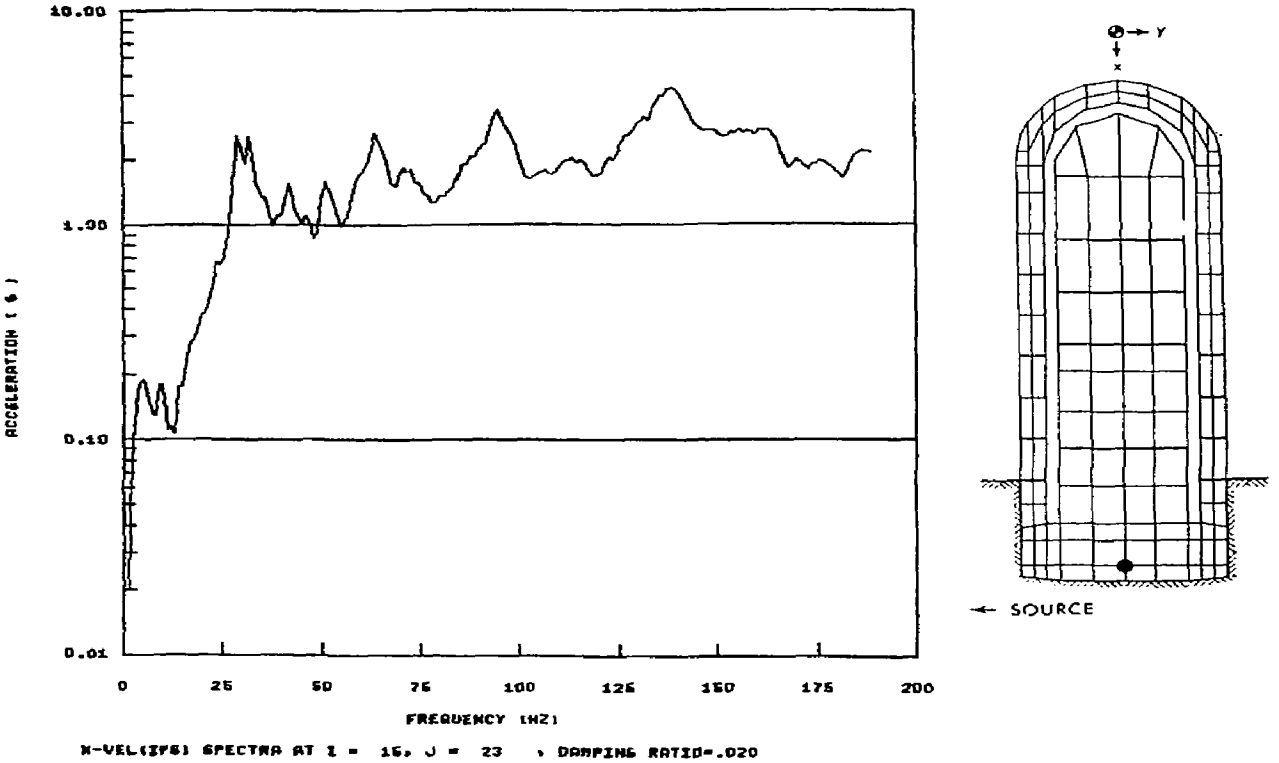

Figure 3-72b. Unfiltered acceleration response spectra of vertical motion of foundation (elev -11.05m, centerline). (See Fig. 3-14b for filtered response spectra.)

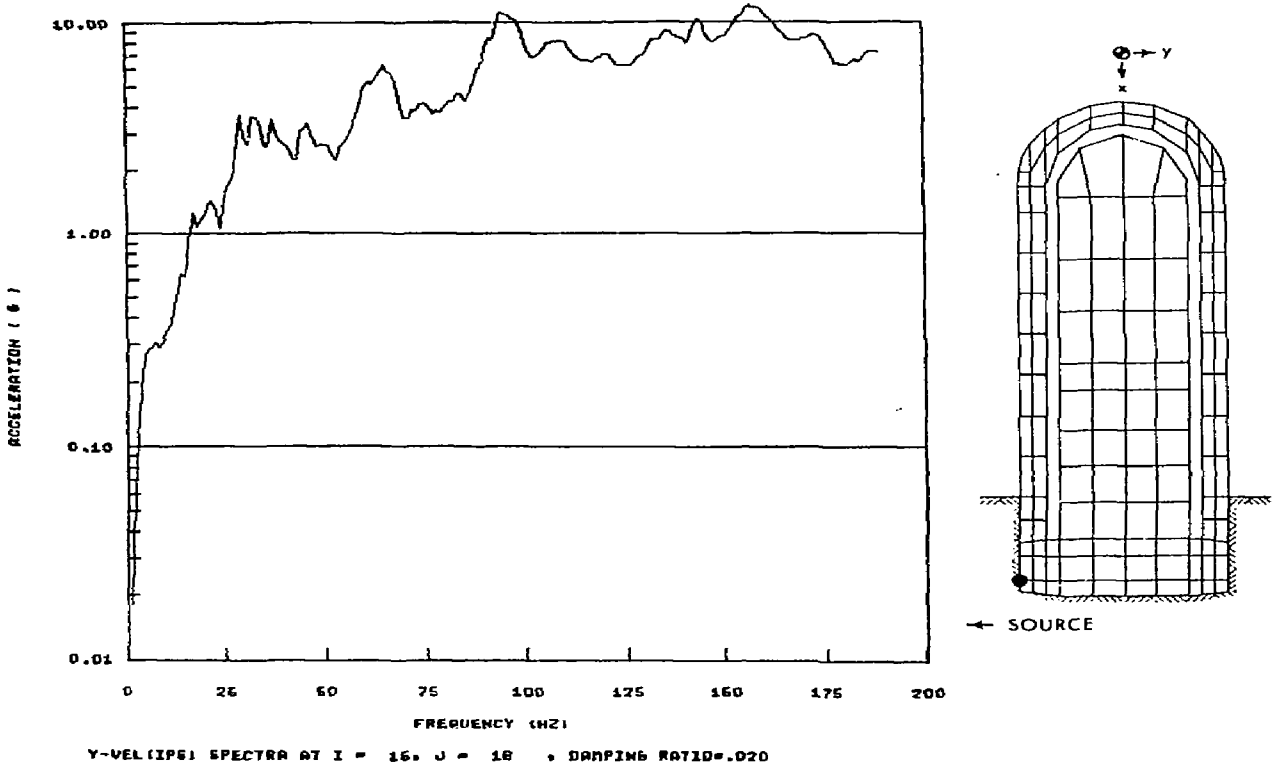

Figure 3-72c. Unfiltered acceleration response spectra of horizontal motion near upstream corner of foundation (elev -11.05m, 11.35m forward of centerline). (See Fig. 3-19b for filtered response spectra.)

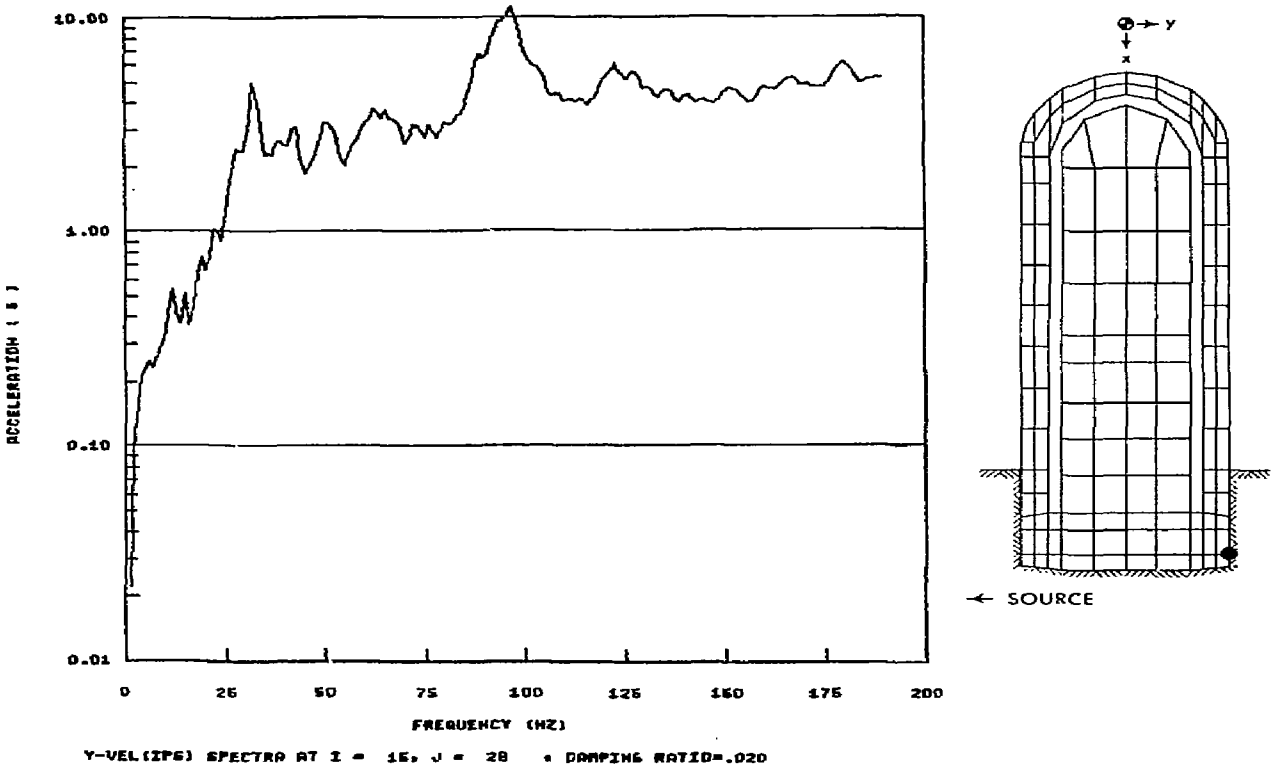

Figure 3-72d. Unfiltered acceleration response spectra of horizontal motion near downstream corner of foundation (elev -11.05m, 11.35m aft of centerline). (See Fig. 3-25b for filtered response spectra.)

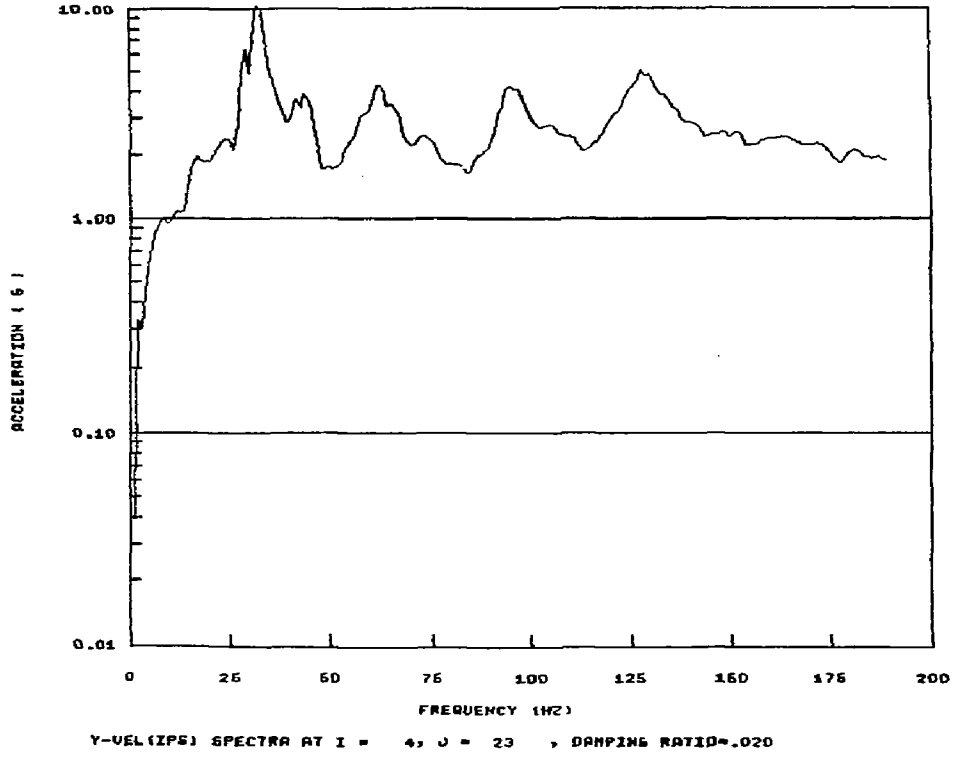

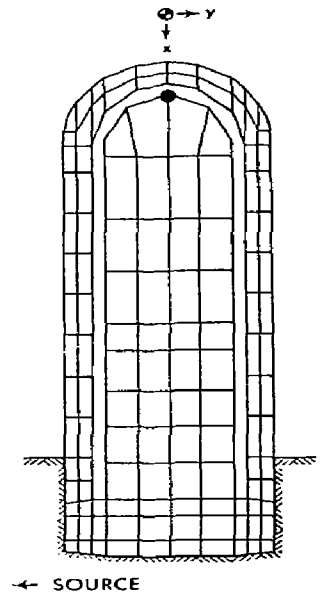

Figure 3-72e. Unfiltered acceleration response spectra of horizontal motion at top of inner structure (elev 47.35m, centerline). (See Fig. 3-31b for filtered response spectra.)

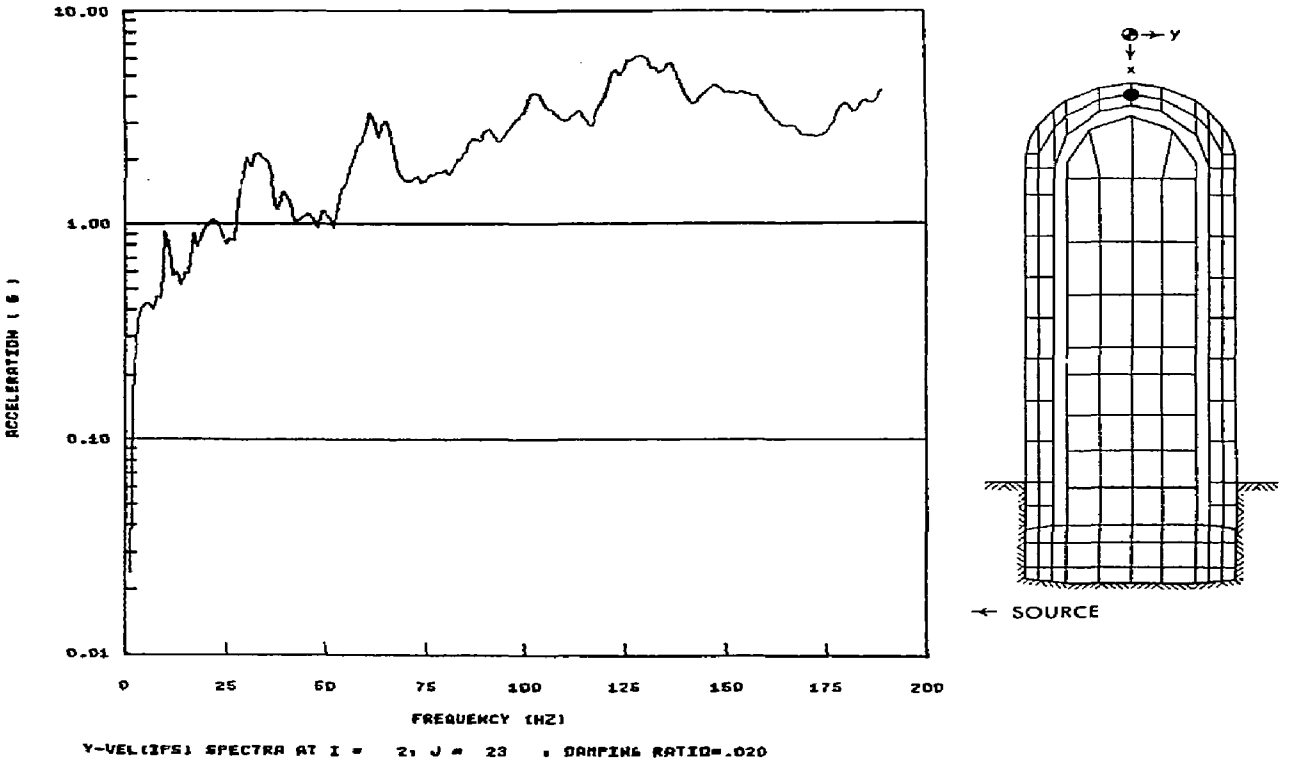

Figure 3-72f. Unfiltered acceleration response spectra of horizontal motion at top of outer structure (elev 50.35m, centerline). (See Fig. 3-55b for filtered response spectra.)

4. SUMMARY AND COMMENTS

1. The goals of the project set forth in Section 1 were achieved.
2. The model of the explosive source contains the greatest uncertainties and potential for introducing error into the overall analysis. A means should be found to evaluate the model of soil-structure interaction and structural response independently of errors introduced through the source model. Increased free field instrumentation, including gages embedded in the soil in front of and beneath the foundation, would be helpful in this regard.
3. The predicted free field spectral response has a peak at about 4-5 Hz, which is a little higher than in previous tests.
4. Soil-structure interaction consists of initial rocking back toward the source, followed by low amplitude rocking oscillations at 1.5-2 Hz. The foundation follows the free field in translating outward and downward. The strong motion of the foundation lasts .3 and .4 seconds. Cavitation (separation between soil and structure) occurs on the upstream side only.
5. Structural response consists of horizontal oscillation of the inner structure at primarily its fundamental frequency of 1.7 Hz. Horizontal oscillation of the outer structure occurs primarily in its second mode at 2.7 Hz. These modes appear to be substantially uncoupled in the TRANAL analysis.

There is also significant response of the inner structure in the third mode at about 7 Hz and of the outer structure in the 4th mode at about 11 Hz. Peak horizontal accelerations range from about .6g at the top of the inner structure to about .1g at piping support points for records filtered above 25 Hz.

REFERENCES

1. _____, "Individual Project 4000 (Earthquake Simulation) Determination of Dynamic Characteristic of Soils — Final Report," PHDR-NR: 4.16/75 BGR, Gesellschaft für Kernforschung (GFK), Hanover, June 1975.

2. Schwab, H., "Project HDR-KAHL: Laboratory Investigations," Testing Institute for Soil Mechanics and Foundation Engineering, May 1979.

3. DiMaggio, F. L. and I. S. Sandler, "Material Models for Soils," J. of Eng. Mech. Div. Proc. ASCE, June 1971, p. 935.

4. Isenberg, J., D. K. Vaughan and I. S. Sandler, "Nonlinear Soil-Structure Interaction," Weidlinger Associates, Final Report to EPRI, NP-945, December 1978.

5. _____, "Dynamic Analysis and Earthqauke Simulation Studies at the Heissdampfreaktor (HDR)," Applied Nucleonics Co., Inc., Final Report 1083-2 to Gesellschaft für Kernforschung, MBH Federal Republic of West Germany, October 1975.

6. _____, "Review of HDR Dynamic Models and Development of Special Purpose Computer Programs," Applied Nucleonics Co., Inc., Final Report 1083-6 to Gesellschaft für Kernforschung, MBH, Federal Republic of West Germany, April 1977.

7. Newmark, N. M. and Emilio Rosenblueth, Fundamentals of Earthquake Engineering, Prentice-Hall Inc., 1971, p. 324.

APPENDIX A

DETERMINATION OF SITE MODEL AND FREE FIELD MOTIONS

A-1. INTRODUCTION

In order to perform three-dimensional structure medium interaction analyses for the Heissdampfreaktor (HDR), three preliminary studies were required. The studies resulted in 1) a site profile, 2) a material model for each layer in the profile, and 3) a source characterization appropriate to provide structure-medium interaction input (free field behavior). These studies are reported here.

A-2. SITE PROFILE

The site profile was inferred from Refs. A-1 and A-2. Based primarily on seismic methods, Ref. A-1 reports the profile shown in Table A-1. Based on the grain size distribution data for two boreholes given in Ref. A-2, it appears that the variability of materials below the 12m depth (Layers 3, 4, 5 of Table A-1) is sufficiently random for all of these materials to be considered as a single composite layer.

Further, from discussions with the personnel of ANCO Engineers, Ref. A-3, it appears that the water table at the site is at a depth of approximately three to five meters. In addition, the mechanical compression tests of Ref. A-1 show very little difference in effective stress-strain behavior across the water table.

The above considerations lead to the site profile shown in Fig. A-1. In this profile the top three meters of the site is dry loose sand and gravel with a primary wavespeed of about 300 m/sec. The second layer, which is also 3m thick, is a more compacted material containing very little water and having a wavespeed of about 400 m/sec. Below this lies a third layer which is still further compacted and contains a substantial amount of water, but is not fully saturated. In this layer the wavespeed is about 700 m/sec. The fourth and last layer, which extends below the depth of 12m, is fully saturated sand, gravel and silt and has a primary wavespeed of about 1600 m/sec.

Table A-2 shows the comparisons of the measured wavespeeds with those in the postulated site profile.

A-3. MATERIAL MODELS

Based on the qualitative and quantitative information discussed above and on the laboratory stress versus strain measurements reported in Ref. A-2, material models were developed to represent the mechanical behavior of the layers in Fig. A-1. These models are valid only at fairly low pressures because the laboratory tests were conducted only up to stresses of two to three megapascals.

The information presented in Ref. A-2 consists of composite effective shear strength and stiffness measurements at varying confining pressures together with stress-strain measurements in unconfined cyclic compression tests.

On the basis of this information, the nonlinear cap constitutive model, Ref. A-4, was constructed to represent the various layers. The basic features of the cap model are shown in Fig. A-2. The model is elastic-plastic with a yield surface which consists of an ideally plastic failure envelope, together with an isotropically hardening cap. For stress points within the yield surface, i.e. for unloading and reloading, the model behaves elastically with wavespeeds corresponding to the seismic moduli. For stress points on either portion of the yield surface, the plastic strain rate is defined by the classical flow rule based on the plastic potential associated with the yield condition. Soil hysteresis in shear is modeled primarily by the failure envelope, while compaction is handled by the cap.

Figure A-2 shows how the cap is used to control dilatancy, which is observed only to a limited extent in most soils during unconfined or triaxial compression. After initial consolidation, during which the cap is pushed out, loading to failure produces dilatancy. As this proceeds, how-

ever, the cap moves back because its position depends on the soil compaction. The dilatancy must stop when the cap returns to the stress point because that point cannot lie outside the yield surface.

Figure A-3 shows the behavior in uniaxial strain obtained from the models constructed for the HDR materials of Fig. A-1. These curves illustrate the increasing stiffness and decreasing compactibility to be expected from the HDR materials as the depth increases. The stress paths associated with the uniaxial strain curves for layers 1 and 4 are shown in Fig. A-4, together with the failure envelopes. Although the stress paths at low pressures are qualitatively similar, the failure envelopes exhibit a fundamental difference between wet and dry materials at higher stress levels. The failure envelope for layer 1, which is dry and therefore a frictional material, is roughly linear to fairly high pressures. The shear strength of layer 4, which is wet, is limited at high pressures because the lubricated intergranular surfaces cannot support high frictional forces in the material.

It should be pointed out that the models for the HDR site are based on extremely limited data. More complete suites of laboratory and field tests would be required to get a good representation of the behavior of these materials. In particular, the low amplitude cyclic hysteresis of the material, for which a recent extension of the cap model, Ref. A-5, was developed, was not modeled for lack of appropriate data.

A-4. SOURCE REPRESENTATION

In order to obtain the proper structural excitation in the HDR calculations, a representation of the source region is required. There are several approaches which can be used to obtain such a representation. One method is to perform an explosive and ground interaction calculation including the details of the source detonation. A second approach is to base the near-structure ground response on purely empirical information. A third method, which combines empirical and computational studies, will be described below. This was the procedure actually employed in this study. The reasons for using it are given below.

A "first-principles" calculation which includes the explosive process itself requires detailed information with respect to the shape of the explosive and the actual excavation, emplacement and tamping procedures employed. Further information as to the explosive's detonation properties and the high temperature-high pressure behavior of the in-situ materials surrounding it would be needed. Even if such information were available, the calculation would be extremely expensive, and quite outside the scope of this effort in both time and cost.

At the opposite extreme is the determination of ground response from previous data. This, in fact, was partially done by ANCO, Ref. A-3, on the basis of data measured during the previous test program at the HDR site. This work focused on the peak ground response and the response spectrum of the ground motion, but it did not give detailed motion or stress waveforms. Because the previous data was obtained from explosive yields much smaller than the 50 kg charge weight used for the current analysis, one would expect that the deeper layers were not as strongly excited. There-

fore the waveforms to be expected in the current case are probably quite different than those previously observed. Simple extrapolation from the earlier measurements at HDR, while satisfactory for predicting approximate excitation levels, are not likely to lead to appropriate ground response histories for interaction analysis.

The third approach, which is the one applied in this study, combines calculations with experimental data. Because realistic ground shock calculations can be performed only where appropriate material models are available (in this case for pressures below a few megapascals) only the far field or low pressure portion of the free field response can be obtained by calculation. It was decided therefore that the field motions would be calculated beyond the ground range at which peak pressure drops to 1.38 megapascals (200 pounds per square inch).

In order to perform the analysis, the range R at which this peak pressure occurs and the pressure time history at this range must be determined. The latter represents the input boundary condition to the far field calculation while the former defines the boundary on which this condition is applied. The range R may be determined from empirical relations for soil pressure as a function of range from buried explosions. The simplest such empirical formula, Refs. A-6, A-7, for deep bursts is

$$P = F\,E\,k\,(R/W^{1/3})^{-3} \qquad \text{(A-1)}$$

where P is the peak pressure, F and E are coefficients (approximately equal to unity for the explosive and burial depth of HDR), k is a soil parameter, R is the range in feet and W is the charge weight in lbs. Solving for R gives

$$R = (kW/P)^{1/3} \qquad \text{(A-2)}$$

for $F \approx E \approx 1$. There is considerable uncertainty in the appropriate value for k. For the HDR site k may range from 10^4 to above 10^5, depending on local material composition. For a peak pressure of 200 psi and charge weight of 50 kg, Eq. A-2 gives a range between 18 ft and 38 ft. Therefore, for lack of better information, a range of 8.5m (28 ft) was chosen for R.

The applied boundary pressure time history was chosen to be a sharp rise followed by an exponential decay. Although this is clearly an idealization, the choice of a more complicated history is not warranted because of the overall problem uncertainties. The actual rise time for the pressure would probably be on the order of a few milliseconds, but this would represent too high a frequency to be carried by a reasonable computational grid. Therefore, an instantaneous rise is appropriate as an idealization for the purpose of the present analysis.

The decay time in the exponential pressure function was chosen to be 100 milliseconds. This is based on Project MOLE measurements, Ref. A-8, made on buried charges of a similar size to the 50 kg size considered here. The characteristic times in MOLE varied with the site properties and scattered over an order of magnitude, but such a choice of time constant seems reasonable. It also seems consistent with previous HDR measurements which show a strong 13 cps motion component from a 10 kg yield. In any event, because of lack of sufficiently relevant in-situ tests, it appears impossible to make a better prediction of the pressure time history than that just described.

The chosen source representation is shown in Fig. A-5. As can be seen from the figure, the spherical boundary to which the input pressure is applied is 8.5m in radius and its center is at a depth of 11.3m (which cor-

responds to the depth to the center of the planned 50 kg charge). To evaluate the source model, axisymmetric free-field calculations were performed using the Weidlinger Associates' LAYER finite difference code. (Actually, several runs were made in which both the peak pressure P_o and the decay time τ were varied. The results, which are not presented here because complete graphical output was not obtained, gave no reason to alter the values of P_o and τ from those shown in Fig. A-5.)

The results of the free-field calculations are shown in Figs. A-6 through A-13. In Figs. A-6 and A-7, the horizontal (outward) and vertical (downward) components of velocity are shown at the 44 ft horizontal range at depths of 1, 19 and 39 feet. These figures show the (still) predominantly radial nature of the motions at this close range, with the nearer surface motions larger and occurring later than the motions at depth. This is due to the softer nature of the upper layers. Figures A-8 and A-9 show the same output at the 74 ft range. Here the magnitudes of the horizontal and vertical velocities are more nearly equal to each other. The vertical velocities are predominantly downward after a short upward phase. The reason for this is that the upper layers, which are driven upward near the source, dissipate much more energy than the deeper layer, which is driven down. As the upper layers dissipate the energy initially deposited in them, the downward motion of the deep layer becomes more and more dominant with range. This layer then drags the upper layers down with it at the further ranges.

The results at the 104 ft range are shown in Figs. A-10 and A-11. This range corresponds roughly to location of the center of the structure. At this range the magnitude of the signal is greatly reduced from the closer-in values. Furthermore, the oscillatory nature of the motion has become ap-

parent, illustrating the important role of the layering of the site in determining the response. Figures A-12 and A-13, which illustrate the results for the 134 ft range, show the further attenuation of the signal and additional development of cyclic motion. At this range, surface and interface waves are probably an important part of the overall ground motion.

One important result which is apparent from Figs. A-10 thorugh A-13 is the rapid variation in the ground motion across the region in which the structure is supposed to be. Therefore, any successful attempt to measure free field ground motions would require a fairly dense array of gauges to adequately resolve systematic variations in ground response with range as differentiated from the random variations resulting from the usual causes of data scatter in ground motion measurements.

A-5. SUMMARY AND COMMENTS

A profile of the HDR site, a set of material models for the several layers at the site, and a source representation of a buried 50 kg explosion at the site have been obtained. This is in a form which can and has been used for three-dimensional structure medium interaction analysis.

Due to the paucity of relevant data, the models for the site and source undoubtedly contain great potential for the introduction of error into the subsequent interaction analysis. Although this is presently unavoidable, appropriate free field measurements could substantially improve the situation for any future efforts of this type.

TABLE A-1. SITE PROFILE FROM REFERENCE A-1

LAYER	DEPTH (m)	SOIL TYPE (according to German Standard)
1	0-6	sandy gravel
2	6-12	coarse-sandy fine gravel
3	12-20	sandy coarse gravel
4	20-26	silty clay, coal
5	>26-	silt, fine sand

TABLE A-2. WAVESPEEDS IN VARIOUS LAYERS

(See Figure A-1)

	LAYER 1	LAYER 2	LAYER 3	LAYER 4
DEPTH (m)	0-3	3-6	6-12	12-
WAVESPEEDS (m/sec)				
Model				
c_p	330.	392.	703.	1585.
c_s	131.	185.	280.	519.
Measured				
c_p	297.	(not measured)	595.	1585.
c_s	——— not measured ———			

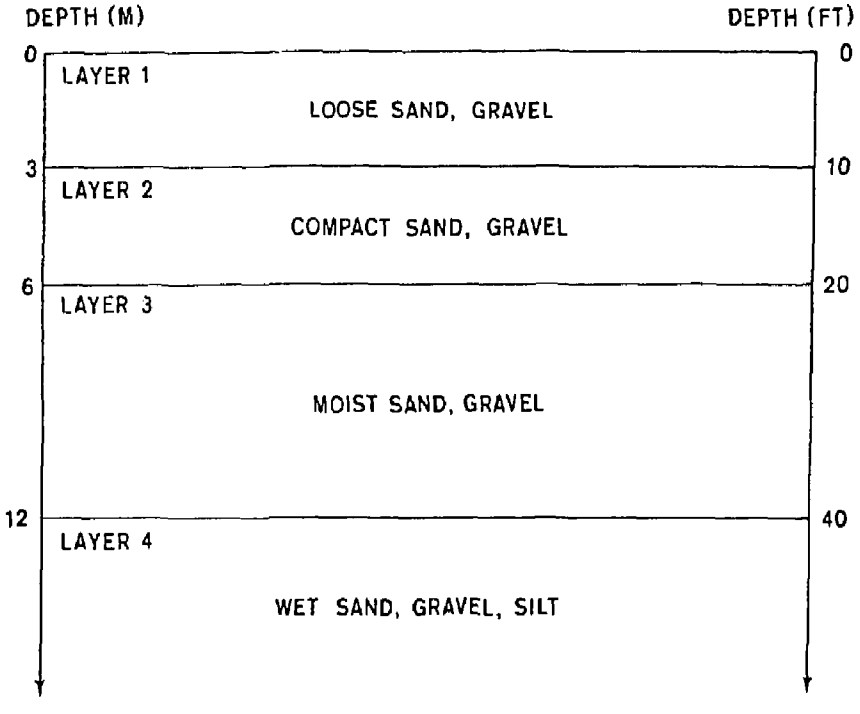

Figure A-1. Site profile used in HDR analysis.

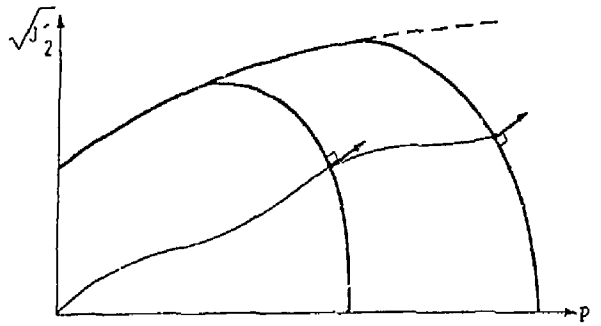

a. Stress point initially pushes cap out

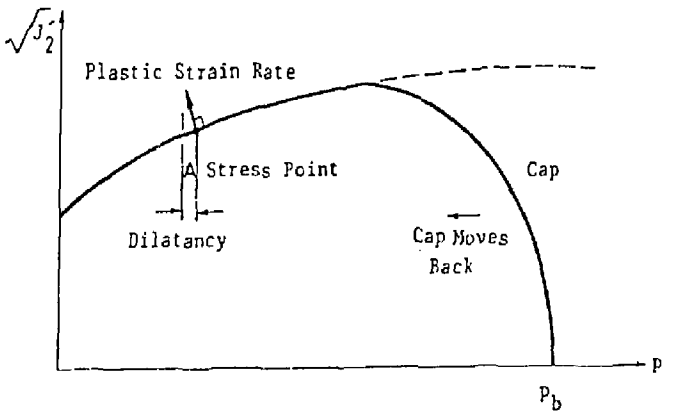

b. In soil model the cap moves back when failure occurs

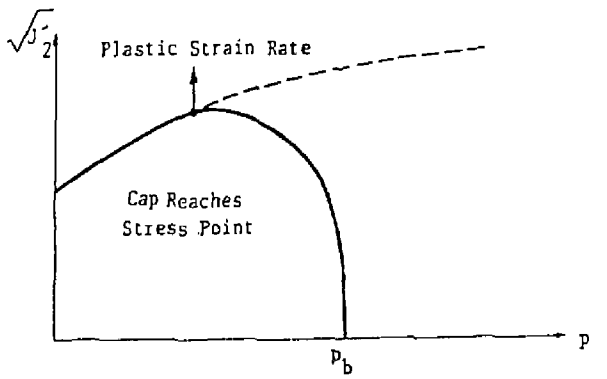

c. The backward cap movement is limited when the cap reaches the stress point

Figure A-2. Cap model used to represent properties of soil in HDR analysis. Stress point on cap pushes cap out. When stress point is on failure surface, cap moves in to control dilatancy.

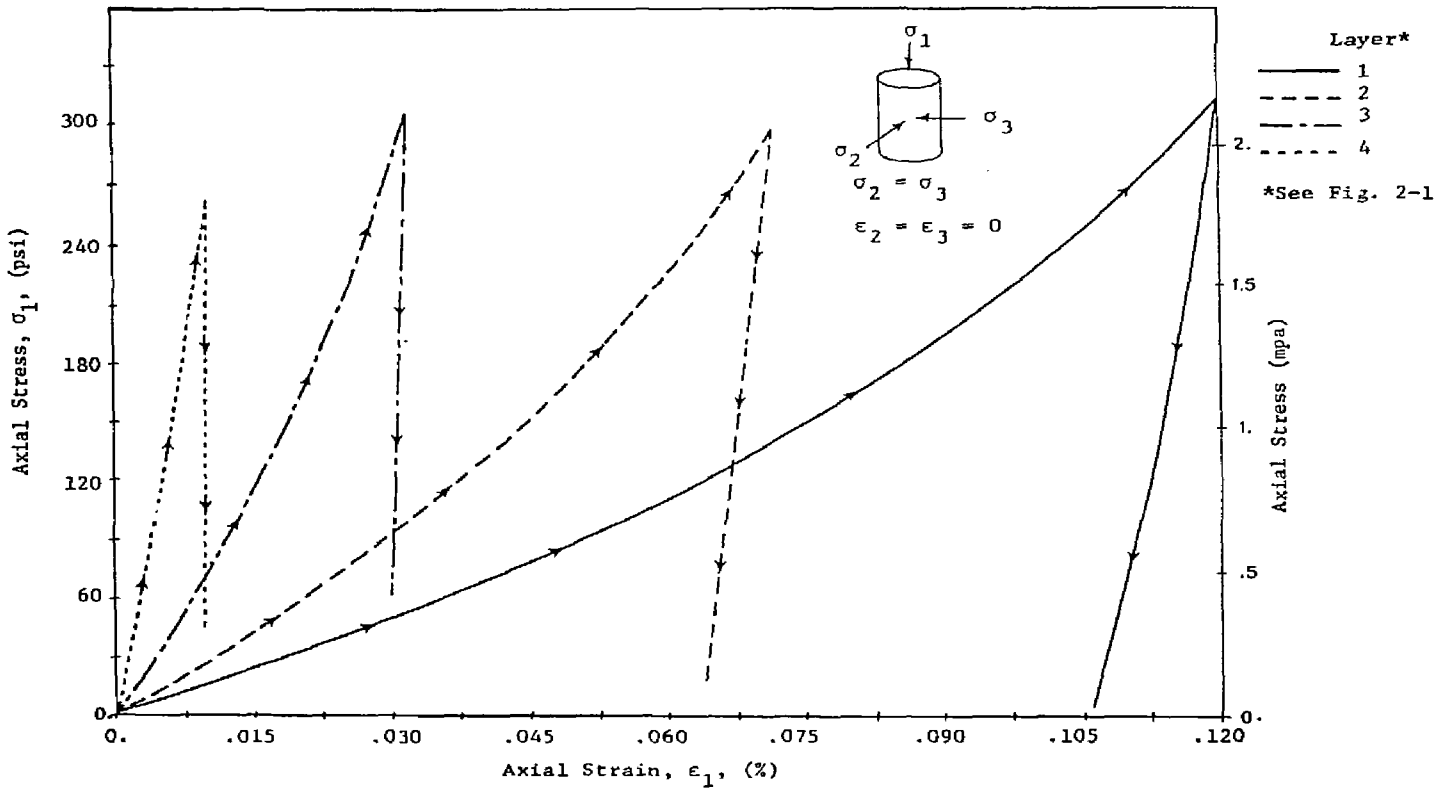

Figure A-3. Stress-strain properties (uniaxial strain) of each layer in HDR site profile.

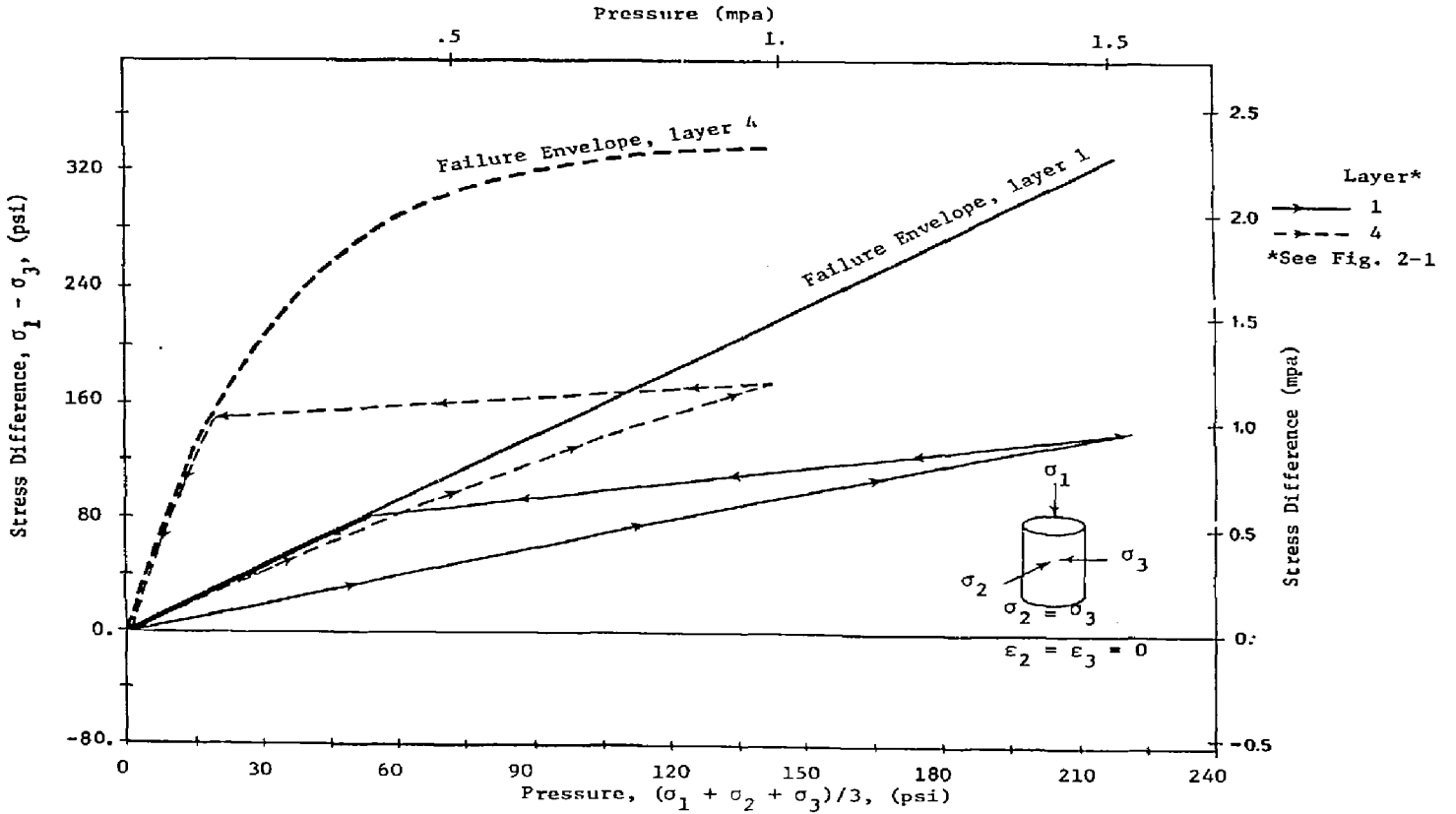

Figure A-4. Stress path experienced by soils in layers 1 and 4 of HDR site profile when subjected to uniaxial strain.

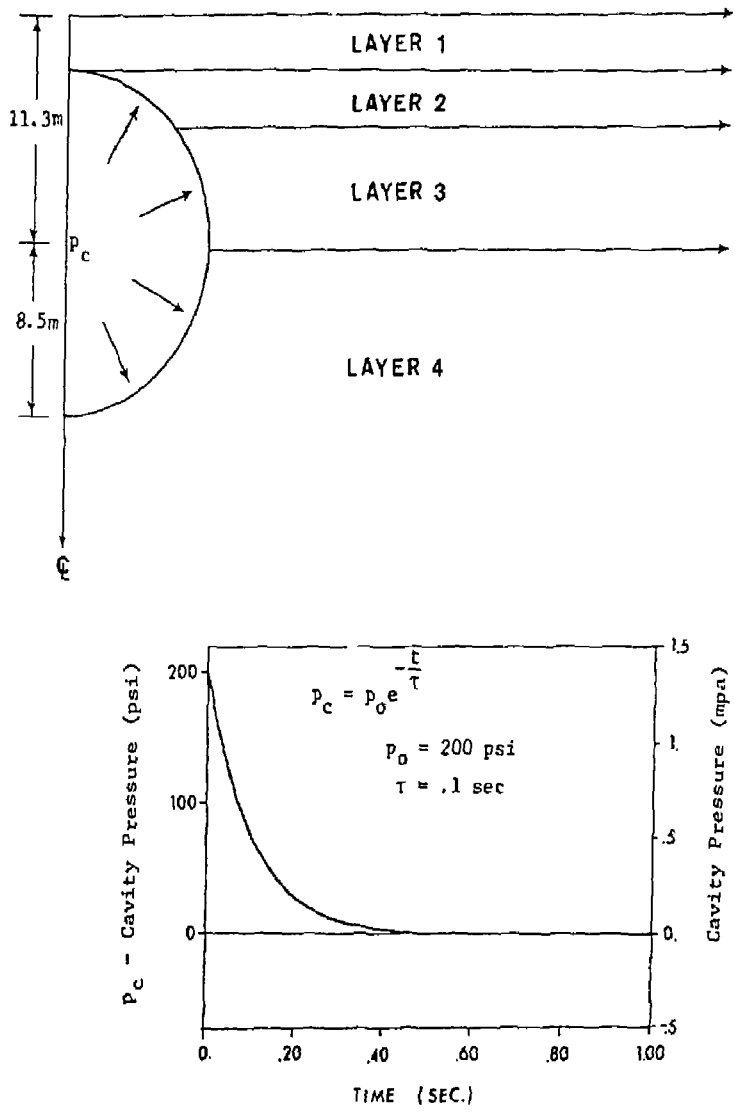

Figure A-5. Model of source used as input for free field and soil-structure interaction analysis.

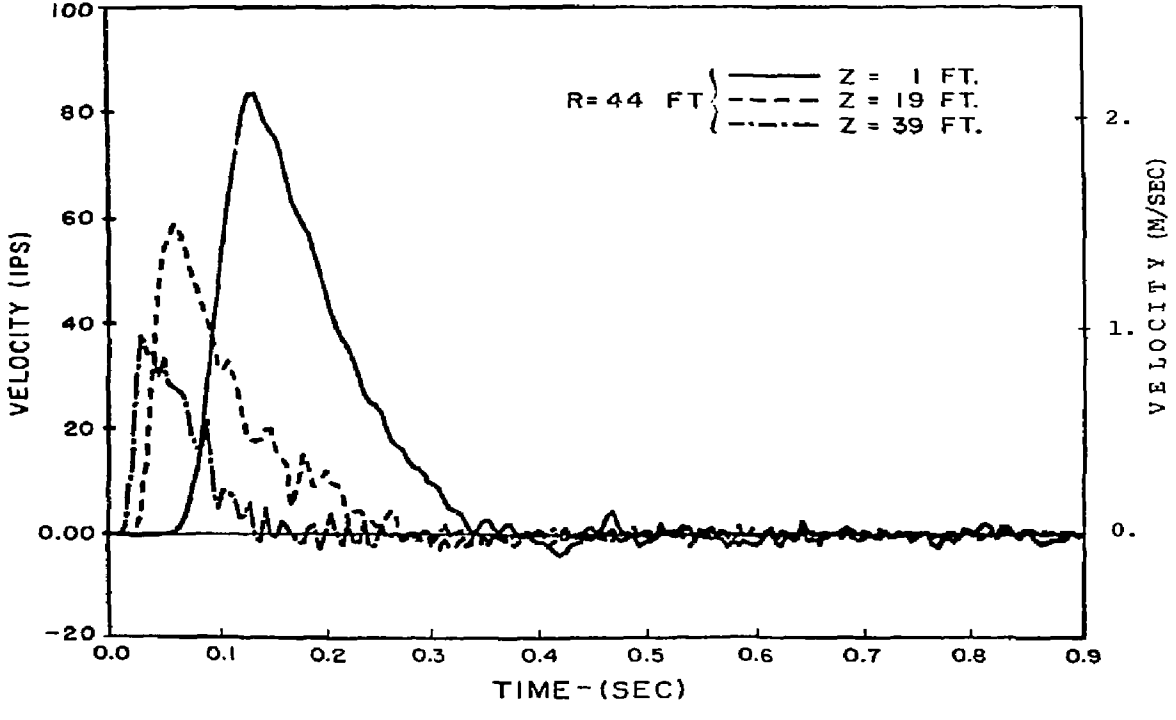

FIG. A6 HDR FREE FIELD

(HORIZONTAL)

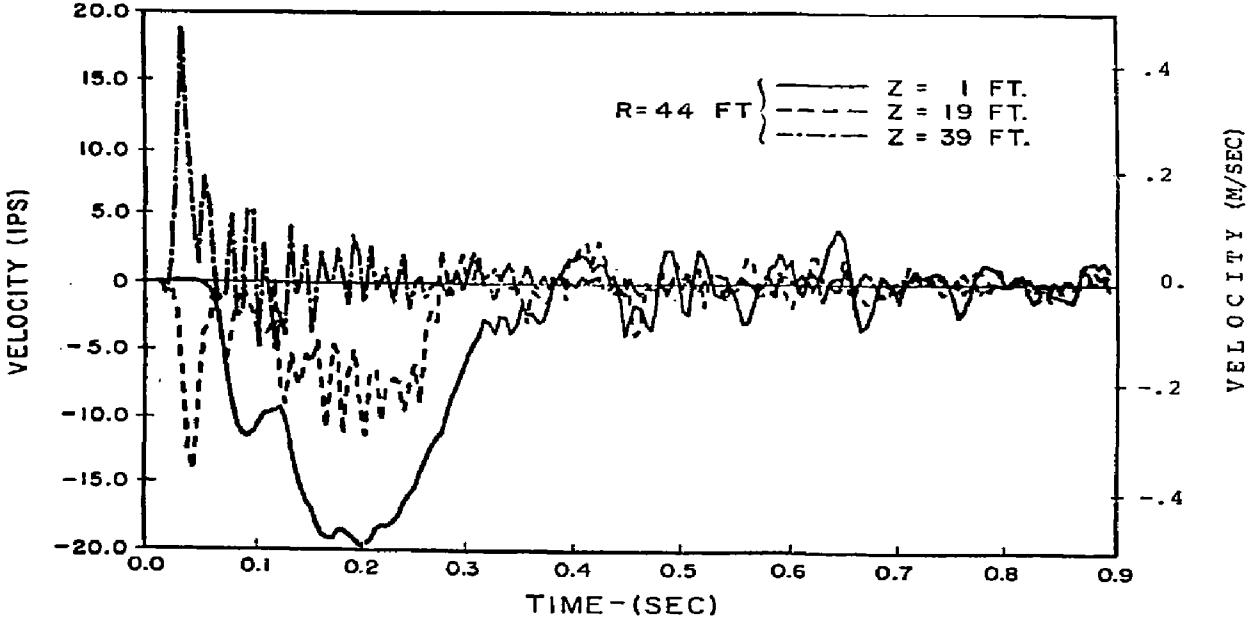

FIG. A7 HDR FREE FIELD

(VERTICAL)

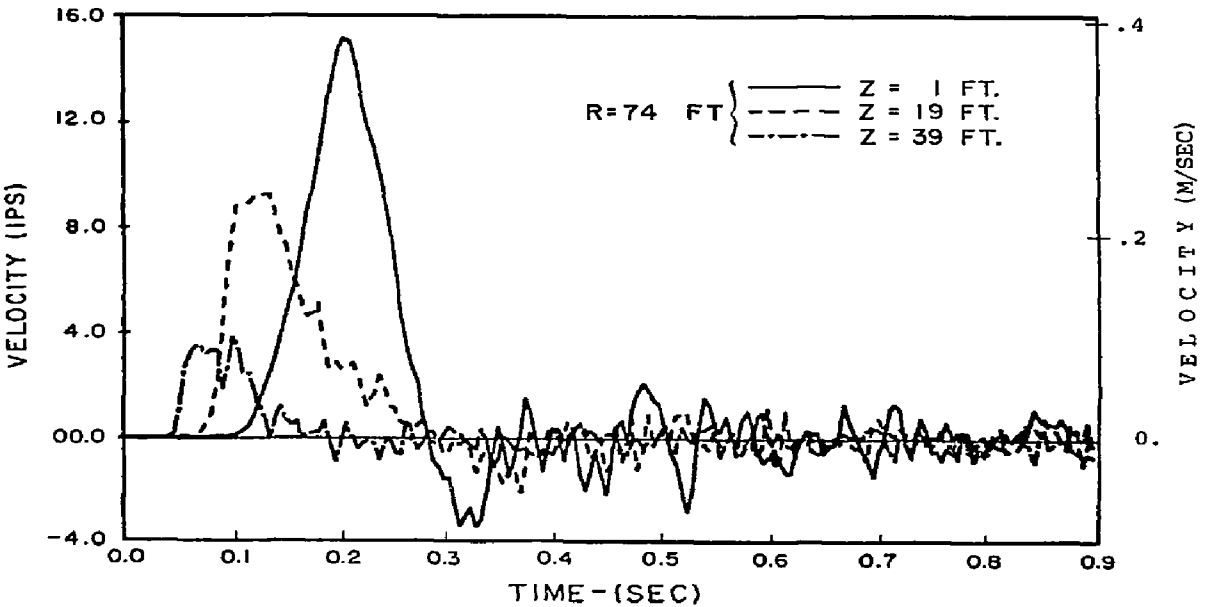

FIG. A8 HDR FREE FIELD

(HORIZONTAL)

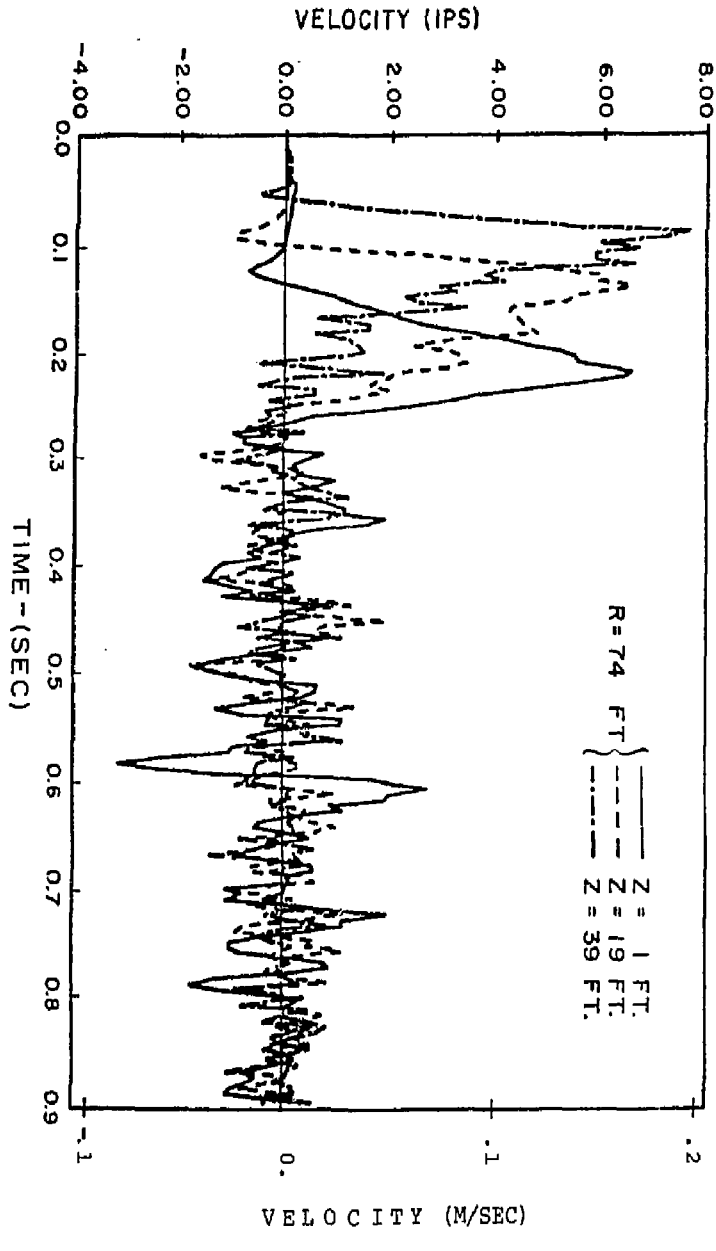

FIG. A9 HDR FREE FIELD

(VERTICAL)

FIG. A10 HDR FREE FIELD

(HORIZONTAL)

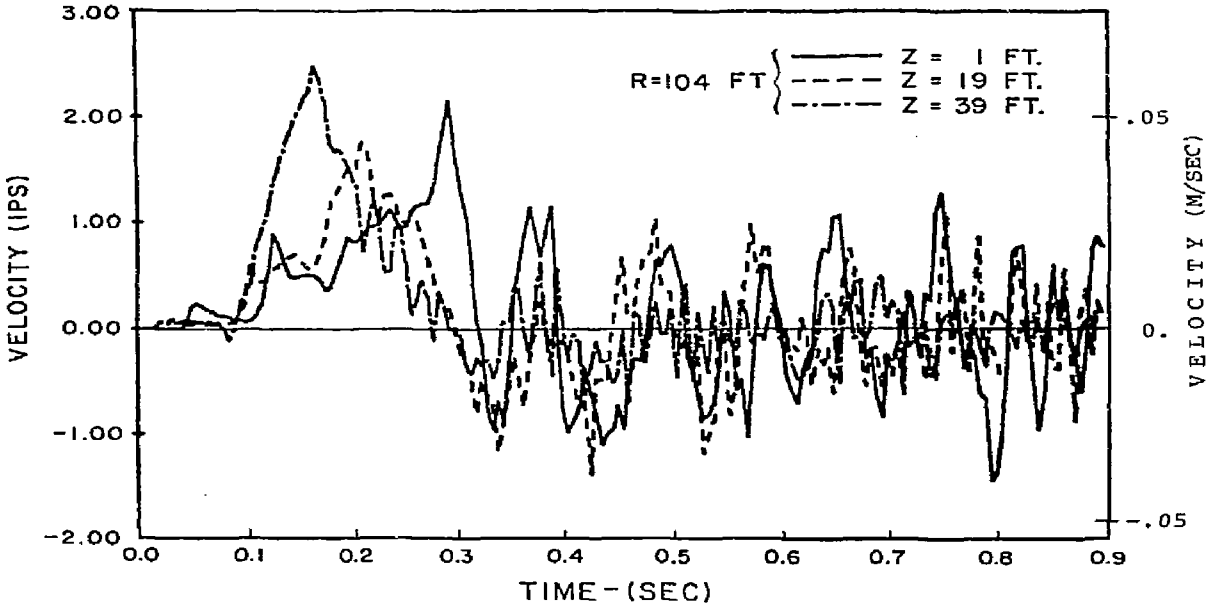

FIG. AII HDR FREE FIELD
(VERTICAL)

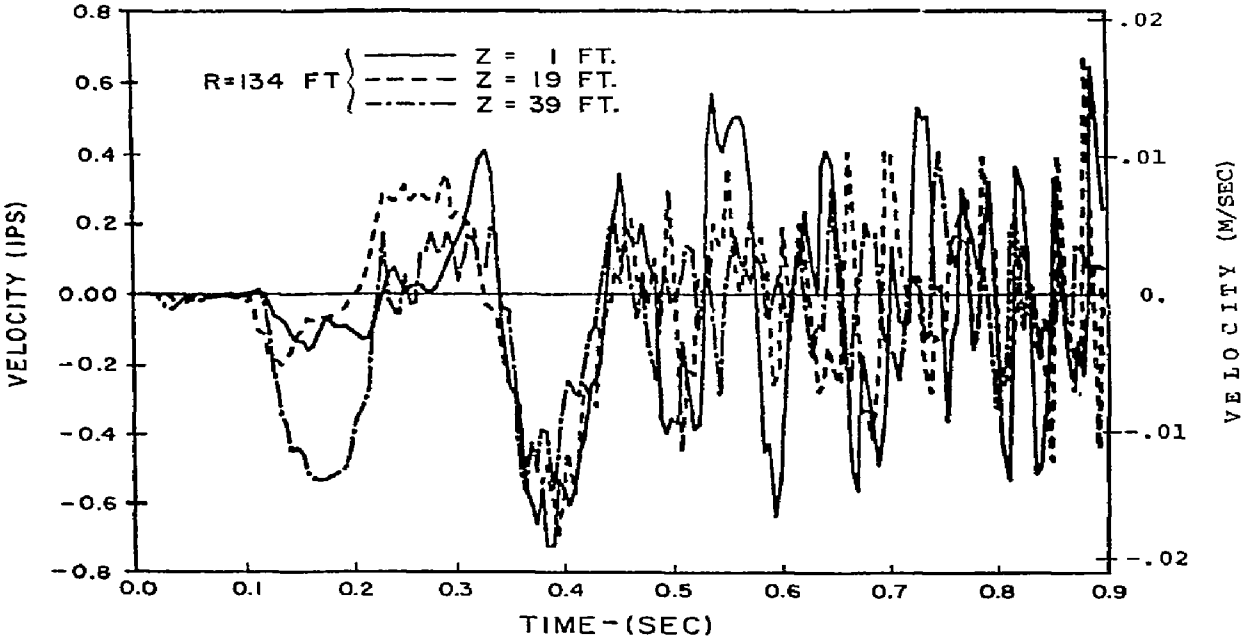

FIG. A12 HDR FREE FIELD

(HORIZONTAL)

FIG. A13 HDR FREE FIELD

(VERTICAL)

REFERENCES — APPENDIX A

A-1. UCIR-1297 English translation of German document No. PHDR-No. 4.16/75 BCR entitled, "HDR Safety Program Individual Project 4000 (Earthquake Simulation) Determination of Dynamic Characteristics of Soils-Final Report."

A-2. UCIR-1291 English translation of German document, "44/78 Project HDR-Kahl; Specifically: Laboratory Investigations."

A-3. Ibanez, P. and W. Gundy — private communication.

A-4. DiMaggio, F. L. and I. S. Sandler, "Material Model for Soils," J. Engrg. Mech., ASCE, 1971.

A-5. Isenberg, J., D. K. Vaughan and I. S. Sandler, "Nonlinear Soil-Structure Interaction, Weidlinger Associates, Final Report to EPRI, NP-945, 1978.

A-6. Lampson, C. W., "Explosions in Earth," Effects of Impact and Explosions, Div. 2, National Defense Research Committee, Vol. 1, 1946.

A-7. Higgins, C. J., R. L. Johnson and G. E. Triandafilidis, "The Simulation of Earthquake-Like Ground Motions with High Explosives," University of New Mexico, Department of Civil Engineering, Report to National Science Foundation, 1978.

A-8. Sachs, D. C. and L. M. Swift, "Small Explosion Tests — Project MOLE," Final Report AFSWP-291, Stanford Research Institute, 1955.